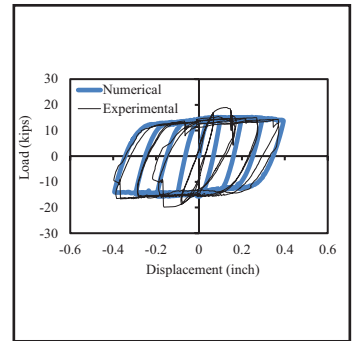
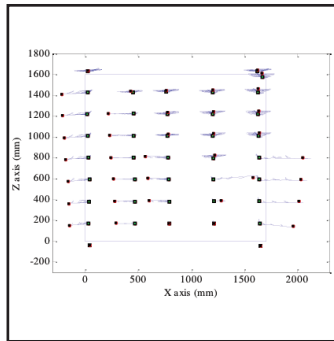
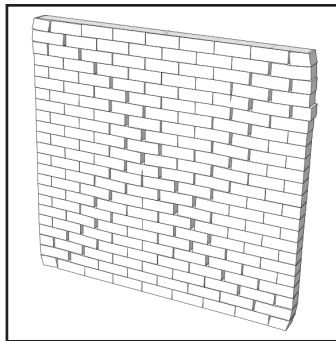


Computational, Analytical, and Experimental Modeling of Masonry Structures

by
Kiarash M. Dolatshahi and Amjad J. Aref



Technical Report MCEER-15-0004

November 16, 2015

NOTICE

This report was prepared by the University at Buffalo, State University of New York as a result of research sponsored by MCEER. Neither MCEER, associates of MCEER, its sponsors, the University at Buffalo, State University of New York, nor any person acting on their behalf:

- a. makes any warranty, express or implied, with respect to the use of any information, apparatus, method, or process disclosed in this report or that such use may not infringe upon privately owned rights; or
- b. assumes any liabilities of whatsoever kind with respect to the use of, or the damage resulting from the use of, any information, apparatus, method, or process disclosed in this report.

Any opinions, findings, and conclusions or recommendations expressed in this publication are those of the author(s) and do not necessarily reflect the views of MCEER, the National Science Foundation, or other sponsors.

Computational, Analytical, and Experimental Modeling of Masonry Structures

by

Kiarash M. Dolatshahi¹ and Amjad J. Aref²

Publication Date: November 16, 2015

Submittal Date: January 5, 2015

Technical Report MCEER-15-0004

MCEER Thrust Area 2, Sustainable and Resilient Buildings

1. Assistant Professor, Department of Civil, Structural and Environmental Engineering, Sharif University of Technology, Tehran, Iran and former Ph.D. Candidate, Department of Civil, Structural and Environmental Engineering, University at Buffalo, State University of New York
2. Professor, Department of Civil, Structural and Environmental Engineering, University at Buffalo, State University of New York

MCEER

University at Buffalo, State University of New York

212 Ketter Hall, Buffalo, NY 14260

E-mail: mceer@buffalo.edu; Website: <http://mceer.buffalo.edu>

[@Seismicisolation](#)

PREFACE

MCEER is a national center of excellence dedicated to the discovery and development of new knowledge, tools and technologies that equip communities to become more disaster resilient in the face of earthquakes and other extreme events. MCEER accomplishes this through a system of multidisciplinary, multi-hazard research, education and outreach initiatives.

Headquartered at the University at Buffalo, State University of New York, MCEER was originally established by the National Science Foundation (NSF) in 1986, as the first National Center for Earthquake Engineering Research (NCEER). In 1998, it became known as the Multidisciplinary Center for Earthquake Engineering Research (MCEER), from which the current name, MCEER, evolved.

Comprising a consortium of researchers and industry partners from numerous disciplines and institutions throughout the United States, MCEER's mission has expanded from its original focus on earthquake engineering to one which addresses the technical and socioeconomic impacts of a variety of hazards, both natural and man-made, on critical infrastructure, facilities, and society.

MCEER investigators derive support from the State of New York, National Science Foundation, Federal Highway Administration, National Institute of Standards and Technology, Department of Homeland Security/Federal Emergency Management Agency, other state governments, academic institutions, foreign governments and private industry.

Existing material models and numerical procedures have been limited to capturing either in-plane or out-of-plane behavior of masonry walls. Similarly, most experimental studies have focused on two-dimensional behavior of walls and buildings, and there is very little data on the interaction of in-plane and out-of-plane response. This report addresses gaps in knowledge pertaining to modeling of masonry structures subjected to extreme loadings by developing robust constitutive material models and three-dimensional numerical procedures, and validating them using experimental data conducted by the authors. The proposed constitutive material models use implicit and explicit formulations, and work seamlessly with commercial finite element software such as TNO DIANA and ABAQUS.

[@Seismicisolation](#)

ABSTRACT

Existing material models and numerical procedures have been limited to capturing either in-plane or out-of-plane behavior of masonry walls. Similarly, most experimental studies have focused on two-dimensional behavior of walls and buildings, and there is very little data on the interaction of in-plane and out-of-plane response. This report addresses gaps in knowledge pertaining to modeling of masonry structures subjected to extreme loadings by developing robust constitutive material models and three-dimensional numerical procedures, and validating them using experimental data conducted by the authors. The proposed constitutive material models use implicit and explicit formulations, and work seamlessly with commercial finite element software such as TNO DIANA and ABAQUS.

[@Seismicisolation](#)

ACKNOWLEDGEMENTS

The studies described in this report were funded by MCEER and the State of New York. This support is gratefully acknowledged. We thank the staff of the Center for Computational Research at the University at Buffalo, the John H. Black Company for donating materials for the experimental studies, and the staff of the Structural and Earthquake Engineering Simulation Laboratory for their assistance in conducting the experiments.

Any opinions, findings, conclusions or recommendations expressed in this report are those of the authors and do not necessarily reflect those of MCEER or the University at Buffalo.

[@Seismicisolation](#)

TABLE OF CONTENTS

SECTION 1 INTRODUCTION.....	1
1.1 Introduction	1
1.2 Research objectives	1
1.3 Report organization	2
SECTION 2 BACKGROUND AND LITERATURE REVIEW	5
2.1 Micro- and meso- scale analysis	6
2.2 Macro-scale analysis	12
2.3 Bidirectional modeling of URM walls	15
2.4 Experimental studies	17
SECTION 3 TWO-DIMENSIONAL COMPUTATIONAL FRAMEWORK OF MESO-SCALE RIGID AND LINE INTERFACE ELEMENTS FOR MASONRY STRUCTURES.	19
3.1 Introduction	19
3.2 Description of the model	19
3.3 Elastic behavior	21
3.4 Plastic behavior	22
3.5 Algorithms to detect and update the contact zones	27
3.6 Dynamic equation of motion.....	29
3.7 Displacement vector	30
3.8 Mass, viscous and stiffness matrix.....	31
3.9 Numerical validation	31
3.9.1 Model #1 - Two rigid blocks per brick model (2PB) under 30 kN load.....	32
3.9.2 Model #2 - Four rigid blocks per brick model (4PB) under 30 kN load	35
3.9.3 Model #1 - Two rigid blocks per brick model (2PB) under 120 kN load (J6D).....	39
3.10 Comparison of the results	41
3.11 Summary and conclusion.....	45
SECTION 4 MODIFIED CAP PLASTICITY MODEL FOR INTERFACE ELEMENTS WITH APPLICATION IN MESO-SCALE ANALYSIS OF MASONRY STRUCTURES 47	
4.1 Introduction	47

TABLE OF CONTENTS (Cont'd)

4.2	Elastic behavior of the interface elements.....	48
4.3	Yield surface for interface elements.....	49
4.4	Plastic behavior of interface elements.....	50
4.4.1	Tension cut-off regime.....	50
4.4.2	Shear regime	51
4.4.3	Cap regime for high compressive stresses	53
4.5	Shortcomings of the existing yield surface	54
4.6	The proposed interpolation functions.....	55
4.6.1	The area under softening-hardening behavior	58
4.6.2	Interaction of different yield surfaces.....	61
4.7	Numerical examples on a single interface element.....	62
4.8	Numerical validation for a masonry wall.....	66
4.9	Lattice model.....	67
4.9.1	Elastic behavior.....	68
4.9.2	Description of the lattice models	69
4.9.3	Comparison of the results	71
4.10	Summary and conclusion.....	76
SECTION 5 THREE-DIMENSIONAL EXPLICIT DYNAMIC PROCEDURES FOR MODELING MASONRY STRUCTURES		77
5.1	Introduction	77
5.2	Description of the finite element model.....	78
5.3	Elastic behavior of joints.....	80
5.4	Plastic behavior of joints	81
5.4.1	Tension regime.....	82
5.4.2	Shear regime	86
5.4.3	Shear and tension interaction regime.....	89
5.4.4	Cap for the yield surface.....	90
5.5	Plastic behavior of the brick elements.....	92
5.6	Explicit dynamic analysis.....	92

TABLE OF CONTENTS (Cont'd)

5.7	Numerical validation	93
5.8	Out-of-plane loading on masonry shear walls.....	105
5.9	Conclusion.....	109
SECTION 6 INTERACTION OF IN-PLANE AND OUT-OF-PLANE DISPLACEMENT OF UNREINFORCED MASONRY WALLS – NUMERICAL STUDY		111
6.1	Introduction	111
6.2	Description of the finite element model.....	112
6.3	Numerical models	114
6.4	Loading protocols.....	116
6.5	Numerical results.....	117
6.6	Cyclic loading	129
6.7	Discussion of the results.....	132
6.8	Conclusion.....	135
SECTION 7 ANALYTICAL PROCEDURES OF IN-PLANE AND OUT-OF-PLANE INTERACTION FOR UNREINFORCED MASONRY WALLS.....		137
7.1	Introduction	137
7.2	Geometry and boundary conditions	138
7.3	Distribution of stresses	139
7.3.1	Out-of-plane loading.....	139
7.3.2	Bidirectional loading.....	140
7.4	Possible failure modes for masonry walls.....	141
7.4.1	Failure modes for mortar	142
7.4.2	Failure mode for the bricks	148
7.5	Implementation in a MATLAB code	150
7.6	Examples	150
7.6.1	Example I – regular/square wall	151
7.6.2	Example II – Wide wall	154
7.6.3	Example III – short wall	157
7.7	Comparison with finite element results.....	160

TABLE OF CONTENTS (Cont'd)

7.8	Conclusion.....	163
SECTION 8 BIDIRECTIONAL EXPERIMENTAL STUDY ON MASONRY WALLS AND VALIDATION OF NUMERICAL MODELS.....		165
8.1	Introduction	165
8.2	Description of the test set-up.....	165
8.3	Material properties	170
8.4	Loading protocols.....	176
8.5	Experimental results.....	176
8.5.1	Testing of Wall 1	176
8.5.2	Testing of Wall 2	188
8.5.3	Testing of Wall 3	202
8.5.4	Testing of Wall 4	213
8.5.5	Testing of Wall 5	226
8.5.6	Testing of Wall 6	243
8.6	Evaluation of the cyclic performance.....	255
8.7	Comparison of the experimental and numerical results with ASCE 41 proposed empirical equations	257
8.8	Conclusion.....	258
SECTION 9 CONCLUSIONS AND RECOMMENDATIONS.....		261
9.1	Summary	261
9.2	Conclusions	261
9.3	Recommendations for future research.....	264
SECTION 10 REFERENCES		271

LIST OF ILLUSTRATIONS

Figure 2-1 Fracture Specimen Consisting of an Array of Rigid Particles and Their Interfaces (Zubelewicz and Bazant 1987)	8
Figure 2-2. (a) Example of two-dimensional tessellation of concrete meso-structure (b) Geometry of a connecting strut (Cusatis et al. 2003).....	11
Figure 2-3 PAVIA wall: experimental crack pattern and damage index at the end of load history (damage areas in black color) (Karapitta et al. 2010).....	12
Figure 2-4. Simulation of a masonry panel with equivalent frame method (Pasticier et al. 2008)	13
Figure 2-5. Composite spring model of a URM panel (Park et al. 2009).....	13
Figure 2-6. Proposed macro-element (Chen et al. 2008).....	14
Figure 2-7. Scheme of an irregular masonry and the ‘unit cell’ defined by four rigid elements (Casolo and S. 2004).....	15
Figure 2-8. Rigid elements subjected to (a) horizontal and (b) vertical axial loading (Casolo and S. 2004).....	15
Figure 2-9. Three-dimensional SAT model of URM infill wall (Hashemi and Mosalam 2007) .	16
Figure 2-10. Infill model using beam-column elements with fiber discretization (Kadysiewski and Mosalam 2009).....	16
Figure 3-1. Line interface element.....	20
Figure 3-2. Two generated meshes for rigid elements-line interface model	20
Figure 3-3. Calculating the stiffness of the interface elements.....	22
Figure 3-4. Model for interface elements “interface cap model” (DIANA 2008).....	23
Figure 3-5. Tensile behavior; experimental results from Pluijm (1992), $f_t = 0.30$ [N/mm ²] and $G_f^I = 0.012$ [N/mm]	24
Figure 3-6. Shear behavior; experimental results by Pluijm [15] for different confinement levels, $c = 0.87$ [N/mm ²]; $\tan\phi = 1.01$; $\tan\phi_r = 0.73$; $G_f^I = 0.058 - 0.13$ [N/mm].....	25
Figure 3-7. Hardening and softening law for cap mode (DIANA 2008).....	25
Figure 3-8. Isotropic softening.....	27
Figure 3-9. Updating contact length and detecting new contacts	28
Figure 3-10. Kinematics of the rigid elements.....	30
Figure 3-11. Step 1 and step 2 for applying the load (Lourenco 1996)	31
Figure 3-12. 2PB Model	32
Figure 3-13. Load-displacement graph for J4D and J5D wall (Based on the model 2PB).....	33
Figure 3-14. Crack path in different stages of loading (Based on the model 2PB - under 30 kN compressive load)	35
Figure 3-15. 4PB Model	36
Figure 3-16. Load-displacement graph for J4D & J5D wall (Based on the model 4PB)	37
Figure 3-17. Crack path in different stages of loading (Based on the model 4PB-under 30 kN) .	38

LIST OF ILLUSTRATIONS (Cont'd)

Figure 3-18. Load-displacement graph for J6D wall (Based on the model 2PB and 4PB)	39
Figure 3-19. Crack path in different stages of loading (Based on the model 2PB-under 120 kN) 40	40
Figure 3-20. Load-displacement graph for J4D and J5D wall (numerical and experimental)	41
Figure 3-21. Load-displacement graph for J6D wall (numerical and experimental).....	42
Figure 3-22. Comparison between the cracks obtained by the numerical and experimental models (J4D and J5D)	43
Figure 3-23. Comparison between the cracks obtained by the numerical and experimental models (J6D)	44
Figure 4-1. Line interface element.....	48
Figure 4-2. Material model for interface elements “interface cap model” (DIANA 2008).....	49
Figure 4-3. State of stress for different types of loadings.....	50
Figure 4-4. Tensile behavior; experimental results from Pluijm (1992), $f_t = 0.30 [N/mm^2]$ and $G_f^I = 0.012 [N/mm]$	51
Figure 4-5. Shear behavior; experimental results by Pluijm [15] for different confinement levels, $c = 0.87 [N/mm^2]$; $\tan\phi = 1.01$; $\tan\phi_r = 0.73$; $G_f^I = 0.058 - 0.13 [N/mm]$	52
Figure 4-6. Hardening and softening law for cap regime (DIANA 2008).....	54
Figure 4-7. The angle associated with the state of stress.....	55
Figure 4-8. Modified Cap Plasticity Model for Interface elements	57
Figure 4-9. Equalizing the energy at the corners to ensure continuity	59
Figure 4-10. The energy under compression	60
Figure 4-11. Variation of the energy by variation of the angle	61
Figure 4-12. Isotropic Softening ($0 \leq m \leq 1$).....	62
Figure 4-13. Response in pure tension.....	63
Figure 4-14. Loading path in shear with different compressive stresses.....	64
Figure 4-15. Response in shear with various compressive stresses.....	65
Figure 4-16. Response of the element to a combination of high compressive and shear stresses 65	65
Figure 4-17. Different steps of loadings (Lourenco 1996)	66
Figure 4-18. Two generated meshes for lattice model.....	68
Figure 4-19. Calculating the stiffness of the interface elements.....	69
Figure 4-20. Different mesh sizes for modeling a brick	70
Figure 4-21. Four different mesh sizes for lattice model.....	70
Figure 4-22. Load-Displacement graph for J4D and J5D wall (numerical and experimental).....	72
Figure 4-23. Load-Displacement graph for J6D wall (numerical and experimental).....	73
Figure 4-24. Comparison between the cracks obtained by the numerical and experimental models (J4D and J5D)	74
Figure 4-25. Comparison between the cracks obtained by the numerical and experimental models (J6D)	75

LIST OF ILLUSTRATIONS (Cont'd)

Figure 5-1. Eight node plane interface element (ABAQUS).....	78
Figure 5-2. Detailed model of brick and mortar	78
Figure 5-3. Numerical modeling of a masonry wall	79
Figure 5-4. Yield surface for the joints	82
Figure 5-5. Cyclic tensile loading (Oliveira and Lourenco 2004)	84
Figure 5-6. Interface element under cyclic tension (a) and shear test (b).....	85
Figure 5-7. The results of an element under tensile force.....	85
Figure 5-8. The results of an element under shear force.....	88
Figure 5-9. Cyclic frictional resistance (Oliveira and Lourenco 2004)	89
Figure 5-10. Stress-strain curves.....	90
Figure 5-11. The damaged specimen after compression test.....	91
Figure 5-12. Stress-strain curves of masonry prism specimens.....	91
Figure 5-13. Concrete damage material model under uniaxial tension and compression test (Abaqus 2005).....	92
Figure 5-14. Step 1 and step 2 for applying the load (Lourenco 1996)	95
Figure 5-15. Comparison of numerical and experimental load - displacement results for wall subjected to 30 kN compressive load	96
Figure 5-16. Numerical load - displacement result for wall subjected to 30 kN compressive load	97
Figure 5-17. Crack pattern of the wall at different stages of load	98
Figure 5-18. Experimental crack pattern at 4 mm displacement (Lourenco 1996)	99
Figure 5-19. Cyclic velocity applied at the top of the wall.....	99
Figure 5-20. Resulting cyclic displacement at the top of the wall.....	100
Figure 5-21. Cyclic load - displacement diagram for wall subjected to 30kN compressive load	101
Figure 5-22. Comparison of numerical and experimental load - displacement diagram for wall under 120kN compressive load.....	102
Figure 5-23. Crack pattern of the wall (J6D) in different stages of loading.....	103
Figure 5-24. Experimental Crack Pattern at 4 mm displacement in wall J6D (Lourenco 1996)	104
Figure 5-25. Load - displacement diagram for wall under 120 kN compressive load (cyclic) ..	105
Figure 5-26. Load-displacement for out-of-plane direction loading	105
Figure 5-27. Deformed shape under out-of-plane loading (notice the openings).....	106
Figure 5-28. Moment diagram for OP load	107
Figure 5-29. Cyclic out-of-plane load.....	108
Figure 5-30. Out-of-plane cyclic load-displacement	108
Figure 5-31. Deformed configuration of the wall under cyclic out-of-plane loading	109
Figure 6-1. Eight node plane interface element (ABAQUS).....	112

LIST OF ILLUSTRATIONS (Cont'd)

Figure 6-2. Detailed model of brick and mortar	112
Figure 6-3. Numerical models	114
Figure 6-4. Step 1 and step 2 for applying the load (Lourenco 1996)	115
Figure 6-5. Top view of the wall	117
Figure 6-6. Deformed shape and load-displacement for IO: 1/0, IO:4/1 and IO:2/1.....	118
Figure 6-7. Deformed shape and load-displacement for IO: 1/1, IO:1/2 and IO:1/3.....	120
Figure 6-8. Deformed shape and load-displacement for IO: IO:1/4, IO:1/5 and IO:1/6	122
Figure 6-9. Deformed shape and load-displacement for IO:1/7, IO:1/8 and IO:1/9.....	123
Figure 6-10. Deformed shape and load-displacement for IO:1/10, IO:1/12 and IO:1/20.....	125
Figure 6-11. Deformed shape and load-displacement for IO:1/30, IO:1/40 and IO:1/50.....	126
Figure 6-12. Bidirectional deformations of the wall.....	127
Figure 6-13. IO:0/1, using the fine mesh	128
Figure 6-14. Load-displacement for fine and coarse mesh - IO:1/3 model	128
Figure 6-15. Displacement-time for the in-plane loading.....	129
Figure 6-16. Load-Displacement for in-plane loading	129
Figure 6-17. Load-Displacement for out-of-plane loading.....	130
Figure 6-18. Total displacement-time for IO:1/3.....	130
Figure 6-19. Load-displacement for IO:1/3 loading	131
Figure 6-20. Load-time for IO:1/3	131
Figure 6-21. Load-Displacement curves for IO:1/3 model.....	132
Figure 6-22. Proposed macro yield surface	134
Figure 6-23. Maximum elastic and ultimate capacity of the wall.....	135
Figure 7-1. A URM shear wall under bidirectional loading	138
Figure 7-2. (a) Out-of-plane loading of URM shear walls (b) Moment diagram	139
Figure 7-3. State of stress for brick and mortar	141
Figure 7-4. Yield surface for the joints	142
Figure 7-5. Interaction between tensile and compressive failure for OP loading.....	144
Figure 7-6. Interaction curve for shear-compression.....	145
Figure 7-7. Interaction curve governed by tensile failure.....	147
Figure 7-8. Lubliner's yield function in plane stress space (Abaqus 2005).....	149
Figure 7-9. Algorithm for the MATLAB code	150
Figure 7-10. Variation of bidirectional load as angle and compressive traction change	152
Figure 7-11. Interaction curve.....	153
Figure 7-12. Expansion and shrinkage of interaction curve by variation of compressive traction	154
Figure 7-13. Variation of bidirectional load as angle and compressive traction change	155
Figure 7-14. Interaction curve for a wide wall	156

LIST OF ILLUSTRATIONS (Cont'd)

Figure 7-15. Expansion and shrinkage of interaction curve by variation of compressive traction	157
Figure 7-16. Variation of bidirectional load as angle and compressive traction change (a) including shear failure in the bricks (b) excluding shear failure in the bricks.....	158
Figure 7-17. Interaction curve for a wide wall (a) including shear failure in the bricks (b) excluding shear failure in the bricks	159
Figure 7-18. (a) General mesh of the wall and (b) General view of the wall	160
Figure 7-19. Load-displacement results obtained by FE analysis for four different loadings....	161
Figure 7-20. Variation of the direction of load for IO:1/3	162
Figure 7-21. Deformed shape obtained by FE analysis	163
Figure 8-1. Different geometrical configurations	166
Figure 8-2. Wall type <i>II</i> (the first row of brick is buried into the mortar)	167
Figure 8-3. Boundary condition for the top plane of the walls	167
Figure 8-4. Test setup	168
Figure 8-5. Specimens for material testing	169
Figure 8-6. Compression test on bricks	169
Figure 8-7. Test setup for measuring the shear properties	170
Figure 8-8. Stress-strain curve for the high strength bricks (brown brick).....	171
Figure 8-9. Stress-strain curve for a low strength brick (red brick).....	171
Figure 8-10. A damaged high strength brick after uniaxial compression test	171
Figure 8-11. Stress-strain curve for masonry prisms constructed by high strength bricks.....	172
Figure 8-12. Stress-strain curve for masonry prisms constructed by low strength bricks	172
Figure 8-13. A damaged masonry prism after compression test	173
Figure 8-14. Idealized stress-strain curve (Lourenco 1996)	173
Figure 8-15. Joint behavior under shear displacement considering different confinement pressures.....	174
Figure 8-16. Mortar properties.....	175
Figure 8-17. Instrumentation of the walls.....	177
Figure 8-18. Deformation of the wall under the axial load ($\times 500$).....	178
Figure 8-19. Loading protocol for wall 1.....	178
Figure 8-20. Axial loads in vertical actuators	179
Figure 8-21. Axial displacement of the north and south vertical actuators	179
Figure 8-22. Load - displacement of wall 1 (experimental)	180
Figure 8-23. Finite element model of wall 1.....	181
Figure 8-24. Comparison of the crack propagation in the experimental and numerical models	182
Figure 8-25. Load-displacement curves of the numerical and experimental models	183

LIST OF ILLUSTRATIONS (Cont'd)

Figure 8-26. Distribution of the axial load in the vertical actuators	185
Figure 8-27. Propagated cracks in wall 1 (experimental) – second phase of the test	186
Figure 8-28. Load-displacement curve for cyclic testing of wall 1	186
Figure 8-29. Comparison of numerical and experimental results	187
Figure 8-30. Crack propagation obtained from the numerical modeling.....	188
Figure 8-31. Experimental set-up for wall 2.....	190
Figure 8-32. Loading protocol for wall 2.....	191
Figure 8-33. Load-displacement curve for wall 2.....	191
Figure 8-34. Displacement of the vertical actuators.....	192
Figure 8-35. OP displacement of the north and south side of the top plane of the wall	193
Figure 8-36. In-plane movement of LED's ($\times 10$)	194
Figure 8-37. Deformation of Krypton LED's in different stages of loading.....	195
Figure 8-38. 3-D movement of LED's (real scale).....	196
Figure 8-39. 3-D displacement of LED's in different stages of loading (real scale)	197
Figure 8-40. Crack propagation of the wall in different stages of loading	200
Figure 8-41. Load-displacement curves obtained by the numerical model considering different OP loads	201
Figure 8-42. Proportion of IP and OP deformations.....	202
Figure 8-43. Cyclic loading protocol for the third wall	202
Figure 8-44. In-plane load-displacement curve of wall 3	203
Figure 8-45. Displacement of the north and south vertical actuators	204
Figure 8-46. Distribution of the axial load in the north and south vertical actuators	204
Figure 8-47. Deformation of the wall under the axial load ($\times 500$).....	205
Figure 8-48. Deformation of the wall under cyclic loading ($\times 10$).....	206
Figure 8-49. Deformation of the wall in different stages of loading	207
Figure 8-50. Crack propagation of the wall in different stages of loading.....	210
Figure 8-51. Loading-protocol for numerical model	210
Figure 8-52. Cyclic load-displacement curves considering different values for stiffness degradation factor	211
Figure 8-53. Comparison of the experimental and numerical load-displacement curves.....	211
Figure 8-54. Numerical simulation of crack propagation in the wall	213
Figure 8-55. Loading protocol for wall 4.....	214
Figure 8-56. Test set-up for out-of-plane load.....	214
Figure 8-57. Support for large out-of-plane deformation of the wall	215
Figure 8-58. Load-displacement of wall 4.....	215
Figure 8-59. Displacement of the north and south vertical actuators	216
Figure 8-60. Axial loads in the south and north vertical actuators	217
Figure 8-61. OP displacement of the north and south side of the top plane	217

LIST OF ILLUSTRATIONS (Cont'd)

Figure 8-62. Deformation map of the wall under cyclic loading ($\times 10$).....	218
Figure 8-63. Deformation of the wall in different stages of loading	219
Figure 8-64. Crack propagation in different stages of loading	221
Figure 8-65. Three-dimensional deformation of the wall under cyclic loading (real scale).....	222
Figure 8-66. Three-dimensional deformation of the wall in different stages of loading (real scale)	224
Figure 8-67. Out-of-plane gap in the joints at the end of the test	224
Figure 8-68. Comparison of the numerical and experimental load-displacement curves.....	225
Figure 8-69. Combination of IP and OP loadings.....	227
Figure 8-70. Cyclic loading protocol of wall 5	227
Figure 8-71. In-plane load-displacement of wall 5	228
Figure 8-72. In-plane load-displacement using Krypton 5x data.....	228
Figure 8-73. Axial displacement of the north and south vertical actuators	229
Figure 8-74. Distribution of the axial load in the north and south vertical actuators	229
Figure 8-75. Out-of-plane displacement of the north and south side of the top plane	230
Figure 8-76. Three-dimensional deformation of the wall under OP loading (real scale)	230
Figure 8-77. Deformation of the wall under cyclic loading ($\times 10$).....	231
Figure 8-78. Deformation of the wall in different stages of loadings.....	233
Figure 8-79. Crack propagation in different stages of loading	235
Figure 8-80. Comparison of the experimental results with the in-plane numerical results	236
Figure 8-81. Crack propagation obtained from the numerical simulations under monotonic IP loading.....	237
Figure 8-82. Crack propagation obtained from the numerical simulation under monotonic OP/IP loading.....	238
Figure 8-83. Comparison of the experimental and numerical results (monotonic loading)	239
Figure 8-84. Numerical loading protocol.....	239
Figure 8-85. Comparison of the numerical and experimental results	240
Figure 8-86. Comparison of the experimental and numerical load-displacement curves.....	240
Figure 8-87. Crack propagation under cyclic loading (numerical).....	241
Figure 8-88. Loading protocol for wall 6.....	243
Figure 8-89. Load-displacement of wall 6.....	244
Figure 8-90 Modified load-displacement curve using krypton 5x results	244
Figure 8-91. Axial displacement of the north and south vertical actuators	245
Figure 8-92. Axial loads in the south and north actuators	245
Figure 8-93. OP displacements of the north and south side of the top plane of the wall	246
Figure 8-94. Deformation of the wall under the axial load ($\times 300$).....	247
Figure 8-95. Three-dimensional deformation of the wall under OP loading (real scale)	247
Figure 8-96. Deformation of the wall under cyclic loading ($\times 10$).....	248

LIST OF ILLUSTRATIONS (Cont'd)

Figure 8-97. Deformation of the wall in different stages of loadings.....	250
Figure 8-98. Crack propagation in different stages of loading	252
Figure 8-99. Comparison of the experimental and numerical load-displacement curves.....	253
Figure 8-100. Comparison of the numerical and experimental results	253
Figure 8-101 Bilinear idealization	256
Figure 8-102 Variation of cumulative normalized dissipated energy.....	257

LIST OF TABLES

Table 3-1. Properties of different types of cracks (J5D/J6D - 2PB).....	33
Table 3-2. Inelastic properties of the joints (J5D/J6D - 2PB).....	33
Table 3-3. Properties of different types of crack (J5D/J6D - 4PB)	36
Table 3-4. Inelastic properties of the joints (J5D/J6D - 4PB).....	36
Table 4-1. Elastic properties of interface element	63
Table 4-2. Inelastic properties of interface element.....	63
Table 4-3. Properties of vertical cracks for model 2.2.....	71
Table 4-4. Properties of horizontal cracks for model 2.2	71
Table 4-5. Properties of potential brick cracks for model 2.2	71
Table 5-1. Stiffness degradation parameter	84
Table 5-2. Properties of different types of cracks (J4D/J5D).....	96
Table 5-3. Inelastic properties of the joints (J4D/J5D).....	96
Table 5-4. Properties of different types of cracks (J6D).....	101
Table 5-5. Inelastic properties of the joints (J6D)	101
Table 6-1. Properties of different types of cracks (J4D/J5D).....	116
Table 6-2. Inelastic properties of the joints (J4D/J5D).....	116
Table 6-3. Loading protocols.....	117
Table 6-4. Yield and ultimate loading points for different loadings.....	133
Table 8-1. Types of brick and geometry for different walls	167
Table 8-2. Material propoerties of high strength brick.....	174
Table 8-3. Material propoerties of low strength brick	174
Table 8-4 . Joint properties for walls constructed by high strengh bricks	175
Table 8-5. Joint properties for walls constructed by low strength bricks	175
Table 8-6. Loading protocols for the walls.....	176
Table 8-7 Characteristic values of the experimental envelopes.....	256
Table 8-8. Comparison between the results	258
Table 8-9. Differences in the results	258

[@Seismicisolation](#)

SECTION 1

INTRODUCTION

1.1 Introduction

Contrary to steel structures, the development of material models for masonry structures seems to be in its early stages. Most of the available material models have been developed to capture either the in-plane or out-of-plane deformation of masonry walls. Similar to the development of numerical models, most of the experimental studies also have been focused on the two-dimensional behavior of walls or buildings. Therefore, to better understand the behavior of masonry structures, more robust modeling procedures are needed along with a well-documented experimental database to validate the new three-dimensional models and constitutive material models. This report investigates existing gaps in knowledge pertaining to masonry and presents a comprehensive study on numerical, analytical and experimental modeling of masonry structures. This study is part of a project that investigates the vulnerability of New York City old masonry buildings under possible earthquake excitations. In the rest of the project, the proposed numerical procedures in this report will be utilized to develop the fragility functions for the masonry buildings in New York City.

1.2 Research objectives

The overarching goals of the research documented in this report are to investigate the three-dimensional behavior of unreinforced masonry walls and study the interaction of in-plane and out-of-plane behavior. The most important scholarly achievements of this report are listed below:

- Development of a new three-dimensional cyclic material model.
- Development of interaction curves for the in-plane and out-of-plane deformations.
- Experimental investigation of the in-plane and out-of-plane deformation of the unreinforced masonry walls, and validation of the proposed numerical procedures.

1.3 Report organization

This report presents a comprehensive study that focuses on analytical, computational and experimental behavior of unreinforced masonry (URM) structures. The report contains nine sections. The second section presents an overview of previous numerical and experimental studies.

The third section presents a simplified two-dimensional model for monotonic in-plane deformation of masonry walls. In this section, a finite element model is utilized where bricks are replaced by rigid elements, connected to each other by interface elements. The interface elements are assumed to be representative of all possible elastic and inelastic behavior of the bricks and mortar. In this section, a FORTRAN code, representing the material model and numerical procedure are developed using an implicit formulation.

A literature review of the existing constitutive material models reveals that, in many cases, the yield surface contains multi-yield surfaces. Similarly, for modeling masonry structures, most of the existing material models for interface elements use multi-yield surfaces. The difficulty in utilizing these kinds of yield surfaces is the sudden change in the response at the points where two yield surfaces meet, while altering the state of stress slightly at the intersection of the yield surfaces. In other words, a slight change in the applied forces will change the associated yield surface and, consequently, will change the associated flow rule. A methodology is proposed in

the fourth section to overcome this problem. Moreover, the material model developed in this section is combined with a proposed lattice model to simulate the in-plane monotonic deformation of masonry walls. A FORTRAN code has been developed which implements the material model and the lattice model in an implicit formulation.

Due to the use of implicit formulations in the previous section, convergence problems have been observed for large deformation cases. To remedy the convergence problems and high computational demands, section five discusses a comprehensive three-dimensional dynamic model in which the material model is developed based on an explicit formulation.

Using the material model presented in the fifth section, a numerical investigation has been performed in the sixth section on bidirectional behavior of unreinforced masonry walls. In this section, an interaction curve has been proposed which shows the yielding point and ultimate capacity of URM walls subjected to a range of bidirectional loading conditions.

Using the finite element method, the computational time is significant to build comprehensive interaction curves for unreinforced masonry wall. In the seventh section, an analytical procedure has been proposed to build the interaction curves for URM walls. The proposed interaction curves play the same role as the yield surface for an element in the plasticity theory. In other words, it shows the maximum elastic capacity of the wall when an in-plane (IP) and out-of-plane (OP) load are imposed to the wall with different proportions.

To generalize the investigation and validate the proposed numerical models, in the eighth section an experimental investigation on the bidirectional behavior of URM walls has been performed. In this section, the results of six experimental walls tested in various combinations of in-plane and out-of-plane direction are presented. Moreover, this section describes the validation

of the 3-D explicit modeling presented in section five. The last section of this report describes a summary of the work, original contributions, conclusions, and future works.

In conclusion, in this report different computational procedures have been developed and the accuracy and computational speed of those approaches have been compared to each other and some recommendations have been made for future studies.

SECTION 2

BACKGROUND AND LITERATURE REVIEW

Masonry structures have been used for many years in building construction. The poor behavior of masonry buildings under earthquake excitations has been observed over the years; however, masonry buildings are still in demand. Although novel structural technologies are utilized in new buildings, masonry components are not omitted from structural usage, and masonry components are still used, especially for infill walls, as they provide a significant stiffness enhancement to the buildings in earthquakes. Whether the masonry structure constitutes the whole structural system or is used as infill walls in a concrete or steel building, their complex failure modes often pose a significant challenge for any computational framework.

At the constituent level, a masonry building is a composite structure constructed by bricks and mortar. Due to cracking, sliding of the bricks relative to each other, and, consequently, formation of new contacts and stress concentration at the corners of bricks, simulating the behavior of masonry structures under extreme loadings, such as earthquakes, is one of the most complex problems in computational mechanics. Different modeling approaches have been implemented for in-plane and out-of-plane behavior of masonry walls. For instance, finite element (FE) method is one of the most commonly used approaches; however, the use of traditional (FE) methods requires extensive computational resources and significant processing time. Therefore, many simplified approaches are presented to decrease the computational time.

Based on the accuracy level and the computational time, different types of computational methods have been utilized to assess the behavior of masonry structures under static and dynamic loadings. These computational methods are mainly categorized into three groups-

namely, micro-, macro-, and meso-scale. Micro-scale modeling has the highest accuracy level, and mainly the accurate response of the structure beside the exact path of cracks is in the point of interest. However, in the macro- and meso-scale analysis of masonry buildings, the general behavior of the structure is important, and not the detailed behavior of each component. The main problem in micro-scale analysis is the high computational effort required to build the numerical model and to run the analysis. Therefore, for large structures, it is more reasonable and convenient to use meso- and macro-scale analysis. Analysis methods based on meso- and macro-scale approaches are usually accompanied by some simplification assumptions to improve the computational efficiency, and clearly, the accuracy of the analysis is less than the micro-analysis. In the following sections, a more detailed description on the micro-, meso- and macro scale modeling of unreinforced masonry structures are presented along with some examples.

2.1 Micro- and meso- scale analysis

Work on numerical modeling of brittle materials such as concrete and masonry has been significant in the past few decades with much of the effort focusing on the micro-, meso- and macro-scale. In one of the early studies, the microstructure of concrete was simulated numerically by Roelfstra (1988). In Roelfstra's model, designated as "numerical concrete", mortar, aggregates, and the interface between them are described by many elements much smaller than the aggregate pieces. Clearly, it is very difficult to build such a model for a large structure and the computational time will be significant. In the mesostructure of Bazant (1991), mortar and the aggregate pieces are modeled by continuum elastic elements, which are connected by nonlinear interface elements. The mixed-mode generalization of the cohesive crack model is assumed for these nonlinear interface elements which represents potential crack lines.

Implementation of this modeling approach leads to an extremely large number of degrees-of-freedom.

Cundall (1971) came up with an easy and efficient model replacing the continuum elements with a system of discrete elements and defining the behavior of the interfaces based on the material properties. He was able to significantly reduce the computational effort using his proposed model. To simulate the behavior of granular materials such as sand, Cundall (1971) used rigid particles which interact only by friction, designated as the discrete element method (DEM).

Zubelewicz (1987) used particle models with nonzero interfacial tensile strength to study fracture growth in geomaterials (see Figure 2-1). In geomaterials such as sand, since tensile strength is not important, the particle interaction law is very simple and the overall behavior is controlled mainly by kinematic restrictions of the particle system. The rigid-body spring model (RBSM) (Kawai 1978), which was presented by Kawai (Kawai 1978), uses a similar assumption. In this model, the material is divided into a number of rigid elements connected by zero length springs placed along their joints. The DEM and the rigid-body spring model (RBSM) are computationally less demanding than modeling with continuum elements.

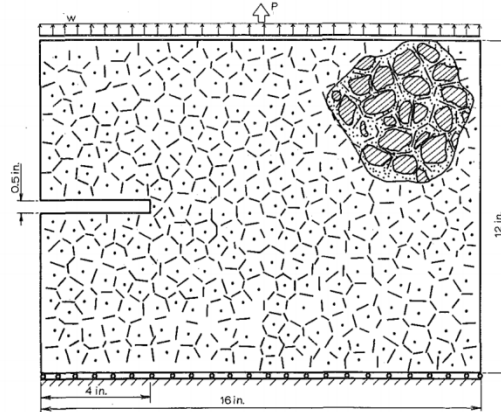


Figure 2-1 Fracture Specimen Consisting of an Array of Rigid Particles and Their Interfaces (Zubelewicz and Bazant 1987)

One of the most functional elements in micro- and meso-scale analysis that tackles the issue of discontinuity is the interface element (IE), which was utilized by several researchers (Beer 1985; Ghabaoussi et al. 1973; Schellekens and De Borst 1993). The interface element initially behaves elastically until reaching the designated yield surface that is defined specifically for each part of structure. Afterward, the IE starts following the plastic behavior. The two parts of the interface element are permitted to separate under tensile or shear loading. However, when compression is the prevailing state of stress, the contact is modeled by penetration of two surfaces into each other. A considerable usage of these IEs has been observed for modeling masonry structures (Chaimoon and Attard 2007; Giambanco et al. 2001; Gilbert et al. 2007; Lourenco 1996; Mohebbkhah et al. 2008; Senthivel and Lourenco 2009; Stavridis 2009).

As an example of early works on meso-scale modeling of masonry structures, Page (1978) suggested using interface elements between bricks. The yield surface in this particular interface model is only defined for tensile and shear failure. Lourenco (1996) modified Page's model by adding a compressive cap to the yield surface. Using the cap in the yield surface, crushing of the masonry bricks was also modeled within the joints. Lourenco's model consists of elastic

elements for bricks and non-linear interface elements to model the joints. Oliveira and Lourenco (2004) later generalized Lourenco's model to assess the cyclic behavior of masonry walls for in-plane loading.

In the model proposed by Lourenco (1996) and Oliveira and Lourenco (2004), bricks are modeled using elastic elements and the nonlinear behavior of the interface elements includes the tensile, shear and compression failures (Lourenco 1996). In other words, all nonlinearity of the model is defined in the interface elements and all other elements in the model are assumed to remain elastic. The constitutive material model in these investigations uses multi-yield surfaces, which are not connected smoothly. Each yield surface is assigned for a specific failure regime, including tensile, shear, and compression failure. Changing from one yield surface to another is associated with a jump in the behavior of the material, either in the softening or hardening regimes. For example, shifting from tension regime to the shear regime will alter the energy associated with softening. However, changing from shear regime to the compression regime will be accompanied by a major and significant change from softening to hardening. Based on the physics of the problem, jump and discontinuity are not realistic and cause convergence problem in the numerical analysis. The discontinuity problem in constitutive material models with multi-yield surfaces is investigated by Cusatis (Cusatis et al. 2003; Cusatis et al. 2003; Cusatis et al. 2006; Cusatis and Cedolin 2007) in numerical modeling of concrete. Cusatis (Cusatis et al. 2003; Cusatis et al. 2003; Cusatis et al. 2006; Cusatis and Cedolin 2007) presented an interpolation function for gradual change from one part to another part of the yield surface while dealing with a two-segment yield surface, which was successfully applied to model the behavior of concrete.

As another example of meso-scale modeling of masonry structures, bricks can be modeled by elastic-plastic elements with interface elements to represent the joints. The interface elements

are capable of modeling the joint separation in tension and shear (Stavridis 2009). Using such interface elements in conjunction with elasto-plastic elements for bricks, Gilbert et al. (2007) used LS-DYNA (1998) to investigate the behavior of a masonry wall subjected to impact loading.

In reality, after reaching the maximum value of the shear or tensile strength, the resisting force does not abruptly drop to zero. Instead, the loading is associated with a particular softening energy (the area under the strain-stress curve or in some cases displacement-stress curve). To simplify the problem, some investigators (2008) have neglected this softening energy and assumed an abrupt failure in the interface. For instance, Mohebkah et al. (2008) used this simplification when investigating the effect of infill walls with openings by the commercial software, UDEC (2004).

To simulate fracture in a continuum, some investigators have used Lattice modeling. The early works regarding lattice modeling refers to Hrennikoff (1941). In Hrennikoff's model, the material was replaced by truss elements, and for taking into account the inherent heterogeneity of materials, different material properties can be assigned for different truss elements. Schlangen and Garboczi (Schlangen and Garboczi 1997) developed a two-dimensional lattice model for studying fracture in concrete. In Schlangen and Garboczi's study and for implementing the lattice model, beam elements with three degrees-of-freedom per node were used. Each beam is considered to be elastic and after the stress exceeds a certain value, failure takes place and the beam is consequently removed. Cusatis (Cusatis et al. 2003; Cusatis et al. 2003; Cusatis et al. 2006) developed the confinement-shear lattice model (CSLM) for concrete. In Cusatis's model, each piece of aggregate is connected to the neighboring aggregates by a number of rigid beams in which the linear and nonlinear behavior of concrete is taking place in a nodal element between

the rigid beams. The rigid beams not only transmit the axial forces but also transmit shear forces. For the shear strength case, both friction and cohesion are exhibited and well defined in the model (Figure 2-2).

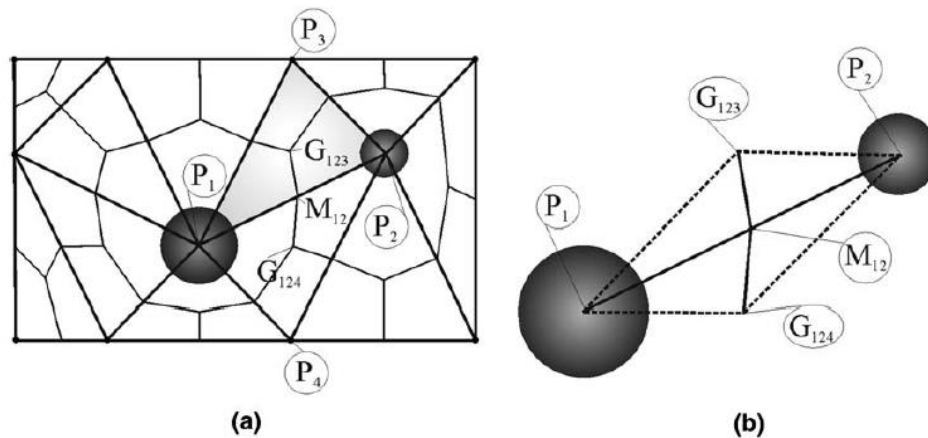


**Figure 2-2. (a) Example of two-dimensional tessellation of concrete meso-structure
(b) Geometry of a connecting strut (Cusatis et al. 2003)**

With respect to the numerical procedures, micro- and meso-scale analysis can be categorized mainly into implicit and explicit analysis. Most of the notable research studies that address the cyclic behavior of masonry structures use implicit finite element solutions. Modeling a masonry structure with an implicit procedure offers some advantages as well as many technical challenges. Based on the most fundamental characteristics of implicit procedures, at each time step, iterations are required to solve a system of equations. The behavior of masonry structures is inherently nonlinear; thus by using implicit procedures it is difficult to achieve a converged solution for some cases. Most of the finite element codes used to analyze masonry structures are based on implicit formulations (Lourenco 1996; Oliveira and Lourenco 2004; Oliveira and Lourenco 2004) that are time consuming when one considers a large displacement domain. The convergence of the numerical solution particularly deteriorates at the point of load reversal

(Oliveira and Lourenco 2004). For this reason, some researchers (Karapitta et al. 2010) have used explicit formulations to remedy the convergence problem. For example, Karapitta (Karapitta et al. 2010) used a homogenization technique within an explicit formulation to capture the cyclic behavior of in-plane masonry panels. Although the homogenization model captured some of the behavior very well, it could not capture the creation and progression of discrete cracks. Instead, a damage parameter is used to show the distorted elements (Figure 2-3).

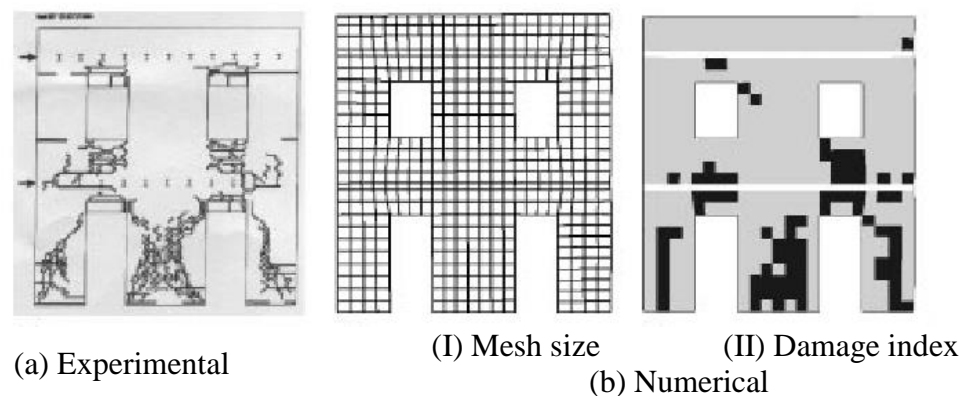


Figure 2-3 PAVIA wall: experimental crack pattern and damage index at the end of load history (damage areas in black color) (Karapitta et al. 2010)

2.2 Macro-scale analysis

Due to the high computational demand associated with micro- and meso-scale analysis, macro-scale analysis is preferred for large structures and particularly for seismic analysis. The macro-scale analysis is associated with many simplified assumptions to reduce the computational time. For example, Pasticier (Pasticier et al. 2008) used a very simple macro-element model to perform two-dimensional seismic analysis, where each panel was divided into smaller panels that were represented by an equivalent frame. In Pasticier's model, a masonry building was modeled with a number of equivalent frames with different hysteretic behavior, as shown in Figure 2-4.

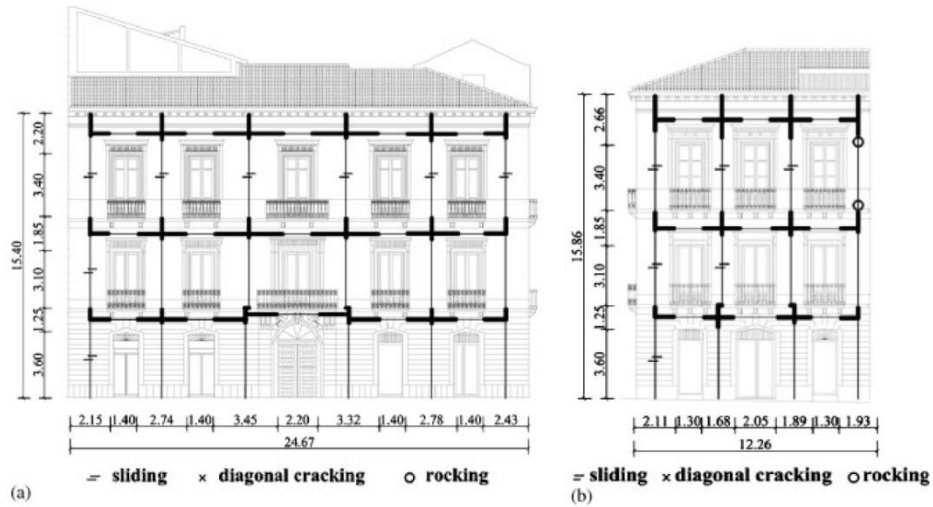


Figure 2-4. Simulation of a masonry panel with equivalent frame method (Pasticier et al. 2008)

To derive the fragility curve for an unreinforced masonry building, Park (Park et al. 2009) used a very simple macro element model. In Park's model, masonry panels were divided into a number of springs with different hysteretic loops (Figure 2-5). According to the aspect ratio of each segment of the wall different hysteresis behavior was assigned for that segment including, rocking, sliding and diagonal crack. Clearly, using this method, it is not possible to find the crack propagation in the structure.

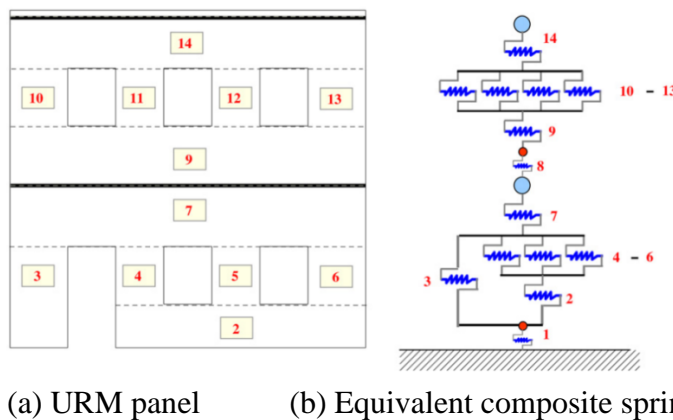


Figure 2-5. Composite spring model of a URM panel (Park et al. 2009)

As another example for macro-scale analysis of masonry buildings, Chen (2008) used nonlinear shear springs in series with rotational springs to simulate both shear and flexural in-plane response of masonry walls. The proposed macro-element includes an axial spring, three shear springs, and two rotational springs to simulate the behavior of masonry walls (Figure 2-6).

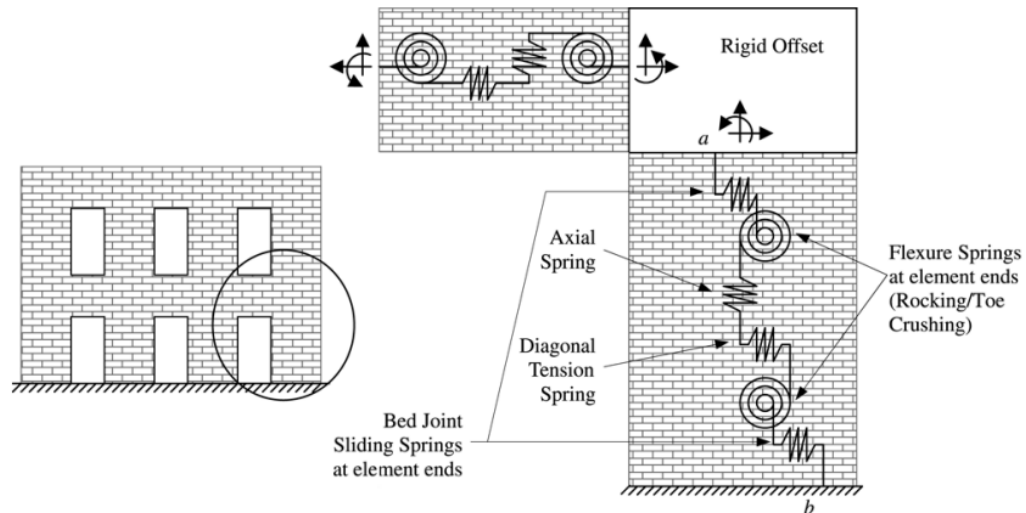


Figure 2-6. Proposed macro-element (Chen et al. 2008)

Using large rigid elements and springs attached between them, Casolo (2004) developed a macro-scale model (Figure 2-7). Casolo compared the frequencies and mode shapes of a masonry wall using his proposed model and finite element model. Later the model was extended to capture the cyclic 2-D behavior of masonry walls and to model masonry walls under earthquake excitations (Casolo and Pena 2007). In the model proposed by Casolo, the propagated cracks of the wall were identified by a damage parameter.

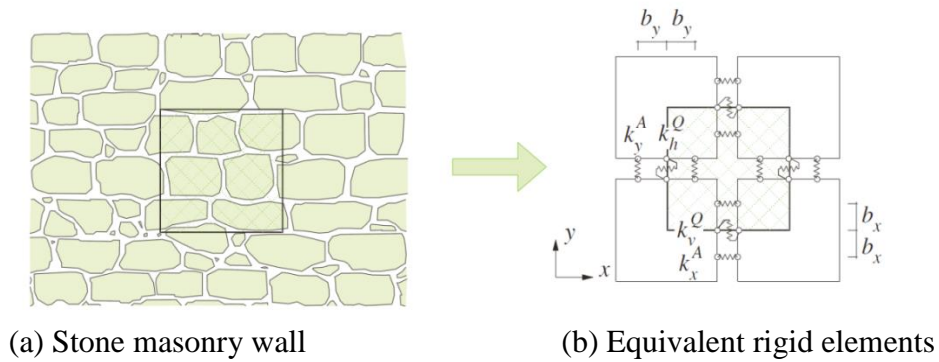


Figure 2-7. Scheme of an irregular masonry and the ‘unit cell’ defined by four rigid elements (Casolo and S. 2004)

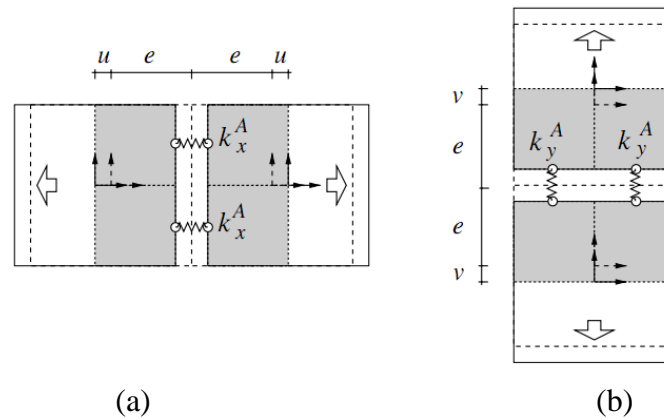


Figure 2-8. Rigid elements subjected to (a) horizontal and (b) vertical axial loading (Casolo and S. 2004)

2.3 Bidirectional modeling of URM walls

Several numerical and experimental investigations (Haider 2007; Lourenco 1996; Oliveira and Lourenco 2004) have focused on either the in-plane (IP) or out-of-plane (OP) behavior of masonry walls. Very few studies have investigated the bidirectional behavior of URM walls. As a very few examples on the bidirectional investigations, Hashemi and Mosalam (2007) used a simple material model to investigate the interaction of an infill URM wall with a steel frame. They considered two degrees-of-freedom (DOF) for an infill wall, one DOF for the in-plane

displacement of the top plane of the wall and one degree of freedom for the out-of-plane displacement of the middle of the infill wall. Figure 2-9 shows the proposed macro model by Hashemi and Mosalam for modeling infill walls. In this figure, the dashed lines represent the nonlinear compression-only members (see the insert of the material model of these struts), and the solid line in the center represents a tension-only elastic link element.

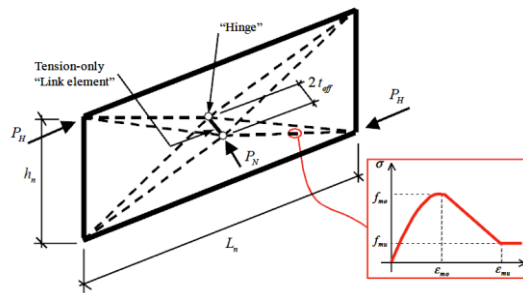


Figure 2-9. Three-dimensional SAT model of URM infill wall (Hashemi and Mosalam 2007)

Later, Kadysiewski and Mosalam (2009) improved the previous study by proposing a simpler macro-element for modeling infill walls (Figure 2-10). In this model the macro element is composed of a nonlinear beam-column element. A nonlinear P-M (moment-axial) hinge is considered at midspan of diagonal, which is modeled using a fiber section (see Figure 2-10).

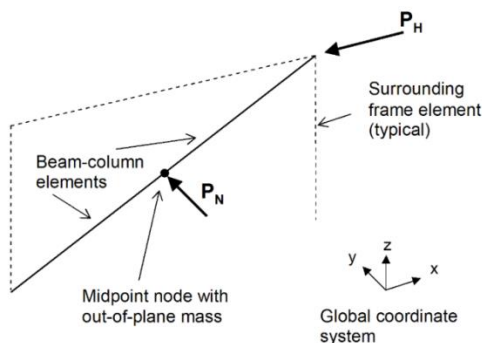


Figure 2-10. Infill model using beam-column elements with fiber discretization (Kadysiewski and Mosalam 2009)

2.4 *Experimental studies*

While this literature review revealed several approaches for numerical modeling of masonry structures, a significant amount of work has been focused on understanding the micro material behavior of masonry components (bricks and mortar) and the macro-behavior of masonry walls by conducting experimental studies. Pluijm (Pluijm 1992; Pluijm 1993; Pluijm and Vermeltfoort 1991) conducted a series of experimental studies to identify the behavior of joints in the monotonic tensile and shear displacement. Stavridis (Stavridis 2009; Stavridis and Shing 2010) presented a mathematical model for the material behavior of mortar joints and bricks in masonry walls, where a wall was comprised of either concrete or clay bricks. The study (Stavridis 2009; Stavridis and Shing 2010) presented a typical range for each mathematical parameter.

De Porto (da Porto et al. 2009) performed a number of in-plane cyclic tests to develop an analytical hysteretic model for masonry walls. A number of cyclic testing was performed on the out-of-plane direction of unreinforced masonry walls by Griffith (Griffith et al. 2007). He showed the effect of the opening on the cyclic behavior of the masonry walls. In addition, the work highlighted the influence of the connection of the perpendicular walls in the out-of-plane behavior.

A considerable number of seismic tests have been also performed on either a whole masonry building (Bothara et al. 2010; Paquette and Bruneau 2006; Paquette et al. 2004) or on a partition wall to investigate the vulnerability of masonry buildings under earthquake excitations. Bothara et al. (Bothara et al. 2010) performed a series of experimental tests on a half scale two-story unreinforced masonry building to identify the dynamic properties of URM buildings. Moreover, they applied several ground motions to the building to investigate the propagated

damages to the building. Finally, using the experimental results, they developed fragility curves for the masonry building. Paquette and Bruneau (Paquette and Bruneau 2006) tested a one-story masonry building by application of a seismic load on its roof, using an actuator. They investigated the effect of flexible wood diaphragm on the seismic behavior of masonry buildings.

Investigations on the behavior of masonry walls have also been conducted in the framework of infill masonry walls (Dolek and Fajfar 2008; Pujol and Fick 2010; Rabinovitch and Madah 2011; Tu et al. 2010). Pujol and Fick (Pujol and Fick 2010) tested a three-story reinforced concrete building, first without and then with infill walls to investigate the effect of infill walls in the seismic behavior of reinforced concrete buildings. Rabinovitch and Madah (Rabinovitch and Madah 2011) performed an experimental study on infill masonry walls in the out-of-plane direction under earthquake loadings. They also developed a finite element model and validated their model using the experimental results. Tu et al. (Tu et al. 2010) tested four reinforced concrete frames with different types of infill masonry walls. They concluded that infill masonry walls exhibit notable resistance to out-of-plane loads via the arching mechanism; however, in the end they collapse under the inertial force caused by their self-weight.

In summary, very few numerical and experimental studies have focused on the three-dimensional behavior of unreinforced masonry walls or buildings. It is clear that most of the stimulus loadings, like wind or earthquake excitations, are three-dimensionally imposed on structures. Therefore, it is necessary to develop new material models and numerical procedures that are capable of simulating the three-dimensional behavior of URM structures. Moreover, a well-documented experimental database is much needed to validate the three-dimensional material models.

SECTION 3

TWO-DIMENSIONAL COMPUTATIONAL FRAMEWORK OF MESO-SCALE RIGID AND LINE INTERFACE ELEMENTS FOR MASONRY STRUCTURES

3.1 Introduction

In this section, a simplified numerical model is presented for simulating the in-plane deformation of the masonry walls. The modeling approach focuses on two dimensions (2-D), whereby the in-plane behavior of components is represented by rigid elements and nonlinear line interfaces instead of modeling by traditional finite elements method. Traditional finite element method is indeed capable of predicting the behavior of large scale masonry structures, but the computational demand will be very high. In the proposed approach, walls are allowed to crack in predefined paths, which based on the experimental tests have more likelihood for propagation. The section discusses the model derivation, implementation, and assessment of mesh sensitivity. A material model is presented and implemented in a user-defined subroutine that is compiled with TNO DIANA (DIANA 2008). The algorithms and material models are validated using well-documented experimental studies to assess the capabilities of the model to simulate the behavior of URM structures.

3.2 Description of the model

In this model, bricks are subdivided into a number of rigid blocks and mortar is represented using six-node line interface elements as shown in Figure 3-1 (Hohberg 1992) (CL12I). Using a

user subroutine (usrifc) in the commercial code TNO DIANA (DIANA 2008), all the elasticity of the material is defined at the edge of the rigid blocks.

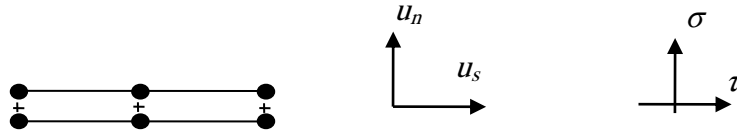


Figure 3-1. Line interface element

Figure 3-2 shows the details of rigid blocks, line interface elements model, and two distinct mesh choices. As illustrated in Figure 3-2, bricks are expanded by half of the dimension of the mortar, and, thus, the interface elements are located at the intersection of the bricks. In Figure 3-2 which shows “Mesh A”, a block is divided into two rigid elements and an interface element is located at the middle of the brick. In Figure 3-2 (Mesh B), a finer mesh is illustrated and a block is subdivided into four rigid blocks, and the interface elements are attached to the line of the mesh associated with the location of the mortar and at the potential crack positions.

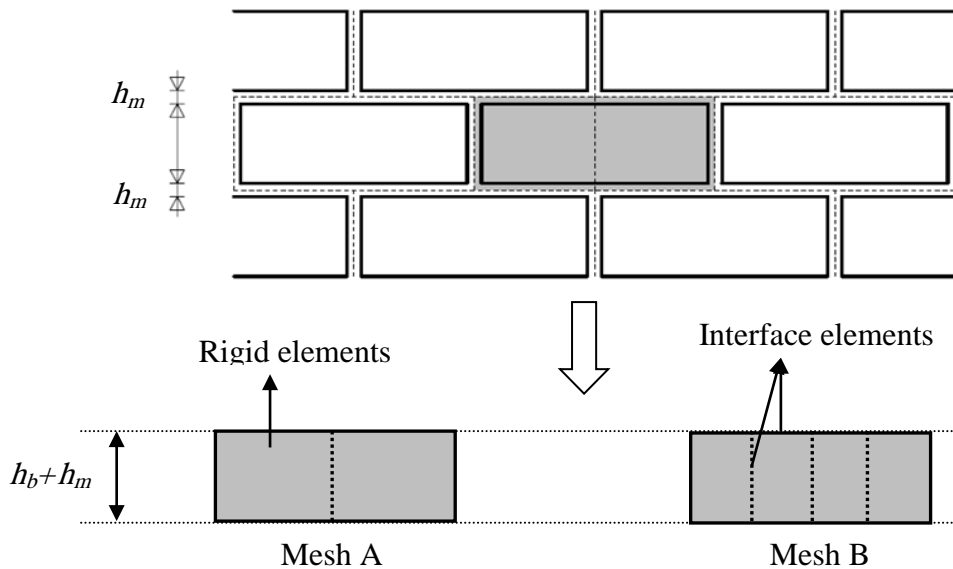


Figure 3-2. Two generated meshes for rigid elements-line interface model

The nonlinear behavior of the materials is defined at the interface elements and pass through brick-mortar joints or at the middle of the bricks. These joints have the most likelihood for cracking and separation (Lourenco 1996). In most cases, for masonry walls, due to weakness of mortar, the path of crack matches well with this assumption. This approach is considered as a meso-scale method, and it is applicable for homogeneous material like concrete; because in meso-scale the exact path of crack is not important, but rather, the general behavior of structure is. The main computational description of the meso-scale model is presented in the following sub-sections, which includes: (1) elastic behavior, (2) plastic behavior, and (3) algorithms for detecting and updating the contact zones.

3.3 Elastic behavior

The behavior of interface elements is initially elastic, i.e., $\mathbf{t} = k \Delta \bar{\mathbf{u}}$, where \mathbf{t} is the traction vector and $\bar{\mathbf{u}}$ is the displacement vector (equations (3-1) to (3-3)).

$$k = \begin{bmatrix} k_n & 0 \\ 0 & k_s \end{bmatrix} \quad (3-1)$$

$$\mathbf{t} = \begin{Bmatrix} \sigma \\ \tau \end{Bmatrix} \quad (3-2)$$

$$\Delta \bar{\mathbf{u}} = \begin{Bmatrix} \Delta u \\ \Delta v \end{Bmatrix} \quad (3-3)$$

where k is the elastic stiffness of the joints, which can be calculated from the properties of both brick and mortar as given by equations (3-4) and (3-5). We note here that for simplifying the model, the effect of Poisson's ratio is neglected. Simply stated, due to the comparatively low value of the Poisson's ratio for the brick, and the notion that most of the behavior of the masonry components is governed by the inelastic behavior of joints, separation of bricks, and sliding at the adjacent interfaces, this assumption is deemed appropriate. The inelastic behavior starts at the

beginning of application of load at different positions within the mesh and completes by a diagonal crack in the wall (for the case of diagonal failure). For determining the stiffness “ k ”, the behavior of the brick and mortar are assumed as two springs in series (Figure 3-3).

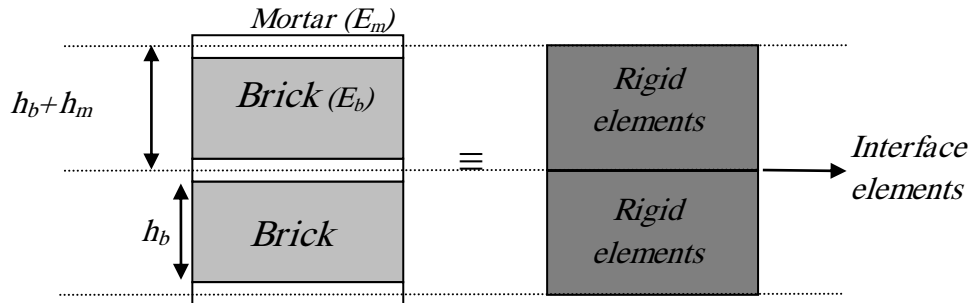


Figure 3-3. Calculating the stiffness of the interface elements

The displacement for the combination of brick and mortar system must be equal to the displacement for the rigid element-line interface system under the same compressive load. Accordingly, the stiffness of the system can be calculated by using equation (3-4) and (3-5).

$$\frac{1}{k_n} = \left(\frac{h_m}{E_m} + \frac{h_b}{E_b} \right) \Rightarrow k_n = \frac{E_m E_b}{E_b h_m + E_m h_b} \quad (3-4)$$

$$\frac{1}{k_s} = \left(\frac{h_m}{G_m} + \frac{h_b}{G_b} \right) \Rightarrow k_s = \frac{G_m G_b}{G_b h_m + G_m h_b} \quad (3-5)$$

where the parameters appeared in equations (3-1) to (3-5) are described in Figure 3-3 and G is the shear modulus of elasticity.

3.4 Plastic behavior

The plastic behavior is better represented by a number of zero-length interface elements, where at each time step, the stresses associated with the elements are compared with elastic stress limit.

As the number of the assumed potential cracks is increased, the accuracy of the analysis will be

elevated. Therefore, the mesh sensitivity must be checked, as presented in the subsequent sections. Based on the observation from experimental tests (Raijmakers and Vermeltoort 1992; Vermeltoort and Raijmakers 1993), most of the cracks and their propagation paths are often located in the mortar or/and the middle of the bricks. Accordingly, three different modes are considered for the interface elements, tension, shear and compression (Figure 3-4).

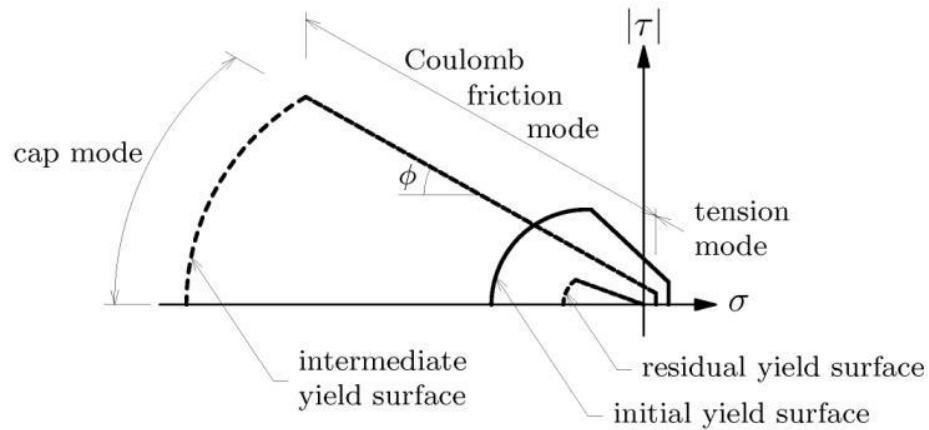


Figure 3-4. Model for interface elements “interface cap model” (DIANA 2008)

Tension and shear modes mostly define the behavior of joints and compression mode mostly is representative of the crushing of the bricks that are considered rigid. Exponential softening is considered for tension and shear mode (Pluijm 1992; Plujim 1993). For tension mode, the yield function (Figure 3-5) is as follows,

$$f_1(\sigma, \kappa_1) = \sigma - \bar{\sigma}_1(\kappa_1) \quad (3-6)$$

$$\bar{\sigma}_1 = f_t \exp\left(-\frac{f_t}{G_f^I} \kappa_1\right) \quad (3-7)$$

In equations (3-6) and (3-7), f_t is the tensile strength of the mortar interface and G_f^I is the mode I fracture energy which shows the area under tensile stress-displacement curve and under net normal displacement κ_1 is equal to $|\Delta u_n^p|$.

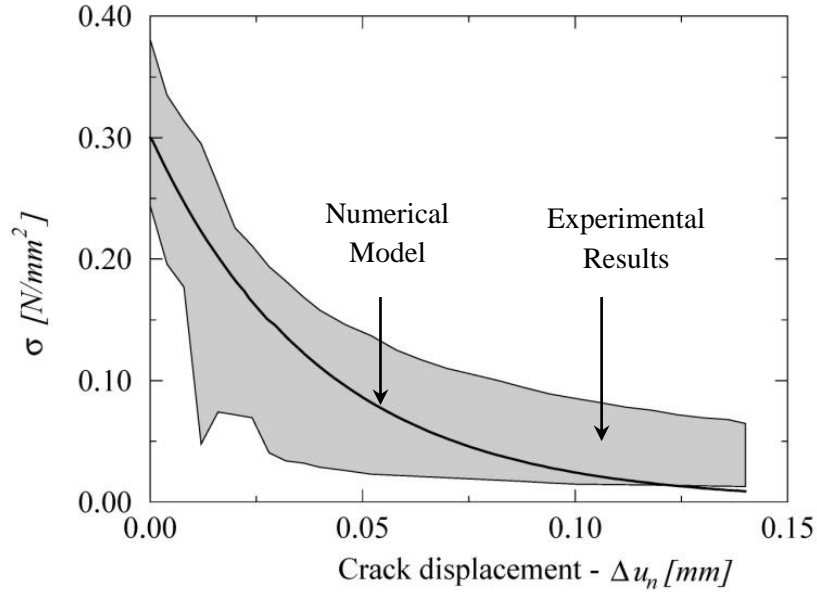


Figure 3-5. Tensile behavior; experimental results from Pluijm (1992), $f_t = 0.30$ [N/mm²] and $G_f^I = 0.012$ [N/mm]

For shear mode the yield function is given by (1992):

$$f_2(\sigma, \kappa_2) = |\tau| + \sigma \tan\phi - \bar{\sigma}_2(\kappa_2) \quad (3-8)$$

$$\bar{\sigma}_2 = c \exp\left(-\frac{c}{G_f^{\text{II}}} \kappa_2\right) \quad (3-9)$$

where c is the cohesion of the unit-mortar interface, ϕ is the friction angle, and G_f^{II} is the mode II fracture energy which shows the area under shear stress-displacement curve (Figure 3-6). In this model the effect of dilatancy angle is neglected, also the friction angle is considered to remain unchanged after cracking. Under a net shear displacement, κ_2 is equal to $|\Delta u_s^p|$.

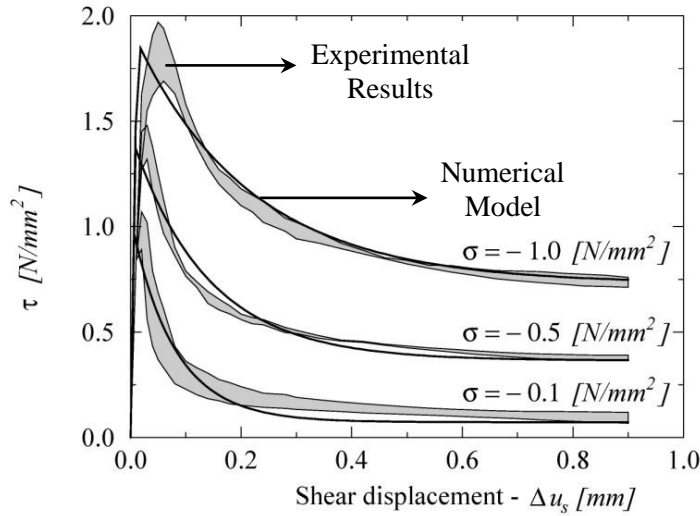


Figure 3-6. Shear behavior; experimental results by Pluijm [15] for different confinement levels, $c = 0.87 \text{ [N/mm}^2]$; $\tan\phi = 1.01$; $\tan\phi_r = 0.73$; $G_f^I = 0.058 - 0.13 \text{ [N/mm]}$

Ellipsoid interface model is considered for cap mode, which was first introduced by Schellekens (1992). The yield function, for a 2-D configuration, is illustrated in Figure 3-7 and given by:

$$f_3(\sigma, \kappa_3) = C_{nn}\sigma^2 + C_{ss}\tau^2 + C_n\sigma - (\bar{\sigma}_3(\kappa_3))^2 \quad (3-10)$$

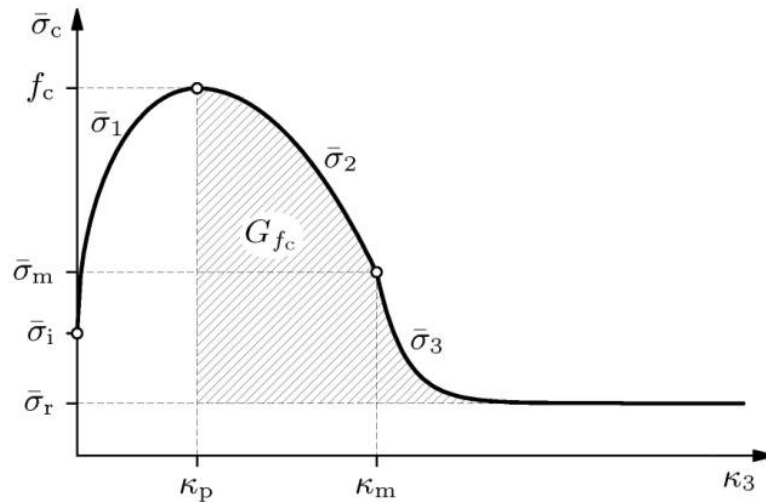


Figure 3-7. Hardening and softening law for cap mode (DIANA 2008)

In equation (3-10), C_{nn} and C_n control the center of the cap region and C_{ss} represents the contribution of the shear stresses. In this study, we consider $C_{nn} = 1$ and $C_n = 0$. $\bar{\sigma}_3(\kappa_3)$ represent the compressive strength and the parameters that appear in Figure 3-7 are described as (Lourenco 1996).

$$\bar{\sigma}_1(\kappa_3) = \bar{\sigma}_i + (f_c - \bar{\sigma}_i) \sqrt{\frac{2\kappa_3}{\kappa_p} - \frac{\kappa_3^2}{\kappa_p^2}} \quad (3-11)$$

$$\bar{\sigma}_2(\kappa_3) = f_c + (\bar{\sigma}_m - f_c) \left(\frac{\kappa_3 - \kappa_p}{\kappa_m - \kappa_p} \right)^2 \quad (3-12)$$

$$\bar{\sigma}_3(\kappa_3) = \bar{\sigma}_r + (\bar{\sigma}_m - \bar{\sigma}_r) \exp \left[2 \left(\frac{\bar{\sigma}_m - f_c}{\kappa_m - \kappa_p} \right) \left(\frac{\kappa_3 - \kappa_m}{\bar{\sigma}_m - \bar{\sigma}_r} \right) \right] \quad (3-13)$$

where all the variables in equations (3-11)-(3-13) are defined in Figure 3-7. Following experimental data for uniaxial compression test, the hardening/softening law for the cap mode is defined by the set below as suggested by Lourenco (Lourenco 1996),

$$\{\sigma_3, \kappa_3\}_i = \left\{ \left(\frac{f_c}{3}, 0.0 \right), (f_c, 0.09), \left(\frac{f_c}{2}, 0.49 \right), \left(\frac{f_c}{7}, \infty \right) \right\}$$

Experimental results are not readily available for the shear-tension paths due to the fact that brittle behavior leads to instability of the test set-up as reported by Lourenco (Lourenco 1996). In the proposed model, isotropic softening is assumed for the coupled behavior between shear and tension (Lourenco 1996). As a consequence of the isotropic softening assumption after applying tensile force and reducing tensile strength to $m\%$ of its initial strength ($0 < m < 100$), the shear strength is also assumed to be reduced by $m\%$ of its initial strength, because in both cases the damage is in the cohesion bonds in the mortar (Figure 3-8).

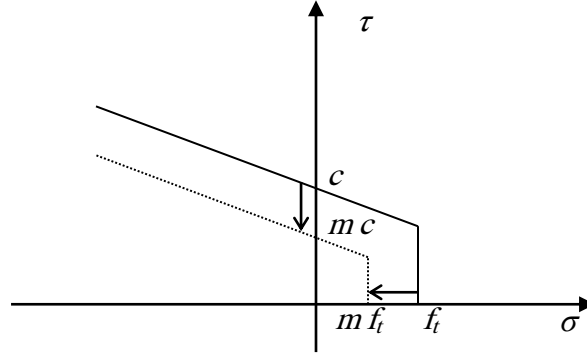


Figure 3-8. Isotropic softening

For example, in the formulation for the total motion leading to tensile stresses in each step, the ultimate shear strength and tensile strength will reduce, which can be defined as

$$\Delta\kappa_{2,n+1} = \frac{G_f^I}{G_f^{II}} \frac{c}{f_t} |\Delta u_n^p| \quad (3-14)$$

Thus, for both displacement in the shear and tension direction, κ_1 and κ_2 are defined as,

$$\kappa_1 = (\Delta u_n^p) + \left(\frac{G_f^I}{G_f^{II}} \frac{c}{f_t} |\Delta u_n^p| \right) \quad (3-15)$$

$$\kappa_2 = (\Delta u_s^p) + \left(\frac{G_f^{II}}{G_f^I} \frac{f_t}{c} |\Delta u_n^p| \right) \quad (3-16)$$

3.5 Algorithms to detect and update the contact zones

After initiation of the horizontal displacement which leads to shearing of the interface elements, the two parts of the interface elements are no longer completely aligned relative to each other (Figure 3-9). Thus, the algorithm is designed to update the normal tractions (equation (3-18)), and based on the Mohr-Coulomb rules the resultant shear strength (equation (3-19)).

$$\xi = \frac{L}{L - u_1} \quad (3-17)$$

$$\text{Updated normal traction} = \sigma \xi \quad (3-18)$$

$$\text{Shear strength} = c - \sigma \xi \tan \phi \quad (3-19)$$

where L is the length of the rigid element and u_1 is shown in Figure 3-9. The effective contact length after application of load “ P ” is shown in Figure 3-9. In this figure, four rigid particles are shown beside each other, under a horizontal (Figure 3-9 (a, b, c)) and vertical load (Figure 3-9 (d, e, f)).

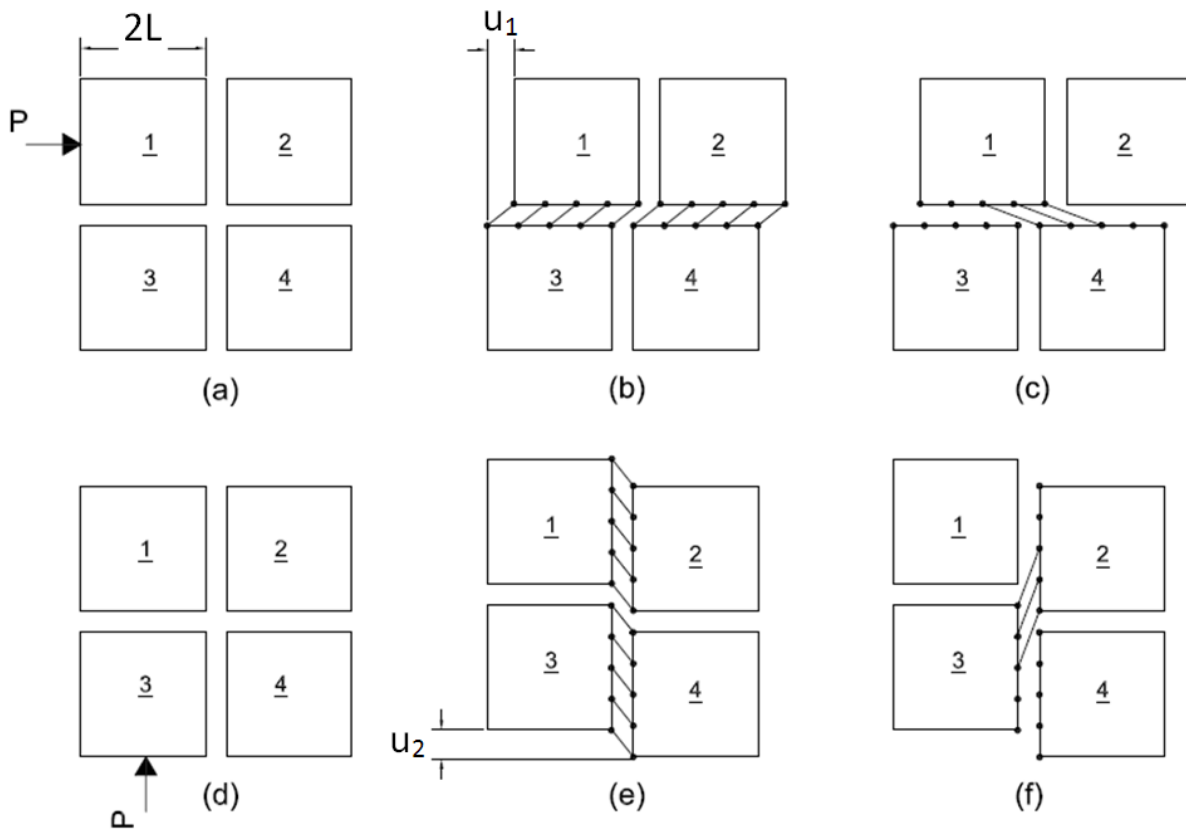


Figure 3-9. Updating contact length and detecting new contacts

In the case of a horizontal loading, after the onset of the transverse displacement, the first and third segments are not completely aligned on top of each other, and for large deformations, a new contact is initiated between the first and fourth segments (Figure 3-9 (b, c)). Equations (3-17) to (3-19) are used to update the normal tractions and shear strength between the first and

third elements. For this case and in order to detect new contacts between the first and fourth elements, auxiliary interface elements are used (as shown in Figure 3-9 (c)). The updating factor for the auxiliary interface elements follows:

$$\eta = \frac{L}{\langle u_1 \rangle} \quad (3-20)$$

where in equation (3-20), $\langle u_1 \rangle$ has been used to indicate that the update factor is just applicable in the case of existing overlap between neighboring particles. For small overlaps, the value of η would be infinite, thus a tolerance should be considered by the user to avoid such numerical instability. Once new contacts are detected, the shear strength for an auxiliary interface element consists of friction force only. For an accurate analysis, auxiliary interface elements should be used for all neighboring segments. Similarly, Figure 3-9 (d, e, f) shows the relation between the third particle and the second and fourth particles under a vertical load.

By using rigid particles at two sides of the interface element, the updating factor (ξ) is the same for all integration points in a single interface element. It is quite evident that the update factor applies to the compressive behavior of the interface.

3.6 *Dynamic equation of motion*

The equation of motion for each constituent of the model (i.e. the rigid blocks, and the interface) can be obtained and represented as follows,

$$[M]\{\ddot{u}\} + [C]\{\dot{u}\} + \{f^0\} + [K_t]\{\Delta u\} = -[M]\{\ddot{u}_g\} \quad (3-21)$$

where $[M]$, $[C]$, and $[K_t]$ represent mass, damping and tangent stiffness matrix, respectively. Time integration can be performed using explicit or implicit method with Newton-Raphson

iterations at each time step (Zienkiewicz OC 1991) to solve the nonlinear system. In the next section, each parameter in the equation of motion is described for the proposed rigid blocks.

3.7 Displacement vector

As described earlier, bricks are defined by a number of rigid elements that are connected to each other by interface elements. The motion of each rigid element can be defined by three degrees-of-freedom (DOF) that will be defined at the center of the rigid elements as illustrated in Figure 3-10. The vector of the applied load is also defined based on the displacement vector.

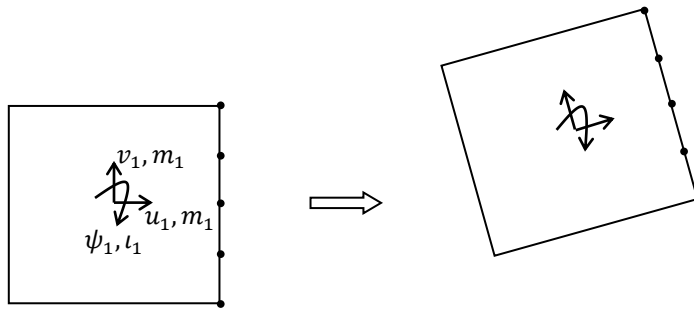


Figure 3-10. Kinematics of the rigid elements

$$\{u\}^T = \{u_1, v_1, \psi_1, u_2, v_2, \psi_2, \dots\} \quad (3-22)$$

$$\{p\}^T = \{p_1, q_1, \mu_1, p_2, q_2, \mu_2, \dots\} \quad (3-23)$$

Thus at each time step, the strain of each node in the interface element (ε) at the boundary of rigid blocks can be defined by the strain-displacement matrix, [B],

$$\{\varepsilon\} = [B]\{u\} \quad (3-24)$$

3.8 Mass, viscous and stiffness matrix

Total mass of each rigid element is concentrated at the center of element; therefore, the mass matrix just depends on the density of the material and the dimensions of each block to define the total mass and the polar moment of inertia.

$$[M] = \text{Diag}[m_1, m_1, I_1, m_2, m_2, I_2, \dots] \quad (3-25)$$

Herein, we consider the damping matrix to be proportional to the mass matrix ($[C] = a_0[M]$).

3.9 Numerical validation

For validating the proposed model, the experimental results of Raijmakers and Vermeltoort (1992) and Vermeltoort and Raijmakers (Vermeltoort 1993) are used (Figure 3-11). They constructed a set of walls with the same geometric configuration and tested them with different values of compressive load. The width and height of the wall are 990 and 1000 mm, respectively, and it has 16 rows of brick. The dimensions of the brick are $210 \times 52 \times 100$ mm and 10 mm thick mortar, built with volumetric cement: lime: sand ratio of 1: 2: 9.

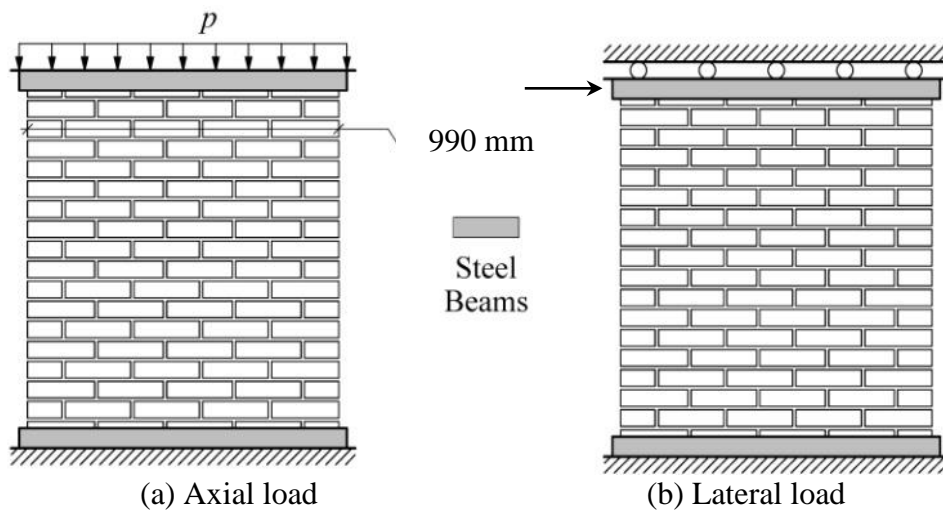


Figure 3-11. Step 1 and step 2 for applying the load (Lourenco 1996)

The wall was subjected to two levels of loading. The total compressive load applied to the first and second walls was 30 kN (J4D and J5D), and for the third wall the compressive load was 120 kN (J6D). After applying the compressive load in the first stage, a monotonic in-plane loading was applied under displacement control.

Different experimental tests were performed to obtain the properties of mortar and bricks by Raijmakers and Vermeltoort (1992). By using the properties of the mortar and brick and according to equations (3-4) and (3-5), the elastic properties of the interface elements can be obtained, which are different for various walls and also for different meshes.

3.9.1 Model #1 - Two rigid blocks per brick model (2PB) under 30 kN load

In this model each brick in the wall is divided into two rigid elements. Elasticity and plasticity of the model are accumulated at the interface elements including the potential cracks and joints between the bricks (Figure 3-12). Using equation (3-4) and (3-5), the properties of the interface elements are determined and given in Table 3-1 and Table 3-2.

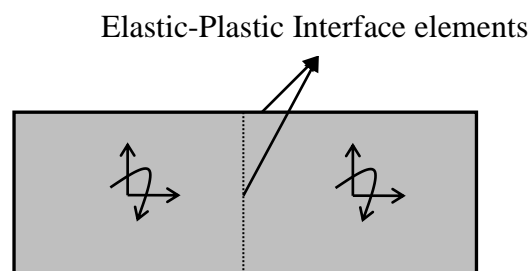


Figure 3-12. 2PB Model

Table 3-1. Properties of different types of cracks (J5D/J6D - 2PB)

(Last two columns are based on the experimental result by Pluijm [14, 15])

	$k_n \frac{N}{mm^3}$	$k_s \frac{N}{mm^3}$	$f_t \frac{N}{mm^2}$	$G_f^I \frac{N}{mm}$
Vertical cracks	53.24/63.78	23.38/28.99	-	-
Horizontal cracks	62.86/78.1	27.60/35.5	-	-
Potential cracks	151.82/151.82	66.66/69	2	0.08

Table 3-2. Inelastic properties of the joints (J5D/J6D - 2PB)

(Based on the experimental result by Pluijm [14, 15])

Tension		Shear			Cap	
$f_t \frac{N}{mm^2}$	$G_f^I \frac{N}{mm}$	$c \frac{N}{mm^2}$	$\tan \phi$	$G_f^{II} \frac{N}{mm}$	$f_m \frac{N}{mm^2}$	C_{SS}
0.25/0.16	0.018/0.012	0.35/0.224	0.75	0.125/0.05	10.5/11.5	9.0

According to the selected mesh size, a finite element model was generated in TNO DIANA (DIANA 2008) along with a user-defined subroutine that consists of the earlier discussion. In these numerical modeling, because deformations were small, there were no use of the auxiliary interface elements. Figure 3-13 shows the load versus the displacement atop the wall. In Figure 3-13 diagonal crack and the ultimate strength of the wall are clearly indicated.

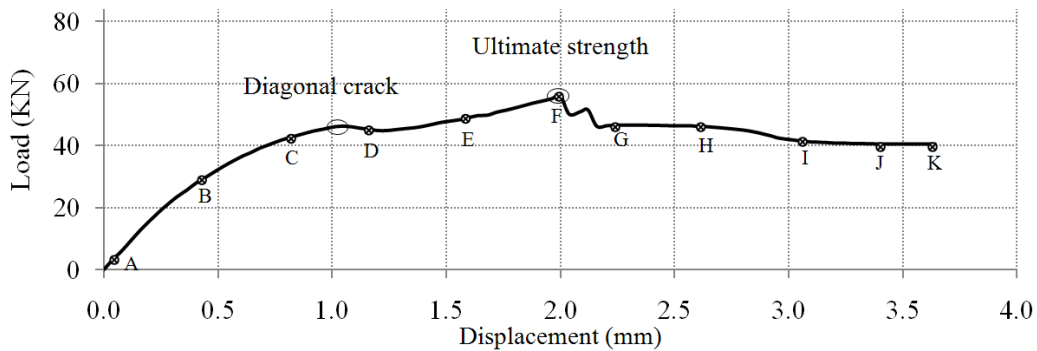
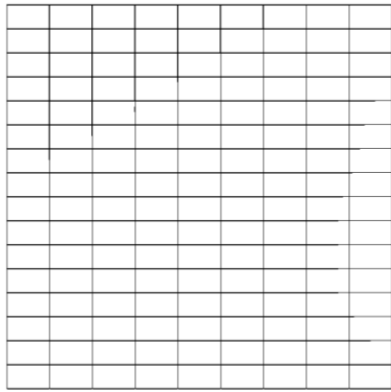
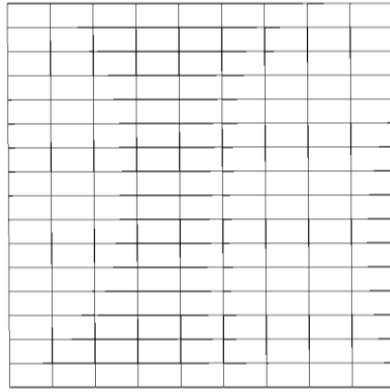


Figure 3-13. Load-displacement graph for J4D and J5D wall (Based on the model 2PB)

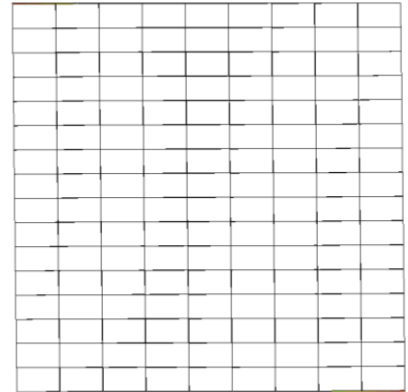
Figure 3-14 shows the crack patterns at different stages of the loading obtained by the proposed model (Displacements are magnified in these figures). Note that the deformation while considering the points (A-K) marked on the graph of Figure 3-13.



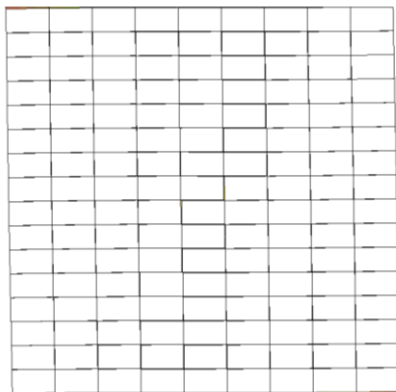
Point A



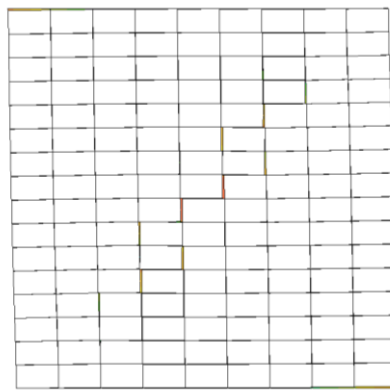
Point B



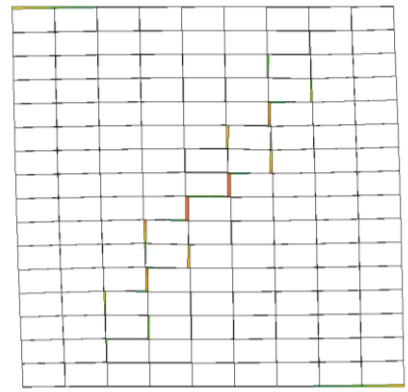
Point C



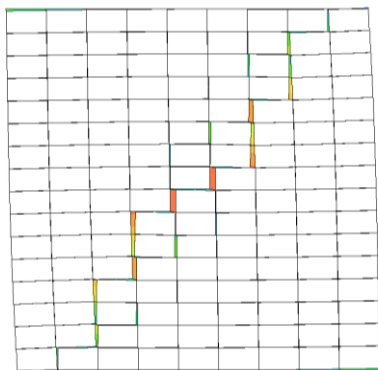
Point D



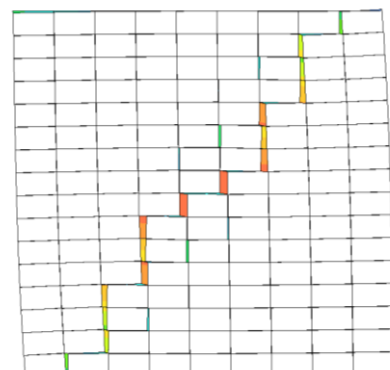
Point E



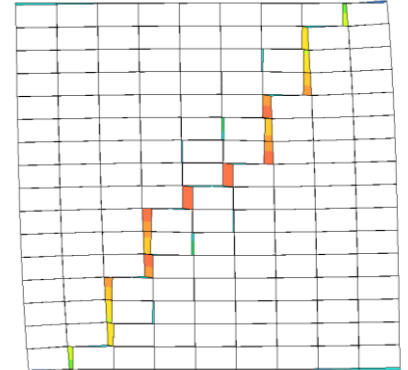
Point F



Point G



Point H



Point I

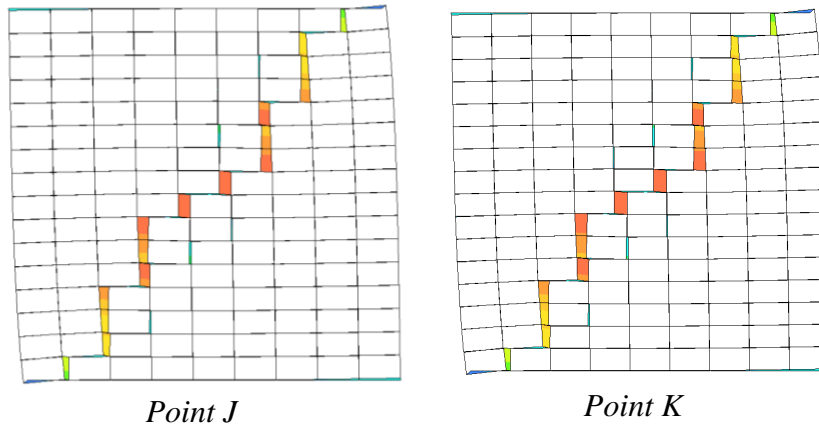


Figure 3-14. Crack path in different stages of loading (Based on the model 2PB - under 30 kN compressive load)

As illustrated in Figure 3-13, there is no clear elastic region for the behavior of the wall, subjected to 30 kN compressive loading. As distinctly shown in Figure 3-14, from the early stages of the loading the top and bottom corners of the wall start to separate from the support. As the load continues to increase, bricks located on the diagonal region and in the middle of the wall start to crack. At a displacement of 1 mm, the diagonal crack has already propagated through the diagonal line. By reaching 2 mm displacement, just the joints between the bricks have started to crack and consequently potential cracks at the middle of the bricks start to propagate. As the load progresses to produce displacements more than 2.5 mm, the behavior of the wall is mostly controlled by frictional forces, because of the sliding of bricks relative to each other, and the diagonal crack starts to open more.

3.9.2 Model #2 - Four rigid blocks per brick model (4PB) under 30 kN load

In this model each brick is divided into four rigid elements. The potential crack is considered in the middle of the brick and two line springs are defined in the quarter of the bricks as shown in Figure 3-15. Elasticity of the model is defined in the interface elements including the potential

cracks, line springs and joints between the bricks, but plasticity is just allowed to occur in the joints between the bricks and the potential cracks.

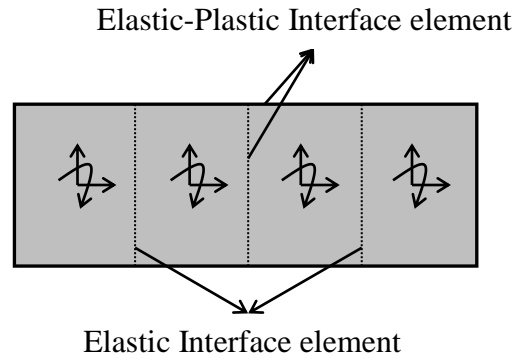


Figure 3-15. 4PB Model

Using equation (3-4) and (3-5) the properties of the interface elements are determined and presented in Table 3-3 and Table 3-4.

Table 3-3. Properties of different types of crack (J5D/J6D - 4PB)

(Last two columns are based on the experimental result by Pluijm [14, 15])

Type	$k_n \frac{N}{mm^3}$	$k_s \frac{N}{mm^3}$	$f_t \frac{N}{mm^2}$	$G_f^I \frac{N}{mm}$
Vertical cracks	80.75/63.78	36.70/28.99	-	-
Horizontal cracks	62.86/78.10	27.60/35.50	-	-
Potential cracks	303.64/303.64	133.30/138.00	2	0.08

Table 3-4. Inelastic properties of the joints (J5D/J6D - 4PB)

(Based on the experimental result by Pluijm [14, 15])

Tension			Shear			Cap		
$f_t \frac{N}{mm^2}$	$G_f^I \frac{N}{mm}$	$c \frac{N}{mm^2}$	$\tan \phi$	$G_f^{II} \frac{N}{mm}$	$f_m \frac{N}{mm^2}$	C_{SS}		
0.25/0.16	0.018/0.012	0.35/0.224	0.75	0.125/0.05	10.5/11.5	9.0		

A finite element model was generated using the described mesh in TNO DIANA (DIANA 2008) and was imposed to the gravity load and in-plane displacement controlled loading.

Figure 3-16 shows the load versus the displacement of the top of the wall. In Figure 3-16, diagonal crack and the ultimate strength of the wall are determined.

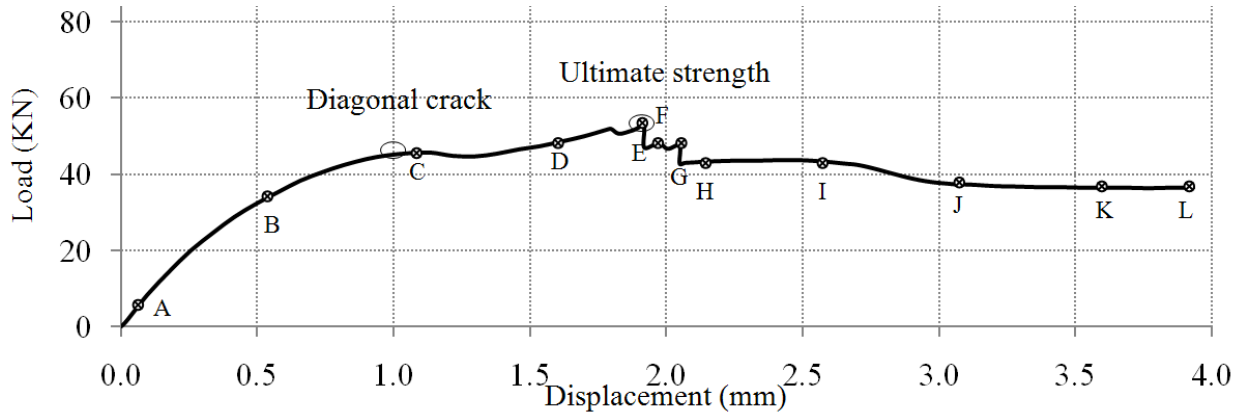
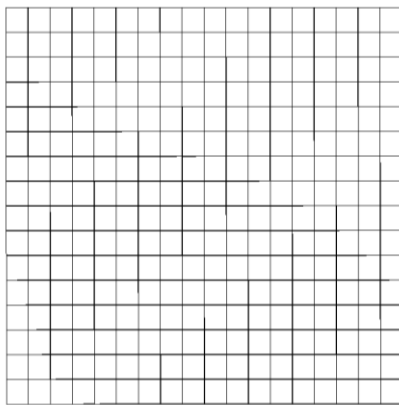
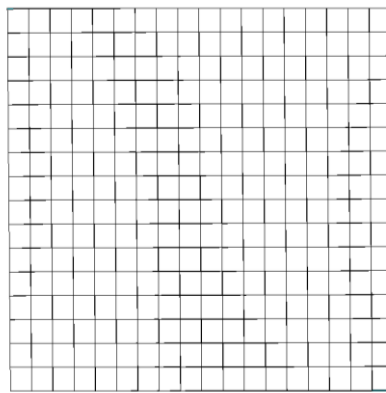


Figure 3-16. Load-displacement graph for J4D & J5D wall (Based on the model 4PB)

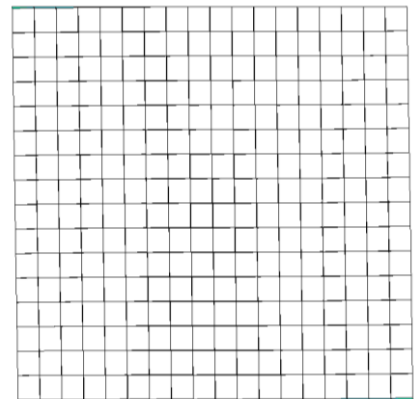
Figure 3-17 shows the crack opening at different stages of loading as simulated by the proposed model. A snap shot of the deformed shape of the wall is associated with the points A-L shown in Figure 3-16.



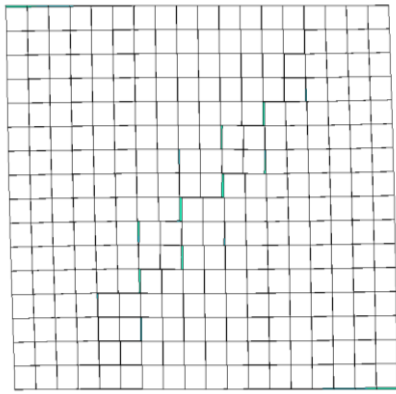
Point A



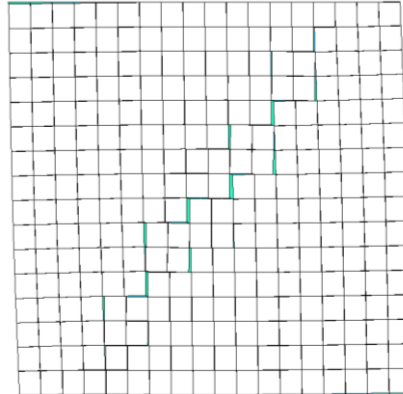
Point B



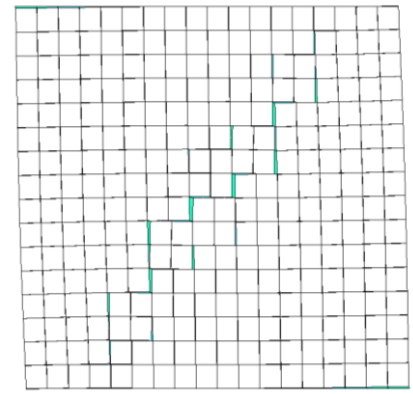
Point C



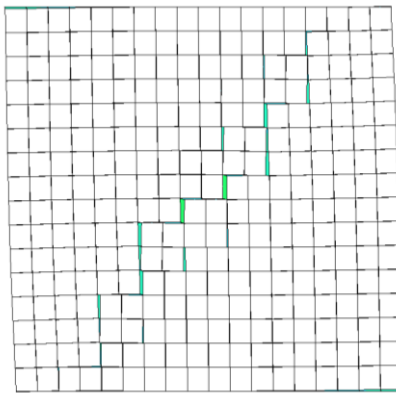
Point D



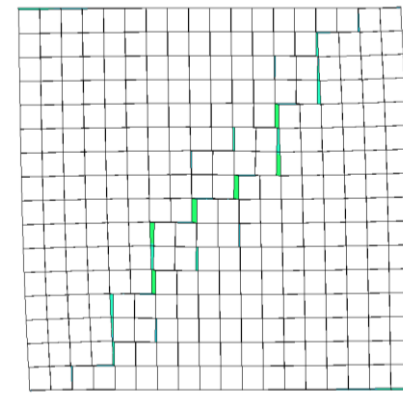
Point E



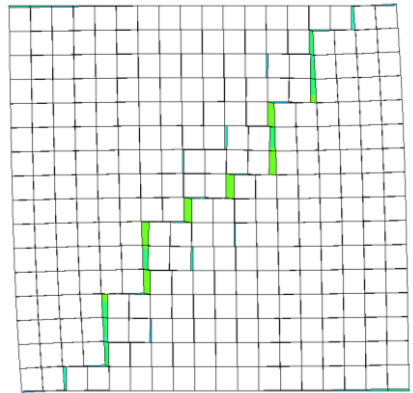
Point F



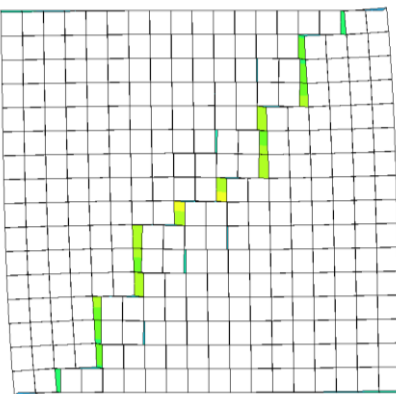
Point G



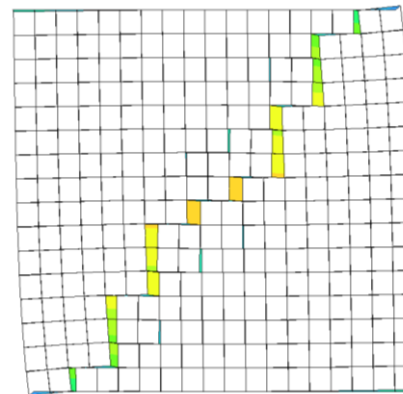
Point H



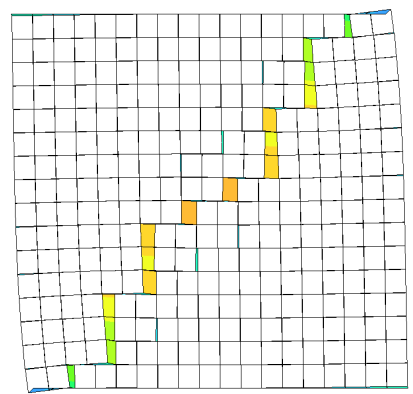
Point I



Point J



Point K



Point L

Figure 3-17. Crack path in different stages of loading (Based on the model 4PB- under 30 kN)

3.9.3 Model #1 - Two rigid blocks per brick model (2PB) under 120 kN load (J6D)

In this case study, the same model described in Figure 3-12 is used using a compressive load of 120 kN at the top of the wall. The applied load versus the displacement and the crack propagation in the wall for both the 2PB- and 4PB-model are given in Figure 3-18 and Figure 3-19, respectively. The snap shots in Figure 3-19 are associated with Figure 3-18 by points A-L.

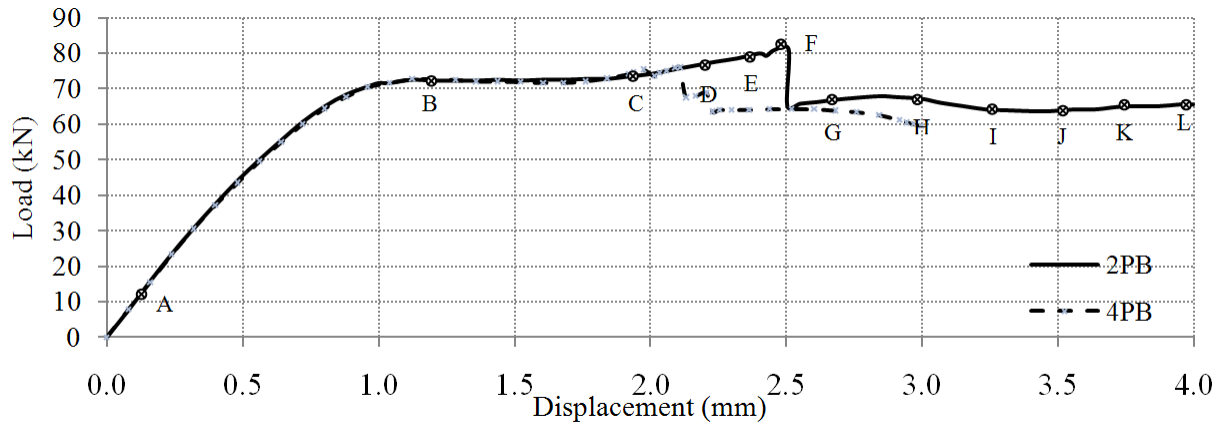
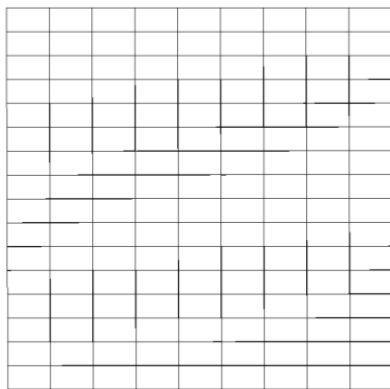
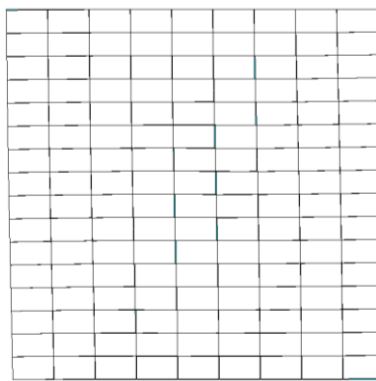


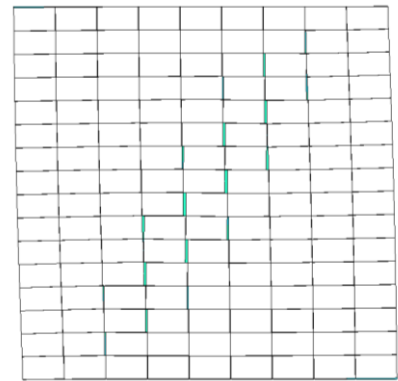
Figure 3-18. Load-displacement graph for J6D wall (Based on the model 2PB and 4PB)



Point A



Point B



Point C

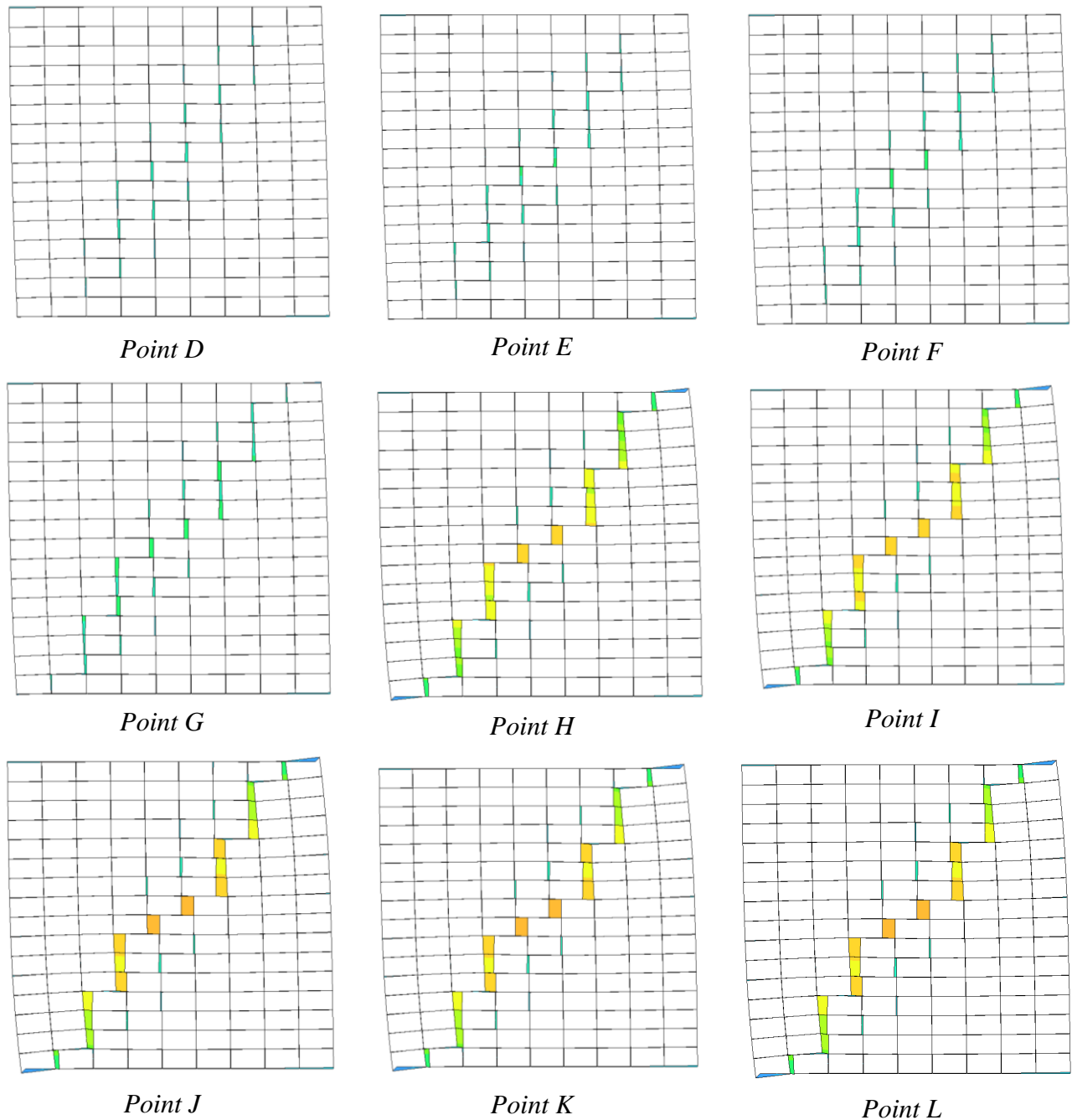


Figure 3-19. Crack path in different stages of loading (Based on the model 2PB- under 120 kN)

In this case (J6D wall as designated by Raijmakers and Vermeltoort (1992; 1993)), the elastic region is more visible in comparison with wall J5D and that is attributed to the higher compressive load. The separation of the bricks at the top and bottom corner of the wall is hence

delayed until the onset of separation of the diagonal joints, which are taking place simultaneously at a displacement around 1 mm. In the J4D-model, because of the low compressive load, bricks start to separate progressively and gradually, one after the other. We note herein that after the diagonal cracks are fully propagated the wall is still in the hardening regime (Figure 3-13), but in the J6D model the diagonal crack suddenly starts and after that the strength of the wall remains almost the same (Figure 3-18).

3.10 Comparison of the results

The comparison of the numerical results of mesh 2PB and 4PB with the experimental results associated with two different compressive loads is presented in Figure 3-20. The two models are compared with the results obtained by the experimental results of Raijmakers and Vermeltoort (Raijmakers 1992) and Vermeltoort and Raijmakers (Vermeltoort 1993). As it is shown in Figure 3-20, even for the two sets of tests with the same material properties and compressive loads, the experimental results are different. Clearly, simulation results have shown good agreement with the experimental results as illustrated in Figure 3-20.

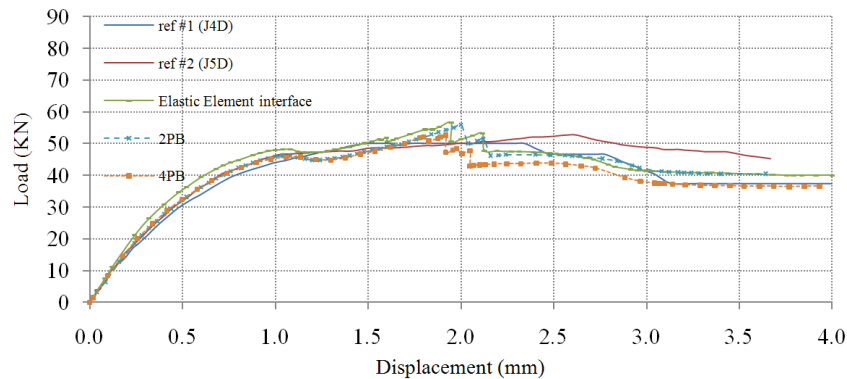


Figure 3-20. Load-displacement graph for J4D and J5D wall

The numerically predicted loads for the diagonal crack and the ultimate strength are within 15% of the loads obtained by the experimental test. Moreover, by comparing the results from two sets of numerical models, it is evident that the rigid blocks and line interface modeling approach are not so sensitive to the mesh size. The same comparison was performed on the specimen designated as J6D wall with the applied 120 kN compressive load and the results are presented in Figure 3-21.

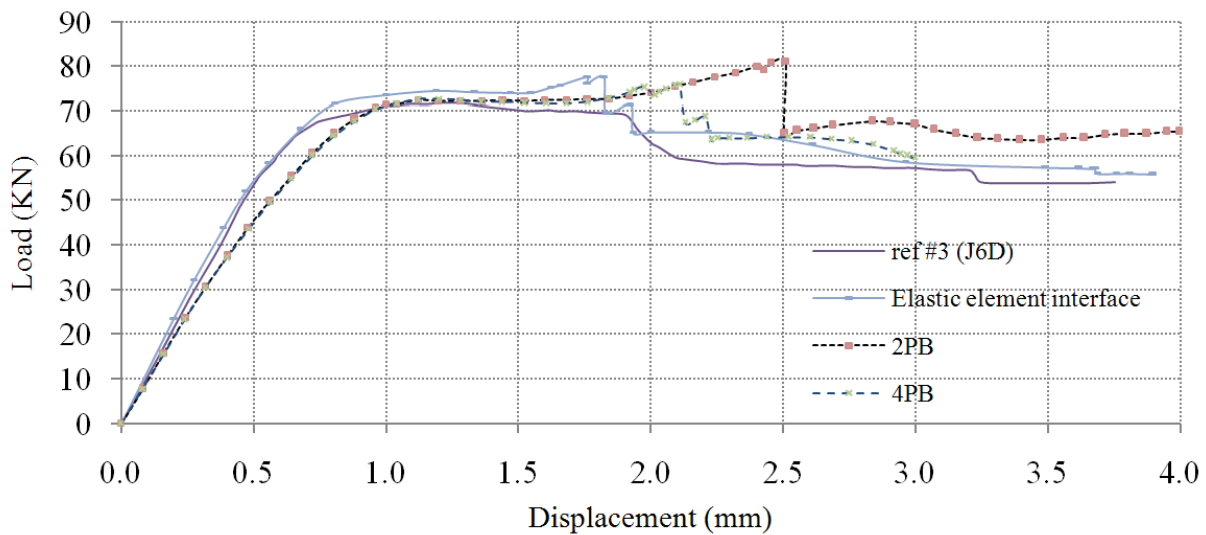


Figure 3-21. Load-displacement graph for J6D wall (numerical and experimental)

Figure 3-22 and Figure 3-23 present the experimental and numerical propagated diagonal cracks. In Figure 3-22, the numerical results for two different mesh sizes are presented, which are very similar.

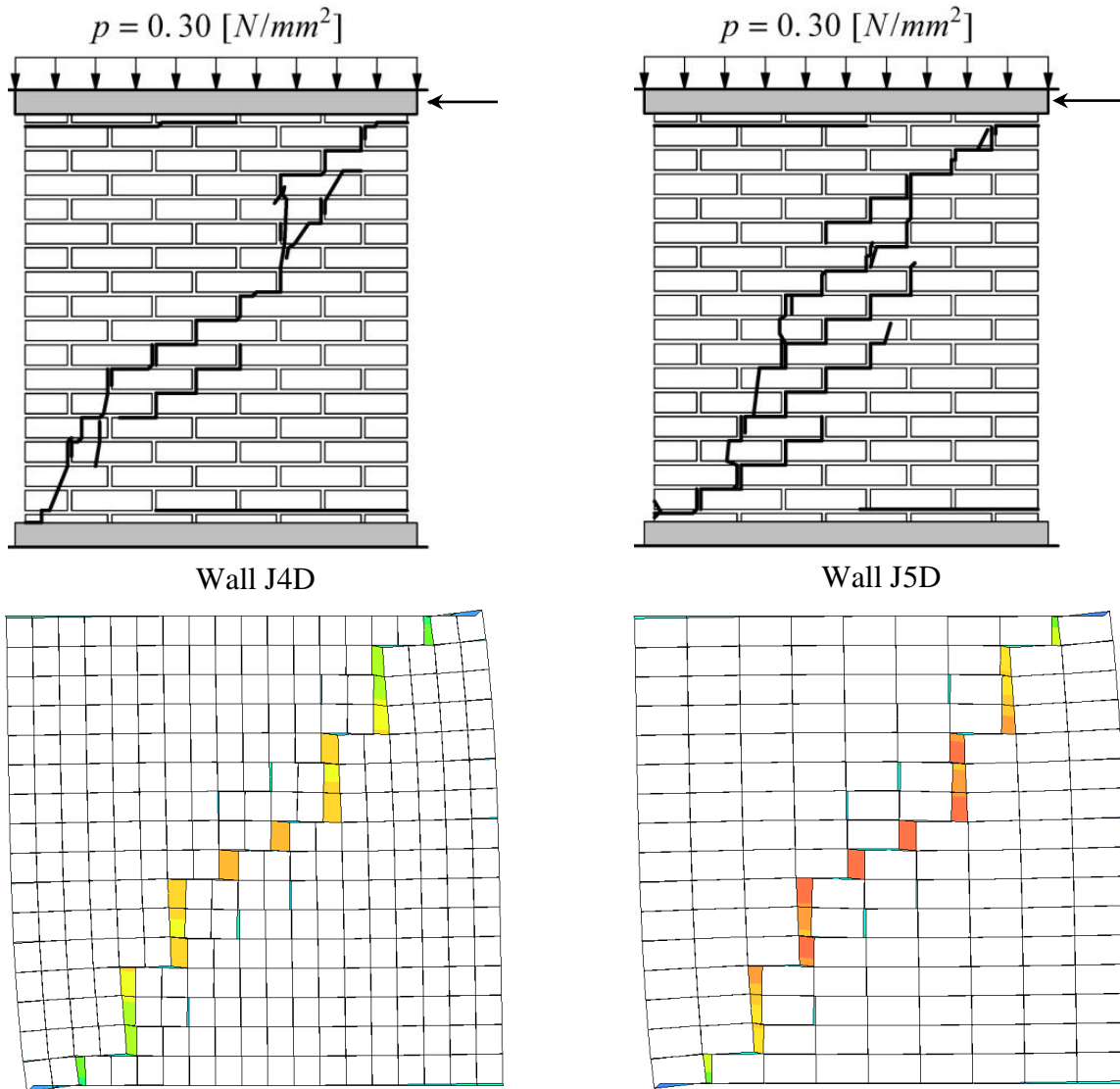


Figure 3-22. Comparison between the cracks obtained by the numerical and experimental models (J4D and J5D)

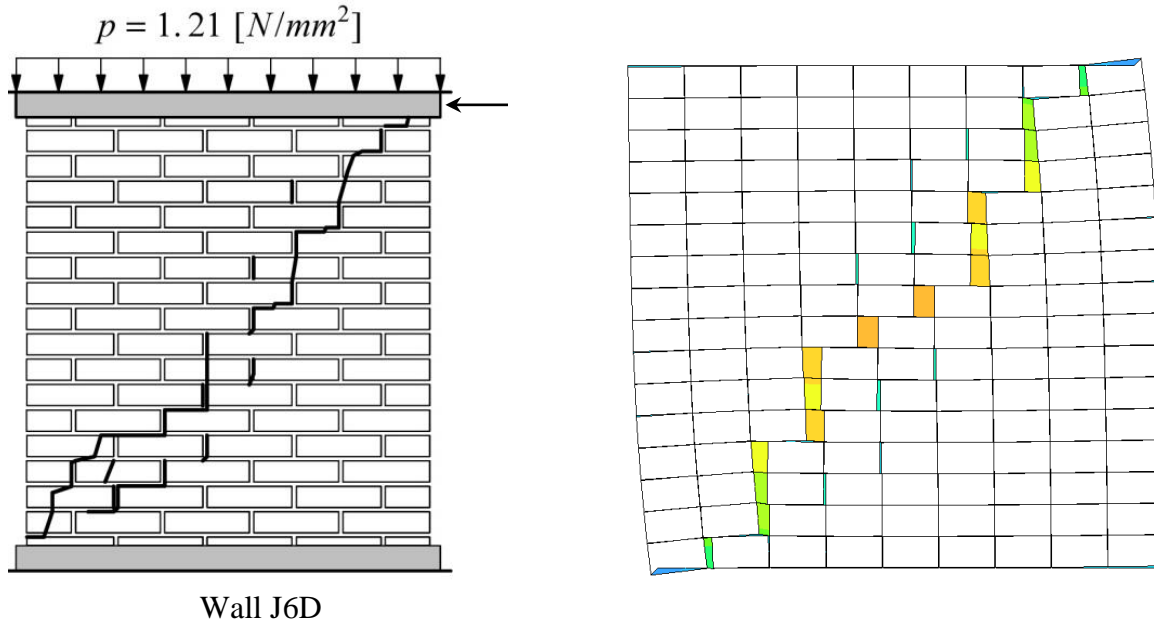


Figure 3-23. Comparison between the cracks obtained by the numerical and experimental models (J6D)

In the proposed modeling approach, the effect of Poisson's ratio has been neglected, so in the elastic range and before cracking, a minor inaccuracy is expected. As depicted in Figure 3-21, difference exists between the experimental and numerical results in the elastic range. However, in Figure 3-20 this assumption (neglecting Poisson's ratio effect) has not influenced the results, and that is attributed to the fact that in wall J4D, the compressive load is less than J6D and as it has been discussed, from the beginning of the loading the inelastic behavior is the dominant behavior, and therefore, there is no discernible elastic region.

In Figure 3-20 and Figure 3-21, the numerical using elastic elements interface model derived by Lourenco (Lourenco 1996) is presented, beside the numerical results obtained with the proposed model in this section. In Lourenco's proposed model, each brick is simulated with eight elastic elements with eight nodes; therefore, each brick has 80 DOF. By utilizing the proposed model in this section, the mesh size is significantly lower than the Lourenco's model. For the 2PB model, the number of DOF is decreased by 92% and in the 4PB model it is

decreased by 85% when comparing to Lourenco's model (Lourenco 1996). In Figure 3-20 and Figure 3-21 it has been shown that although the number of DOF has been reduced significantly, the accuracy of the model has not been reduced. Hence, the proposed model provides an efficient and accurate response with a low computational cost.

3.11 Summary and conclusion

In this section, by using rigid blocks and line interface elements, a fast computational algorithm with accurate response is proposed, to model URM walls under monotonic in-plane loadings. By writing a subroutine in the commercial finite element code (DIANA) elasticity and all different cracking paths are defined in the interface elements. To achieve more accuracy, the subroutine features a rationale for updating the length of contact and consequently the normal traction and shear strength at each time step of the analysis.

Two different mesh sizes have been used to generate the finite element model for an experimentally tested wall. In the first and second numerical models, each brick was divided into two or four rigid blocks, respectively, and the interface elements were located between the rigid blocks. All the linear and nonlinear behavior of the brick and mortar were defined in the interface elements. It was shown that the obtained numerical results are very close to the experimental results. Moreover, by comparing the numerical results of the two mesh sizes, it was concluded that the proposed model is not highly sensitive to the mesh size.

Comparing to the nodal interface elements derived by other researchers, line interface elements prevent the free rotation in the interfaces. Moreover, by using line interface elements, contacts in the corner of the bricks after separation of the bricks are accurately modeled. Based on the literature review conducted by the author, it is the first time that the idea of the rigid

elements with an accurate material model is applied to the meso-scale modeling to simulate the cracking of masonry walls. By comparing to other rigid body spring models available in the literature, the proposed material models are more accurate. The proposed meso-scale modeling approach along with the material models clearly shows high computational efficiency when compared with other modeling approaches.

SECTION 4

MODIFIED CAP PLASTICITY MODEL FOR INTERFACE ELEMENTS WITH APPLICATION IN MESO-SCALE ANALYSIS OF MASONRY STRUCTURES

4.1 Introduction

Several constitutive material models have been proposed for different types of materials over the past decades, which use multiple yield surfaces to simulate the behavior of the materials in the nonlinear regime. The main difficulty in using such material models is the abrupt changes in the behavior of the material, particularly for brittle materials, while moving from one yield surface to another. These abrupt changes lead to convergence problems in the numerical analysis. A set of interpolation functions has been introduced in this section that generates smooth transition between yield surfaces.

To make the problem more practical, an existing and widely used material model for application of meso-scale modeling of masonry structures has been chosen and the proposed interpolation functions in this section have been used to improve the behavior of this material model. The available meso-scale yield surface has three distinct yield surfaces, which are representative of several cracking modes, associated with tensile, shear, and compression failure. The material model is intended specifically for application in the interface elements, either nodal or line interface elements, which find much use in modeling discontinuous models as in the case of mortar and bricks.

Using few examples, it is shown how the application of the proposed interpolation functions in this section generates smooth transition between the yield surfaces. Finally the developed material model has been utilized in modeling masonry walls using lattice model (Cusatis et al. 2003; Cusatis et al. 2003; Cusatis et al. 2006; Cusatis and Cedolin 2007; Schlangen 1995; Schlangen and Garboczi 1997), and the mesh sensitivity issues of the model have been investigated. In the following sections, first the elastic and plastic behavior of the existing material model is presented, and then it is shown how the behavior of the material will be improved by employing the proposed interpolation.

4.2 Elastic behavior of the interface elements

The behavior of an interface element is initially elastic, i.e., $\Delta \mathbf{t} = k \Delta \bar{\mathbf{u}}$, where k is the elastic stiffness of joints (see equations (4-1), (4-2), (4-3) - Figure 4-1). In this case, the stiffness matrix will directly relate the displacement increments to the stress tensor increments.

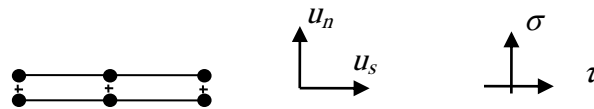


Figure 4-1. Line interface element

$$k = \begin{bmatrix} k_n & 0 \\ 0 & k_s \end{bmatrix} \quad (4-1)$$

$$\mathbf{t} = \begin{Bmatrix} \sigma \\ \tau \end{Bmatrix} \quad (4-2)$$

$$\Delta \mathbf{u} = \begin{Bmatrix} u \\ v \end{Bmatrix} \quad (4-3)$$

where k_n and k_s are the normal and transverse stiffness of the interface element, respectively. The normal stress is represented with σ and τ corresponds to the shear stress in equation (4-2).

4.3 Yield surface for interface elements

Using the experimental results for tension, shear and compression tests, different yield surfaces were suggested by several researchers (Lourenco 1996; Oliveira and Lourenco 2004; Page 1978; Stavridis and Shing 2010). Page (1978) suggested using interface elements along with the yield surface presented in Figure 4-2, excluding the cap mode. Lourenco (1996) added the cap mode and represented the yield surface of Figure 4-2.

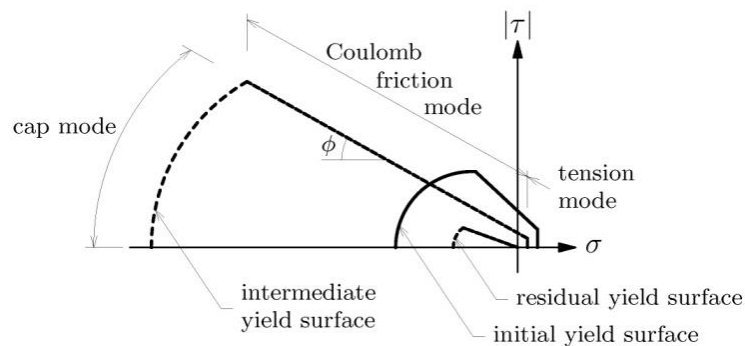


Figure 4-2. Material model for interface elements “interface cap model” (DIANA 2008)

Figure 4-3 (a), (b) and (c) demonstrate the state of stresses under tensile, shear and uniaxial compression stresses, respectively. For example in Figure 4-3 (a) after application of the tensile stress (normal stress), the state of stress moves toward the negative direction of the horizontal axis until reaching the yield surface. By employing compressive stress, the sign of the normal stress changes in Figure 4-3 (c). Figure 4-3 (d) represents the state of stress in the combination of shear and high compressive stresses.

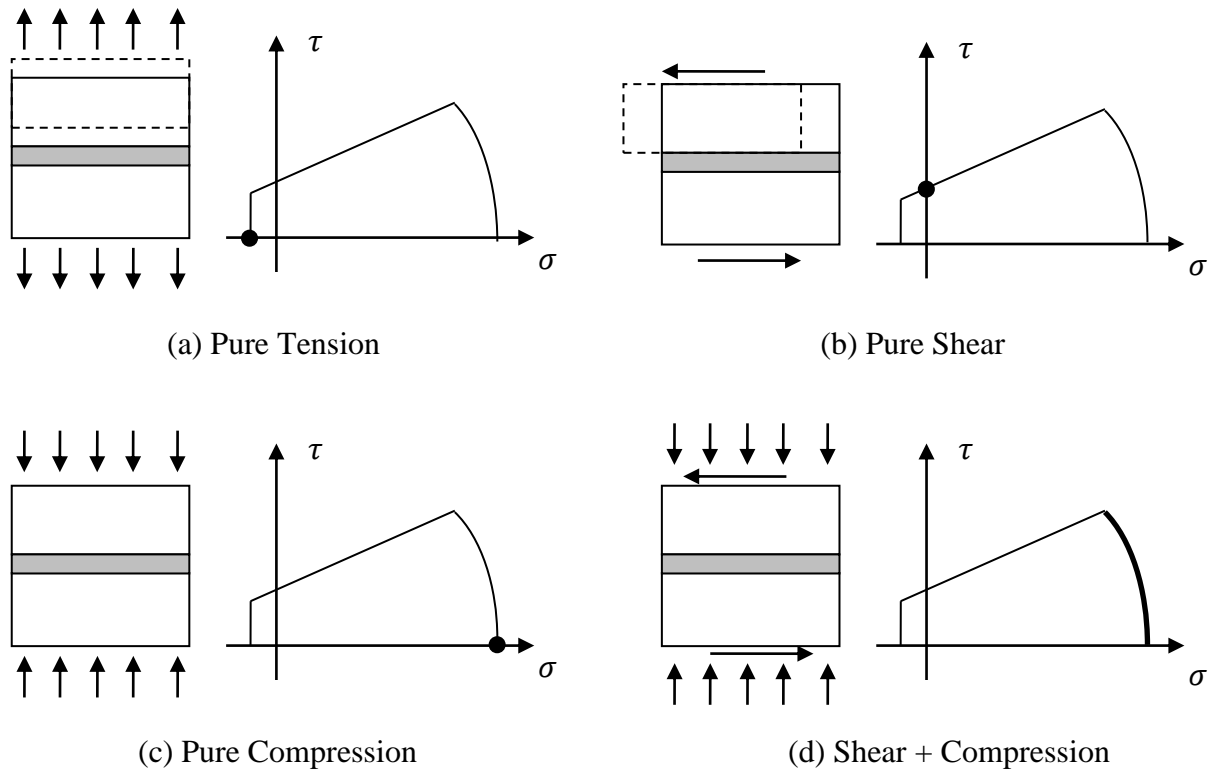


Figure 4-3. State of stress for different types of loadings

In the following sections the behavior of the material is presented after reaching the yield surface, and the nonlinear behavior of different parts of the yield surface is described.

4.4 Plastic behavior of interface elements

Three common experimental tests have been conducted by several researchers on different types of brittle materials such as masonry samples (Pluijm 1992; Pluijm 1993; Vermeltoort 1991). The test series include tension, shear and uniaxial compression tests. Based on these experimental tests, the following nonlinear behaviors are proposed by different researchers.

4.4.1 Tension cut-off regime

In an experimental study, Pluijm (Pluijm 1992; Pluijm 1993) performed a series of tension tests. He tried to propose a numerical model for the tensile softening behavior (Figure 4-4). It is

reported by Pluijm (Pluijm and Vermeltoort 1991) that an exponential curve representing the softening is in accord with the experimental results, and given by

$$f_1(\sigma, \kappa_1) = \sigma - \bar{\sigma}_1(\kappa_1) \quad (4-4)$$

$$\bar{\sigma}_1 = f_t \exp\left(-\frac{f_t}{G_f^I} \kappa_1\right) \quad (4-5)$$

where f_t is the tensile strength of the brick-mortar interface and G_f^I is the first mode fracture energy that represents the area under tensile stress-displacement curve and can be determined by experimental data. Under net normal displacement, κ_1 is equal to $|\Delta u_n^p|$.

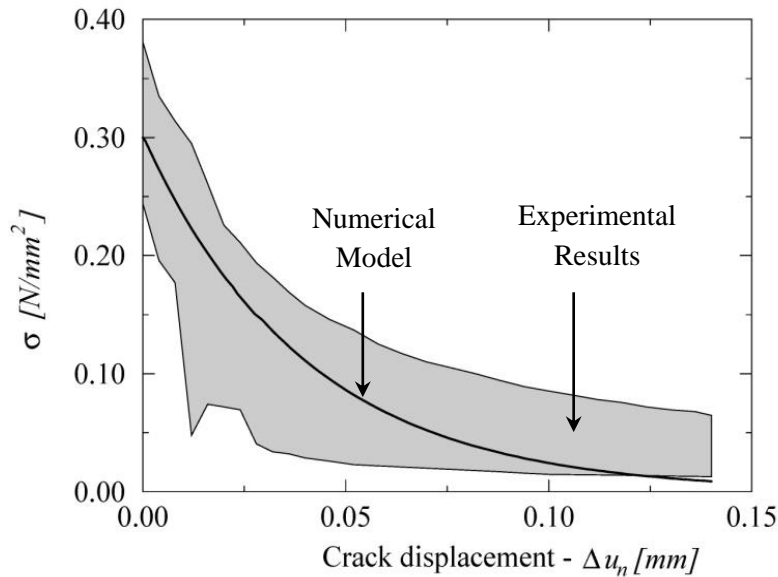


Figure 4-4. Tensile behavior; experimental results from Pluijm (1992), $f_t = 0.30$ [N/mm²] and $G_f^I = 0.012$ [N/mm]

4.4.2 Shear regime

A number of shear tests in combination with different compressive stresses was performed by Pluijm (Pluijm 1992; Pluijm 1993). Again it was shown that the softening behavior is in good

agreement with the exponential curve representing softening and the maximum shear strength is given by the Mohr-Coulomb plasticity model, which takes the following form,

$$f_2(\sigma, \kappa_2) = |\tau| + \sigma \tan\phi - \bar{\sigma}_2(\kappa_2) \quad (4-6)$$

$$\bar{\sigma}_2 = c \exp\left(-\frac{c}{G_f^{II}} \kappa_2\right) \quad (4-7)$$

where c is the cohesion of the brick-mortar interface, ϕ is the friction angle, and G_f^{II} is the second mode fracture energy (i.e. shear mode – Figure 4-5) which shows the area under shear stress-displacement curve. Pluijm (Pluijm 1993) reported that in the high confinement pressures the dilatancy angle tends to go to zero. Therefore, in this model the effect of dilatancy angle is neglected. The friction angle is also considered to remain unchanged after cracking in this model.

Under a net shear displacement, κ_2 is equal to $|\Delta u_s^p|$.

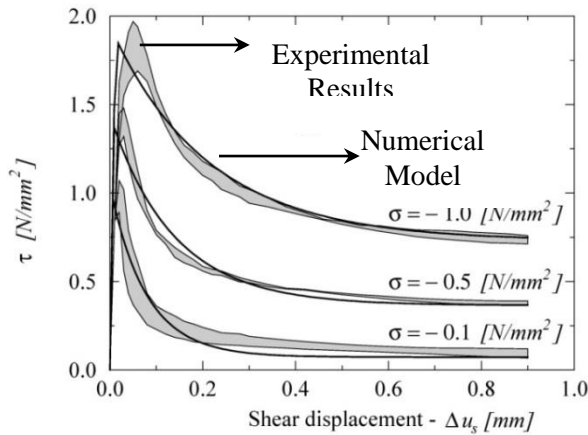


Figure 4-5. Shear behavior; experimental results by Pluijm [15] for different confinement levels, $c = 0.87 \text{ [N/mm}^2\text{]}$; $\tan\phi = 1.01$; $\tan\phi_r = 0.73$; $G_f^{II} = 0.058 - 0.13 \text{ [N/mm]}$

4.4.3 Cap regime for high compressive stresses

Ellipsoid interface model is considered for the cap mode as shown in Figure 4-2, which was originally introduced by Schellekens (Schellekens 1992) for the first time. The yield function for a 2-D model is given by:

$$f_3(\sigma, \kappa_3) = C_{nn}\sigma^2 + C_{ss}\tau^2 + C_n\sigma - (\bar{\sigma}_3(\kappa_3))^2 \quad (4-8)$$

where C_{nn} and C_n control the center of the cap, and C_{ss} represents the contribution of the shear stress, and the compressive strength is shown by $\bar{\sigma}_3(\kappa_3)$. For modeling masonry, Lourenco (1996) suggested C_{nn} and C_n , to be 1 and 0, respectively.

The hardening/softening law for the cap mode is defined using a combination of three functions presented by equations (4-9) to (4-11) (Lourenco 1996). In this study, equation (4-11) has been modified to tend to zero. The reason for this modification is described in section 4.6.2. In equations (4-9) to (4-11), all the parameters are defined in Figure 4-6 except the parameter “ m ”, which will be defined later in section 4.8 and equation (4-20).

$$\bar{\sigma}_a(\kappa_3) = \bar{\sigma}_i + (\bar{\sigma}_p - \bar{\sigma}_i) \sqrt{\frac{2\kappa_3}{\kappa_p} - \frac{\kappa_3^2}{\kappa_p^2}} \quad \text{for } 0 \leq \kappa_3 \leq \kappa_p \quad (4-9)$$

$$\bar{\sigma}_b(\kappa_3) = \bar{\sigma}_p + (\bar{\sigma}_m - \bar{\sigma}_p) \left(\frac{\kappa_3 - \kappa_p}{\kappa_m - \kappa_p} \right)^2 \quad \text{for } \kappa_p \leq \kappa_3 \leq \kappa_m \quad (4-10)$$

$$\bar{\sigma}_c(\kappa_3) = \bar{\sigma}_m \exp\left(m \left(\frac{\kappa_3 - \kappa_m}{\bar{\sigma}_m} \right)\right) \quad \text{for } \kappa_m \leq \kappa_3 \quad (4-11)$$

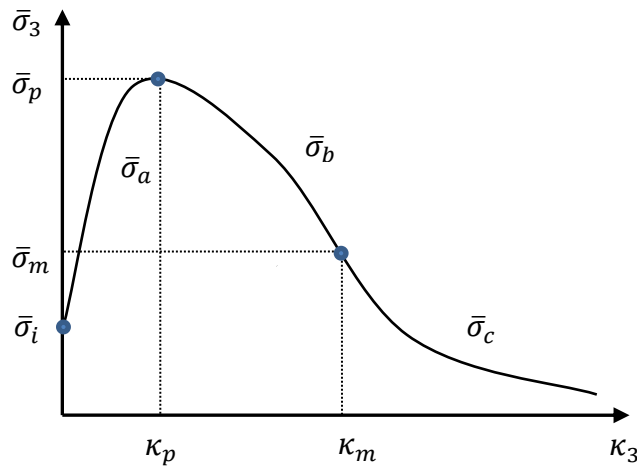


Figure 4-6. Hardening and softening law for cap regime (DIANA 2008)

4.5 Shortcomings of the existing yield surface

The three yield surfaces of Figure 4-7 intersect at two corners (marked as corner *I* and corner *II*) as shown in Figure 4-7. Within a numerical analysis the state of stress in an element continually changes and it might move from one yield surface to the other (in either corner *I* or *II*), which is therefore associated with a sudden change in the behavior of the material. The smooth change between the yield surfaces is expected on the basis of the physics of the problem. Furthermore, any abrupt change in the behavior of an element causes convergence problems in the numerical analysis. This report seeks to provide a new methodology to improve the behavior of this yield surface and overcome the adverse effects associated with such sudden jumps.

Moreover, due to the brittle behavior of a masonry sample, measurement of the load-displacement under the combination of tension and shear or high compression and shear is difficult. Thus, there is paucity of experimental data in such cases. In this study, a set of interpolation functions is developed which determines the behavior of the material in the combination of tension and shear or compression and shear, knowing the stress-strain curves

under shear, tension and compression stresses (which can be determined with the experimental tests). The interpolation function facilitates the extraction of the dual mode of either tension and shear, or compression and shear.

4.6 The proposed interpolation functions

Based on the angle ω (see Figure 4-7) at which stresses are approaching the yield surface, the interpolation function follows three segments (Figure 4-7). The three segments are: $(0 \leq \omega < \pi/2)$, $(\pi/2 \leq \omega < \omega_0)$ and $(\omega_0 \leq \omega \leq \pi)$. The interpolation function $H(\omega)$ is bounded by the interval $[0, 1]$, i.e., $0 \leq H(\omega) \leq 1$.

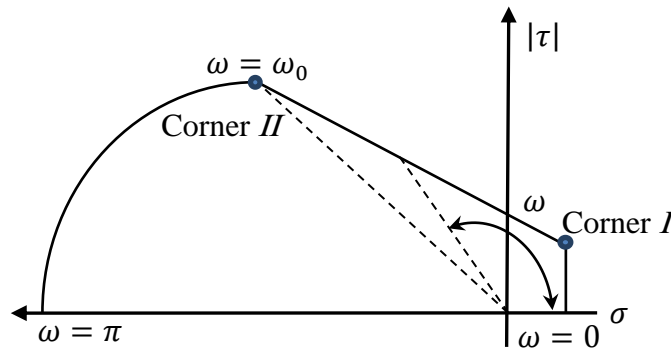


Figure 4-7. The angle associated with the state of stress

For $0 \leq \omega < \omega_0$ the plastic behavior is related to the tensile and shear regimes and the nonlinear behavior follows softening. Therefore, the interpolation function is directly used to change the softening energy between the tensile and shear regimes. Accordingly, the interpolation functions ($H(\omega)$) for $(0 \leq \omega < \pi/2)$ and $(\pi/2 \leq \omega < \omega_0)$ is defined as:

1. *Interpolation between pure tension and pure shear* ($0 \leq \omega < \pi/2$):

$$H(\omega) = \left(\omega/\left(\frac{\pi}{2}\right)\right)^n \quad G(\omega) = G(0) + H(\omega) \left(G\left(\frac{\pi}{2}\right) - G(0)\right) \quad (4-12)$$

where n shows the order of interpolation function and in this study for simplification it is assumed to have unit value, which indicates a linear interpolation. Based on equation (4-12), for $\omega = 0$ the softening energy is $G(0)$ that corresponds to the softening energy of the tensile test and is available from the experimental results. For $\omega = \pi/2$ the softening energy is $G(\pi/2)$ that represents the softening energy of the shear test without any confinement pressure, and is also available from the experimental results.

2. *Interpolation between pure shear and corner II* ($\pi/2 \leq \omega < \omega_0$):

$$H(\omega) = \left(\frac{\omega - \frac{\pi}{2}}{\omega_0 - \frac{\pi}{2}} \right)^n \quad G(\omega) = G\left(\frac{\pi}{2}\right) + H(\omega) (G(\omega_0) - G\left(\frac{\pi}{2}\right)) \quad (4-13)$$

where ω_0 is the angle associated to the corner II (Figure 4-7). According to equation (4-13), for $\omega = \pi/2$ the softening energy is $G(\pi/2)$ and it gradually changes to $G(\omega_0)$ for the state of stress at corner II.

3. *Interpolation between corner II and pure compression* ($\omega_0 \leq \omega \leq \pi$):

The behavior of the existing material model at the corner II for $\omega = \omega_0 + \varepsilon$ is hardening/softening, and for $\omega = \omega_0 - \varepsilon$ the nonlinear behavior is associated with softening (where ε tends to zero). In other words, a slight change in the state of stress of an element leads to a significant change in the material behavior, which is not realistic.

For $\omega_0 \leq \omega \leq \pi$, the interpolation function controls the material behavior in such a way that, for $\omega = \omega_0 + \varepsilon$ the plastic behavior is completely softening (see Figure 4-8 and the curve related to $\omega = \omega_0$), similar to what takes place in the shear regime for $\omega = \omega_0 - \varepsilon$, and as the angle of stresses increases to $\omega = \pi$, gradually hardening takes place and finally for $\omega = \pi$ the

nonlinear behavior exactly matches the experimental results for uniaxial compression test (see Figure 4-8 and the curve related to $\omega = \pi$). This has been done by interpolating the parameters that define the stress-strain curve in Figure 4-6, and is shown in equations (4-15) to (4-18) and Figure 4-8. In section 4.6.1, it will be shown that by interpolating hardening/softening parameters, the energy under hardening-softening curve will be interpolated as well, and that leads to a smooth change as the angle tracing the stress values changes.

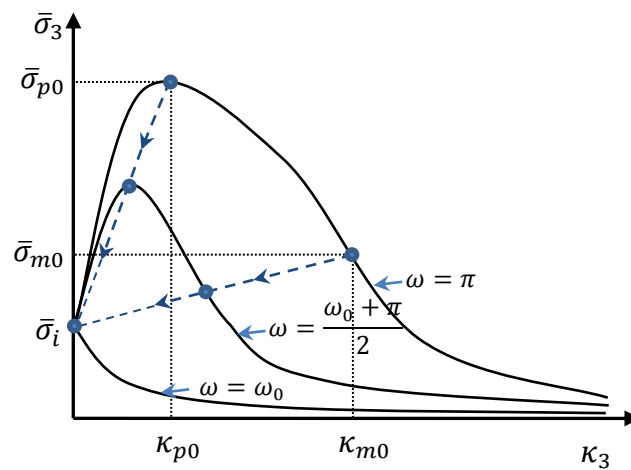


Figure 4-8. Modified Cap Plasticity Model for Interface elements

$$H(\omega) = \left(\frac{|\omega| - |\omega_0|}{\pi - |\omega_0|} \right)^n \quad (4-14)$$

As shown in equations (4-9) to (4-11), five independent parameters define the hardening/softening behavior. The interpolation function of equation (4-14) is used to obtain four parameters ($\kappa_p(\omega), \kappa_m(\omega), \bar{\sigma}_p(\omega)$ and $\bar{\sigma}_m(\omega)$) which are illustrated in Figure 4-8 and equations (4-15) to (4-18). The fifth parameter (m) will be calculated and discussed subsequently in equation (4-20), using the known set of parameters.

$$\kappa_p(\omega) = H(\omega) \kappa_{p0} \quad (4-15)$$

$$\kappa_m(\omega) = H(\omega) \kappa_{m0} \quad (4-16)$$

$$\bar{\sigma}_p(\omega) = \bar{\sigma}_i + H(\omega) (\bar{\sigma}_{p0} - \bar{\sigma}_i) \quad (4-17)$$

$$\bar{\sigma}_m(\omega) = \bar{\sigma}_i + H(\omega) (\bar{\sigma}_{m0} - \bar{\sigma}_i) \quad (4-18)$$

where $\kappa_{p0}, \kappa_{m0}, \bar{\sigma}_{p0}$ and $\bar{\sigma}_{m0}$ correspond to the hardening/softening parameters for the uniaxial compression test (i.e., $\omega = \pi$, see Figure 4-8). Interpolation does not apply for $\bar{\sigma}_i$ and this parameter is obtained from the experimental stress-strain curve for the uniaxial compression test.

4.6.1 The area under softening-hardening behavior

Using the proposed interpolation function in the previous section the material behavior for $\omega = \omega_0 + \varepsilon$ has changed to softening, similar to the material behavior for $\omega = \omega_0 - \varepsilon$. To generate smooth transition from the shear regime to the cap regime, the softening energy for $\omega_0 + \varepsilon$ and $\omega_0 - \varepsilon$ should be identical (where ε tends to zero). According to Figure 4-8 and equations (4-15) to (4-18), hardening does not take place in the plastic behavior of $\omega = \omega_0 + \varepsilon$ and segment $\bar{\sigma}_c(\kappa_3)$ is the only function that is activated for the nonlinear response (Figure 4-8). The integration of function $\bar{\sigma}_c(\kappa_3)$ over its defined domain ($0 \leq \kappa_3 < \infty$) gives the softening energy as,

$$\int_{\kappa_m}^{\infty} \bar{\sigma}_c(\kappa_3) d\kappa_3 = \bar{\sigma}_m(\kappa_m) \exp\left(m \frac{\kappa_3 - \kappa_m}{\bar{\sigma}_m}\right) = -\frac{\bar{\sigma}_m^2}{m} \quad (4-19)$$

To make a smooth transition from the shear phase to the cap phase, this value must be equal to $G^f(\omega_0)$ as shown in Figure 4-9. Thus, with employing such condition, the value of “ m ” is calculated by the following equation. (For $\omega = \omega_0, \bar{\sigma}_m = \bar{\sigma}_i$)

$$G^f(\omega_0) = -\frac{\bar{\sigma}_m^2}{m} \Rightarrow m = \frac{-\bar{\sigma}_m^2}{G^f(\omega_0)} = \frac{-\bar{\sigma}_i^2}{G^f(\omega_0)} \quad (4-20)$$

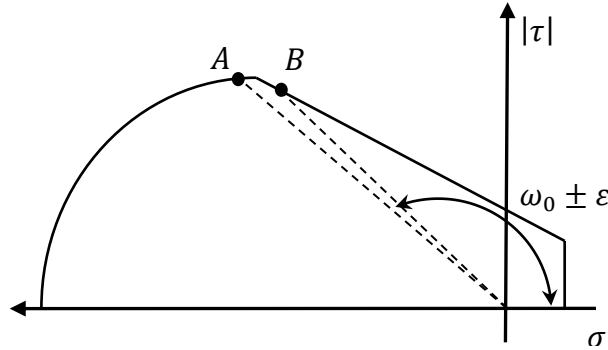


Figure 4-9. Equalizing the energy at the corners to ensure continuity

As such, for calculating the energy under uniaxial compression ($\omega = \pi$), both $\bar{\sigma}_b(\kappa_3)$ and $\bar{\sigma}_c(\kappa_3)$ functions are active (refer to Figure 4-10 and equations (4-21) to (4-23)).

$$\int_{\kappa_p}^{\kappa_m} \bar{\sigma}_b(\kappa_3) d\kappa_3 = \bar{\sigma}_p (\kappa_m - \kappa_p) + (\kappa_m - \kappa_p) \left(\frac{\bar{\sigma}_m - \bar{\sigma}_p}{3} \right) = (\kappa_m - \kappa_p) \frac{2\bar{\sigma}_p + \bar{\sigma}_m}{3} \quad (4-21)$$

$$\int_{\kappa_m}^{\infty} \bar{\sigma}_c(\kappa_3) d\kappa_3 = \bar{\sigma}_m(\kappa_3) \exp\left(m \frac{\kappa_3 - \kappa_m}{\bar{\sigma}_m}\right) = -\frac{\bar{\sigma}_m^2}{m} \quad (4-22)$$

$$G^f(\pi) = -\frac{\bar{\sigma}_{m0}^2}{m} + (\kappa_{m0} - \kappa_{p0}) \frac{2\bar{\sigma}_{p0} + \bar{\sigma}_{m0}}{3} \quad (4-23)$$

By knowing all the parameters except κ_{m0} , this parameter can be calculated by equation (4-23).

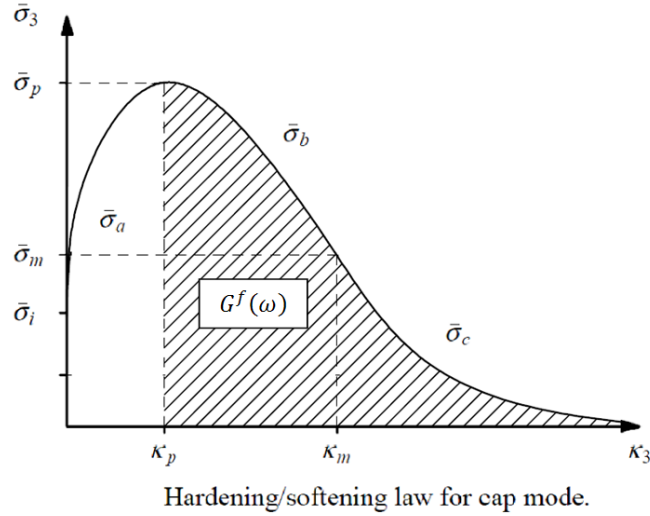


Figure 4-10. The energy under compression

For $\omega_0 \leq \omega \leq \pi$

$$G^f(\omega) = \frac{-\bar{\sigma}_m^2}{m} + (\kappa_m - \kappa_p) \frac{2\bar{\sigma}_p + \bar{\sigma}_m}{3} \quad (4-24)$$

By using $\bar{\sigma}_{m0} = 0.7\bar{\sigma}_{p0}$ (Lourenco 1996) for masonry it can be concluded,

$$2\bar{\sigma}_p + \bar{\sigma}_m = 2(\bar{\sigma}_i + H(\omega)(\bar{\sigma}_{p0} - \bar{\sigma}_i)) + (\bar{\sigma}_i + H(\omega)(\bar{\sigma}_{m0} - \bar{\sigma}_i)) \quad (4-25-a)$$

$$= 3\bar{\sigma}_i + 2H(\omega)(\bar{\sigma}_{p0} - \bar{\sigma}_i) + H(\omega)(\bar{\sigma}_{m0} - \bar{\sigma}_i)$$

$$\bar{\sigma}_m^2 = (\bar{\sigma}_i + H(\omega)(\bar{\sigma}_{m0} - \bar{\sigma}_i))^2 \quad (4-25-b)$$

Therefore,

$$\Rightarrow G^f(\omega) = a H(\omega)^2 + b H(\omega) + c \quad (4-26)$$

where a , b and c are constant values. According to equation (4-26) by using the interpolation function for $\kappa_p(\omega)$, $\kappa_m(\omega)$, $\bar{\sigma}_p(\omega)$ and $\bar{\sigma}_m(\omega)$, the softening/hardening energy, $G^f(\omega)$, for $\omega_0 \leq \omega \leq \pi$ will also be interpolated. Figure 4-11 shows the variation of softening energy,

while the angle of stresses (ω) changes. This figure indicates that for $0 \leq \omega \leq \pi$ the variation of softening energy is continuous and no abrupt change takes place in the material behavior.

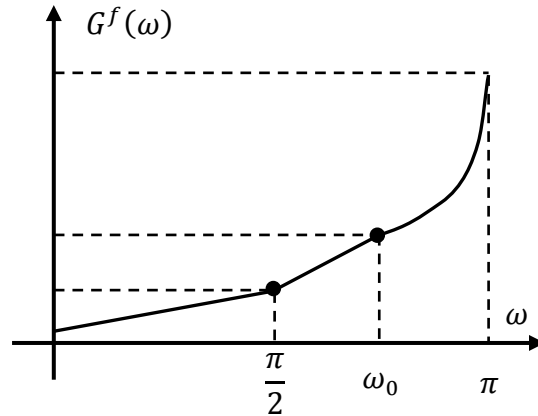


Figure 4-11. Variation of the energy by variation of the angle

4.6.2 Interaction of different yield surfaces

For monotonic and quasi-static loadings large stress redistribution is not expected, compared to cyclic loading. Therefore, throughout an analysis, the state of stress either remains on a particular yield surface or moves to a neighboring yield surface. For instance, the state of stress for an element that initially reaches the yield surface at the tensile regime by the end on analysis will not change to the cap regime. Thus, it is enough to investigate the interaction of the neighboring yield surfaces.

The tensile and shear strength are directly influenced by the cohesion of the mortar at the interface of bricks. Therefore, isotropic softening is appropriate for the interaction between shear and tension regimes (Lourenco 1996) (Figure 4-12).

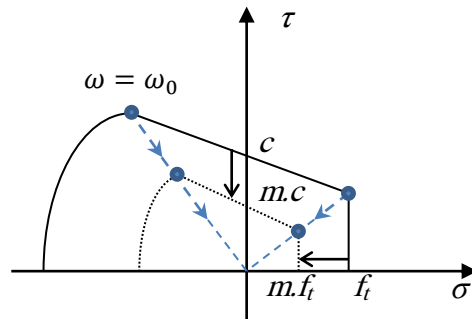


Figure 4-12. Isotropic Softening ($0 \leq m \leq 1$)

For $\omega = \omega_0 + \varepsilon$ and $\omega = \omega_0 - \varepsilon$, the damage takes place in the cap and shear regimes, respectively, and the nonlinear behavior follows softening. Moreover, after the damage occurred in the cap regime, the material degenerates into powder form and no shear strength is retained. Therefore, isotropic softening is also assumed for interaction between cap and shear regimes. For any kind of loading, the associated angles tracing the stress for corner *I* and *II* remain constant throughout the numerical analysis. These angles are the characteristic properties of a material (see Figure 4-12).

By using a number of examples in the following section, the idea of the interpolation function is fully illustrated, and the accuracy and efficacy of the developed material model are assessed.

4.7 Numerical examples on a single interface element

Based on the proposed material model by the author, a FORTRAN subroutine has been developed in the commercial finite element code TNO DIANA (DIANA 2008). In this section and to illustrate the robustness of the material model, a line interface element (CL12I) is subjected to a number of loading tests (Figure 3-1). The length of this plane stress element is 100 mm and its width is 100 mm. To show how the interpolation function in the proposed material

model works, the loading conditions have been considered in different regimes. Table 4-1 and Table 4-2 show typical material properties of a masonry wall which are considered in the following examples.

Table 4-1. Elastic properties of interface element

$k_n(N/mm^3)$	$k_s(N/mm^3)$
82	36

Table 4-2. Inelastic properties of interface element

Tension		Shear				Cap		
$f_t \frac{N}{mm^2}$	$G_f^I \frac{N}{mm}$	$c \frac{N}{mm^2}$	$\tan \phi$	$G_f^{II} \frac{N}{mm}$	$f_m \frac{N}{mm^2}$	C_{ss}	$G_f^c \frac{N}{mm}$	k_{p0}
0.25	0.018	0.35	0.75	0.125	10.5	9.0	5.0	0.093

Figure 4-13 shows the behavior of the element in response to a tensile displacement-controlled loading ($\omega = 0$). The nonlinear behavior is associated with softening and according to Figure 4-11 it has the lowest softening energy, in comparison to other possible load cases.

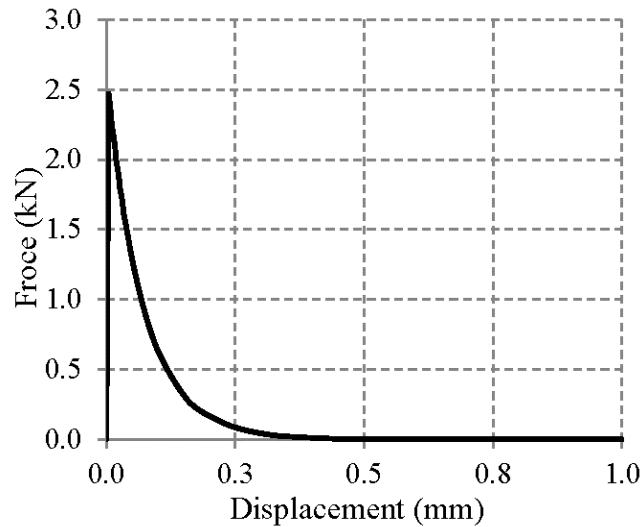


Figure 4-13. Response in pure tension

In the next phase of the numerical assessments (Figure 4-14 and Figure 4-15), the load has been applied on a single interface element in two steps. In the first step, a compressive stress has been applied followed by the second step in which a shear displacement-controlled loading has

been applied. The three compressive stresses are shown in Figure 4-14 and designated as *A*, *B* and *C*. The compressive stress for point *A* is zero and for point *B* and *C* are 0.5 N/mm^2 and 0.75 N/mm^2 , respectively.

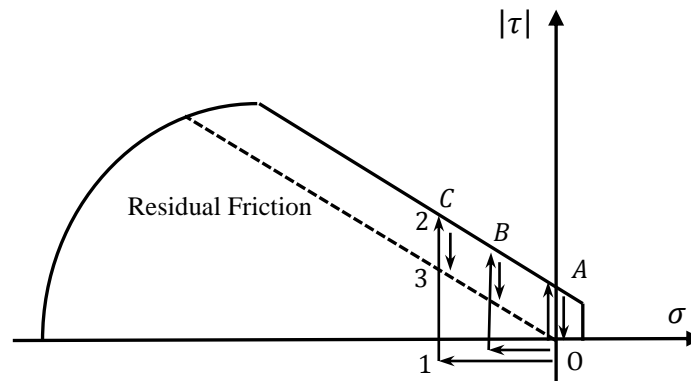


Figure 4-14. Loading path in shear with different compressive stresses

For example, in Figure 4-14 for the highest compressive stress (*C*), first the compressive stress has been applied (P_{01} , which is the path from point "0" to point "1"). In this part, the state of stress is located inside the yield surface and the material behavior is completely elastic. Then the transverse load is applied (P_{12} , which implies from point "1" to "2"). In this region the behavior is elastic as well; however, after reaching point "C" the shear strength softens (Figure 4-15) until reaching the residual friction line (P_{23} , which implies from point "2" to "3"). As the shear strength softens, the angle of loading changes and consequently the softening energy (see equation (4-13)).

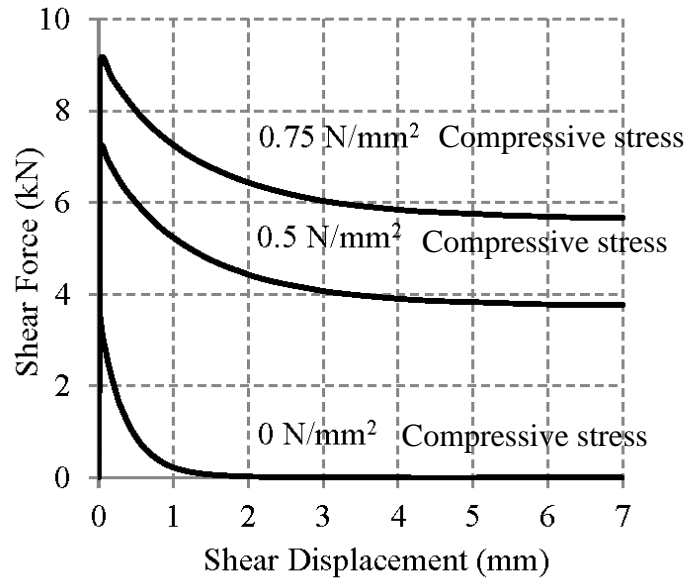


Figure 4-15. Response in shear with various compressive stresses

As shown in Figure 4-15 while the compressive stress increases, the slope of the softening behavior decreases. This is due to the fact that as the angle associated with the stress level increases, the softening energy increases as well.

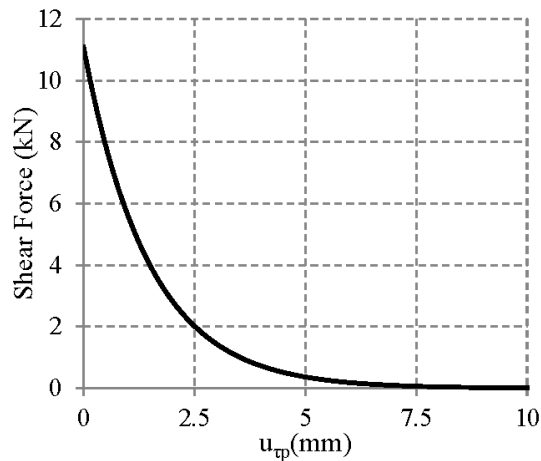


Figure 4-16. Response of the element to a combination of high compressive and shear stresses

Figure 4-16 shows the nonlinear response of the element for a particular load that follows path OB (Figure 4-9). In this case, the shear and normal stresses start from point B (with an angle of ω_0) and gradually shrink to the origin. This case has the most attainable energy for the softening when compared to the other cases shown in Figure 4-15.

4.8 Numerical validation for a masonry wall

In this section, the experimental results by Raijmakers and Vermeltoort, and Vermeltoort and Raijmakers (Raijmakers 1992; Vermeltoort and Raijmakers 1993) are used to validate the developed material model by the author (Figure 4-17). The results of this experimental test have been already used in many investigations to validate different material models developed by others (Lourenco 1996; Oliveira and Lourenco 2004; Oliveira and Lourenco 2004). In the following sections, first the idea of lattice modeling for masonry walls will be proposed along with implementations of the material model presented earlier in this section, and then the obtained numerical results will be presented and discussed.

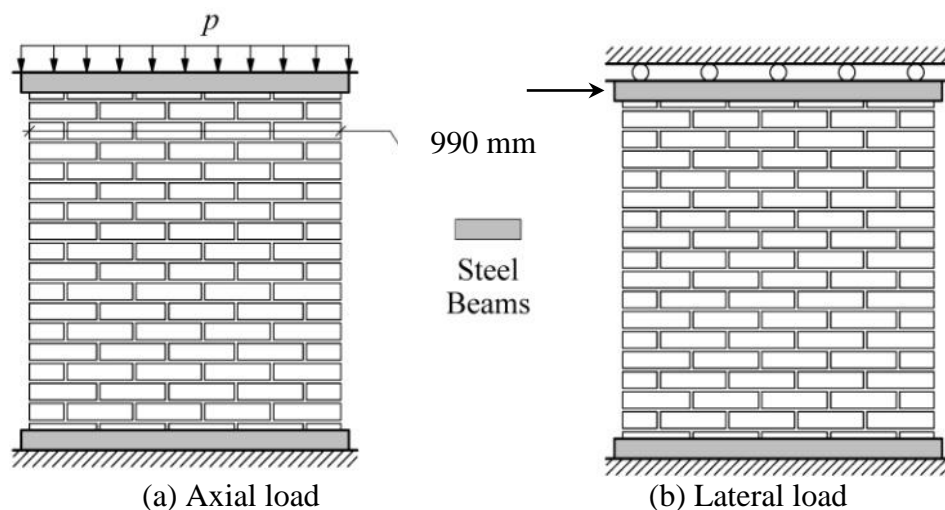


Figure 4-17. Different steps of loadings (Lourenco 1996)

4.9 *Lattice model*

The early works regarding lattice modeling refers to Hrennikoff (1941). In Hrennikoff's model the material was replaced by truss elements. In this model, to take into account the heterogeneity of materials, different materials can be assigned for different truss elements. Schlangen (Schlangen and Garboczi 1997) developed a two-dimensional lattice model for studying fracture in the concrete. In this study for conducting the lattice model, beam elements with three degrees of freedom per node were used. Each beam is linearly elastic and after its stress exceeds a certain value, failure happens and the beam is removed. Cusatis (Cusatis et al. 2003; Cusatis et al. 2003; Cusatis et al. 2006) developed the confinement-shear lattice model (CSLM) for concrete. In his model, each aggregate is connected to the neighbor aggregates by some rigid beams in which all the linear and nonlinear behavior of concrete are taking place in a nodal element between these two aggregates.

In the lattice model proposed by the author for masonry structures, the in-plane behavior of walls is simulated using rigid beams and nonlinear nodal interface elements, instead of modeling by continuum models. The rigid beams not only transmit the axial forces but also transmit shear forces. For the shear strength, both friction and cohesion are accounted in the model, as discussed in earlier sections.

To build a lattice model for masonry walls, bricks are expanded by the half of the dimension of the mortar and nodal interface elements are located at the intersection of the bricks and within the bricks (Figure 4-18). Figure 4-18 (a) and (b) show two different meshes for lattice model of a brick.

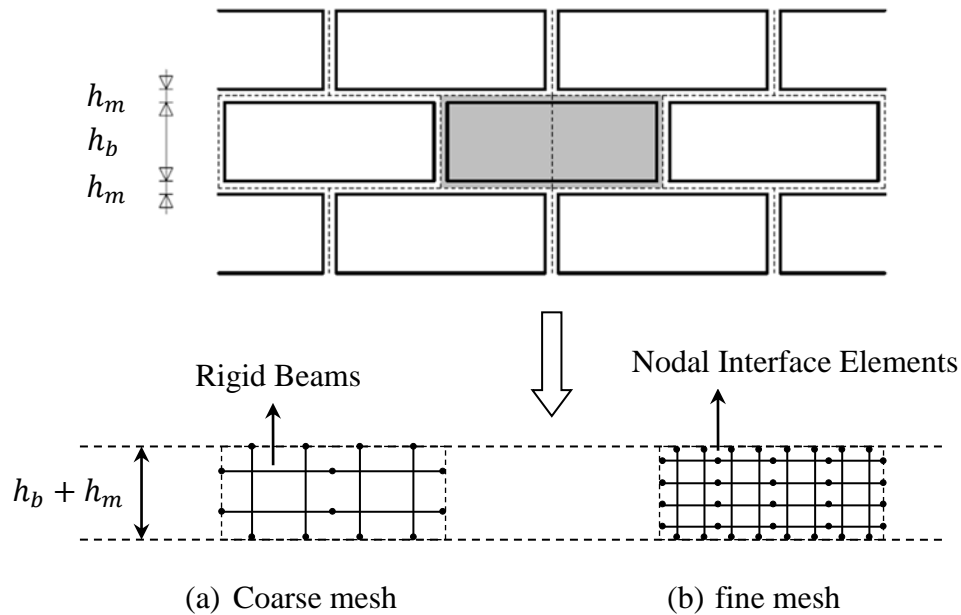


Figure 4-18. Two generated meshes for lattice model

4.9.1 Elastic behavior

In this method and by substituting continuum elements with rigid beams, the effect of Poisson's ratio is inherently neglected. The Poisson's ratio for materials such as brick and concrete is low and mostly the behavior of masonry walls is governed by the inelastic behavior of joints; therefore, this assumption is appropriate. In order to calculate the stiffness " k ", the brick and mortar are assumed to behave as two springs connected in series (Figure 4-19). Under the same compressive load, the displacement associated with the combination of the brick and mortar system must be equal to the displacement of the lattice model. Therefore, the stiffness of the system can be calculated by using equations (4-27) and (4-28).

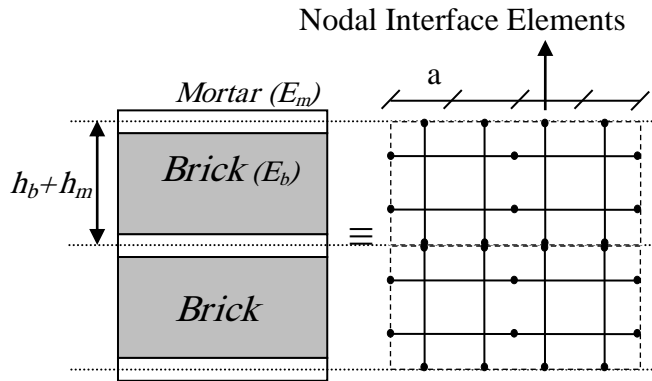


Figure 4-19. Calculating the stiffness of the interface elements

$$\frac{1}{k_n} = \left(\frac{h_m}{E_m a b} + \frac{h_b}{E_b a b} \right) \Rightarrow k_n = \frac{E_m E_b}{E_b h_m + E_m h_b} a b \quad (4-27)$$

$$\frac{1}{k_s} = \left(\frac{h_m}{G_m a b} + \frac{h_b}{G_b a b} \right) \Rightarrow k_s = \frac{G_m G_b}{G_b h_m + G_m h_b} a b \quad (4-28)$$

where a corresponds to the active width for each nodal element (Figure 4-19) and b corresponds to the thickness of the wall and G is shear modulus of elasticity.

4.9.2 Description of the lattice models

One of the issues raised in any numerical simulation is the mesh sensitivity. To study the mesh sensitivity of the lattice model, four different meshes have been considered as shown in Figure 4-20. In all of these models, the nonlinearity is localized at the nodal interface elements located at the outer edge of the brick and on the nodes located in the middle of the brick. In two particular models “2.2-2” and “4.4-2”, elastic nodal interface elements are also considered at quarter point of the brick to have a better distribution of the stresses within the brick.

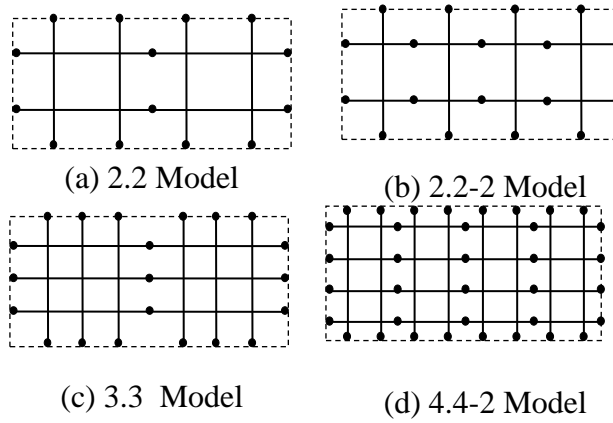


Figure 4-20. Different mesh sizes for modeling a brick

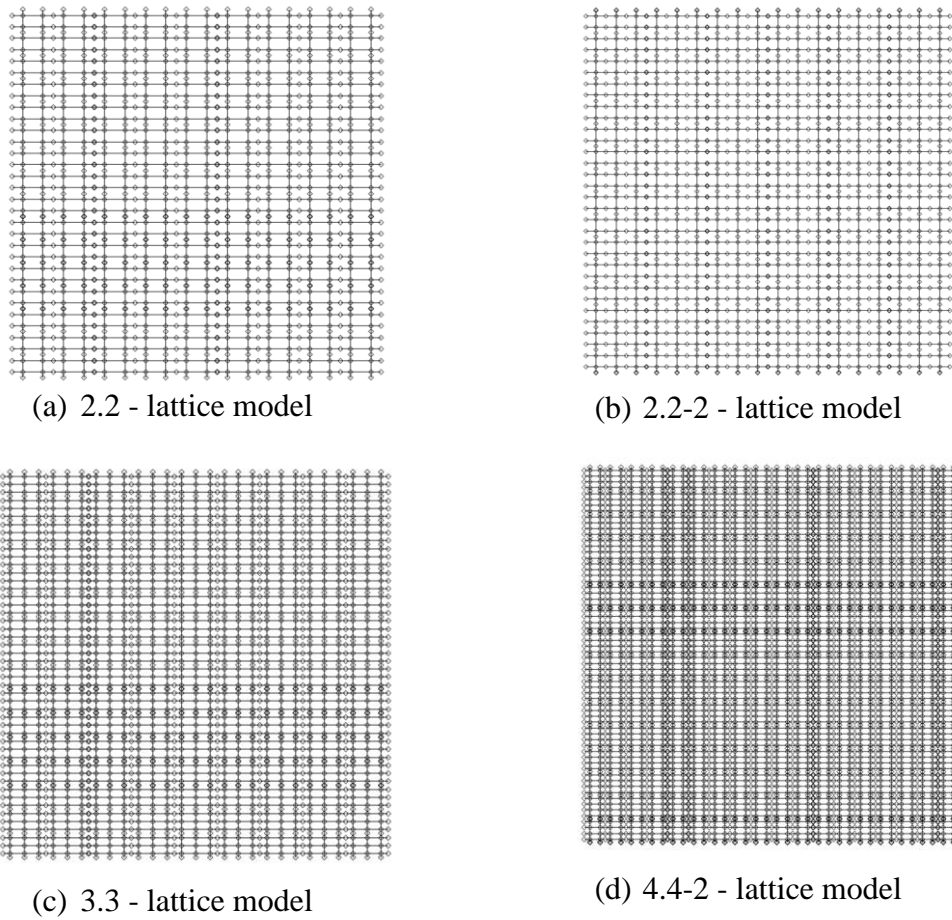


Figure 4-21. Four different mesh sizes for lattice model

Figure 4-21 (a) to (d) show four different lattice models with different mesh sizes for the masonry wall based on the geometry of the wall tested by Raijmakers and Vermeltoort (Raijmakers and Vermeltoort 1992; Vermeltoort 1993). In Table 4-3, 4-4 and 4-5, the material properties are adopted for model 2.2 (based on the value of “a” and “b” in Figure 4-19).

Table 4-3. Properties of vertical cracks for model 2.2

$k_n \times 1000$ (N/mm)	$k_s \times 1000$ (N/mm)	f_t (N)	G_f^I (N.mm)
165/197.7	72.5/89.9	6200	248

Table 4-4. Properties of horizontal cracks for model 2.2

$k_n \times 1000$ (N/mm)	$k_s \times 1000$ (N/mm)	f_t (N)	G_f^I (N.mm)
345.7/429.5	151.8/192.3	11000	440

Table 4-5. Properties of potential brick cracks for model 2.2

$k_n \times 1000$ (N/mm)	$k_s \times 1000$ (N/mm)	f_t (N)	G_f^I (N.mm)
470.6/470.6	206.6/213.9	-	-

Following the experimental data for uniaxial compression test, the hardening/softening law for the cap mode is defined by the set $\{\sigma_3, \kappa_3\}_i = \{ (f_m / 3, 0.0) ; (f_m, 0.09) ; (f_m / 2, 0.49) ; (f_m / 7, + \infty) \}$.

4.9.3 Comparison of the results

The numerical results obtained from all mesh sizes of Figure 4-20 are presented in Figure 4-22 and Figure 4-23 for the compressive loading of 30 kN and 120 kN, respectively. In these figures, the numerical results are also compared with the results obtained by the experimental tests (J4D and J5D for 30 kN, and J6D for the 120 kN compressive load). As shown in Figure 4-22, even for the two sets of tests with the same properties of material and compressive loads, the experimental results are different due to the heterogeneous properties of bricks and mortar and construction

anomalies. Figure 4-22 and Figure 4-23 clearly show that, the proposed numerical model is capable of predicting the load at which the diagonal crack takes place (at about 1 mm displacement). By examining the numerical results and comparing to the experimental results (Figure 4-22 and Figure 4-23), the mesh sensitivity issue is negligible. Finally the numerical simulation terminated at 2 mm deformation due to numerical convergence issue.

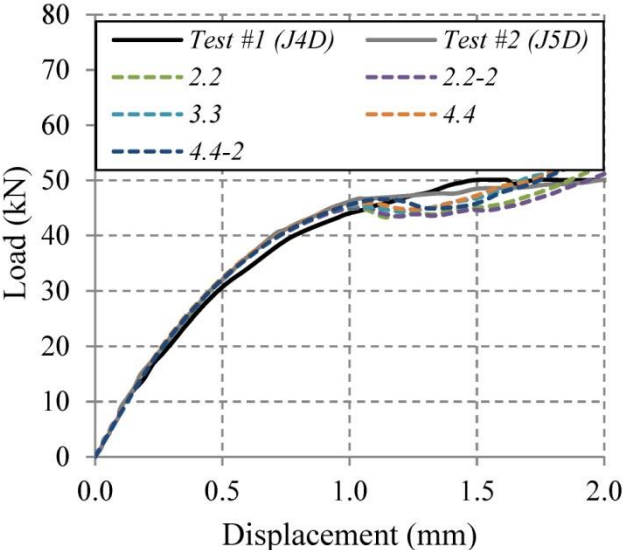


Figure 4-22. Load-Displacement graph for J4D and J5D wall (numerical and experimental)

The same procedure was repeated for the wall J6D with 120 kN compressive load and the results are shown in Figure 4-23.

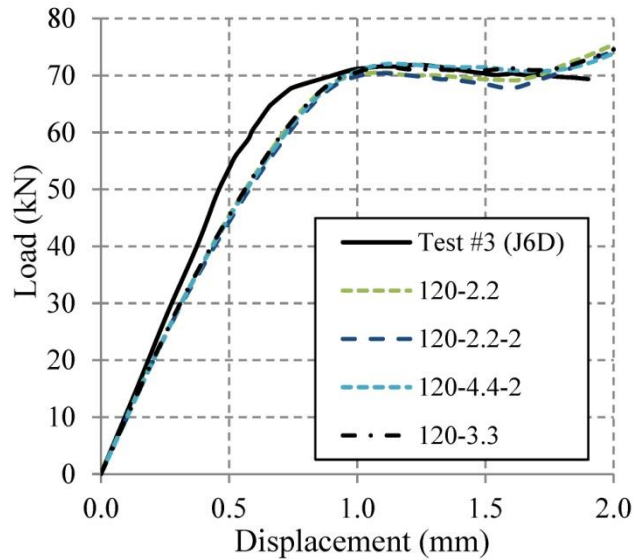
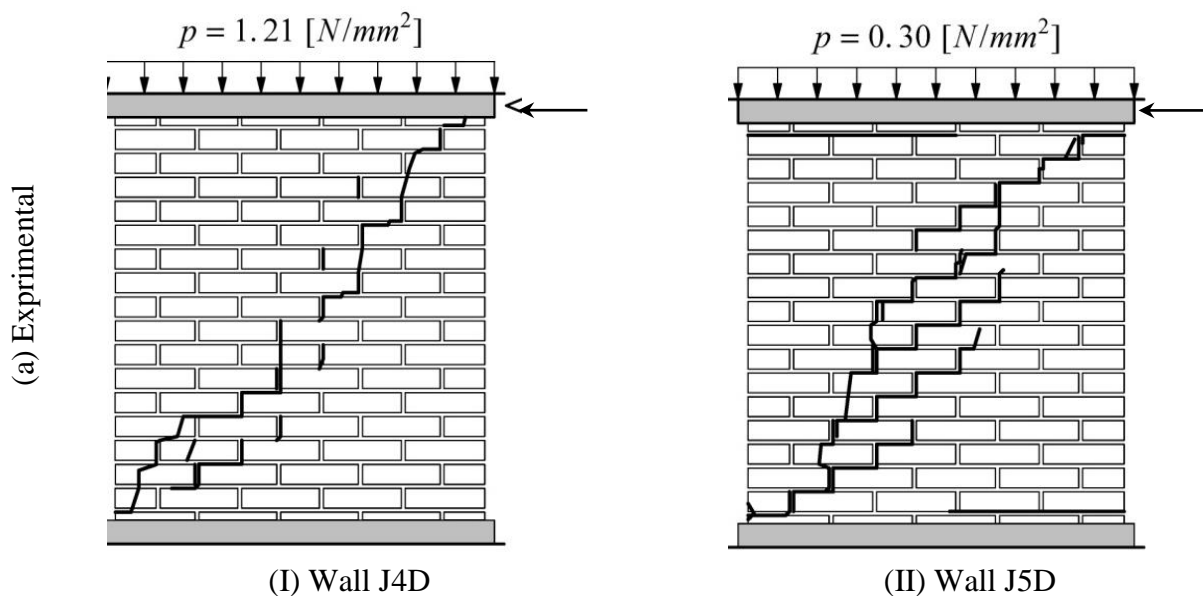
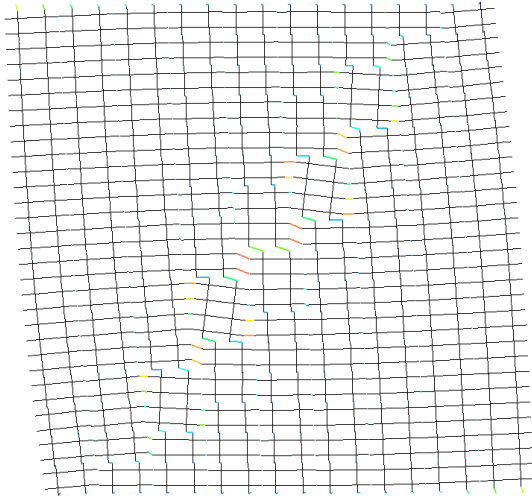


Figure 4-23. Load-Displacement graph for J6D wall (numerical and experimental)

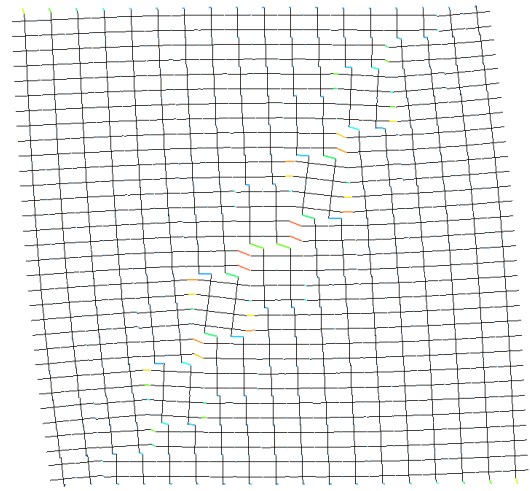
Figure 4-24 and Figure 4-25 present the resultant diagonal cracks for wall J4D and J6D at the end of loading. In these figures, the propagated diagonal cracks have been compared between the experimental tests and numerical models. Moreover, the numerical results of different mesh sizes have been compared. In all numerical models, diagonal crack is the dominant failure mode.



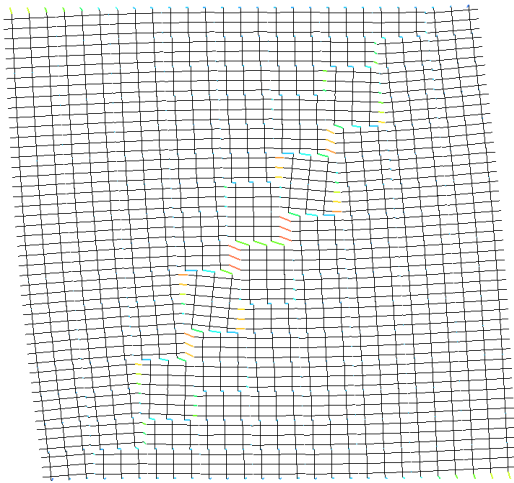
(b) Numerical



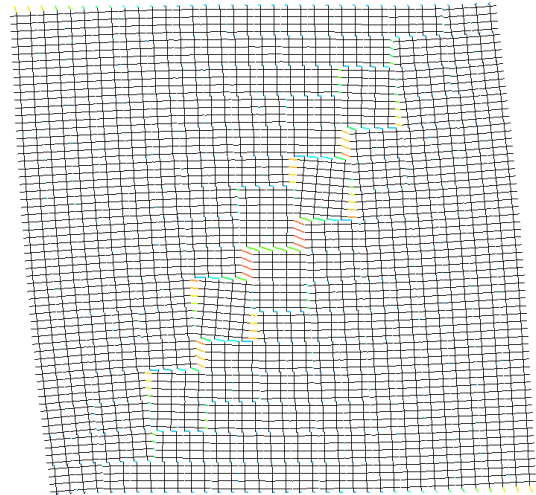
(I) Model 2.2



(II) Model 2.2-2



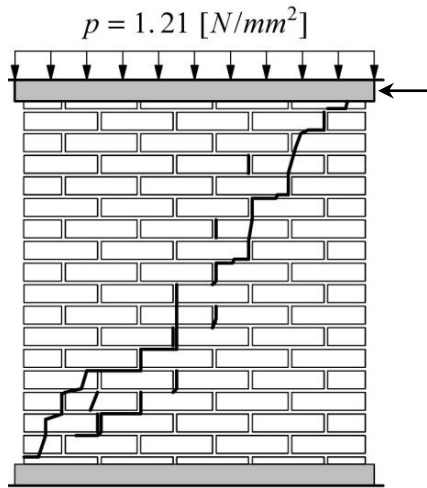
(III) Model 3.3



(IV) Model 4.4-2

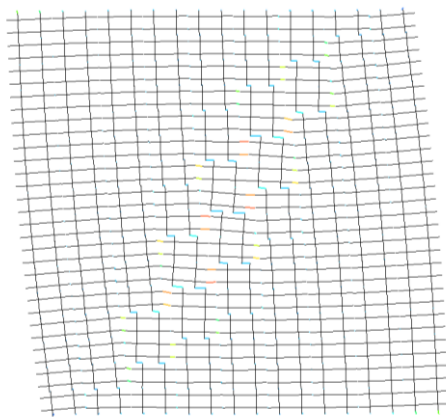
Figure 4-24. Comparison between the cracks obtained by the numerical and experimental models (J4D and J5D)

(a) Experimental

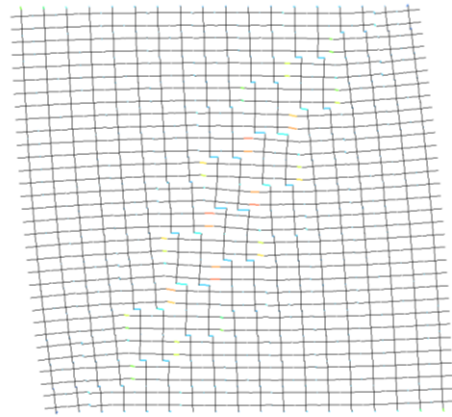


Wall J6D

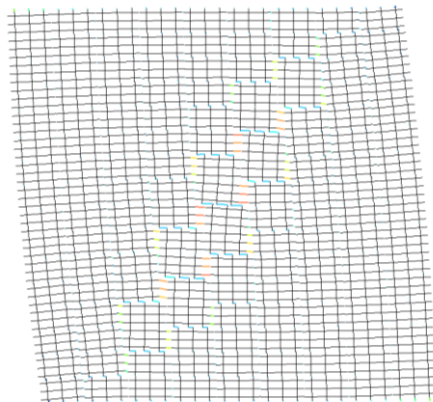
(b) Numerical



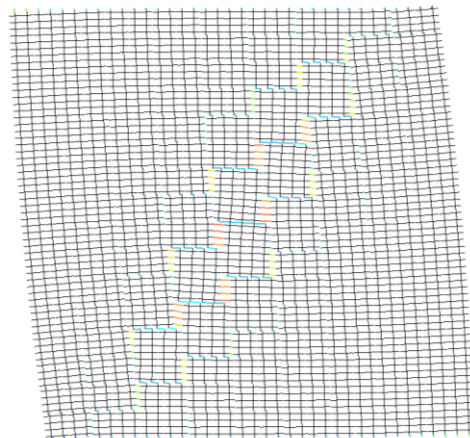
(I) Model 2.2



(II) Model 2.2-2



(III) Model 3.3



(VI) Model 4.4-2

Figure 4-25. Comparison between the cracks obtained by the numerical and experimental models (J6D)

4.10 Summary and conclusion

In many numerical analyses, it is necessary to employ two or three yield surfaces in the constitutive material models. The main concern is the discontinuity of the yield surface which will cause jump in the behavior when state of stress moves from one regime to the other, and consequently convergence issues are encountered in the numerical analysis. Using the interpolation functions proposed in this report, the nonlinear behavior of an existing material model with three distinct yield surfaces is modified. The constitutive material model herein has three yield surfaces. Two yield surfaces with softening and one with hardening/softening nonlinear behaviors. The interpolation functions were able to remedy the discontinuity problem when transition from neighboring yield surfaces with softening nonlinear behavior (tensile and shear regimes) occurs, and also in the transition from a yield surface with softening (shear regime) to a yields surface with hardening/softening nonlinear behavior (cap regime).

Using a number of numerical evaluations on a single interface element, it has been shown that the developed interpolation functions are indeed capable of building a smooth transition between the yield surfaces. A lattice model for simulating the behavior of masonry walls is proposed along with the developed material model. It has been shown that the calculated numerical results are in good agreement with well-documented experimental results available in archival literature. Moreover, by comparing the results of four different mesh sizes, the lattice model does not exhibit mesh sensitivity issues.

Although the developed material model is intended for masonry structures, it can be adopted to model other brittle materials. Moreover, the developed interpolation functions can be used in other material models with multi-yield surfaces to remedy the discontinuity issue.

SECTION 5

THREE-DIMENSIONAL EXPLICIT DYNAMIC PROCEDURES FOR MODELING MASONRY STRUCTURES

5.1 *Introduction*

Three-dimensional (3-D) cyclic analysis and constitutive material model are needed to better understand the behavior of masonry buildings under earthquake excitations. So far, most of the developed constitutive material models in the field of masonry structures have focused on two-dimensional and monotonic modeling. In addition, most of these studies have used implicit dynamic procedures in the time domain. Based on the inherent features of implicit formulations for nonlinear problems, a number of iterations are required at each time step for convergence, which leads to intensive computations. Moreover, several researchers have reported convergence problems, while modeling masonry walls with an implicit procedure, especially for cyclic loadings (Lourenco 1996; Oliveira and Lourenco 2004; Oliveira and Lourenco 2004).

In this section, a 3-D cyclic constitutive material model with an explicit analysis procedure is proposed that can be used to model the large deformation behavior of masonry walls. A comprehensive study that addresses both static and dynamic 3-D modeling of masonry walls is presented. The material model is implemented in a user-defined subroutine that is compiled with ABAQUS (Abaqus 2005). The subroutine is then tested by several numerical examples on a single element under cyclic normal and transverse forces to illustrate the behavior of the material model. Finally, the numerical procedures are used to analyze several masonry walls and

validated with well documented experimental results to assess the robustness and predictive capabilities of the material model and numerical solution.

5.2 Description of the finite element model

To create the finite element model (FEM) of a URM wall, bricks and mortar are distinctly defined in the proposed model by two types of elements. Bricks are modeled with solid elements (C3-D8R) in ABAQUS (Abaqus 2005) and mortar is modeled with plane interface elements (COH3-D8) as shown in Figure 5-1. Based on Figure 5-2, bricks are expanded by half the mortar thickness and interface elements are located between the solid elements that represent the mortar.

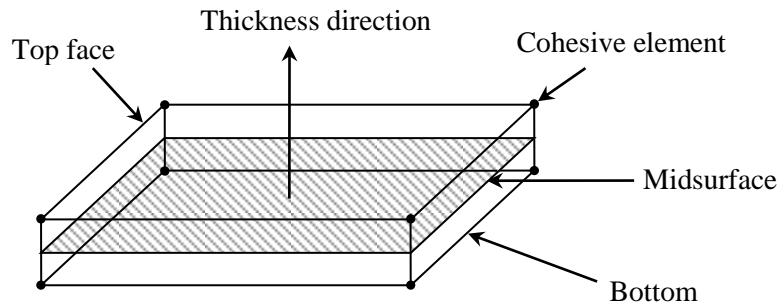


Figure 5-1. Eight node plane interface element (ABAQUS)

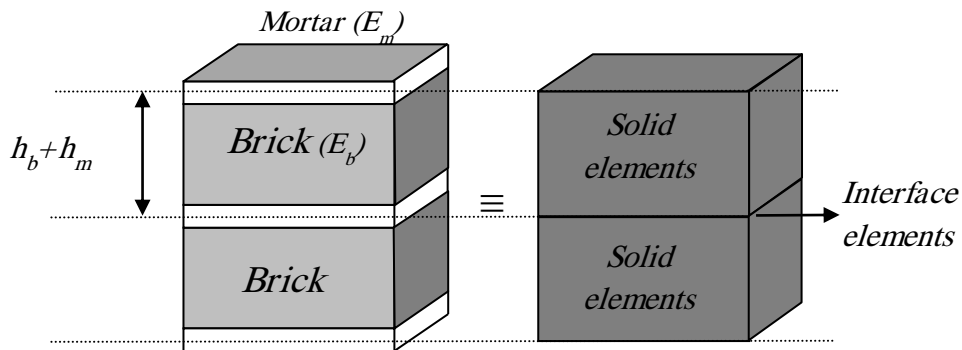


Figure 5-2. Detailed model of brick and mortar

Experimental observations indicate that in majority of test cases most of the cracks pass through either the mortar joint or the middle of the bricks. Therefore, to capture an accurate behavior of the wall and to guarantee the possibility of crack propagation in the middle of the bricks, bricks are divided into two parts and a potential crack is placed in the middle of the bricks. The idea of using potential cracks has been employed by many researchers in 2-D analysis (Lourenco 1996; Oliveira and Lourenco 2004; Oliveira and Lourenco 2004; Stavridis and Shing 2010). A potential crack is an interface element located in the middle of a brick which has the same material properties of a brick. Figure 5-3 shows the generated FE mesh for the wall and a general view of the wall considered in the subsequent examples presented in this section. As indicated earlier, in Figure 5-3 (b) all the bricks are divided into two parts from the middle.

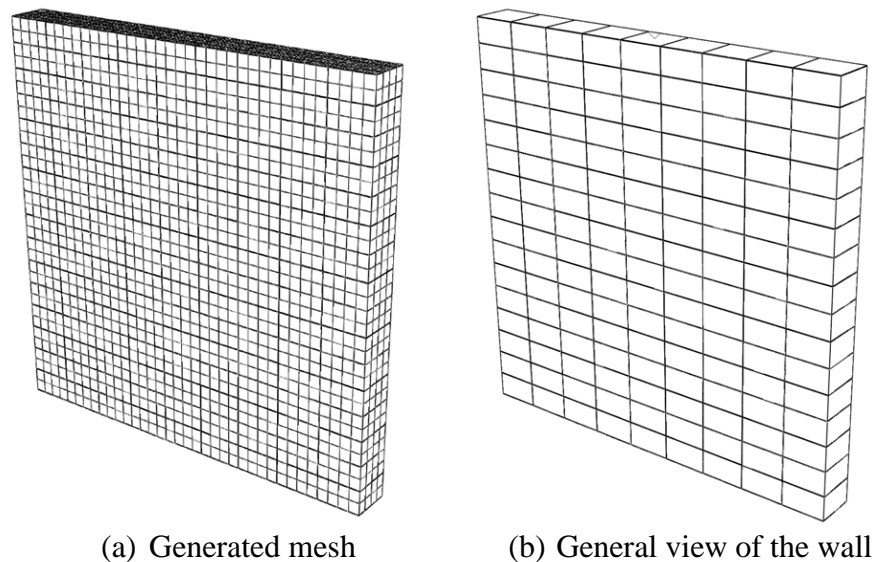


Figure 5-3. Numerical modeling of a masonry wall

Due to the distinct definition of linear and nonlinear behavior for each part (i.e., bricks and mortar), the model can be considered as a micro-scale model. However, it can also be considered as a meso-scale model because the mortar is not defined in detail and is represented by a zero-

thickness plane element. In the following sections, the linear and nonlinear behavior of elements used in the finite element model are described.

5.3 Elastic behavior of joints

The behavior of the interface elements is initially elastic, i.e., $\Delta \mathbf{t} = k \Delta \bar{\mathbf{u}}$, where k is the elastic stiffness of joints and is calculated from the properties of both the brick and mortar (equations (5-1)-(5-3)), and \mathbf{t} is the traction vector.

$$k = \begin{bmatrix} k_n & 0 & 0 \\ 0 & k_{sx} & 0 \\ 0 & 0 & k_{sy} \end{bmatrix} \quad (5-1)$$

$$\mathbf{t} = \begin{Bmatrix} \sigma \\ \tau_x \\ \tau_y \end{Bmatrix} \quad (5-2)$$

$$\bar{\mathbf{u}} = \begin{Bmatrix} u \\ v_x \\ v_y \end{Bmatrix} \quad (5-3)$$

where k_n is the normal stiffness of the interface element and k_{sx} and k_{sy} are the transverse stiffness in the x and y directions, respectively. To determine the normal and shear stiffness, the brick and mortar are assumed to be elastic springs connected in series. The displacement for the combination of the brick and mortar system must be equal to the displacement of the solid element-plane interface system under the same compressive and shear loads (for example Figure 5-2 under a compressive load). Accordingly, the stiffness of the system is calculated by using

$$k_n = \frac{1}{h_m} \frac{E_m E_b}{E_b - E_m} \quad (5-4)$$

$$k_s = \frac{1}{h_m} \frac{G_m G_b}{G_b - G_m} \quad (5-5)$$

where G is the shear modulus and the rest of parameters that appeared in equations (5-4) and (5-5) are shown in Figure 5-2. Based on the explicit formulation in each time step, the strain and displacement increment are calculated first. Total strains and displacements in the new step ($i+1$) are then generated by adding these increments to the strains and displacements obtained in the previous step (step i - equation (5-6)). The trial stress increments are calculated knowing the strain increments. However, to calculate the new stresses in step $i+1$ and before adding the stress increments to the stresses of step i , they must be checked to determine whether they are located in the elastic region or not (equation (5-7)). Section 5.4 addresses the case when the stresses are found to be outside the yield surface.

$$\begin{aligned} u_{i+1} &= u_i + du \\ v_{x_{i+1}} &= v_{x_i} + dv_x \\ v_{y_{i+1}} &= v_{y_i} + dv_y \end{aligned} \quad (5-6)$$

$$\begin{cases} \sigma^{trial} = \sigma_i + du K_n \\ \tau_x^{trial} = \tau_{x_i} + dv_x K_{sx} \\ \tau_y^{trial} = \tau_{y_i} + dv_y K_{sy} \end{cases} \quad (5-7)$$

where u , v_x and v_y are the normal and transverse deformations in the x and y direction, respectively

5.4 Plastic behavior of joints

Three distinct modes are considered for the interface elements namely, tension, shear, and tension-shear intersection (Figure 5-4). After calculating the trial stresses using equation (5-7), the status of these trial stresses must be checked with respect to all yield surfaces. If the state of

stress in step $i+1$ falls inside the yield surfaces, the material is in the linear regime and the trial stresses are correct. If the stresses fall outside the yield surfaces, the stresses must be modified based on the respective plastic domain.

$$\text{Linear Regime} \rightarrow \begin{cases} \text{If } \sigma^{trial} < \bar{\sigma}_1(\kappa_1) & \text{for tension regime} \\ \text{and} \\ \text{If } \sqrt{(\tau_x^{trial})^2 + (\tau_y^{trial})^2} < \sigma \tan\phi - \bar{\sigma}_2(\kappa_2) & \text{for shear regime} \end{cases}$$

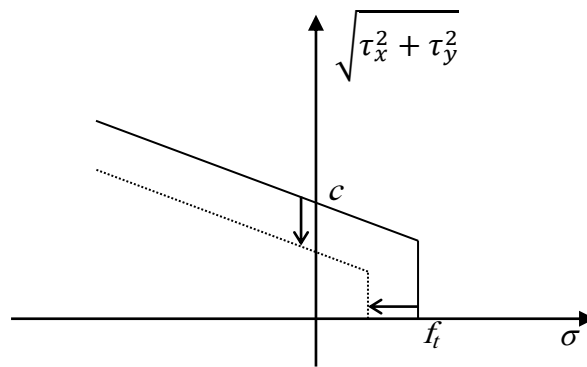


Figure 5-4. Yield surface for the joints

Each part of the yield surface of Figure 5-4 is defined distinctly for tension, shear, and shear and tension regime in the following sections.

5.4.1 Tension regime

Exponential softening is considered for monotonic behavior of the joints in the tension domain following the work of Pluijm (Pluijm 1992; Pluijm 1993). In the tension mode, the yield function (Pluijm 1992) is.

$$f_1(\sigma, \kappa_1) = \sigma - \bar{\sigma}_1(\kappa_1) \tag{5-8}$$

$$\bar{\sigma}_1 = f_t \exp\left(-\frac{f_t}{G_f^I} \kappa_1\right) \quad (5-9)$$

In equations (5-8) and (5-9), f_t is the tensile strength of the brick-mortar interface and G_f^I is the mode I fracture energy, which indicates the area under stress-displacement curve of a body under tensile force. Under net normal displacement, κ_1 is equal to $|\Delta u_n^p|$.

According to the normality rule (Lubliner 1990), at any point of the yield surface the outward normal vector is proportional to the plastic strain increments. Moreover, while the material is in the nonlinear regime at any time step, the stress state should remain on the yield surface. Therefore, equation (5-10) shows the stress corrector factor which modifies the trial stresses in the explicit formulation.

$$\begin{cases} \frac{\partial f}{\partial \sigma} d\sigma + \frac{\partial f}{\partial \kappa_p} d\kappa_p = 0 \\ d\sigma = C \left(-d\lambda \frac{\partial f}{\partial \sigma}\right) \end{cases} \rightarrow d\lambda = \frac{-K_n d\varepsilon_n}{\frac{f_t^2}{G_f^I} \exp\left(-\frac{f_t}{G_f^I} \kappa_p\right) - K_n} \quad (5-10)$$

By employing $d\lambda$, the new expression for the stresses becomes,

$$\begin{cases} \sigma_{i+1} = \sigma^{trial} - d\lambda K_n \\ \tau_{x_{i+1}} = \tau_x^{trial} \\ \tau_{y_{i+1}} = \tau_y^{trial} \end{cases} \quad (5-11)$$

Based on the results of cyclic experimental tests performed on brittle materials such as concrete or bricks, following the strength degradation the stiffness will also degrade (Gopalaratnam and Shah 1985; Reinhardt 1984). According to the experimental data, at each time step the ratio between κ_1 and κ_t in

Figure 5-5 must remain constant. Typical values for the stiffness degradation parameter (Gopalaratnam and Shah 1985; Reinhardt 1984) are presented in Table 5-1.

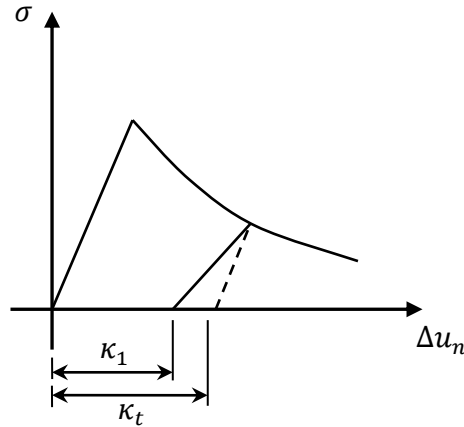


Figure 5-5. Cyclic tensile loading (Oliveira and Lourenco 2004)

Table 5-1. Stiffness degradation parameter

Numerical Simulation	κ_1/κ_t
Gopalaratnam and Shah (1985)	0.76
Reinhardt (1984)	0.73

Equations (5-1) to (5-11) have been added in FORTRAN as a plasticity algorithm. To better illustrate the axial behavior of the proposed material model, an interface element (Figure 5-6 (a)) is subjected to a cyclic axial load (Figure 5-7(a)). The element is considered to have a normal stiffness $k_n = 82 \text{ N/mm}^3$ and tensile strength $f_t = 0.25 \text{ N/mm}^2$ with a softening energy $G_f^I = 0.018 \text{ Nmm/mm}^2$. The response of this element is shown in Figure 5-7 (b). As depicted in Figure 5-7 (a), first a monotonic displacement-controlled load is applied up to point “A”. Consequently, the normal stress reaches the maximum tensile strength of 0.25 N/mm^2 (see Figure 5-7 (c)) and subsequently the strength degrades following an exponential curve. After load reversal takes place at point “A”, the stress decreases with a modified (i.e., degraded) stiffness. Note that the degraded stiffness is only considered for the positive

displacement due to the joint closure under the compressive load. Based on the experimental tests conducted by Reinhardt (Reinhardt 1984) on brittle materials, such as concrete or mortar, the point where the joint closes does not exactly coincide with the zero displacement. However, as a simplification it can be considered to be at zero displacement.

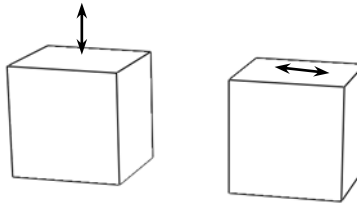


Figure 5-6. Interface element under cyclic tension (a) and shear test (b)

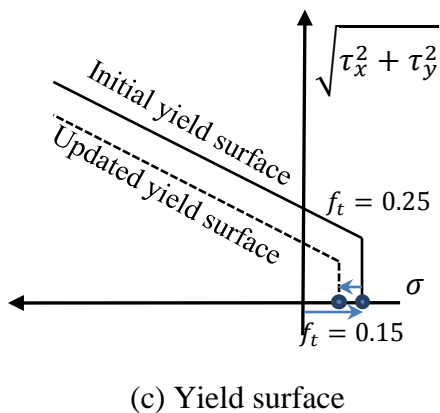
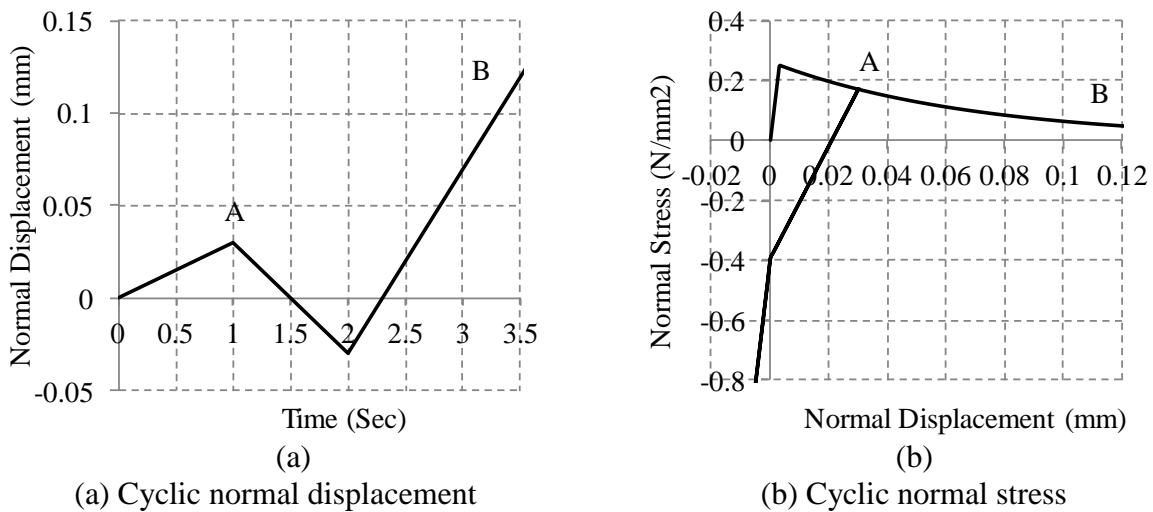


Figure 5-7. The results of an element under tensile force

5.4.2 Shear regime

The yield surface for the shear regime follows equation (5-12). The yield surface and nonlinear behavior in the shear dominated mode is presented in ref. (Pluijm 1993) for 2-D models. Here they are extended for 3-D models.

$$f_2(\sigma, \kappa_2) = \sqrt{\tau_x^2 + \tau_y^2} + \sigma \tan\phi - \bar{\sigma}_2(\kappa_2) \quad (5-12)$$

$$\bar{\sigma}_2 = c \exp\left(-\frac{c}{G_f^{II}} \kappa_2\right) \quad (5-13)$$

where c is the cohesion of the brick-mortar interface, ϕ is the friction angle, and G_f^{II} is the mode II fracture energy (the area under stress-transverse displacement curve) appearing in equations (5-12) and (5-13). In equation (5-12), the friction angle is coupled with cohesion softening,

$$\tan\phi = \tan\phi_0 + (\tan\phi_r - \tan\phi_0) \frac{c - \bar{\sigma}_2}{c} \quad (5-14)$$

where ϕ_0 is the initial friction angle and ϕ_r is the residual friction angle. The flow rule follows the non-associated plastic potential of,

$$g_2 = \sqrt{\tau_x^2 + \tau_y^2} + \sigma \tan\psi - c \quad (5-15)$$

where ψ represents the dilatancy angle. Similar to equation (5-10), by employing the normality rule and considering the fact that in the nonlinear regime the state of stress remains on the yield surface, the stress corrector factor is calculated by

$$d\lambda = \frac{\tan\psi K_n d\varepsilon_n + \frac{\tau_x}{\sqrt{\tau_x^2 + \tau_y^2}} K_{sx} d\varepsilon_{\tau_x} + \frac{\tau_y}{\sqrt{\tau_x^2 + \tau_y^2}} K_{sy} d\varepsilon_{\tau_y}}{\frac{c^2}{G_f^{II}} \exp\left(-\frac{c}{G_f^{II}} \kappa_p\right) - \left(\tan^2\psi K_n + \frac{\tau_x^2}{\tau_x^2 + \tau_y^2} K_{sx} + \frac{\tau_y^2}{\tau_x^2 + \tau_y^2} K_{sy}\right)} \quad (5-16)$$

Thus, according to the plasticity rules and following explicit formulations, the modified stresses in step $i+1$ can be calculated using

$$\begin{cases} \sigma_{i+1} = \sigma^{trial} - d\lambda K_n \tan(\psi) \\ \tau_{x_{i+1}} = \tau_x^{trial} - d\lambda K_{sx} \frac{\tau_x}{\sqrt{\tau_x^2 + \tau_y^2}} \\ \tau_{y_{i+1}} = \tau_y^{trial} - d\lambda K_{sy} \frac{\tau_x}{\sqrt{\tau_x^2 + \tau_y^2}} \end{cases} \quad (5-17)$$

As an example of the behavior of the proposed material model herein, consider an interface element (Figure 5-6(b)) subjected to a transverse cyclic deformation (Figure 5-8(a)). Following typical values for masonry, the element is considered to have a transverse stiffness $k_s = 36 \text{ N/mm}^3$ and shear strength $c = 0.35 \text{ N/mm}^2$ with a softening energy $G_f^{II} = 0.125 \text{ Nmm/mm}^2$. Shear stress has been plotted against cyclic transverse displacement in Figure 5-8(b). As expected, as soon as the shear stress reaches the initial yield surface (0.35 N/mm^2 – see Figure 5-8(c)), the exponential strength degradation starts to govern the behavior until the loading reversal takes place at point “A”. In point “A” the shear strength is 0.2 N/mm^2 . In the load reversal, the absolute value of the stress decreases (with the degraded stiffness) until the shear stress intersects the updated yield surface (0.2 N/mm^2 – see Figure 5-8(c)). Again, the strength degradation continues until the second load reversal at point “B”. In Figure 5-8(b), stiffness and strength degradation are clear in different stages of loading.

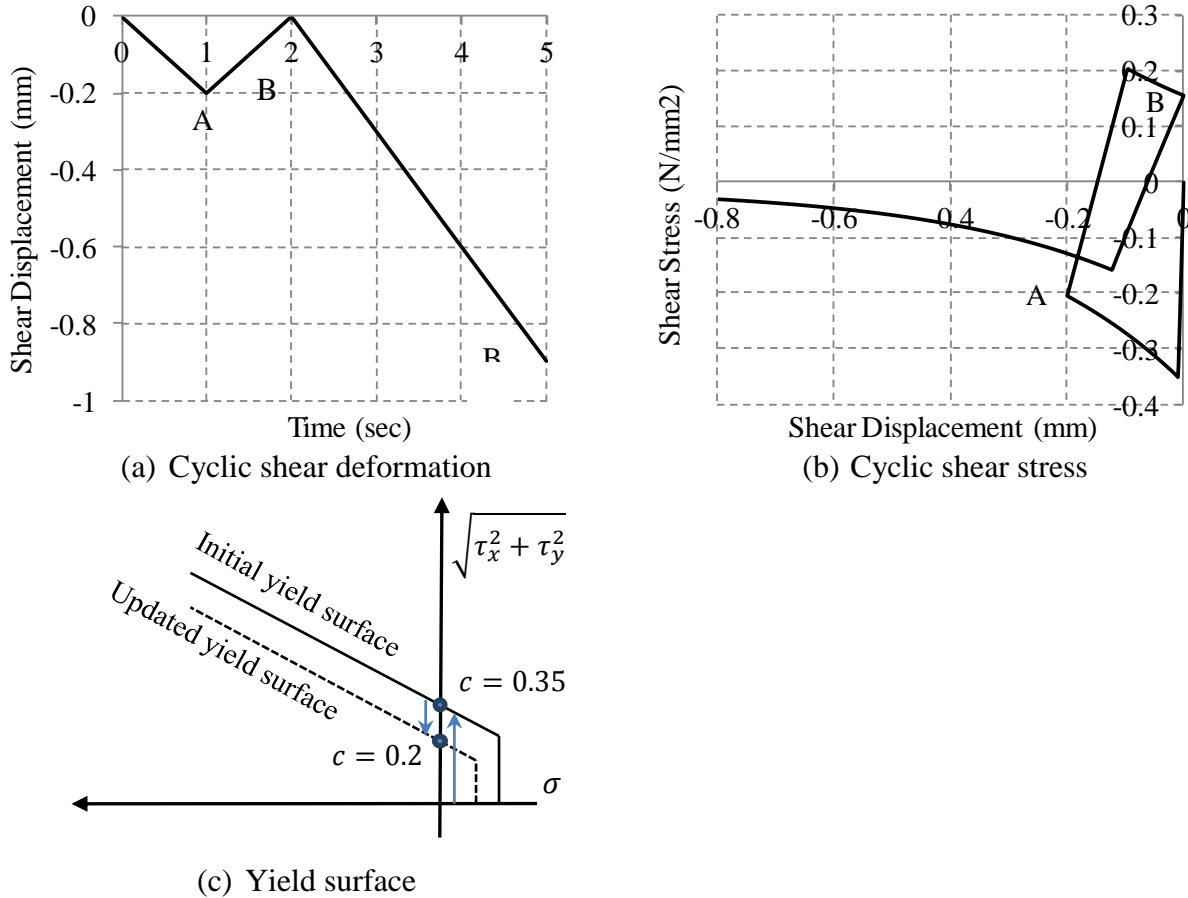


Figure 5-8. The results of an element under shear force

Experimental results indicate no stiffness degradation for frictional resistance when a joint is subjected to cyclic transverse loading with the absence of cohesion (Oliveira and Lourenco 2004) (Figure 5-9). In contrast to tensile strength and according to Mohr-Coulomb rule, the shear strength is a combination of cohesion and friction. Therefore, for the formulation of stiffness degradation in the transverse cyclic loading, it is assumed that for the portion of the shear strength where cohesion is involved, the stiffness degradation is similar to that used for tension (Figure 5-5). However, for the portion where friction is involved, no stiffness degradation is considered. Hence, for the final value of the stiffness, in each time step the average of the two values should be calculated. In other words, for the situation similar to Figure 5-8(b) where no compressive load exists, a formulation similar to tension is used. For an element with a high

compressive load, where the frictional force is predominant, no stiffness degradation is considered.

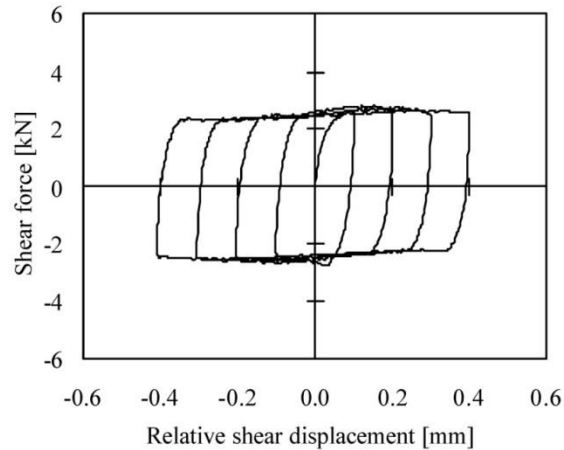


Figure 5-9. Cyclic frictional resistance (Oliveira and Lourenco 2004)

5.4.3 Shear and tension interaction regime

The cohesion behavior of the joint is coupled in tension and shear, since both have the same source, which comes from the cementation of the mortar. Brittle results were found with potential instability of the test set-up, therefore, experimental results are not available for the shear-tension paths (Lourenco 1996).

In the model presented herein, isotropic softening is assumed for the coupled behavior between the shear and tension, similar to the approach adopted by Lourenco (Lourenco 1996). In other words, that after applying tensile force and reducing tensile strength to $m\%$ of its initial strength ($0 < m < 100$), the shear strength is also assumed to be reduced by $m\%$ of its initial strength. Therefore, in the formulation, for the total motion in the tensile direction in each time step, along the reduction of the tensile strength, the ultimate shear strength is also reduced. This is shown as (Lourenco 1996)

$$\Delta\kappa_{2,n+1} = \frac{G_f^I}{G_f^{II}} \frac{c}{f_t} |\Delta u_n^p| \quad (5-18)$$

Therefore, for deformations in the shear and tensile direction:

$$\kappa_1 = (\Delta u_n^p) + \left(\frac{G_f^I}{G_f^{II}} \frac{c}{f_t} |\Delta u_n^p| \right) \quad (5-19)$$

$$\kappa_2 = (\Delta u_s^p) + \left(\frac{G_f^{II}}{G_f^I} \frac{f_t}{c} |\Delta u_n^p| \right) \quad (5-20)$$

5.4.4 Cap for the yield surface

An experimental study has been performed by the author, to identify the necessity of using cap regime for the yield surface of the mortar under high compression forces. Two different types of bricks have been selected with two different levels of compressive capacities, including a high strength brick and a low strength brick, to construct masonry prism samples. In constructing masonry prisms, only one type of mortar has been used (type “N”) for both types of the bricks. The stress-strain curves of uniaxial compression test for high and low strength bricks in addition to the cubic mortar samples are presented in Figure 5-10. The high strength brick was about three times stronger than the low strength brick and the mortar as shown in Figure 5-10.

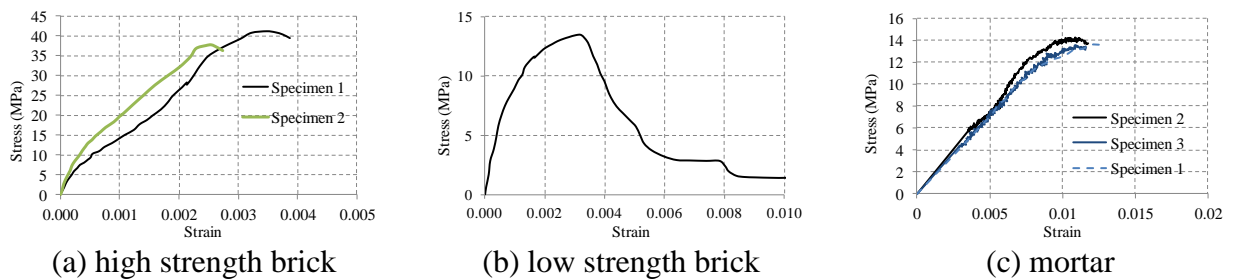


Figure 5-10. Stress-strain curves

Figure 5-11 shows a damaged brick prism after uniaxial compression test. For both types of bricks, it was observed that even though the bricks (for high strength bricks) were stronger than the mortar, only bricks were crushed and the mortar was extracted without any significant

damage. The reason for this behavior is attributed to the small thickness of the mortar and the high level of confinement of the mortar induced by the adjacent bricks.



Figure 5-11. The damaged specimen after compression test

The stress-strain curves of the masonry prisms constructed with high and low strength bricks are presented in Figure 5-12 (a) and (b), respectively. Based on Figure 5-12 (a) the strength of the masonry prism constructed using high strength brick was three times greater than the strength of the cubic mortar sample used between the bricks. These observations indicate that no cap regime should be defined in the yield surface of the mortar if the brick is modeled using elasto-plastic elements.

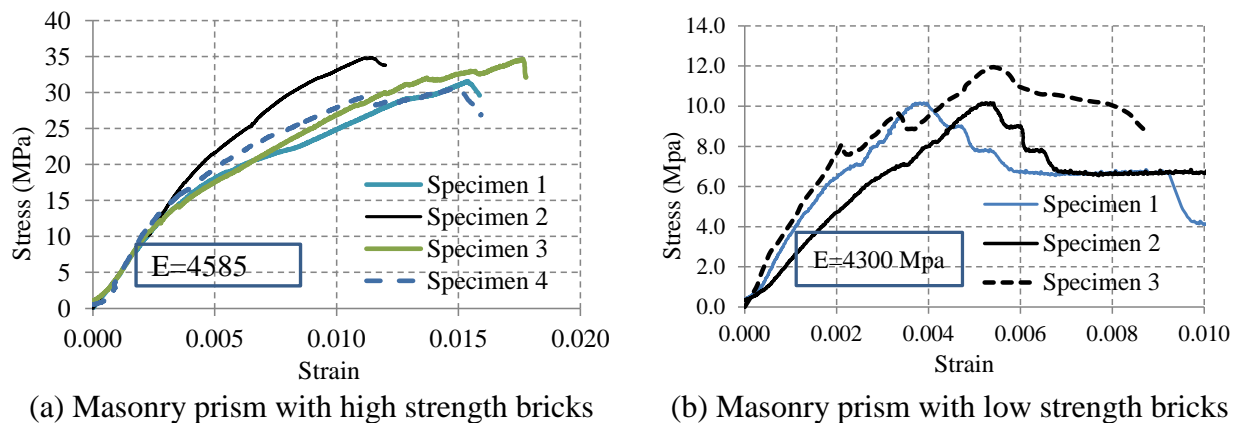


Figure 5-12. Stress-strain curves of masonry prism specimens

5.5 Plastic behavior of the brick elements

The concrete damaged plasticity material model in ABAQUS was used to model the nonlinear behavior of the bricks. This material model is specifically written for concrete. However, it can be used for other brittle materials including bricks. The model assumes that the main two failure mechanisms for brittle materials are tensile cracking and compressive crushing. In this material model, the position of the yield surface is always controlled by two hardening variables, ε_t^{pl} , ε_c^{pl} , tensile and compressive plastic strain, respectively. This material behavior is also formulated to capture the cyclic behavior of brittle material by considering stiffness degradation (Figure 5-13).

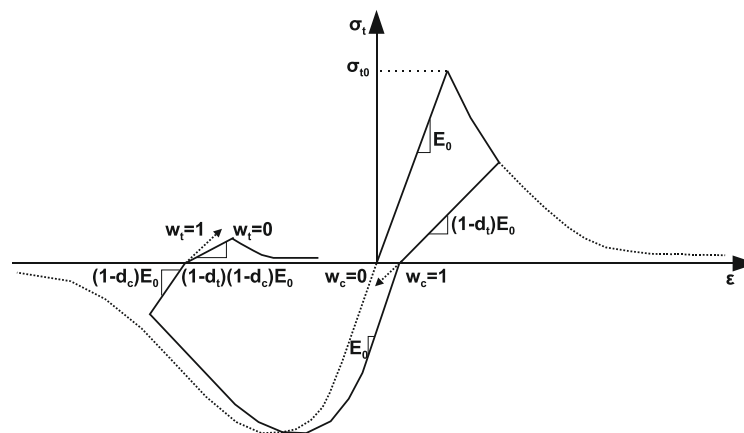


Figure 5-13. Concrete damage material model under uniaxial tension and compression test (Abaqus 2005)

5.6 Explicit dynamic analysis

Explicit analysis has been used to solve the dynamic equations of motion with impulsive loading such as blast. However, it can also be used to model quasi-static problems as described in the following section. In contrast to the implicit procedures, the explicit procedure requires no iterations and no formation of the tangent stiffness matrix. The progress of analysis in the time

domain is performed by using many small increments dictated by the stability criterion (Bathe 1995).

The explicit dynamic analysis procedure is derived from explicit central difference integration scheme. In order to have a stable analysis, the time increment is the only constraint that needs to be controlled; and this parameter should be checked with the highest natural frequency of the elements. In other words, to have a conditionally stable central difference operator, the time increment (Δt) should be less than the stability limit (Δt_{max}). In ABAQUS, by using the highest eigenvalue in the system (ω_{max}), the time increment is estimated by using the following inequality (Abaqus 2005):

$$\Delta t \leq \frac{2}{\omega_{max}} \left(\sqrt{1 + \zeta^2} - \zeta \right) \quad (5-21)$$

where ζ is the corresponding fraction of the critical damping in the highest mode. Alternatively, this limit can be estimated from the element dimension L_e and the current effective, wave velocity C_d as follows:

$$\Delta t_{max} \leq \frac{L_e}{C_d} \quad (5-22)$$

where $C_d = \sqrt{\frac{E}{\rho}}$, ρ is the density and E is the modulus of elasticity. In nonlinear analysis, by changing the modulus of elasticity, the stability limit will change. A complete discussion of the explicit dynamic function can be found in ABAQUS manual (Abaqus 2005).

5.7 Numerical validation

The experimental and well-documented results by Raijmakers and Vermeltoort (Raijmakers and Vermeltoort 1992) and Vermeltoort and Raijmakers (Vermeltoort and Raijmakers 1993) were

used to verify the proposed constitutive material model. Vermelfoort and Raijmakers performed an experimental study on three masonry walls with different compressive loads. The walls were subjected to two different types of compressive loading; for the first (J4D) and second (J5D) walls the compressive load was 30 *kN*, the load on the other wall was 120 *kN*. The compressive load was increased for the third wall to investigate the influence of compressive load on failure mode.

The height and width of the walls were 1,000 and 990 mm, respectively, and had 16 active rows of brick. The dimensions of the bricks were 210 × 52 × 100 *mm* and the mortar was 10 *mm* thick, prepared with a volumetric cement: lime: sand ratio of 1: 2: 9 (Figure 5-14). The compressive load was applied first (Figure 5-14(a)) and the vertical displacement of the top surface was constrained. A monotonic displacement-controlled load was then imposed horizontally on top of the wall (Figure 5-14 (b)).

Different experimental tests were also performed to obtain the properties of the mortar and bricks (Raijmakers and Vermelfoort 1992; Vermelfoort 1993). This author did not have complete access to the material properties of the bricks used in the concrete damaged material model. Typical material properties were selected from a range provided by Stavridis (Stavridis 2009) for bricks with compressive strength of 10.5 *N/mm²* (for J4D and J5D walls), and 11.5 *N/mm²* (for J6D wall).

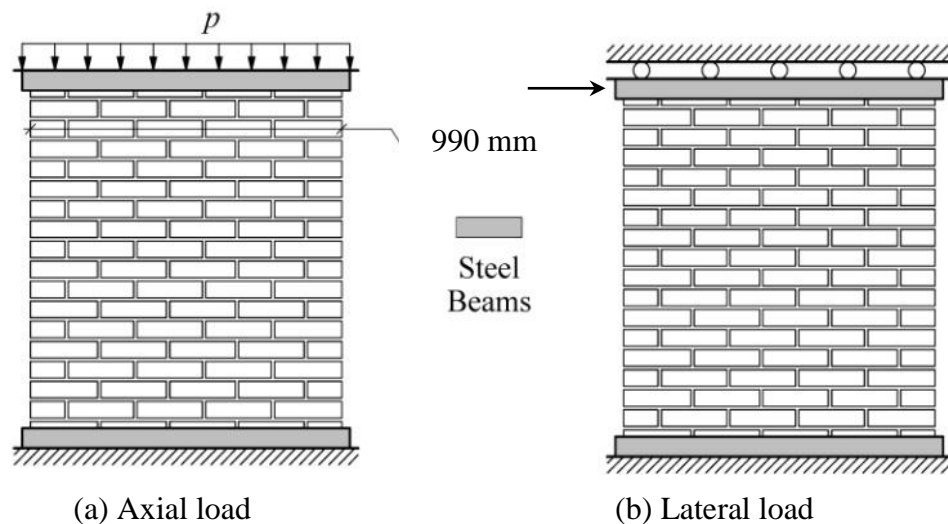


Figure 5-14. Step 1 and step 2 for applying the load (Lourenco 1996)

The FEM of the wall was created according to the description of section 5.2 using the material properties given in Table 5-2 and Table 5-3. Vertical/ Horizontal cracks in Table 5-2 and Table 5-3 represent the properties of the interface elements located in the horizontal and vertical mortar joints. After imposing the compressive load on the top plane of the wall, the vertical deformation of the top plane of the wall was restrained.

To impose the horizontal loading in Figure 5-14, two different approaches can be considered. Numerical modeling can be performed by using either quasi-static or dynamic analysis. In this section, the latter procedure is employed to show the capabilities of the model in dynamic simulations. Thus, by applying a constant velocity at the top plane of the wall, the load-displacement curve in Figure 5-15 was created. In this figure, the dashed line represents the solution obtained using the proposed constitutive material model and numerical procedure. The two solid lines correspond to the experimental results. In contrast to implicit procedures, the proposed model based on the explicit formulation convergences.

Table 5-2. Properties of different types of cracks (J4D/J5D)

(Based on the experimental result by (Raijmakers and Vermeltoort 1992; Vermeltoort and Raijmakers 1993))

Type	k_n (N/mm^3)	k_s (N/mm^3)
Vertical/ Horizontal cracks	82	36
Potential cracks	1000	1000

Table 5-3. Inelastic properties of the joints (J4D/J5D)

(Based on the experimental result by (Raijmakers and Vermeltoort 1992; Vermeltoort and Raijmakers 1993))

Type	Tension				Shear				
	f_t	$\frac{N}{mm^2}$	G_f^I	$\frac{N\ mm}{mm^2}$	c	$\frac{N}{mm^2}$	$\tan \phi$	G_f^{II}	$\frac{N\ mm}{mm^2}$
Vertical/ Horizontal cracks	0.25		0.018		0.35		0.75		0.125
Potential cracks	2		0.08		2.8		0.75		0.55

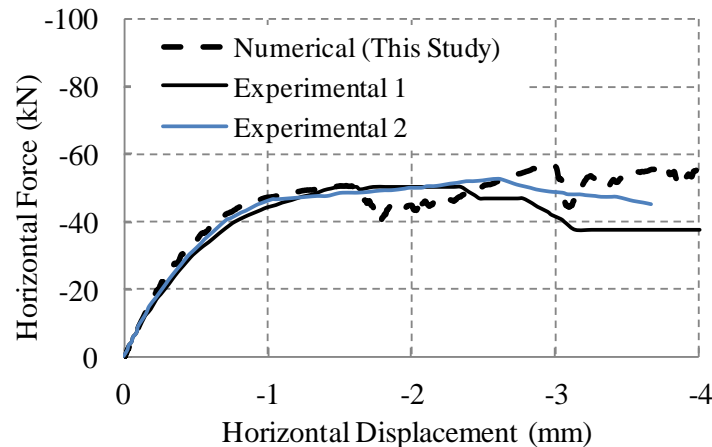


Figure 5-15. Comparison of numerical and experimental load - displacement results for wall subjected to 30 kN compressive load

Figure 5-16 shows the numerical results for 10 mm of horizontal displacement. As expected, after the diagonal crack completed, the wall continued to resist the loading by the frictional force at the cracked surfaces, which is evident by the horizontal force remaining almost unchanged after 6 mm, as shown in Figure 5-16. Using this method, it is possible to achieve large displacements. However, to obtain more accurate results for large displacements, a very fine

mesh should be used. Within the analysis new contacts are created and a fine mesh is needed to accurately find the new length of contacts.

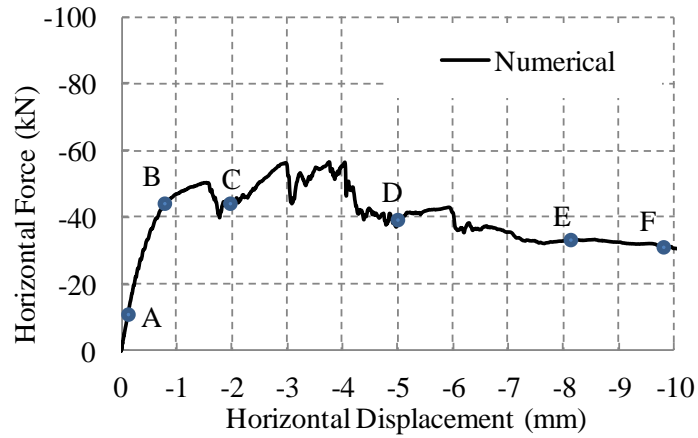


Figure 5-16. Numerical load - displacement result for wall subjected to 30 kN compressive load

The crack pattern at different stages of loading is shown in Figure 5-17. To indicate the path of the crack in the early stages of loading, different magnification factors are used for each snapshot. In the first three figures, the displacements are magnified 40 times (40×), but in the last three figures where the deformations are higher, a magnification factor of five (5×) is used. Figure 5-17 shows that initially the crack propagated from the two corners and continued to a full diagonal crack.

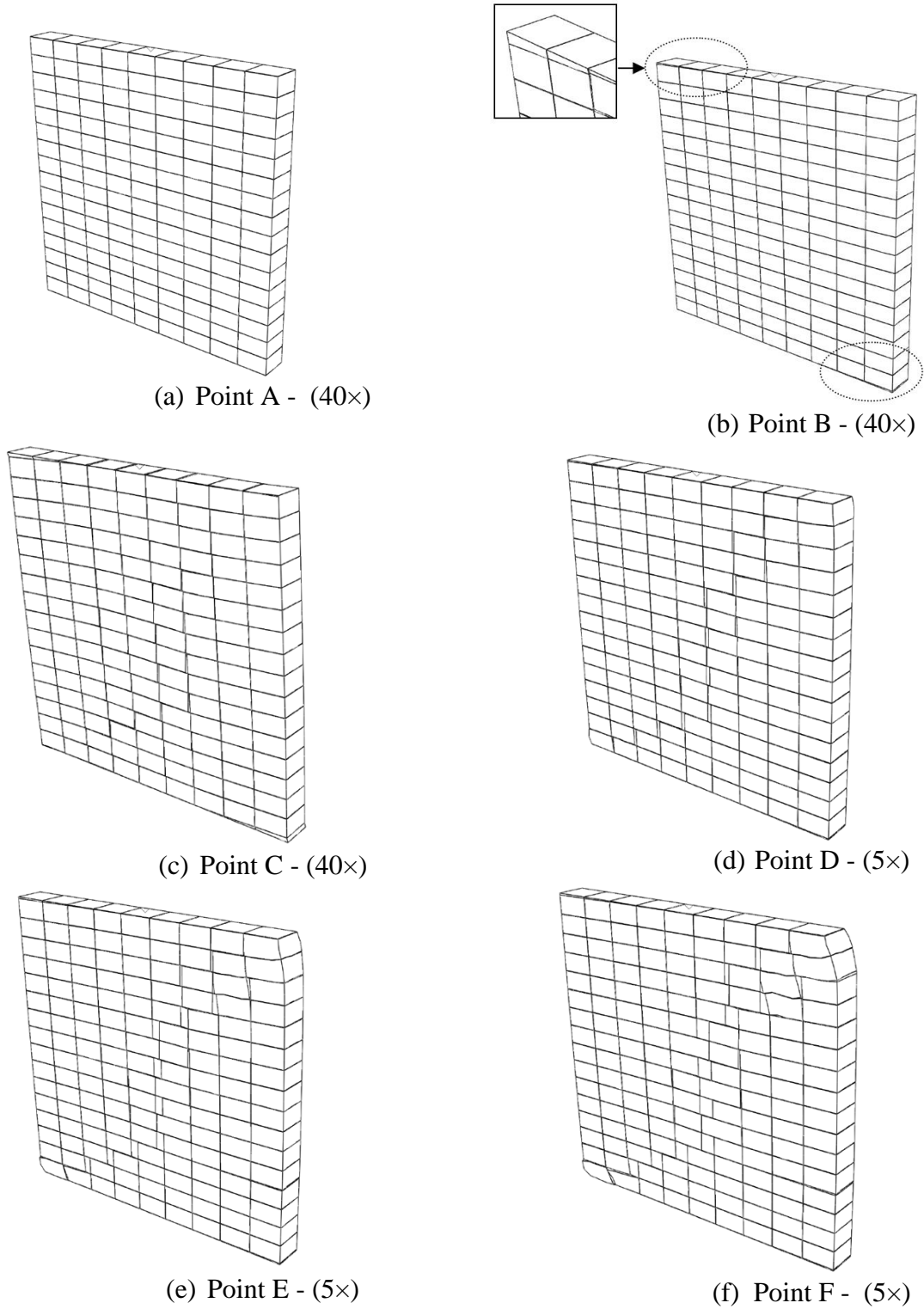


Figure 5-17. Crack pattern of the wall at different stages of load

Figure 5-18 shows the experimental crack pattern at a displacement of 4 mm. It is seen that even for two walls with the same material properties and loading, the crack patterns are distinctly different, primarily due to the heterogeneity of the mortar and brick materials. However, they are in good agreement with the numerical results.

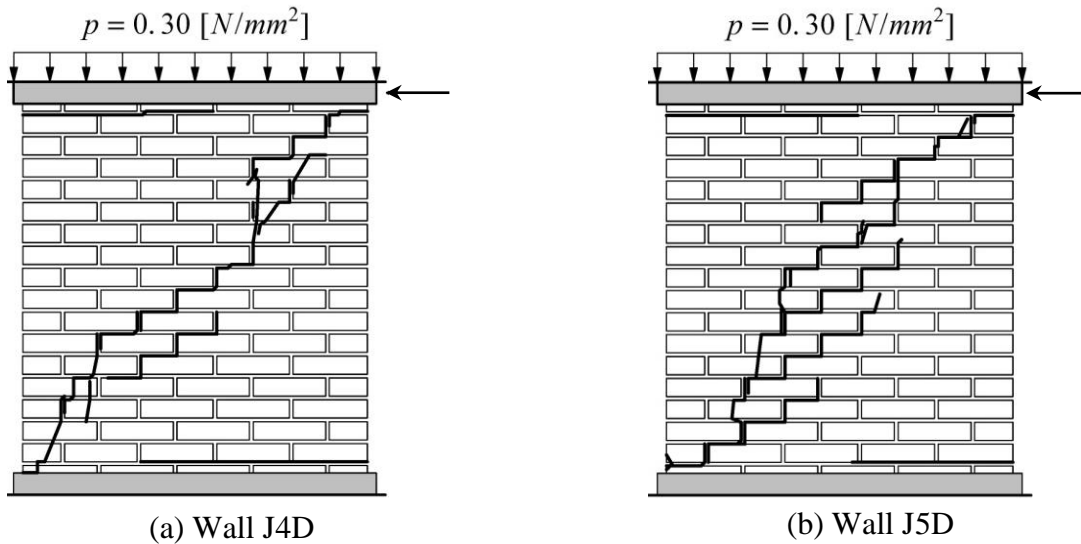


Figure 5-18. Experimental crack pattern at 4 mm displacement (Lourenco 1996)

As the second phase of numerical modeling, a cyclic loading was applied to the same wall used in the first example. To obtain the cyclic loading of Figure 5-20, a varying velocity was applied at the top plane of the wall according to Figure 5-19.

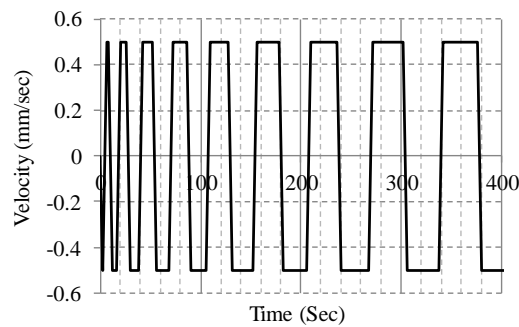


Figure 5-19. Cyclic velocity applied at the top of the wall

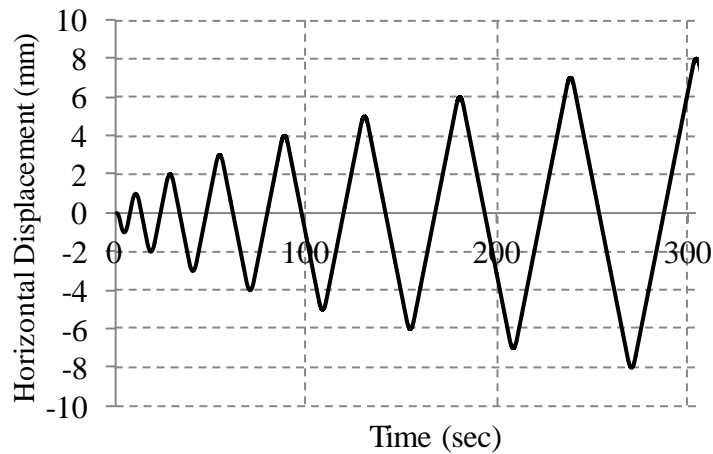


Figure 5-20. Resulting cyclic displacement at the top of the wall

The result of the cyclic loading along with the result of monotonic loading is shown in Figure 5-21. In this figure, strength and stiffness degradation are clearly evident. As seen in Figure 5-21, after a few cycles the frictional force that is associated with some strength degradation governs cyclic response. The top plane of the wall is constrained in the vertical direction while the horizontal force was applied; therefore, after crushing of the bricks located at the corners, the total compressive load decreases and subsequently the resisting frictional force decreases. This is one of the reasons that the resisting force decreases in the cyclic loading depicted in Figure 5-21. Based on Figure 5-21, the peak in the cyclic loading curve takes place sooner and with a slightly higher value when compared to the monotonic loading curve. This observation is also reported in the associated experimental work (Haider 2007).

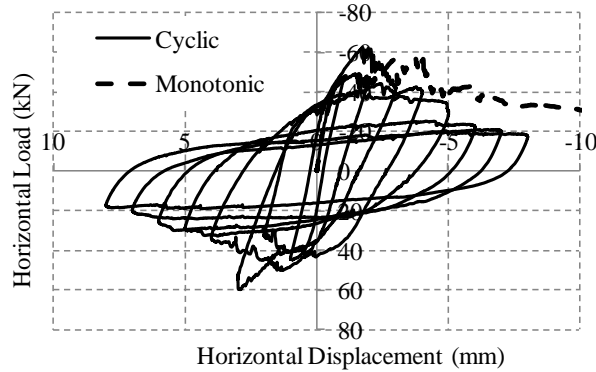


Figure 5-21. Cyclic load - displacement diagram for wall subjected to 30kN compressive load

The same numerical analysis has been repeated on a wall with the same geometrical configuration of the previous example with 120 kN compressive load (J6D) and the results are presented in Figure 5-22. The material properties of Table 5-4 and Table 5-5 provided by Vermelfoort and Raijmakers (Raijmakers and Vermelfoort 1992; Vermelfoort and Raijmakers 1993) have been used in the FEM.

Table 5-4. Properties of different types of cracks (J6D)

(Based on the experimental result by (Raijmakers and Vermelfoort 1992; Vermelfoort and Raijmakers 1993))

Type	$k_n (N/mm^3)$	$k_s (N/mm^3)$
Vertical/ Horizontal cracks	110	50
Potential cracks	1000	1000

Table 5-5. Inelastic properties of the joints (J6D)

(Based on the experimental result by (Raijmakers and Vermelfoort 1992))

Type	Tension			Shear		
	f_t	G_f^I	c	$\tan \phi$	G_f^{II}	
Vertical/ Horizontal cracks	$\frac{N}{mm^2}$	$\frac{N}{mm}$	$\frac{N}{mm^2}$		$\frac{N}{mm}$	
	0.16	0.012	0.224	0.75	0.05	
Potential cracks	2	0.08	2.8	0.75	0.55	

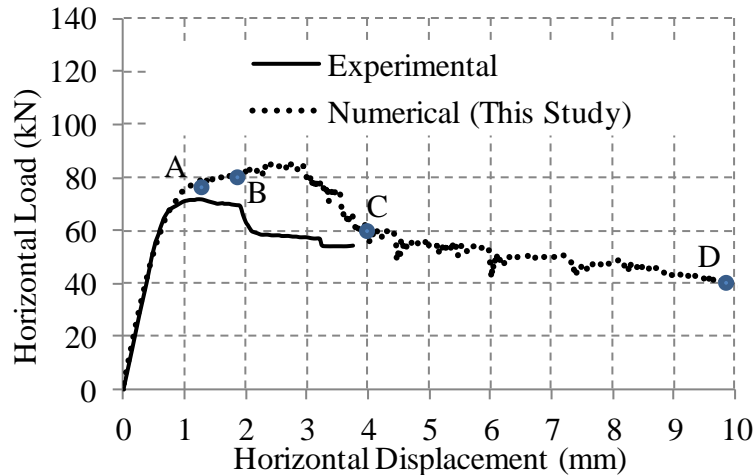


Figure 5-22. Comparison of numerical and experimental load - displacement diagram for wall under 120kN compressive load

In Figure 5-22 the solid line represents the experimental results and the dashed line corresponds to the numerical analysis. In the linear part, the numerical results are consistent with the experimental results. It will be noted that there is some discrepancy between the experimental and numerical results in the nonlinear regime even though the gross behavior is virtually identical. As mentioned earlier, this author did not have access to the exact properties of the brick material, and compressive stress-strain parameters were chosen from typical material data for bricks with 11.5 N/mm^2 compressive strength (Stavridis 2009). A better match between the numerical and experimental results would be achieved using measured material properties. Figure 5-23 shows the numerical crack propagation in the wall in different stages of loading, which shows a diagonal crack in the wall.

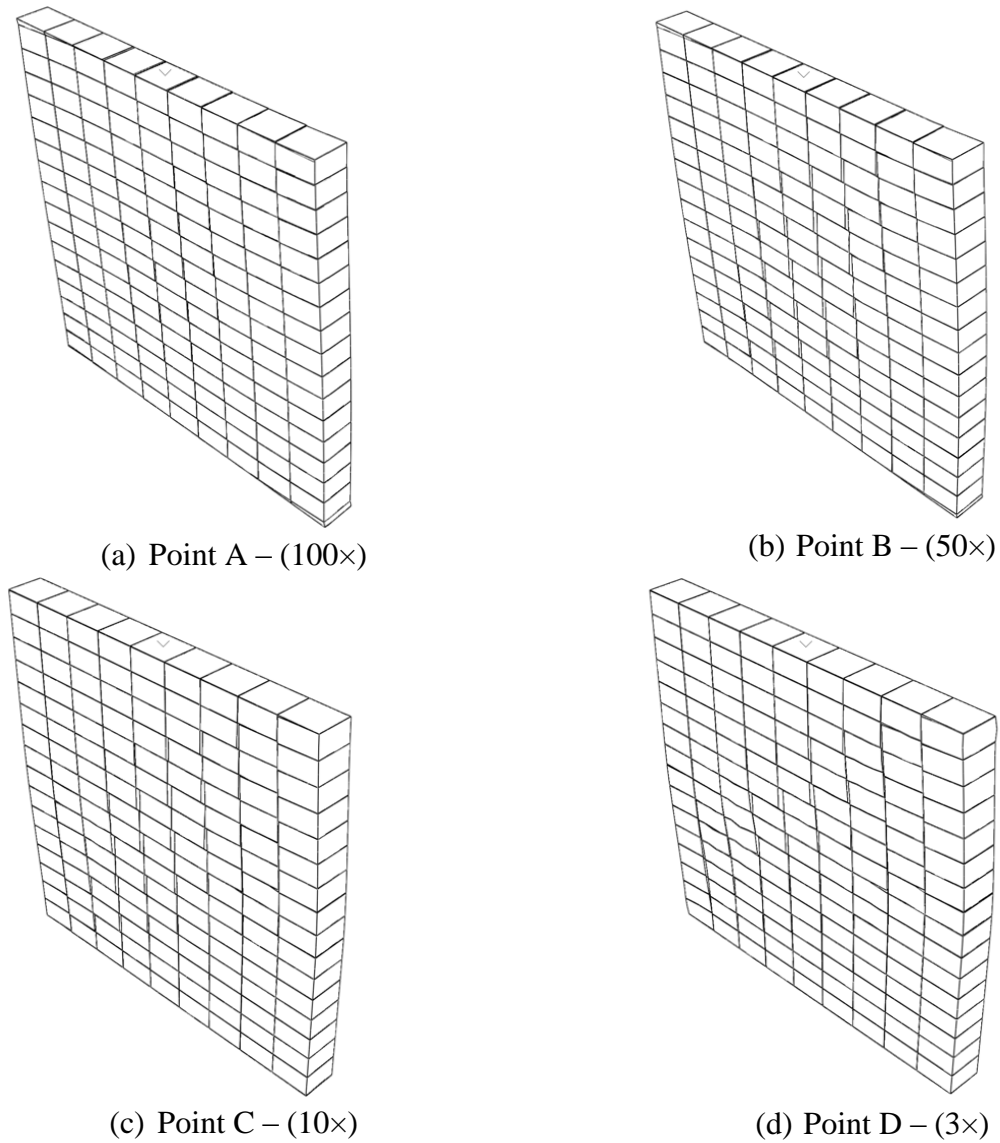


Figure 5-23. Crack pattern of the wall (J6D) in different stages of loading

Figure 5-24 presents the propagated crack for the experimentally tested wall that is in good agreement to the numerical results in Figure 5-23 (b) and (c).

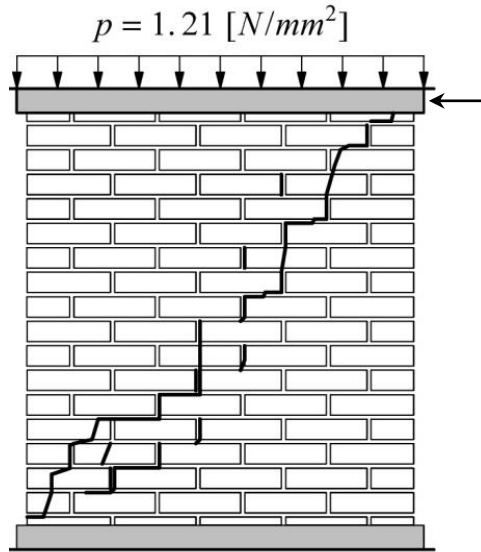


Figure 5-24. Experimental Crack Pattern at 4 mm displacement in wall J6D (Lourenco 1996)

Wall J6D has been subjected to a cyclic loading with the compressive load of 120 *kN* and the results are shown in Figure 5-25. As depicted in Figure 5-25, the cyclic backbone curve follows the monotonic curve presented in Figure 5-22. Figure 5-25 shows that after 5 *mm* displacement in the cyclic curve, the behavior of the wall is controlled by the frictional force, which is generated in the diagonal cracks. In this example (J6D wall), due to the use of greater compressive force, more bricks have entered the nonlinear regime (comparing to J4D wall), especially the bricks located in the corners. As mentioned earlier while the cyclic load was being applied, the top plane of the wall was constrained. The total compressive load decreases due to the crushing and the relaxation of the bricks in the corners. Due to the use of greater compressive load in wall J6D, the strength degradation for wall J6D is more than wall J4D.

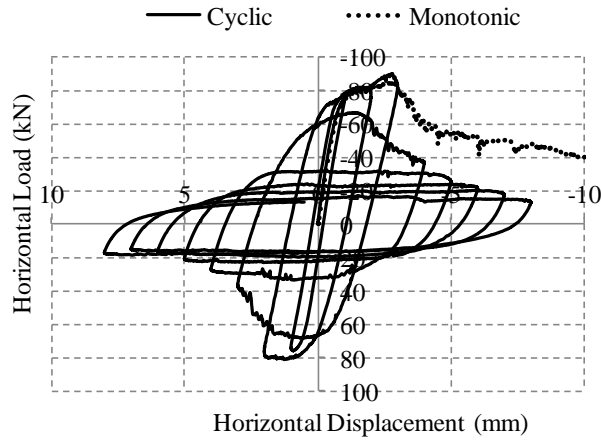


Figure 5-25. Load - displacement diagram for wall under 120 kN compressive load (cyclic)

5.8 Out-of-plane loading on masonry shear walls

In this section, the masonry wall discussed in the previous section is subjected to a monotonic out-of-plane displacement. The boundary conditions are the same as the examples in the previous section, except for the top plane which is not constrained in the vertical direction. Figure 5-26 shows the load-displacement of the wall under monotonic out-of-plane loading. This figure illustrates that after a specific out-of-plane deformation (about 100 mm) the wall became unstable.

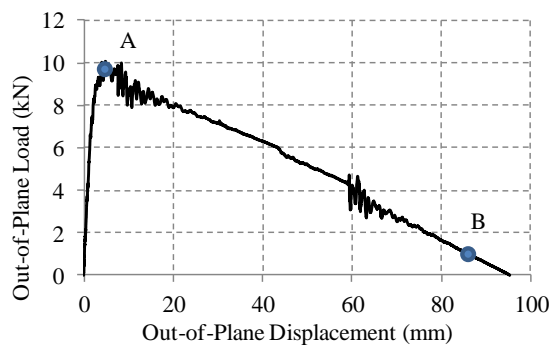


Figure 5-26. Load-displacement for out-of-plane direction loading

The deformed configuration of the wall under out-of-plane loading in points “A” and “B” of Figure 5-26 is presented in Figure 5-27. Point “A” shows the configuration of the wall when it has the most resisting force and point “B” corresponds to the point where the wall will be unstable for the larger deformation. Most of the damage is located on the last three rows of the mortar in the top and bottom of the wall, as shown in Figure 5-27. The more deformation of the wall in point “B” has opened more the existing cracks in point “A”.

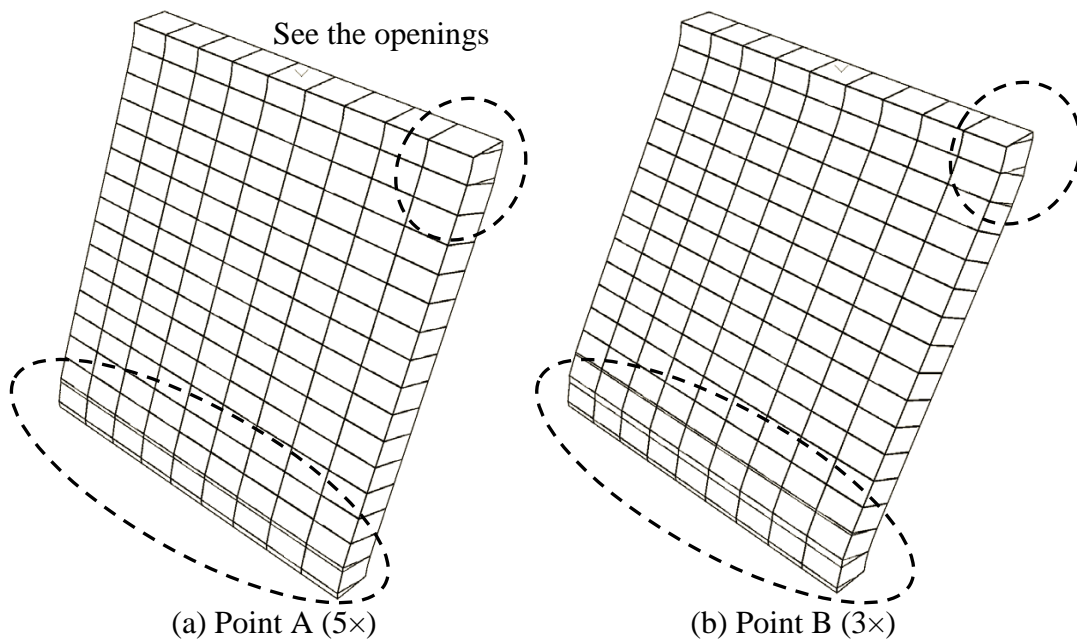


Figure 5-27. Deformed shape under out-of-plane loading (notice the openings)

Figure 5-28 presents the moment diagram of the wall under OP loading. According to Figure 5-28 (a), by writing the moment equilibrium equation under point “O”, the maximum value of the resisting force (R) can be calculated. Note that, based on Figure 5-27 (a) in the deformation associated to the maximum OP force (point “A” in Figure 5-26), the top and bottom planes are already separated from the supports and mortar cohesion does not contribute in the OP resisting force.

$$\Sigma M_O = 120 (50 - \Delta) + \frac{R 1000}{2} - R 1000 = 0 \quad (23)$$

where Δ represents the OP deformation of the wall associated to the maximum OP resisting force. According to Figure 5-26 and point “A”, for $\Delta = 7 \text{ mm}$ equation (21) yields $R = 10.3 \text{ kN}$ which is very close to the finite element results presented in Figure 5-26.

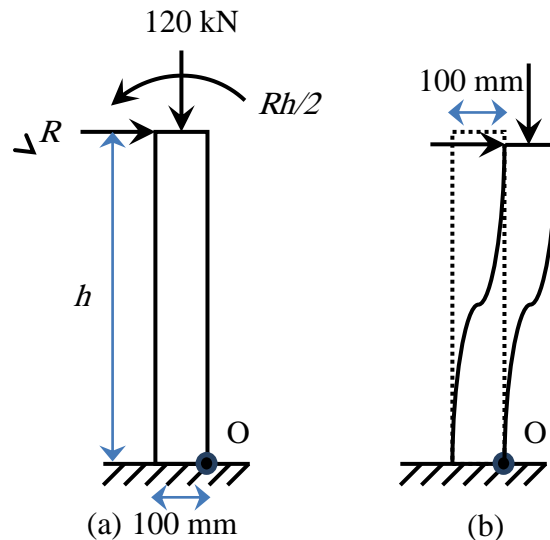


Figure 5-28. Moment diagram for OP load

As shown in Figure 5-28 (b) after about 100 mm out-of-plane deformation, the top and bottom planes do not have any overlap and the wall loses its stability under the gravity load. This conclusion is in accord with the finite element results in Figure 5-26 (point “B”). The same wall is subjected to the cyclic out-of-plane loading of Figure 5-29. The resultant cyclic load-displacement curve is shown in Figure 5-30.

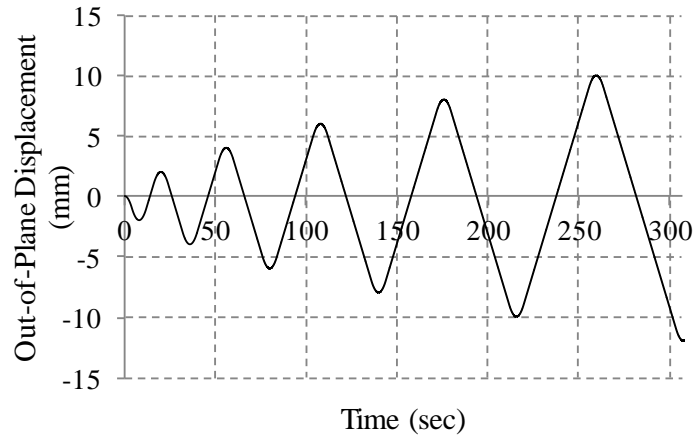


Figure 5-29. Cyclic out-of-plane load

Figure 5-30 illustrates the rocking behavior of the wall. This behavior is expected based on the low aspect ratio of the wall in the out-of-plane direction. The loss of strength in Figure 5-30 is a function of the strength degradation in both the mortar and brick. The stiffness degradation in the mortar can be controlled by the proposed material model in this report and the stiffness degradation in the brick can be controlled by the respective parameters in the concrete damaged material model of ABAQUS. In this example, due to the significant damages in the corners of the top and bottom bricks under the gravity and cyclic loadings, high strength degradation has taken place.

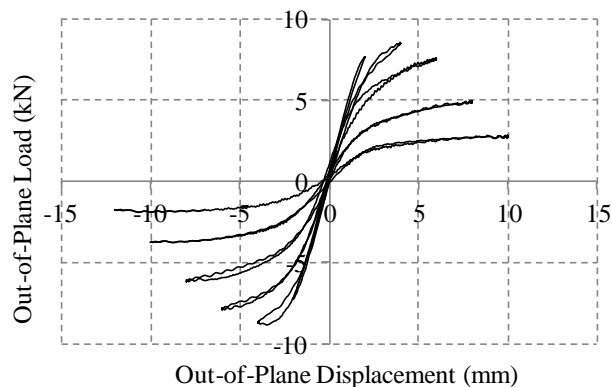


Figure 5-30. Out-of-plane cyclic load-displacement

Figure 5-31 shows the deformed shape (rocking) of the wall under out-of-plane cyclic load. The circular dashed lines in Figure 5-31 show the opening of the mortar at the end of the cycles. This figure well indicates the correct functionality of the discussed material model in the simulation of opening and closing of the joints.

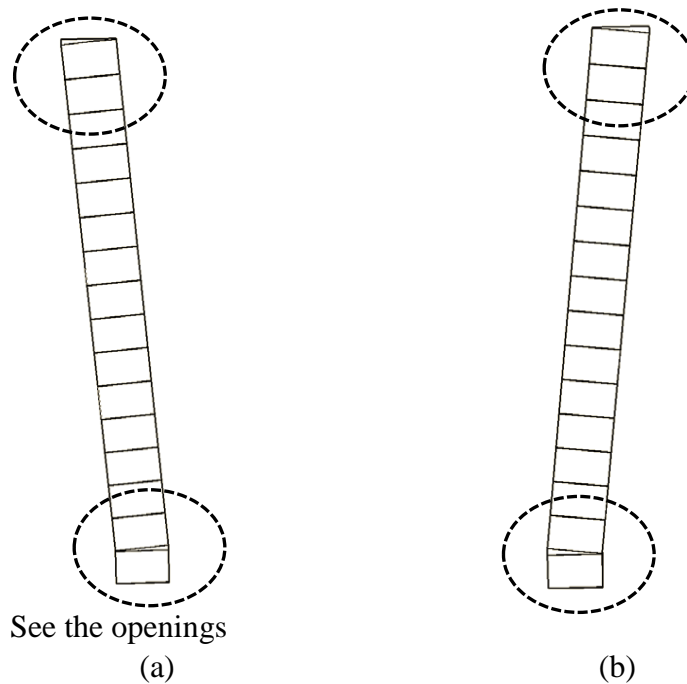


Figure 5-31. Deformed configuration of the wall under cyclic out-of-plane loading

5.9 Conclusion

This section developed a robust modeling strategy for masonry structures subjected to 3-D loadings. A description of the material model was presented first, along with its implementation in a user-defined subroutine used with ABAQUS. Then, to show the robustness of the proposed model, various walls were modeled and the numerical results were compared with experimental results. The numerical results were in a good agreement with the experimental results.

The most difficult problem in previous investigations of modeling masonry structures was convergence of the numerical simulations. Using an explicit formulation, convergence was

achieved. The derived constitutive material model in this section is formulated with the capabilities to perform three-dimensional analyses of masonry buildings under earthquake excitations. In addition, this modeling strategy offers efficient and low computational demand. Thus, the algorithm is useful for both research and professional practices.

SECTION 6

INTERACTION OF IN-PLANE AND OUT-OF-PLANE

DISPLACEMENT OF UNREINFORCED MASONRY WALLS –

NUMERICAL STUDY

6.1 Introduction

Most of the studies related to modeling masonry structures have so far investigated either the in-plane (IP) or out-of-plane (OP) behavior of unreinforced masonry walls. However, earthquake excitations mostly cause masonry buildings to simultaneously experience in-plane and out-of-plane demands, and therefore, there is a need to investigate the three-dimensional and interaction behavior of unreinforced masonry walls. Using the validated finite element model of the previous section, in this section a set of masonry walls is subjected to 22 different loading protocols; of those loading conditions, 19 are monotonic bidirectional loadings, and three loadings are cyclic in different directions. Each time, the direction of the load is changed to investigate the influence of the loading direction on the behavior of the wall. Moreover, deformed shapes are presented for each wall to show the associated failure mode. Finally, the results are organized and interaction curves are proposed which show the elastic range and the ultimate load in different directions.

6.2 Description of the finite element model

A detail description of the 3-D finite element modeling of unreinforced masonry walls was presented in the previous section. In this section, numerical procedures are employed to examine the interaction between in-plane and out-of-plane behavior.

To create the finite element model (FEM) of a URM wall, bricks and mortar are distinctly defined in the proposed model by two types of elements. Bricks are modeled with solid elements (C3-D8R) in ABAQUS (Abaqus 2005) and mortar is modeled with plane interface elements (COH3-D8) as shown in Figure 6-1.

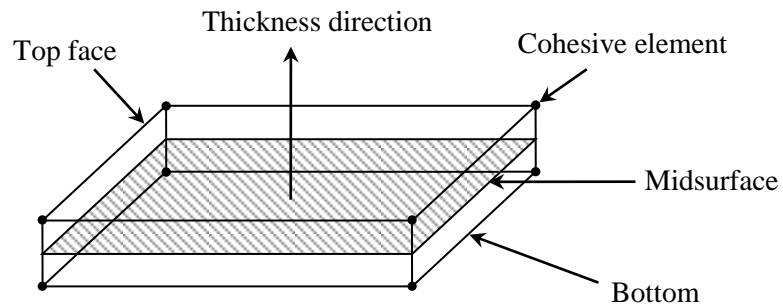


Figure 6-1. Eight node plane interface element (ABAQUS)

Based on Figure 6-2, bricks are expanded by half the mortar dimension and interface elements are located between the solid elements that represent the mortar.

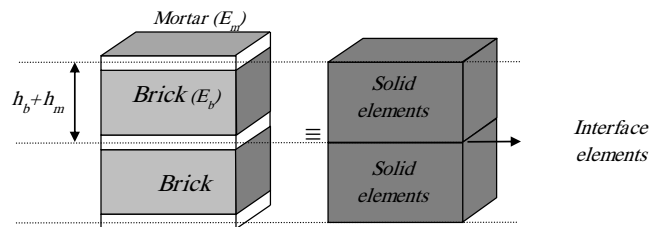


Figure 6-2. Detailed model of brick and mortar

Experimental observations indicate that, in majority of cases, most of the crack paths pass through either the mortar joint or middle of the bricks. Thereby, to capture the exact behavior of the wall and to guarantee the possibility of crack propagation in the middle of the bricks, bricks are divided into two parts and a potential crack is placed in the middle of the bricks. The idea of using potential cracks has been already employed by many researchers in 2-D analysis (Lourenco 1996; Oliveira and Lourenco 2004; Oliveira and Lourenco 2004; Stavridis and Shing 2010). Figure 6-3 shows the generated FE mesh for the wall and a general view (bricks and mortar) of the wall considered in the subsequent examples of this section. In order to assess the mesh sensitivity issue, a fine mesh with 95,888 elements has also been used for some analysis cases. Since the time of analysis for the fine mesh is much higher than the coarse mesh, for the rest of the analyses, only the coarse mesh is used.

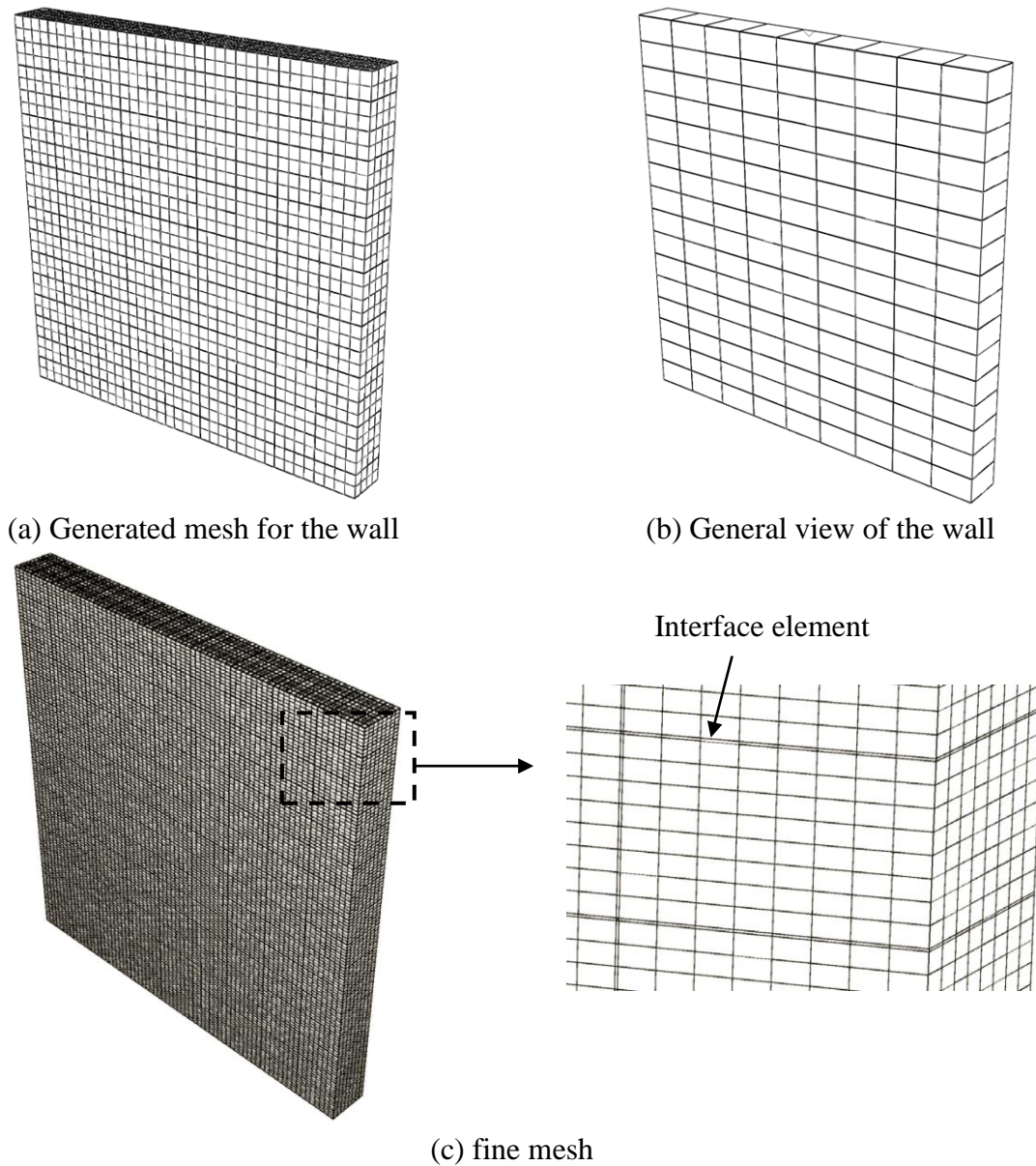


Figure 6-3. Numerical models

6.3 Numerical models

In order to explore the interaction issue, the wall experimentally tested by Vermelfoort and Raijmakers (1992) has been used in this section. The height and width of the walls was 1,000 and 990 mm, respectively, and had 16 active rows of brick. The dimensions of the bricks were

210 × 52 × 100mm and 10mm thick mortar, prepared with a volumetric cement: lime: sand ratio of 1: 2: 9 (Figure 6-4). In all numerical models, the boundary condition for the bottom plane is completely fixed. The top plane is free in the vertical direction and all rotational degrees of freedom are restrained for the top plane. The loadings have been applied in two steps, first the compressive load was applied (Figure 6-4 (a)), and while keeping the compressive load constant, a monotonic displacement-controlled load was applied horizontally on top plane of the wall (Figure 6-4(b)).

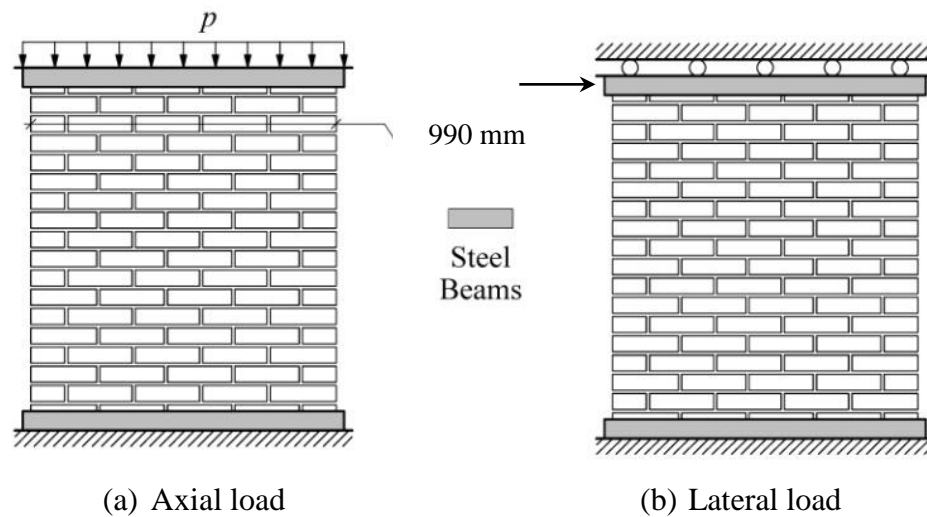


Figure 6-4. Step 1 and step 2 for applying the load (Lourenco 1996)

Different experimental tests were also performed to obtain the properties of the mortar and bricks by Vermeltoort and Raijmakers (Raijmakers and Vermeltoort 1992; Vermeltoort 1993). The author did not have complete access to the material properties of the bricks used in the concrete damaged material model. Due to the missing properties, typical material properties were selected from a range provided by Stavridis (Stavridis 2009) for bricks with compressive strength of 11.5 N/mm^2 . The material properties used in the finite element model are presented in Table 6-1 and Table 6-3.

Table 6-1. Properties of different types of cracks (J4D/J5D)

(Based on the experimental result by (Raijmakers and Vermeltfoort 1992; Vermeltfoort and Raijmakers 1993))

Type	(N)	(N)
Vertical/ Horizontal cracks	82	36
Potential cracks	1000	1000

Table 6-2. Inelastic properties of the joints (J4D/J5D)

(Based on the experimental result by (Raijmakers and Vermeltfoort 1992; Vermeltfoort and Raijmakers 1993))

Type	Tension			Shear	
	—	—	—	—	—
Vertical/ Horizontal cracks	0.25	0.018	0.35	0.75	0.125
Potential cracks	2	0.08	2.8	0.75	0.55

6.4 Loading protocols

The wall was subjected to 22 different loadings, where 19 cases were monotonic. In each case, the direction of the load was changed. Three cyclic loadings were also performed in different directions to investigate the variation of the cyclic behavior/mechanism as the direction of the loading changes. Table 6-3 summarizes the loading protocols used in this study. A simple symbol “IO:x/y” is used to facilitate the naming of the loading protocols. In this symbolic numbering, x and y represent the proportion of the in-plane and out-of-plane displacement of the wall, respectively, in the imposed displacement-controlled loading (Figure 6-5).

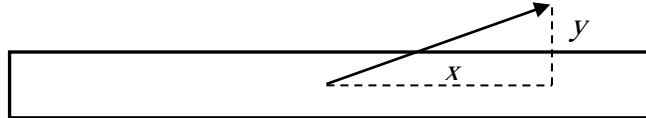


Figure 6-5. Top view of the wall

Table 6-3. Loading protocols

Type	Direction
Monotonic	I-O:1/0, I-O:4/1, I-O:2/1, I-O:1/1, I-O:1/2
	I-O:1/3, I-O:1/4, I-O:1/5, I-O:1/6, I-O:1/7
	I-O:1/8, I-O:1/9, I-O:1/10, I-O:1/12, I-O:1/20
Cyclic	I-O:1/30, I-O:1/40, I-O:1/50, I-O:0/1
	I-O:1/0, I-O:1/3, I-O:0/1

6.5 Numerical results

In this section the load-displacement curves and the deformed shapes of the wall are presented for different loading protocols. The results for the monotonic loading cases are presented first, and subsequently, the results for the cyclic loadings. In the load-displacement curves two specific points are in the point of interest; the maximum elastic load (yielding point) designated by point “A” and point “B” which correspond to the ultimate resisting load. Later the information of these two specific points is used to build the interaction curves.

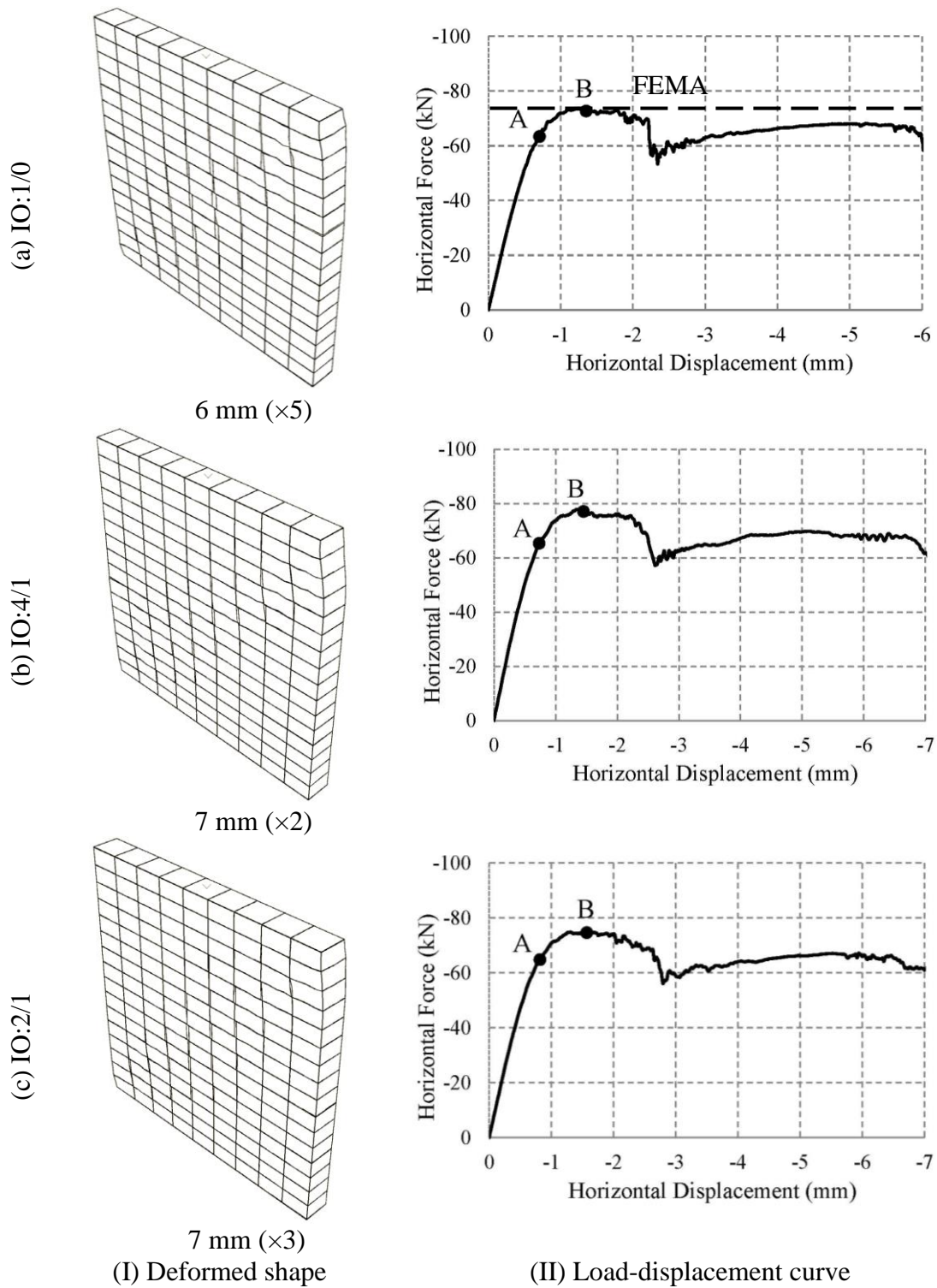


Figure 6-6. Deformed shape and load-displacement for IO: 1/0, IO:4/1 and IO:2/1

Figure 6-6 (a) shows the deformed shape of the wall after 6 mm in-plane deformation. As shown in this figure, diagonal crack is the predominant failure mode for this loading case. The ultimate capacity of the wall can also be validated using FEMA 356 proposed formulation (ENGINEERS 2000),

$$v_{me} = \frac{0.75 \left(v_{te} + \frac{P_{CE}}{A_n} \right)}{1.5} \quad (6-1)$$

where,

v_{me} = Expected shear strength

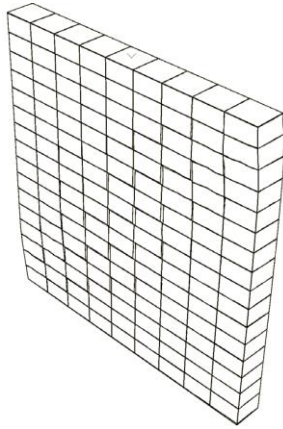
P_{CE} = Expected gravity compressive force applied to a wall

A_n = Area of net mortared/grouted section of a wall or pier

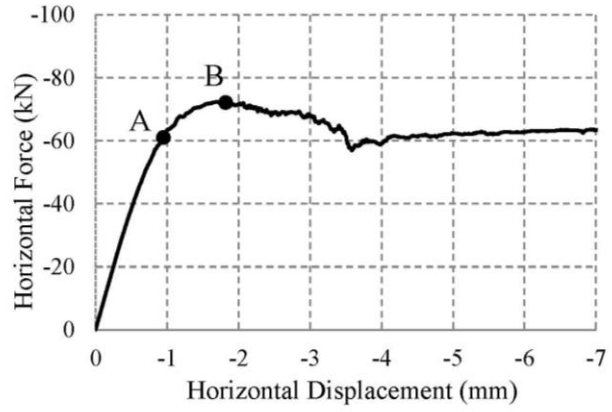
v_{te} = Average bed-joint shear strength

Using equation (6-1) the ultimate in-plane resisting load is 77.5 kN, which is very close to the numerical results presented in Figure 6-6 (a). Figure 6-6 (b) and Figure 6-6 (c) clearly show that, while the direction of the load is changing, no major change is taking place in the ultimate capacity of the wall. Initial stiffness is the only parameter which is evidently changing in model IO:4/1 and IO:2/1 and that is due to the participation of the OP deformation. It should be noted that, in contradiction to the results of model IO:1/0 and IO:0/1, in the rest of the models with participation of both IP and OP deformations, the direction of the load is not necessarily in the direction of the deformation, particularly in the nonlinear regime. This is due to the nonlinear response of the wall and is similar to the normality rule in the plasticity (Bathe 1995). Therefore, in the cases with participation of the IP and OP deformations, the absolute of the total force are presented. Later, the variation of the direction of the load is investigated for a specific wall (model IO:1/3).

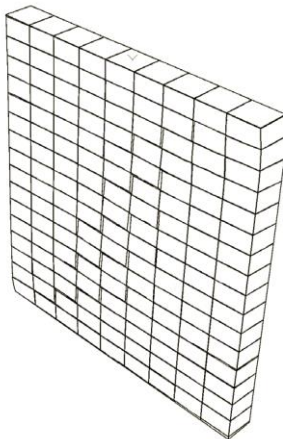
(a) IO:1/1



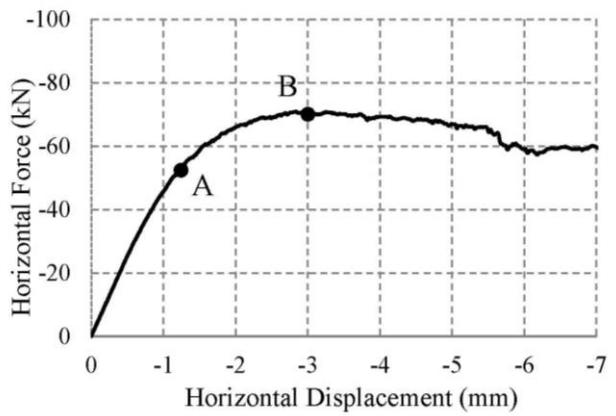
7 mm (×5)



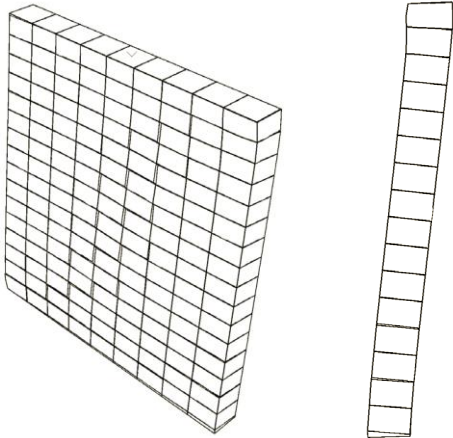
(b) IO:1/2



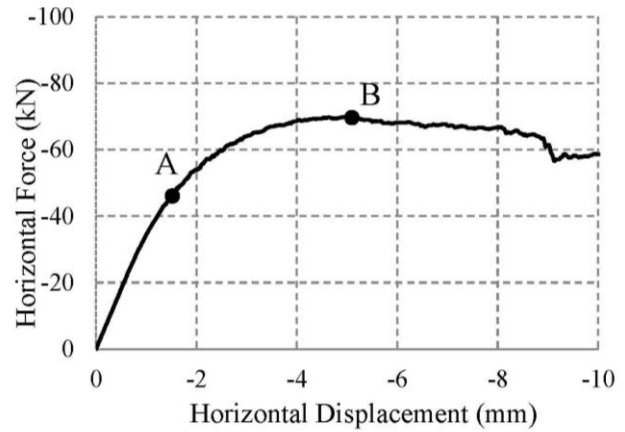
7 mm (×7)



(c) IO:1/3



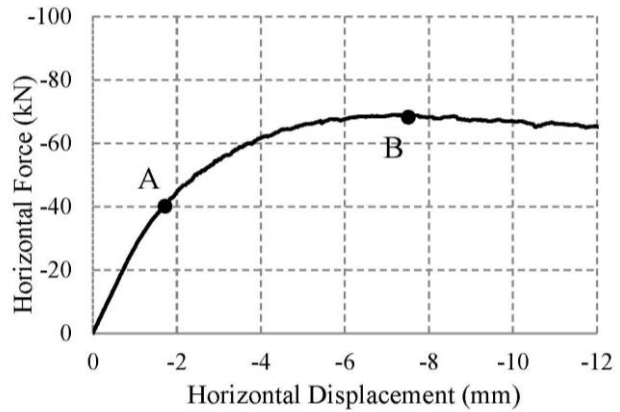
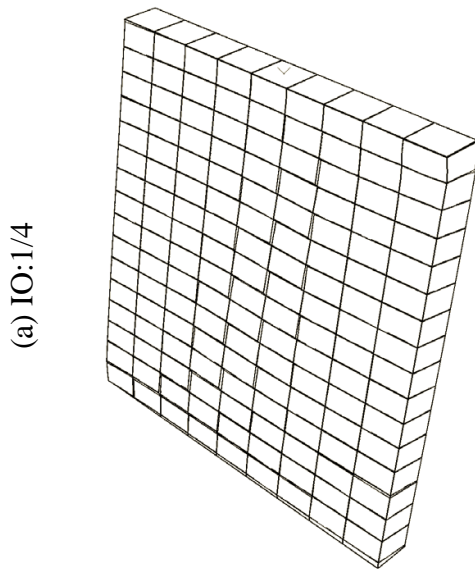
10 mm (×7)
(I) deformed shape



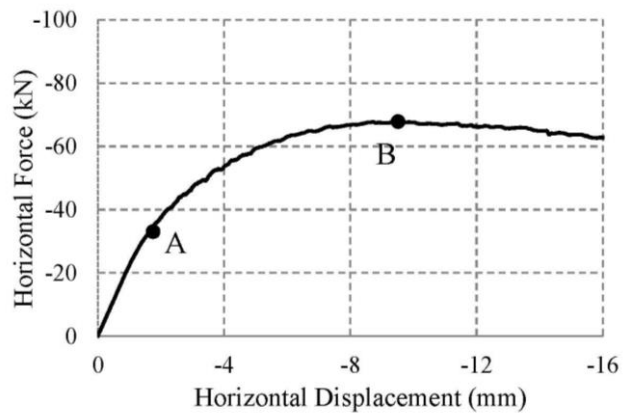
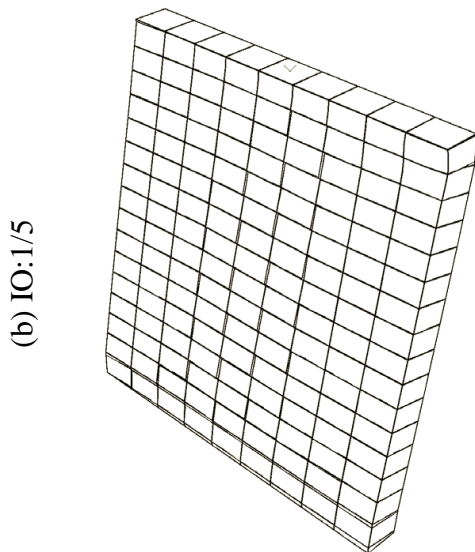
(II) Load-displacement curve

Figure 6-7. Deformed shape and load-displacement for IO: 1/1, IO:1/2 and IO:1/3

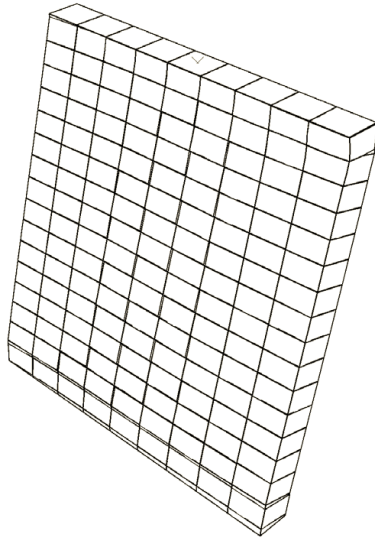
The participation of the in-plane and out-of-plane displacements are equal in the loading protocol of model IO:1/1. It is interesting to note that the ultimate capacity of this model is very close to the in-plane ultimate load depicted in Figure 6-6 (a). Along with increase of OP deformation in model IO:1/2 and IO:1/3, in addition to diagonal crack the top and bottom planes of the wall gradually start to separate from the support due to the out-of-plane deformation. Another side view has been presented in Figure 6-7(c) for model IO:1/3 to highlight the out-of-plane deformation.



12 mm (×7)

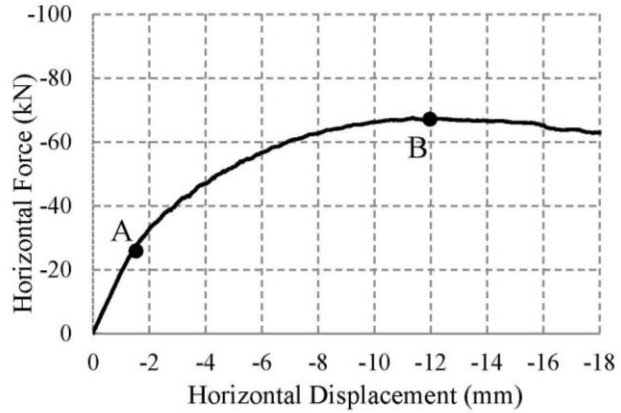


(c) IO:1/6



18 mm ($\times 7$)
(I) deformed shape

16 mm ($\times 7$)

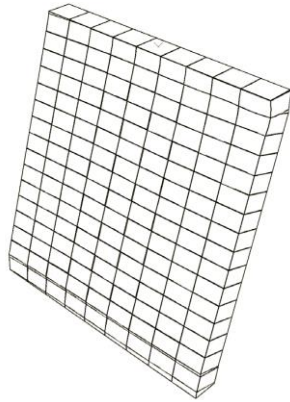


(II) Load-displacement curve

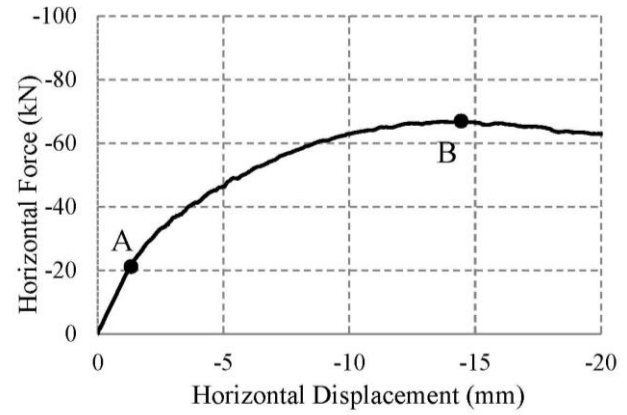
Figure 6-8. Deformed shape and load-displacement for IO: IO:1/4, IO:1/5 and IO:1/6

While the loading is changing from model IO:1/4 to model IO:1/6, the diagonal crack is gradually disappearing and separation of the bottom and top planes from the supports is dominating the failure mode. By examining the load-displacement curves, it is abundantly clear that the maximum elastic load (yielding point) and the ultimate resisting load are decreasing by increase of OP deformations; however, the respective deformations are increasing. For instance, in Figure 6-8 (c) point “A” has a lower force when compared to Figure 6-7 (a), and it is associated with a larger deformation.

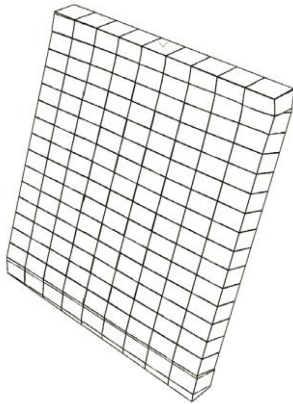
(a) IO:1/7



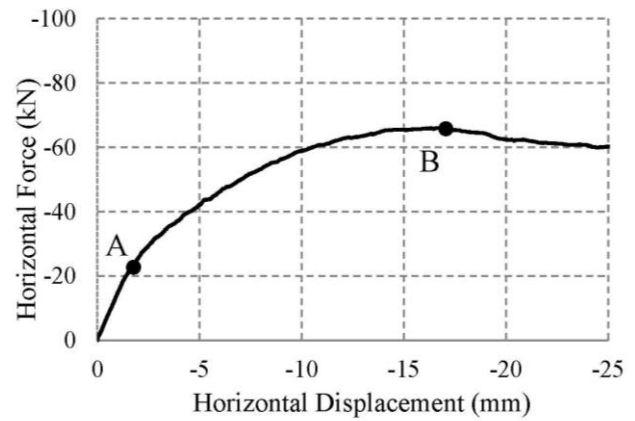
20 mm ($\times 7$)



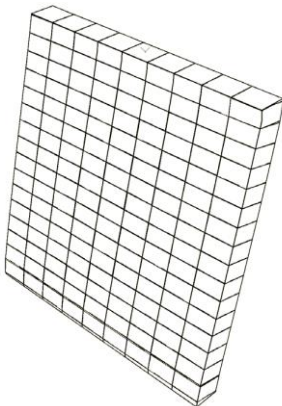
(b) IO:1/8



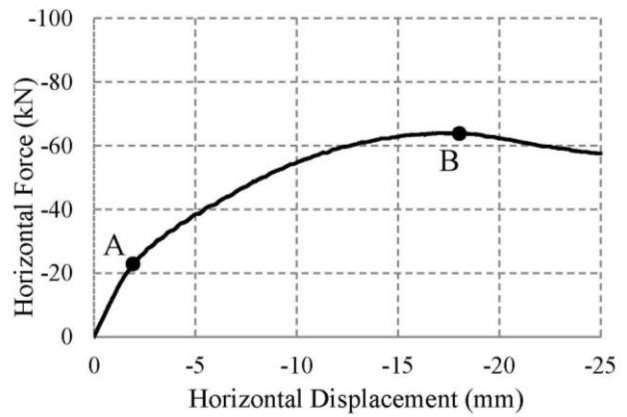
24 mm ($\times 7$)



(c) IO:1/9



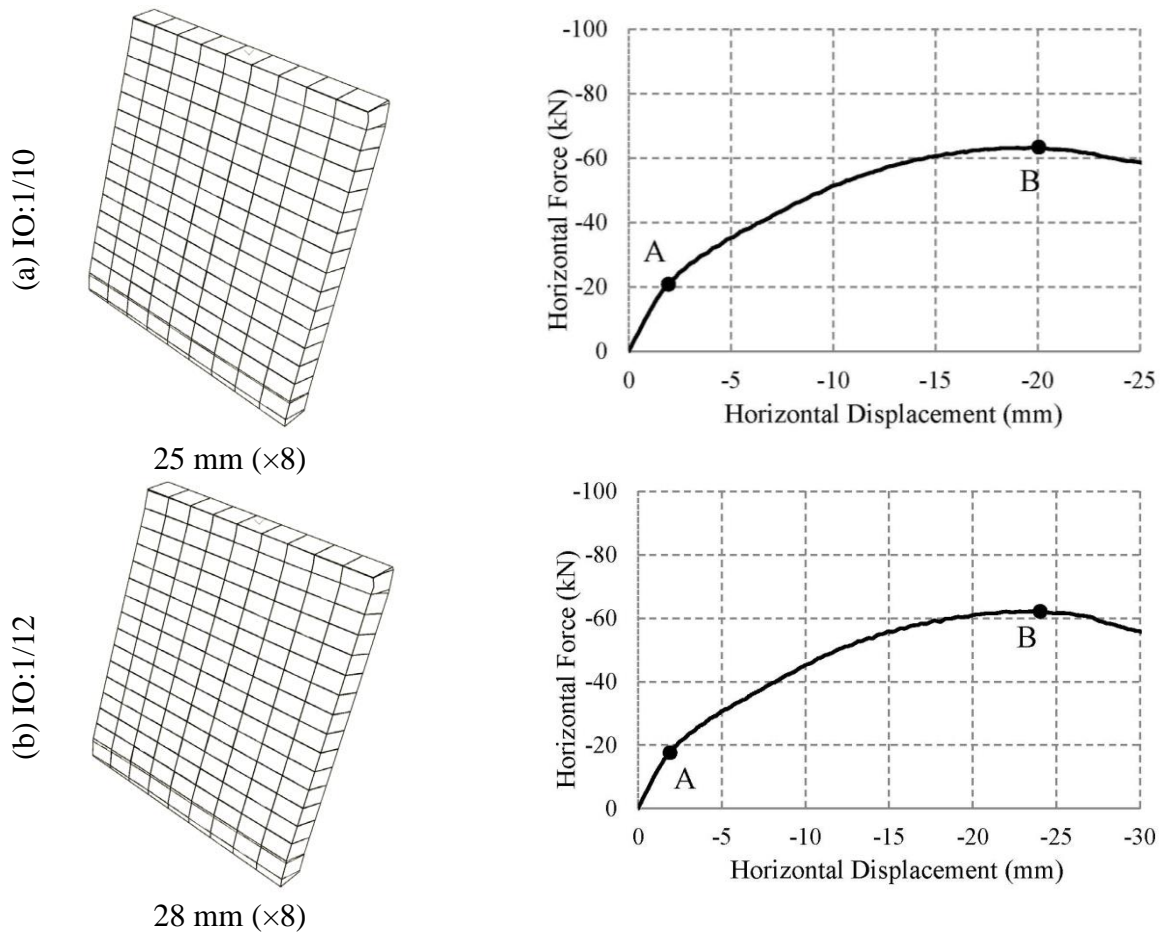
24 mm ($\times 8$)
(I) deformed shape



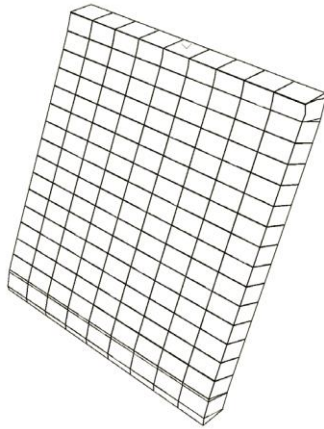
(II) Load-displacement curve

Figure 6-9. Deformed shape and load-displacement for IO:1/7, IO:1/8 and IO:1/9

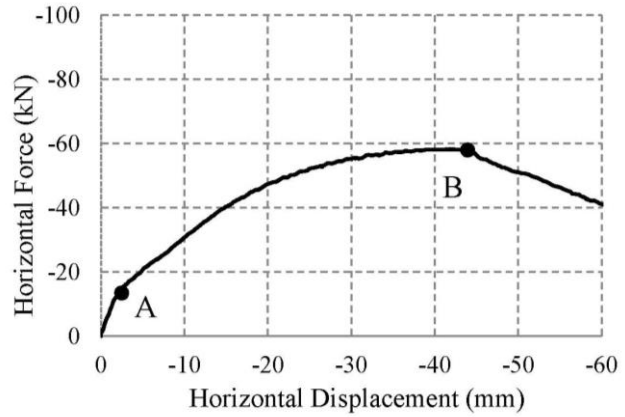
Participation of the OP deformation in model IO:1/7, IO:1/8 and IO:1/9 (Figure 6-9) is much higher than the IP deformation. In these models, by increase in the participation of OP deformation, the diagonal crack has almost disappeared. Therefore, it can be concluded that by increasing the participation of the out-of-plane displacement, the dominated failure mode in models IO:1/7 to IO:1/9 changes to separation of the bottom and top planes of the wall without any visible diagonal crack (Figure 6-9). The generated in-plane load of the wall is much more stiffer and stronger than the out-of-plane load, thereby even a low participation of the in-plane deformation has generated a large force in models IO:1/7, IO:1/8 and IO:1/9.



(c) IO:1/20



60 mm ($\times 5$)
(I) deformed shape

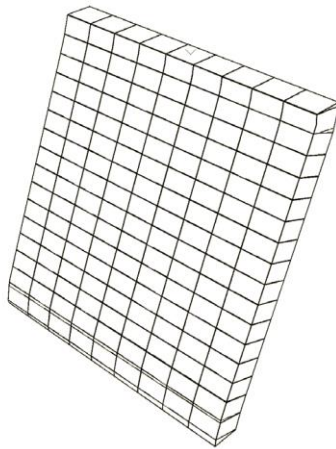


(II) Load-displacement curve

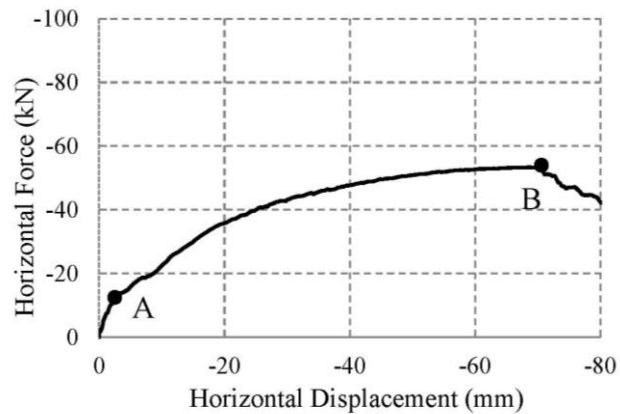
Figure 6-10. Deformed shape and load-displacement for IO:1/10, IO:1/12 and IO:1/20

As shown in Figure 6-10 models IO:1/10, IO:1/12 and IO:1/20 have no visible diagonal crack. In these models due to the low participation of the in-plane deformation, still the wall has a high ultimate capacity load.

(a) IO:1/30



80 mm ($\times 3$)



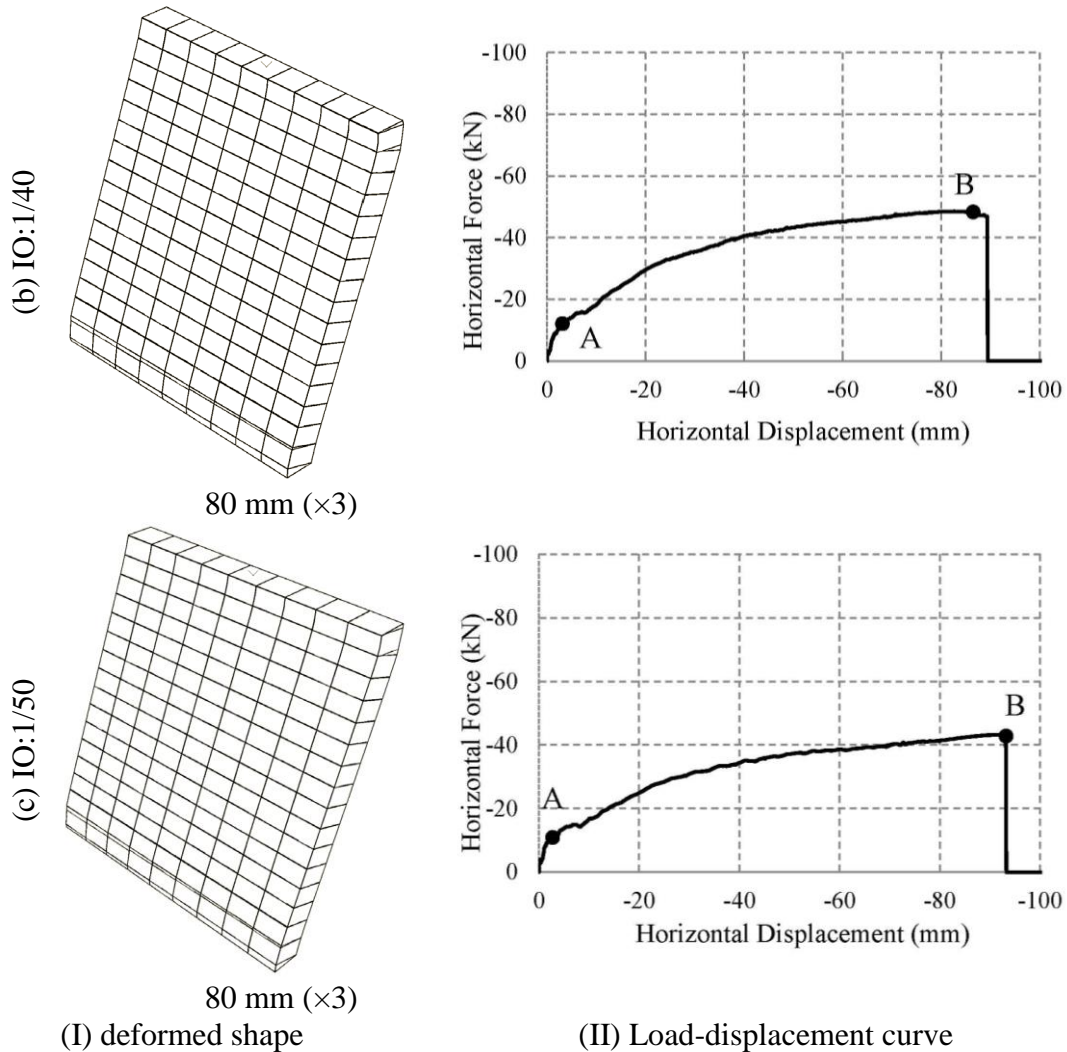
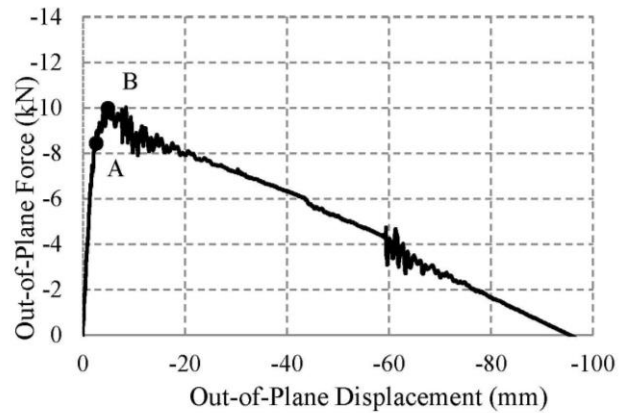
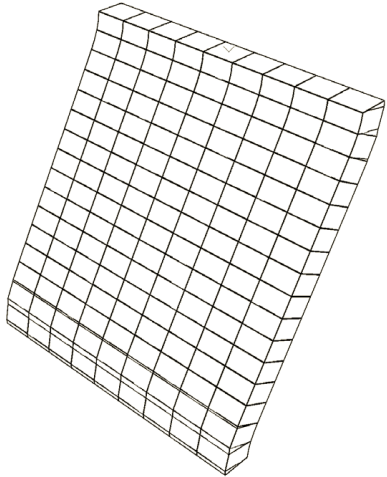


Figure 6-11. Deformed shape and load-displacement for IO:1/30, IO:1/40 and IO:1/50

Figure 6-11 (b) and (c) illustrate that, in models IO:1/40 and IO:1/50 before the load-displacement curve reaches the highest possible point and before initiation of the softening behavior, the wall loses its stability. In other words, although the in-plane force is still increasing, due to the large out-of-plane deformation the wall will be unstable.



IO:0/1 deformed shape at 85 mm ($\times 3$)

Figure 6-12. Bidirectional deformations of the wall

Figure 6-12 presents the out-of-plane force-displacement curve for model IO:0/1. In this model since no in-plane deformation has participated, the ultimate load capacity of the wall is significantly lower than the previous models. Figure 6-13 shows the same results, obtained from the fine mesh (see Figure 6-3 (c, d)). It can be concluded that the results for the fine and coarse meshes match and, consequently, the finite element model is not mesh sensitive. In the out-of-plane load-displacement curve obtained from coarse mesh, some vibrations took place at 60 mm deformation. The reason was attributed to the high velocity of the dynamic loading used for this model. Moreover, high stress concentration took place at 60 mm deformations, in the corners of the bricks, at bottom and top of the wall. These vibrations are almost omitted in the load-displacement curve using fine mesh, as shown in Figure 6-13.

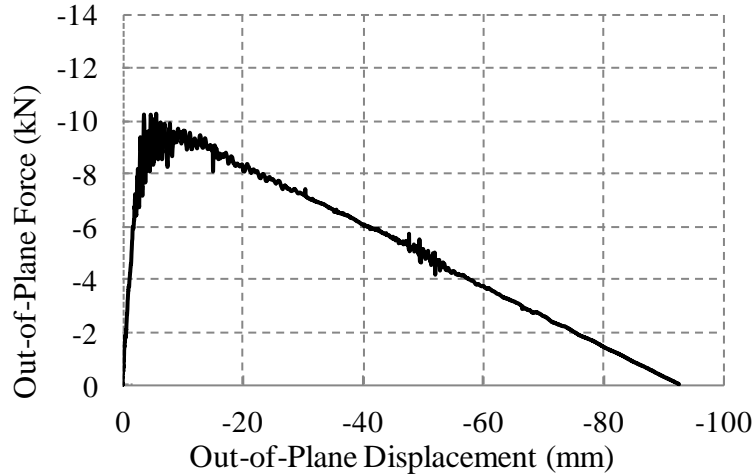


Figure 6-13. IO:0/1, using the fine mesh

To assess the mesh sensitivity issue for the bidirectional loadings, the load displacement curves of model IO:1/3 using the fine and course meshes are present in Figure 6-14. Since different loading rates are used for the fine and coarse meshes, a little discrepancy can be seen between the results. However, a good agreement exists between the results.

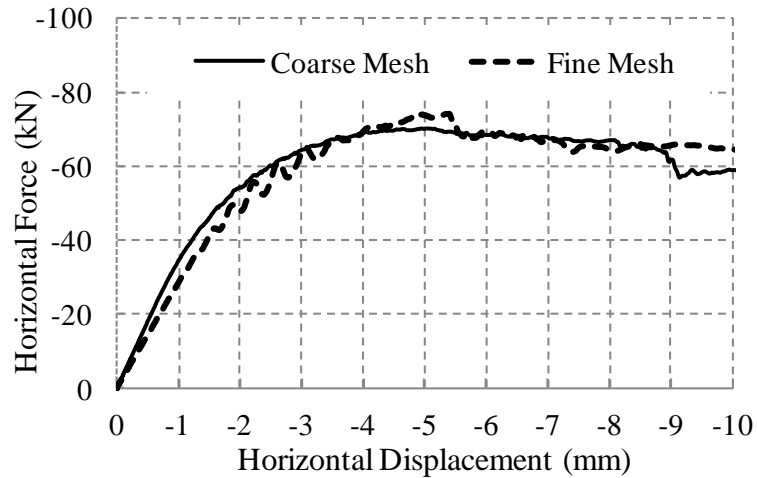


Figure 6-14. Load-displacement for fine and coarse mesh - IO:1/3 model

6.6 Cyclic loading

Three different directions are chosen to perform the cyclic loadings, including models IO:1/0, IO:1/3 and IO:0/1. To perform the in-plane cyclic loading, a varying velocity has been applied at the top plane of the wall to create the cyclic displacement-controlled loading of Figure 6-15.

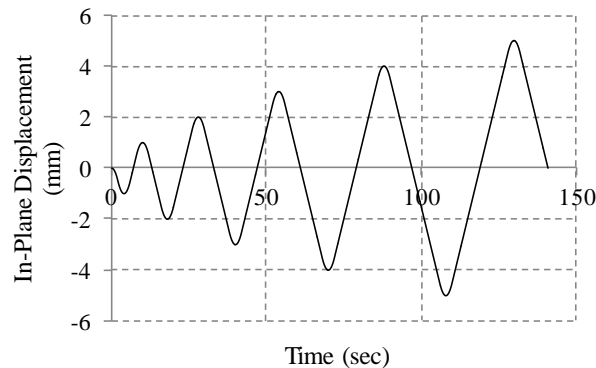


Figure 6-15. Displacement-time for the in-plane loading

Figure 6-16 shows the in-plane cyclic behavior of the masonry wall. As depicted in Figure 6-16, in the nonlinear regime frictional force is controlling the general behavior. Stiffness and strength degradation are evidently clear in this figure when the amplitude of the load increases.

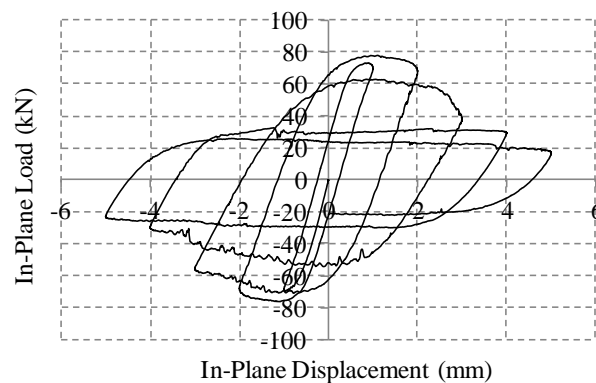


Figure 6-16. Load-Displacement for in-plane loading

The next cyclic loading has been performed in the out-of-plane direction as depicted in Figure 6-17. In this loading case due to the low aspect ratio of the wall in the OP direction, rocking is the dominant failure mechanism.

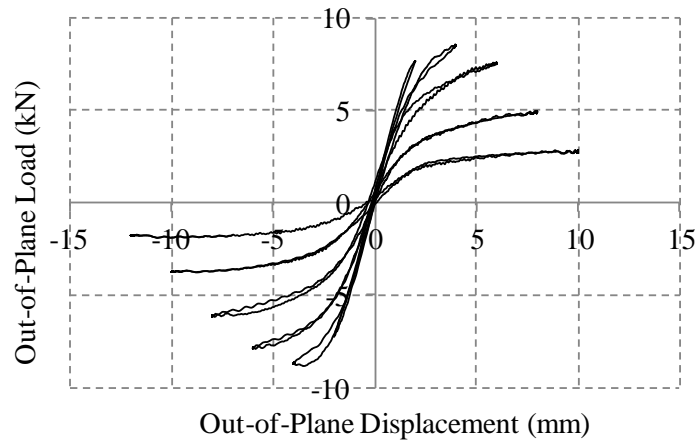


Figure 6-17. Load-Displacement for out-of-plane loading

A new direction between in-plane and out-of-plane directions (IO:1/3), which represents a loading angle of 71 degree, has been selected to investigate the variation of the cyclic behavior as the direction of the loading is changing from the in-plane to out-of-plane. Figure 6-18 demonstrates the cyclic displacement of the top plane of the wall in the selected direction versus time.

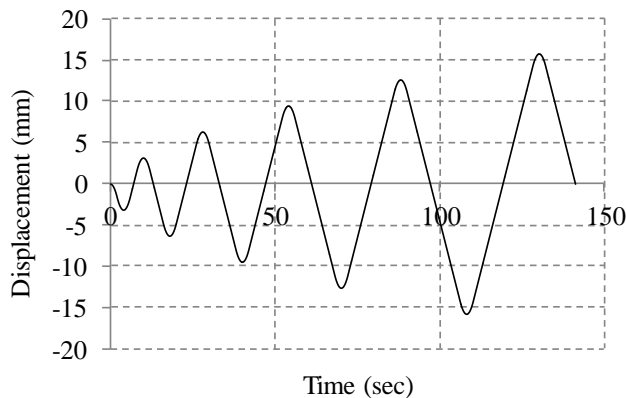


Figure 6-18. Total displacement-time for IO:1/3

As mentioned earlier, in the nonlinear regime the direction of the load is not necessary in the direction of displacement. Therefore, for this model the load displacement results are presented in different ways. Figure 6-19 (a) shows the in-plane force versus the in-plane displacement. The cyclic out-of-plane force versus the out-of-plane deformation is presented in Figure 6-19 (b).

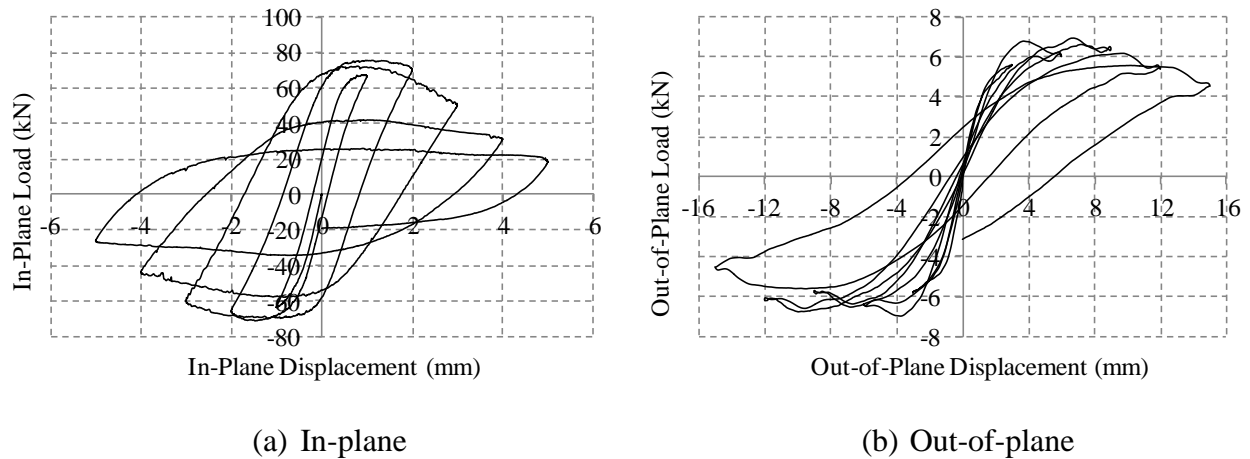


Figure 6-19. Load-displacement for IO:1/3 loading

By comparing Figure 6-19 (a) and Figure 6-19 (b), it is clear that the IP resisting force is significantly higher than the OP resisting force. Moreover, in comparison to IP cyclic mechanism, rocking is governing the OP resisting force. The magnitude of the total force versus time has been plotted in Figure 6-20, which shows the strength degradation of the wall for large deformation.

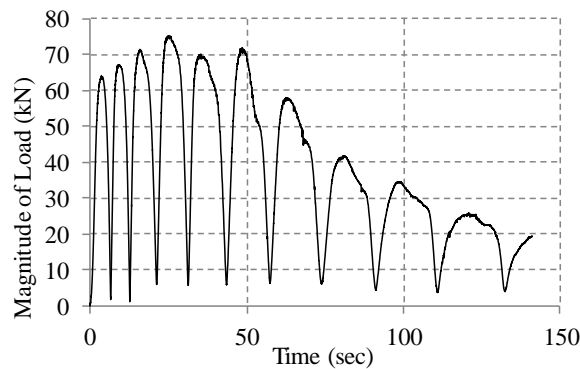


Figure 6-20. Load-time for IO:1/3

Figure 6-21 presents the same results of Figure 6-19, however, in a different form. In this figure, the load displacement curves are presented in the direction of the load (Figure 6-21 (a)) and perpendicular to the loading direction (Figure 6-21 (b)). As shown in Figure 6-21 (a), the behavior is a combination of the in-plane and the out-of-plane behaviors.

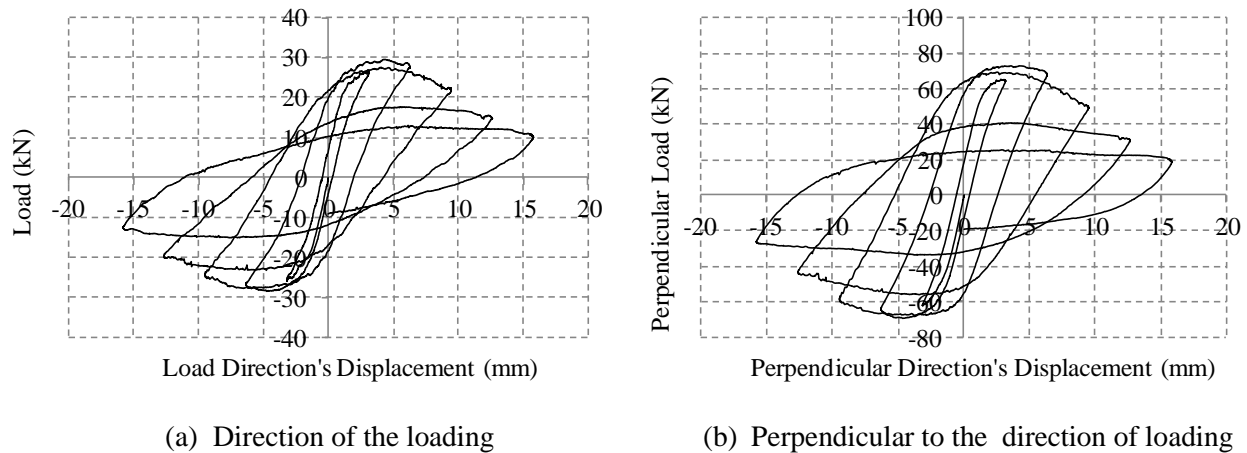


Figure 6-21. Load-Displacement curves for IO:1/3 model

6.7 Discussion of the results

In summary, by looking at the deformed shapes of the walls, it is clear that while the load is changing from model IO:1/0 (purely in-plane) to model IO:1/1 (45° with respect to in-plane direction), the diagonal crack is predominantly controlling the behavior or failure mechanism. Starting from model IO:1/2, in addition to diagonal cracking and due to the high out-of-plane deformation, some cracks have taken place at bottom and top planes of the wall. As the loading angle tends to “IO:0/1” (purely out-of-plane), gradually the diagonal crack disappears and the separation of the top and bottom planes of the wall from the supports controls the nonlinear behavior.

Table 6-4 summarizes the maximum elastic and the ultimate capacity of the walls in addition to respective deformations, using the information of points “A” and “B” in Figure 6-6 to

Figure 6-11. It is clear that, as the contribution of the out-of-plane displacement increases, the maximum elastic load (point A) decreases; however, the associated deformations gradually increase, especially for the models with a low contribution of out-of-plane displacement. The same conclusions are applicable for the ultimate load capacity (point B).

Table 6-4. Yield and ultimate loading points for different loadings

Direction	A (Displacement-mm)	A (Load - kN)	B (Displacement-mm)	B (Load - kN)
I-O-1/0	0.7	64	1.2	73
I-O-4/1	0.76	65	1.35	77
I-O-2/1	0.78	65	1.25	75
I-O-1/1	0.92	61	1.7	72
I-O-1/2	1.29	55	2.85	71
I-O-1/3	1.47	50	5	70
I-O-1/4	1.72	44	7.1	68
I-O-1/5	1.87	37	9.1	66
I-O-1/6	2	33	11.2	66
I-O-1/7	2	30	14	66
I-O-1/8	2	23	16	65
I-O-1/9	2	21	17	64
I-O-1/10	2	20	19	63
I-O-1/12	2	18	23	62
I-O-1/20	2	14	42	59
I-O-1/30	2	13	70	54
I-O-1/40	2	12	85	49
I-O-1/50	2	10	92	44
I-O-0/1	2	8.2	5	10

Figure 6-22 shows the response of the walls in the in-plane and out-of-plane load space. In this figure all the results are presented from the onset of the loading until the yielding point (point A). Since all the results are obtained using dynamic analysis with application of relatively high velocity at top plane of the wall, some nonlinearity can be seen within the results. The gross behavior up to the yielding point is linear.

A close examination of the results achieved in the numerical section reveals that the yielding point for the in-plane and out-of-plane loads are 8200 N and 64000 N, respectively . A

trend line shows that an elliptic shape connecting points (64000,0) and (0,8200) can be interpreted as the macro yield surface for this wall.

$$\text{Yield surface: } \left(\frac{P_{IP}}{P_{y-IP}} \right)^2 + \left(\frac{P_{OP}}{P_{y-OP}} \right)^2 = 1 \quad (6-2)$$

where P_{y-IP}, P_{y-OP} show the yielding load when the deformation is in the purely in-plane and out-of-plane directions, respectively.

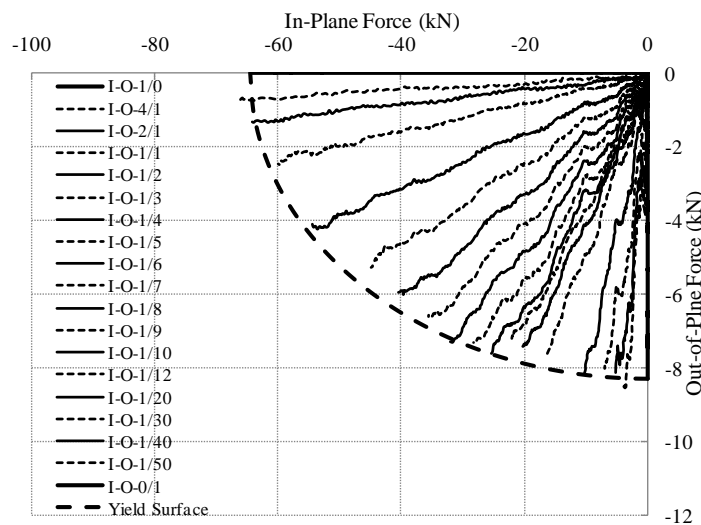


Figure 6-22. Proposed macro yield surface

The information of Table 6-4 is plotted in a polar coordinate presentation in Figure 6-23, to better investigate the maximum capacity of the wall in different load configuration. In Figure 6-23, the distance from the origin to the dashed line shows the magnitude of the applied load and the angle with x axis shows the direction of the applied load. In this figure, the solid line represents the elastic range (yield surface) and the dashed line corresponds to the ultimate load in the respective load direction. The most interesting point in this figure is that the dashed line has almost a circular shape. This explicitly means that the ultimate strength of the wall in every direction is similar to the resisting force in the IP direction (except for the pure out-of-plane

direction). Nevertheless, contrary to the out-of-plane loading, the ultimate strength of the in-plane loading is taking place in a much smaller deformation (almost one millimeter). Therefore, although the participation of the in-plane deformation in the cases similar to model “IO:1/30” is very low, the in-plane participation generates a large force. Note that in bidirectional load cases, the direction of the load does not remain constant, and in large deformations it changes toward the in-plane direction.

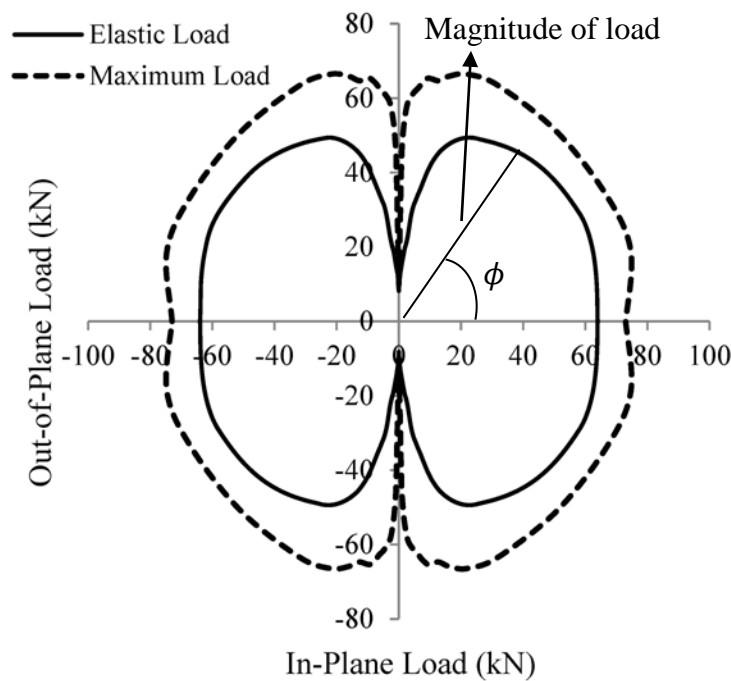


Figure 6-23. Maximum elastic and ultimate capacity of the wall

6.8 Conclusion

In this section, a set of 22 walls was subjected to different loading protocols, including monotonic and cyclic loadings. The main intent of this study is to explore different failure modes for various loading directions. It is shown that, for this specific unreinforced masonry wall under a compressive load of 120 kN, as the loading direction changes, the associated failure mode

changes as well; the diagonal crack is the respective failure mode for the in-plane loading and it gradually changes to rocking mode for the out-of-plane loading. For any loading direction between the in-plane and out-of-plane directions, the failure mode will be a combination of diagonal crack and rocking modes. A macro yield surface was presented that shows the maximum elastic capacity of the wall in bidirectional deformations. Furthermore, the ultimate load capacity of the wall is depicted in a polar coordinate. It is shown that, except for the pure out-of-plane loading (and angles close to the OP), the ultimate capacity of the wall for the bidirectional loadings would be almost similar to the in-plane ultimate capacity, however in a much larger deformation for the walls with higher participation of OP deformations. In bidirectional loading cases, direction of the load changes toward the IP direction for large deformation, if direction of the imposed displacement is constrained.

SECTION 7

ANALYTICAL PROCEDURES OF IN-PLANE AND OUT-OF-PLANE INTERACTION FOR UNREINFORCED MASONRY WALLS

7.1 *Introduction*

In this section interaction curves for bidirectional loadings imparted on unreinforced masonry walls (URM) with different aspect ratios are developed. Interaction curves are generated considering various possible failure modes for bricks and mortar-including tensile, crushing and a combination of shear and compression/tension failures. Two parameters are repeatedly changed to derive the interaction curves for any wall with particular dimensions, which include compressive traction atop the wall that represents the gravity loading, and the loading angle that represents various stimulus such as earthquake or wind. The derived interaction curves show the initiation of the failure in the wall as the compressive traction and loading angle change. Moreover, to aid in understanding the effects of various parameters on the derived interaction curves, several examples are presented with different aspect ratios. Finally for a specific case, the derived interaction curve is compared with the nonlinear finite element results obtained by author in section 5. The aim of producing the interaction curves is to ultimately help engineers in design and simplified analysis procedures of masonry buildings. This section is organized in four major sections. In the first section, a general description of the model is presented, including the boundary conditions and applied forces. The second section describes the distribution of stresses in the wall based on the applied forces and imposed boundary conditions followed by the third section that describes the possible failure modes for different components of URM walls.

Finally, in the fourth section, and by using a MATLAB code, interaction curves are generated for a set of walls with varying aspect ratios.

7.2 Geometry and boundary conditions

A rectangular wall with a thickness, width and height of t , a and h , respectively, has been considered to generate the interaction curves in this section (Figure 7-1). The wall is completely constrained at the bottom plane. All rotational degrees of freedom are restrained for the top plane; however, the top plane is not restrained in the vertical direction. The wall is under a compressive traction (q), and simultaneously under an in-plane (IP) and out-of-plane (OP) forces, p_I and p_O as depicted in Figure 7-1.

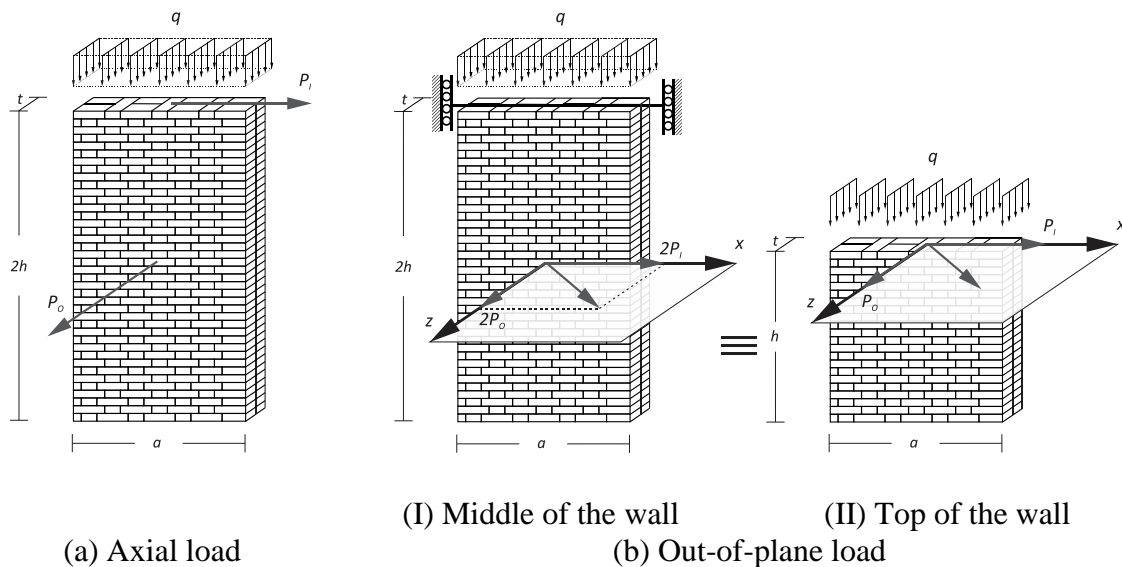


Figure 7-1. A URM shear wall under bidirectional loading

Based on the boundary conditions of a wall in a building and based on the connection details between adjacent walls, two different positions could mostly be considered for the out-of-plane degree-of-freedom. One could be considered at the middle of the wall (Figure 7-1 (a)) and the other at the top of the wall (Figure 7-1 (b)). In this study, the concentration will follow the latter configuration (see Figure 7-1 (b)). However, by comparing the distribution of the moment

diagram, the obtained interaction curves could be easily converted to represent the former configuration depicted in Figure 7-1 (a).

7.3 Distribution of stresses

In order to consider the issue of stress distribution and clarify the problem, first we consider an out-of-plane loading. Following this brief discussion, the results are then extended to the bidirectional loading.

7.3.1 Out-of-plane loading

According to the described boundary conditions, a URM wall can be considered as a fixed-fixed beam with a load at the mid-height. By considering symmetry, half of the geometry and load are considered to investigate the problem as shown in Figure 7-2.

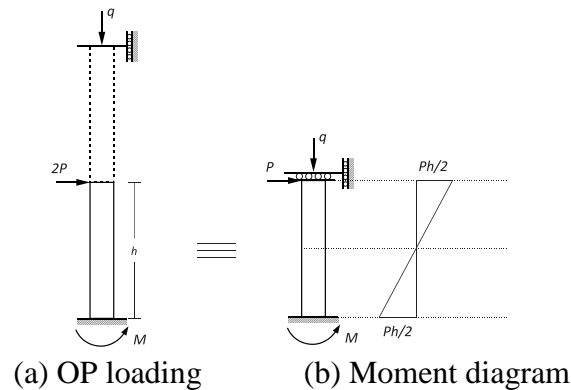


Figure 7-2. (a) Out-of-plane loading of URM shear walls (b) Moment diagram

According to Figure 7-2, the maximum moment will take place at the supports. Equation (7-1) shows the distribution of the compressive/tensile stress at the face of supports.

$$\sigma_{yy}(z) = \frac{6 h P_0}{a t^3} z + q \quad (7-1)$$

where z is the displacement from the middle of the wall and other parameters appearing in equation (7-1) are defined in Figure 7-1. The variation of shear stress within the thickness of the wall can be easily represented by equation (7-2).

$$\tau_{yz}(z) = \frac{P_o}{t a} \left(\frac{3}{2} - \frac{6}{t^2} z^2 \right) \quad (7-2)$$

The same formulation can be used for the in-plane direction and in a similar fashion.

7.3.2 Bidirectional loading

In the case of bidirectional loading, the direction of compressive/tensile stresses caused by the IP and OP loadings are in the same direction (y direction). Equation (7-3) shows the distribution of the resultant compressive/tensile stress due to bidirectional loading. Note that, in this section the concentration is on the stress distribution and not the deformation of the wall.

$$\sigma_{yy}(x, z) = \frac{6 h P \cos\theta}{t a^3} x + \frac{6 h P \sin\theta}{a t^3} z + q \quad (7-3)$$

where x and z represent the distance to the center of the wall, and the rest of parameters appearing in equation (7-3) are introduced in Figure 7-1. Similar to IP and OP loadings, the corners of supports have the highest value of compressive/tensile stress in the bidirectional loadings.

The resultant shear stresses due to IP and OP forces are perpendicular to each other. The total shear force will be derived by integrating the perpendicular shear stresses. Equation (7-4) shows the variation of shear stress in a plane parallel to the supports,

$$\tau(x, z) = \sqrt{\tau_{yx}(x)^2 + \tau_{yz}(z)^2} = \sqrt{\frac{P^2 \cos^2 \theta}{t^2 a^2} \left(\frac{3}{2} - \frac{6}{a^2} x^2 \right)^2 + \frac{P^2 \sin^2 \theta}{t^2 a^2} \left(\frac{3}{2} - \frac{6}{t^2} z^2 \right)^2} \quad (7-4)$$

Therefore, the stress tensor for a brick element can be written as,

$$\sigma_{ij} = \begin{bmatrix} \sigma_{xx} & \tau_{xy} & \tau_{xz} \\ \tau_{yx} & \sigma_{yy} & \tau_{yz} \\ \tau_{zx} & \tau_{zy} & \sigma_{zz} \end{bmatrix} = \begin{bmatrix} 0 & \tau_{xy} & 0 \\ \tau_{yx} & \sigma_{yy} & \tau_{yz} \\ 0 & \tau_{zy} & 0 \end{bmatrix} \quad (7-5)$$

In many finite element analyses of masonry structures, mortar has been represented by the interface elements (Lourenco 1996; Oliveira and Lourenco 2004; Oliveira and Lourenco 2004). For this type of elements the traction vector has two components, including normal traction (compressive or tensile) and shear traction,

$$\left(\sigma_{yy}, \sqrt{\tau_{yx}^2 + \tau_{yz}^2} \right) \quad (7-6)$$

Figure 7-3 shows the components of stress tensor described in Equations (7-3)-(7-6) for the brick and mortar elements.

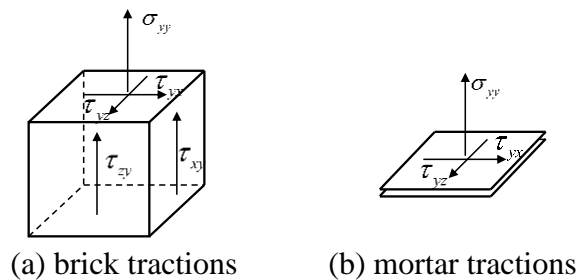


Figure 7-3. State of stress for brick and mortar

7.4 Possible failure modes for masonry walls

In this section, failure modes for bricks and mortar have been described. Based on the applied forces on a wall, the onset of failure can be in either bricks or mortar. In order to derive the interaction curves, at each stage and based on the existing compressive traction and loading angle, the relevant failure forces for bricks and mortar are calculated and the predominant failure mode will follow either one, particularly the controlling one.

7.4.1 Failure modes for mortar

Two distinct failure modes are considered for mortar—namely, tension and shear/tension regimes (Figure 7-4). This model has been validated in many experimental investigations (Pluijm 1992; Pluijm 1993) and has been used in finite element modeling of masonry structures (Lourenco 1996; Oliveira and Lourenco 2004).

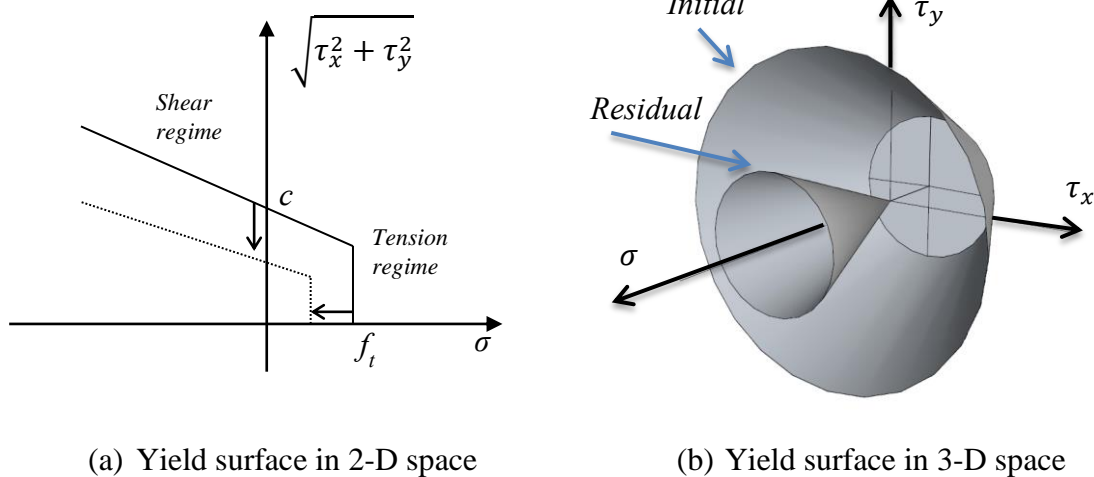


Figure 7-4. Yield surface for the joints

In the following sections, first the interaction curve for a wall with an out-of-plane loading is described, considering tensile and shear failure of mortar as the only source of failure. Due to the simplicity of the problem for the OP loading in comparison to the bidirectional case, the interaction curve for OP loading is parametrically described in terms of geometry and material properties of the wall. Afterward, the description will be generalized to bidirectional loadings.

7.4.1.1 Out-of-plane loading

(a) Tensile mode

Following the work of Pluijm (Pluijm 1992; Pluijm 1993), the yield function in the tension mode is (tension cutoff) (Pluijm 1992),

$$f_1(\sigma, \kappa_1) = \sigma_{yy} - f_t \quad (7-7)$$

where f_t is the tensile strength of the brick-mortar interface. Based on equation (7-1) and (7-3) the most vulnerable point is located at the corner of the supports, which will cause the mortar to separate from the supports. In order to calculate the failure force, the tensile stress due to this moment should be compared with the maximum tensile capacity of the mortar.

$$\frac{M}{S} - q = f_t \Rightarrow \frac{\frac{2 P_o 2h}{8}}{\frac{a t^2}{6}} - q = f_t \Rightarrow P_o = \frac{(f_t + q) a t^2}{3 h} \quad (7-8)$$

According to equation (7-8), as the compressive traction increases, the failure load increases linearly. However, for high compressive traction the failure mode will be dominated by the failure in bricks. As a simple case, herein, crushing by compressive stress can be considered as the only possible failure mode for bricks. Thus, the opposite side in the corner would be the most vulnerable point for bricks.

$$\frac{M}{S} + q = f_{ce} \Rightarrow \frac{\frac{2 P_o 2h}{8}}{\frac{a t^2}{6}} + q = f_{ce} \Rightarrow P_o = \frac{(f_{ce} - q) a t^2}{3 h} \quad (7-9)$$

where f_{ce} shows the maximum compressive capacity of bricks before crushing. The out-of-plane capacity of the wall for $q = 0$ (no compressive traction) and based on the tensile failure would be,

$$P_o = \frac{1}{3} \frac{a t^2}{h} f_t \quad (7-10)$$

For $q = f_{ce}$ the wall would have no capacity for any OP loading,

$$P_o = 0$$

Based on equations (7-8) and (7-9) and considering tensile failure, P_o increases as q increases, however, for compression failure P_o decreases as q increases (Figure 7-5). Thus,

$$q_0 = \frac{f_{ce} - f_t}{2} \quad (7-11)$$

where q_0 shows the compressive traction which the mode of failure changes from tensile to crushing failure (Figure 7-5).

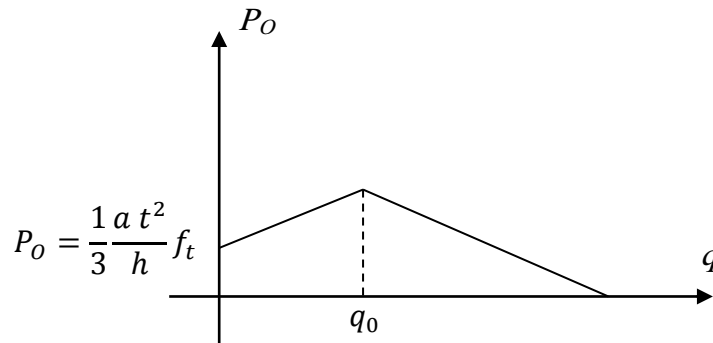


Figure 7-5. Interaction between tensile and compressive failure for OP loading

(b) *Shear/tension regime*

In the shear/tension dominated mode, the yield function is given by Pluijm (Pluijm 1993) as follows,

$$f_2(\sigma, \kappa_2) = \sqrt{\tau_{yx}^2 + \tau_{yz}^2} + \sigma \tan\phi - c \quad (7-12)$$

where c is the cohesion of the brick-mortar interface and ϕ is the friction angle. According to equation (7-12) and by considering $\tan\phi = 0.75$ as a typical value, the shear strength at the support faces will be,

$$F_s(z) = c - 0.75 \left(\frac{6 h P_o}{a t^3} z - q \right) \quad (7-13)$$

By comparing equations (7-13) and (7-2), the failure force obtained by shear failure can be calculated,

$$c - 0.75 \left(\frac{6 h P_o}{a t^3} z - q \right) \geq \frac{P_o}{t a} \left(\frac{3}{2} - \frac{6}{t^2} z^2 \right) \quad (7-14)$$

$$P_o = \frac{(c + 0.75 q)}{\left(\frac{4.5 h}{a t^3} z + \frac{3}{2} \frac{1}{t a} - \frac{6}{a t^3} z^2 \right)} \quad (7-15)$$

Equation (7-15) should be minimized in respect to "z" in order to find the lowest load which causes the shear failure. Therefore, the expression in the denominator gets it highest value at $z_{opt.} = 0.375 h$. The optimal value of z is constrained to the boundary conditions below,

$$-\frac{t}{2} \leq z_{opt.} \leq \frac{t}{2}$$

For $0.375 h < \frac{t}{2}$, by substituting the $z_{opt.}$ in equation (7-15) we get the following value for P_o ,

$$P_o = \frac{(c + 0.75 q)}{\left(\frac{0.844 h^2}{a t^3} + \frac{3}{2} \frac{1}{t a} \right)} \quad (7-16)$$

Equation (7-16) shows that as the compressive traction increases the shear failure force increases linearly. Figure 7-6 displays the interaction between shear and compression failures.

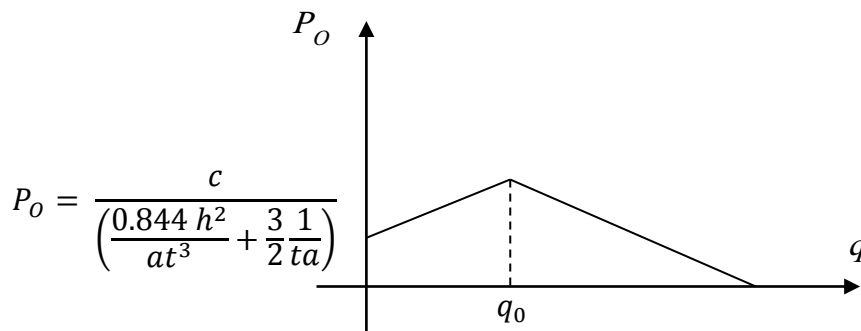


Figure 7-6. Interaction curve for shear-compression

7.4.1.2 Bidirectional loadings

The formulations of bidirectional loading are more difficult than OP loading, and parametric study in this case is difficult. Most of the descriptions about the variation of the behavior for this case will be presented in the numerical examples.

(a) Failure in tension

By comparing equation (7-3) and (7-7), tensile failure force for bidirectional loading can be calculated as,

$$\frac{6hP \cos\theta}{ta^3}x + \frac{6hP \sin\theta}{at^3}z - q \leq f_t \quad (7-17 \text{ (a)})$$

For $x = \frac{a}{2}$, $z = \frac{t}{2}$,

$$\frac{3hP \cos\theta}{ta^2} + \frac{3hP \sin\theta}{at^2} - q \leq f_t \quad (7-17 \text{ (b)})$$

Figure 7-7 shows the interaction curve for a URM wall with a constant compressive traction, while the direction of load changes from IP to OP. In this case, the tensile failure is considered to be the only source of failure.

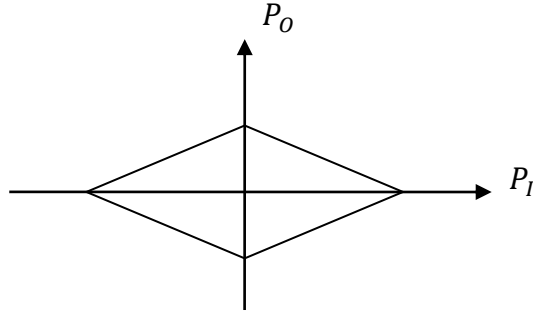


Figure 7-7. Interaction curve governed by tensile failure

(b) *Shear/tension failure*

According to equation (7-12), the shear strength at the support faces will be ($\tan\phi = 0.75$),

$$F_s(x, z) = c - 0.75 \left(\frac{6hP\cos\theta}{ta^3}x + \frac{6hP\sin\theta}{at^3}z - q \right) \quad (7-18)$$

Comparing equation (7-18) to equation (7-4), the failure force under shear stress can be calculated by,

$$\begin{aligned} c - 0.75 \left(\frac{6hP\cos\theta}{ta^3}x + \frac{6hP\sin\theta}{at^3}z - q \right) \\ = \sqrt{\frac{P^2 \cos^2 \theta}{t^2 a^2} \left(\frac{3}{2} - \frac{6}{a^2} x^2 \right)^2 + \frac{P^2 \sin^2 \theta}{t^2 a^2} \left(\frac{3}{2} - \frac{6}{t^2} z^2 \right)^2} \end{aligned} \quad (7-19)$$

Therefore, the failure force will be,

$$P = \frac{f_s + 0.75q}{W} \quad (7-20)$$

where,

$$W = \left(\sqrt{\frac{\cos^2 \theta}{t^2 a^2} \left(\frac{3}{2} - \frac{6}{a^2} x^2 \right)^2 + \frac{\sin^2 \theta}{t^2 a^2} \left(\frac{3}{2} - \frac{6}{t^2} z^2 \right)^2} + 0.75 \left(\frac{6 h \cos \theta}{t a^3} x + \frac{6 h \sin \theta}{a t^3} z \right) \right) \quad (7-21)$$

To find the shear failure force, the value of x and z should be calculated in a way that maximize the value of W . In the code written for this section a numerical minimization has been performed to derive the shear failure force for interaction curves.

7.4.2 Failure mode for the bricks

Different yield surfaces are presented for brittle materials such as brick and concrete. For representing interaction curves in this study, the yield surface introduced by Lubrilier et al. (1989) and extended by Lee and Fenves (Lee and Fenves 1998) has been utilized. This yield surface also has been used in ABAQUS (2005). The yield function reads,

$$\bar{F} = \frac{1}{1 - \alpha} (\alpha I_1 + \sqrt{3} J_2 + \beta \langle \sigma_{max} \rangle) - f_{cv} \quad (7-22)$$

where, f_{cv} is the compressive strength of the material, $\langle \sigma_{max} \rangle$ is the maximum positive principal effective stress, and α, β are dimensionless constants (equations (7-25), (7-26)).

$$I_1 = tr(\sigma) \quad (7-23)$$

$$J_2 = \frac{1}{2} s:s \quad (7-24)$$

$$\alpha = \frac{f_{bv} - f_{cv}}{2f_{bv} - f_{cv}} \quad (7-25)$$

f_{bv} is the ratio of initial equibiaxial compressive yield stress to initial uniaxial compressive yield stress (the default value is 1.16).

$$\beta = \frac{f_{cv}}{f_{bv}}(\alpha - 1) - (\alpha + 1) \quad (7-26)$$

where σ (in equation (7-23)) represents the principles stresses. Based on the state of stresses presented in equation (7-5), the principle stresses would be,

$$\begin{aligned} \sigma_1 &= 0 \\ \sigma_2 &= \frac{\sigma_{yy}}{2} - \frac{1}{2} \sqrt{4(\tau_{xy}^2 + \tau_{yz}^2) + \sigma_{yy}^2} \\ \sigma_3 &= \frac{\sigma_{yy}}{2} + \frac{1}{2} \sqrt{4(\tau_{xy}^2 + \tau_{yz}^2) + \sigma_{yy}^2} \end{aligned} \quad (7-27)$$

A plane cross section of the yield surface in the principal stress space is shown in Figure 7-8.

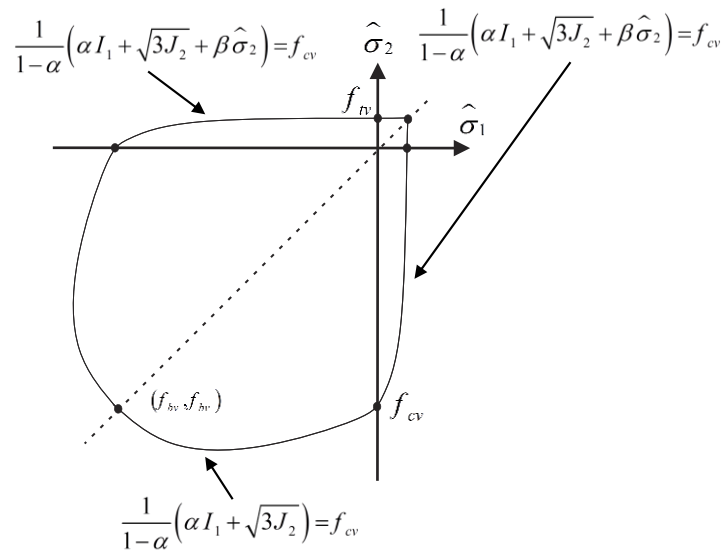


Figure 7-8. Lubliner's yield function in plane stress space (Abaqus 2005)

In equation (7-22), the failure force is implicitly involved in the equation. Numerical minimization in respect to “x” and “z” should be performed to find the failure force in the bricks.

7.5 Implementation in a MATLAB code

To generate the interaction curves for a particular wall, failure forces should be calculated based on the existing compressive traction and loading angle. A MATLAB code is intended to perform the analysis (see appendix A). As shown in Figure 7-9, the resultant forces of each failure mode — mortar failure (tensile-shear/tensile) and brick failure — should be compared to each other. The minimum force will be the failure force for that particular compressive traction and loading angle. As described earlier, in each step numerical minimization is performed to find the location of the failure in the wall and the respective failure force.

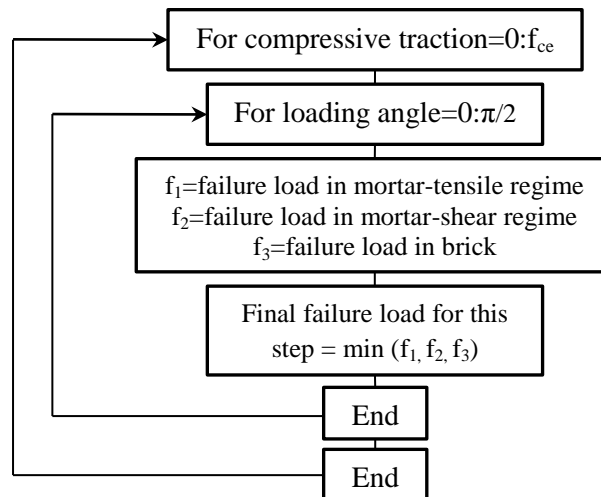


Figure 7-9. Algorithm for the MATLAB code

7.6 Examples

To clarify the possible interaction curves, based on the described failure mechanisms, three different examples are presented in this part of the section designated as, regular, wide, and short walls with aspect ratios of (h/a) of 1, 1/8, 1/10, respectively. Different aspect ratios have been selected to activate different possible failure modes to illustrate the derivations described in the previous sections.

7.6.1 Example I – regular/square wall

This example explores the interaction curve for a regular wall with the following dimensions,

$h=1000$; $a=1000$; $t=100$, which represents a regular wall with aspect ratio (h/a) of 1.0.

The material properties below have been considered for the wall.

$c=0.35$; $f_t=0.25$; $f_{ce}=3.5$; $\tan\phi = 0.75$

Figure 7-10 shows the variation of the bidirectional load while the compressive traction and loading angle change. This figure indicates a sharp drop as the loading angle changes from in-plane to out-of-plane direction. This drop starts with a sharp slope in the beginning and has lower slope for greater values of the loading angle. Figure 7-10 also clearly indicates that for various loading angles, by increasing the compressive traction, initially the bidirectional loading increases, subsequently, in a specific compressive traction (which is identical for different loading angles) the capacity of the wall starts to decline until reaching zero i.e., total loss of elastic capacity.

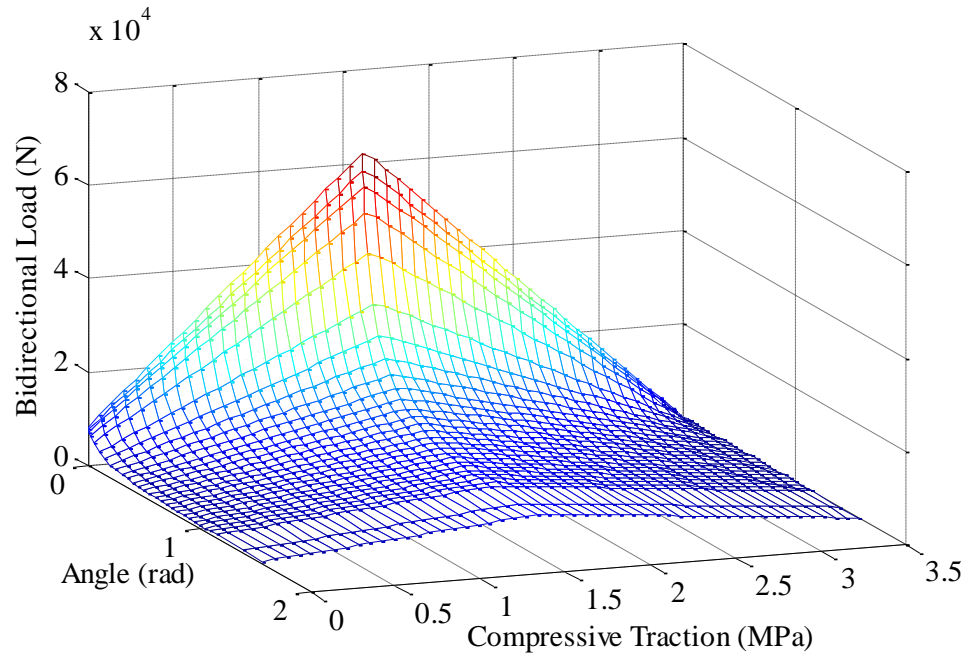


Figure 7-10. Variation of bidirectional load as angle and compressive traction change

Figure 7-11 investigates the variation of in-plane and out-of-plane loads while the compressive tractions change. In this particular example tensile and compressive failures are governing the general behavior of the wall, with no apparent contribution of shear failure. Thus, the interaction curve is composed of two planes that intersect each other as shown in Figure 7-11. This figure indicates that in the absence of compressive traction the wall has a low strength, and, for the maximum value of the compressive traction (f_{ce}) the interaction curve has a zero value (i.e. no more elastic capacity)

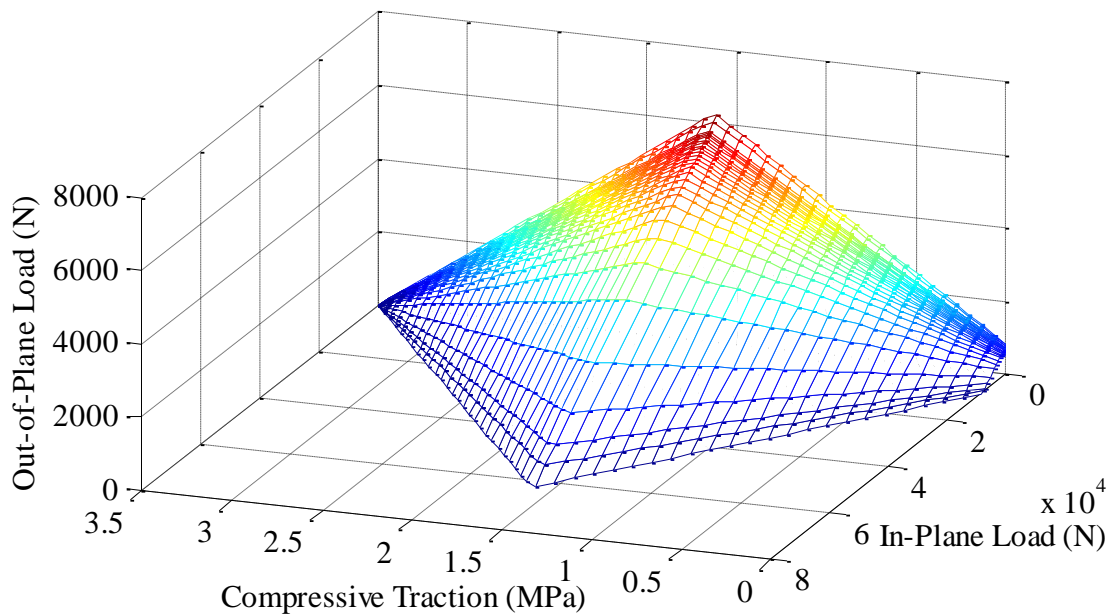


Figure 7-11. Interaction curve

To further clarify Figure 7-11, several cross sections are presented in Figure 7-12 that represent slicing the interaction surface at various compressive traction levels. Figure 7-12 clearly demonstrates that, initially, while compressive traction increases the interaction curve expands (Figure 7-12 (a)). However, it starts to shrink after a specific compressive traction that exists at the intersection of two planes (Figure 7-12 (b)). For this particular wall, since tensile and compressive failures are exclusively controlling the interaction curve, the final interaction curve is composed of a set of rhomboidal shapes.

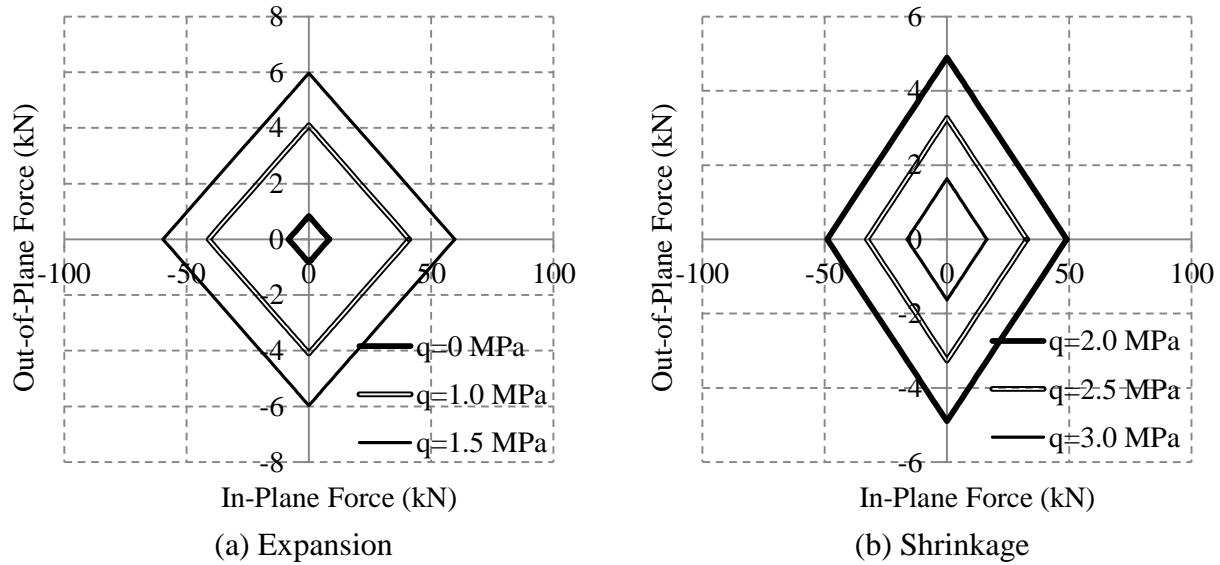


Figure 7-12. Expansion and shrinkage of interaction curve by variation of compressive traction

7.6.2 Example II – Wide wall

The second example in this section investigates the interaction curve for a wide URM wall with the following properties;

$h = 1000$; $a = 8000$; $t = 100$; which gives rise to aspect ratio h/a of $1/8$.

$c = 0.35$; $f_t = 0.25$; $f_{ce} = 3.5$; $\tan\phi = 0.75$

Figure 7-13 presents the variation of the magnitude of bidirectional load while the loading angle and compressive traction change. As mentioned before, in Figure 7-10 for different loading angles a unique compressive traction exists which changes the trend of the bidirectional load. However, in Figure 7-13 this compressive traction changes while the loading angle varies.

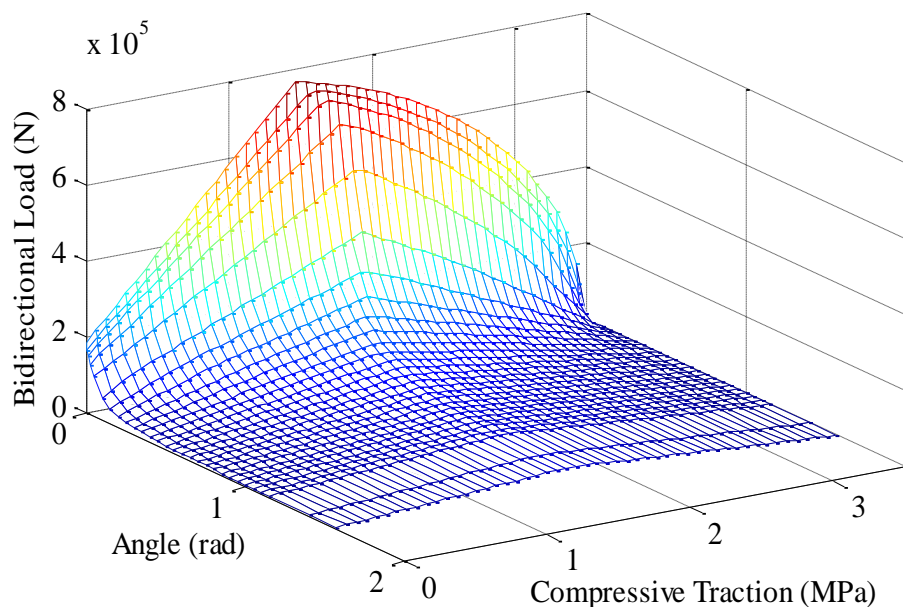


Figure 7-13. Variation of bidirectional load as angle and compressive traction change

Figure 7-14 shows the variation of the in-plane and out-of-plane loads as the compressive traction changes (interaction curve). Due to the low aspect ratio of the wall, shear failure has a high participation in the shape of the interaction curve, in comparison to the previous example. That is why the interaction curve in Figure 7-14 has no longer a rhombus shape.

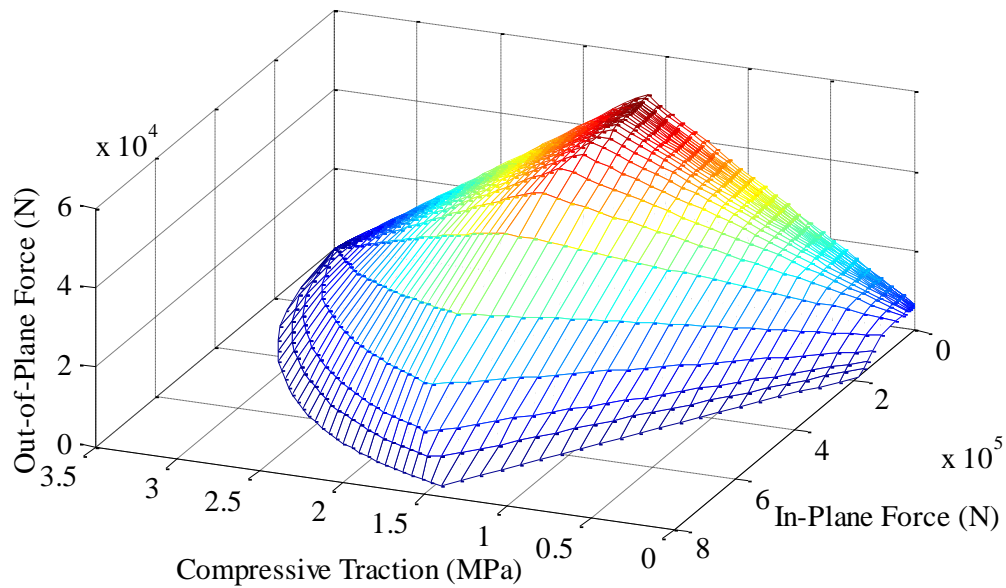


Figure 7-14. Interaction curve for a wide wall

Several cross sections are presented in Figure 7-15 which represent slicing the interaction surface at various compressive traction levels. Contrary to the simple rhombus shape illustrated in Figure 7-12, the interaction curve in this case would not have a simple plane shape and varies for different level of compressive tractions. Cross sections of Figure 7-15 (a) and Figure 7-15 (b) are associated to the failure in the mortar and bricks, respectively. For higher compressive tractions the failure force is dominated by the failure in the bricks and the presented cross sections in Figure 7-15 (b) have an elliptical shape.

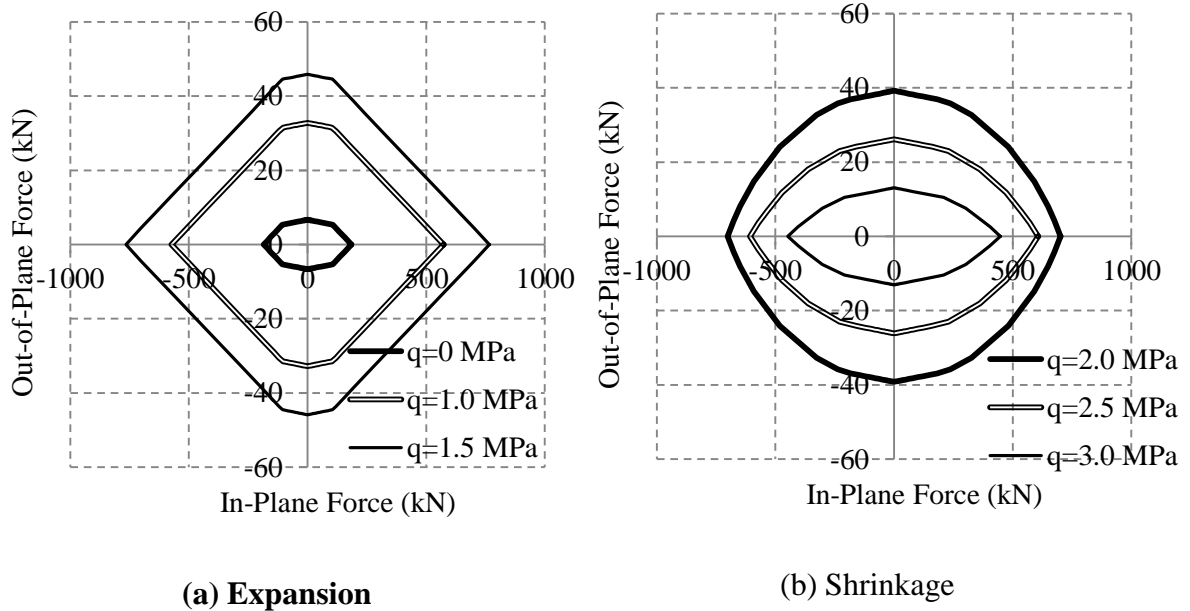


Figure 7-15. Expansion and shrinkage of interaction curve by variation of compressive traction

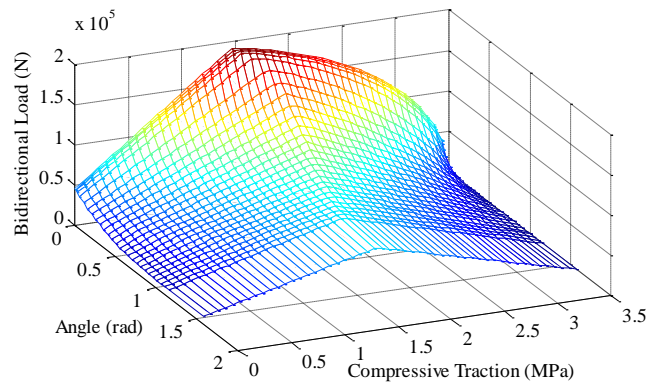
7.6.3 Example III – short wall

The third example on this section deals with a short wall with the following dimensions and material properties;

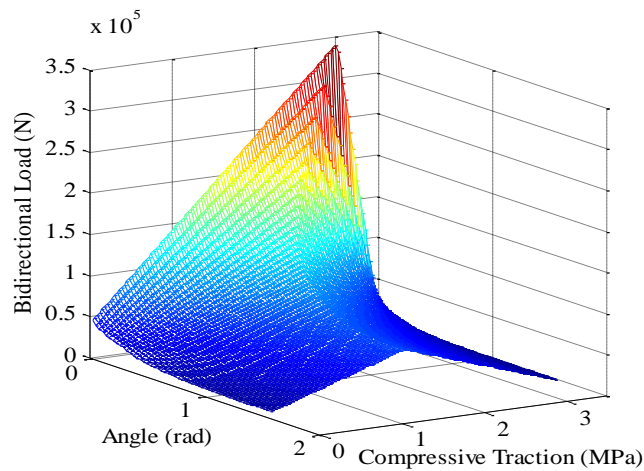
$h=200$; $a=2000$; $t=100$; $c=0.35$; $f_i=0.25$; $f_{ce}=3.5$; $\tan\phi = 0.75$; which gives rise to aspect ratio h/a of $1/10$.

In order to show the effect of shear stress in the failure of the bricks, interaction curves are presented with two assumptions in this example, including and excluding the shear effect. For the interaction curves considering the shear effect in the failure of the bricks, the same formulations of section 7.4.2 are used. Only compressive failure has been considered for the failure of bricks in generation of the interaction curves, excluding the shear effect. Figure 7-16 (a) and Figure 7-16 (b) show the variation of bidirectional force when the wall is loaded with different compressive tractions and when the loading angle changes. In Figure 7-16 (a), the effect

of shear stress has been considered in the failure of bricks. However, in Figure 7-16 (b) this effect has been neglected. According to Figure 7-16 (a), it is clear that for the region dominated by the failure in the bricks, including shear effect has lowered the failure force. In addition, for the lower values of loading angles (close to in-plane) the curve tracing the surface will change from a linear shape to a parabolic shape.



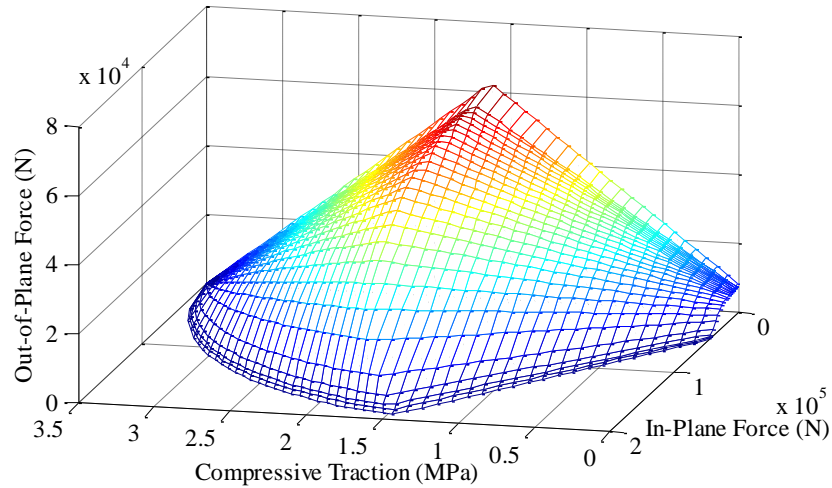
(a)



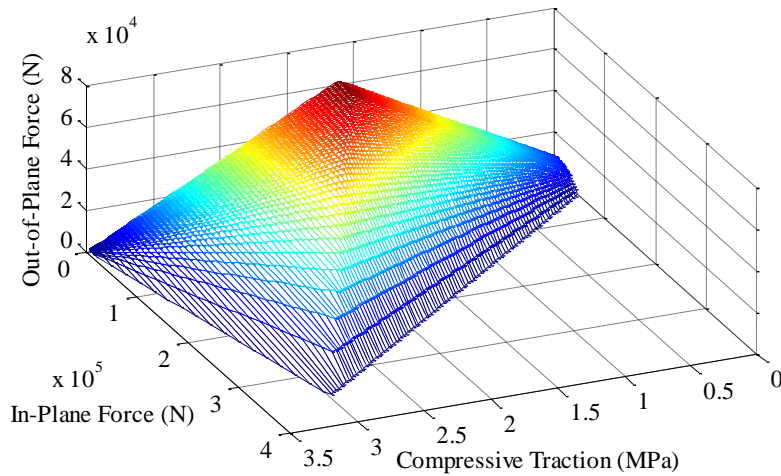
(b)

Figure 7-16. Variation of bidirectional load as angle and compressive traction change (a) including shear failure in the bricks (b) excluding shear failure in the bricks

Figure 7-17 (a) and Figure 7-17 (b) show the interaction curves including and excluding the effect of shear stress for the brick failure, respectively. By examining Figure 7-17 (a) and Figure 7-17 (b), it can be concluded that considering shear stress in the failure of the bricks have significant effect on the in-plane strength, in comparison to the out-of-plane strength.



(a)



(b)

Figure 7-17. Interaction curve for a wide wall (a) including shear failure in the bricks (b) excluding shear failure in the bricks

7.7 Comparison with finite element results

To validate the obtained analytical curves and also to examine the behavior of the wall after intersecting the interaction curves, in this section for a particular case of URM shear walls a non-linear finite element (FE) investigation has been performed. The utilized finite element model in this study is originally developed in the fifth section and has been validated with several well documented experimental results. Figure 7-18 shows a general view of the wall which was built in ABAQUS (2005) and the generated finite element mesh. The considered wall in this section is exactly similar to the first analytical example (regular/square wall) and has the dimensions of 1000, 1000 and 10 mm in height, width and thickness, respectively, with the same material properties of the analytical examples.

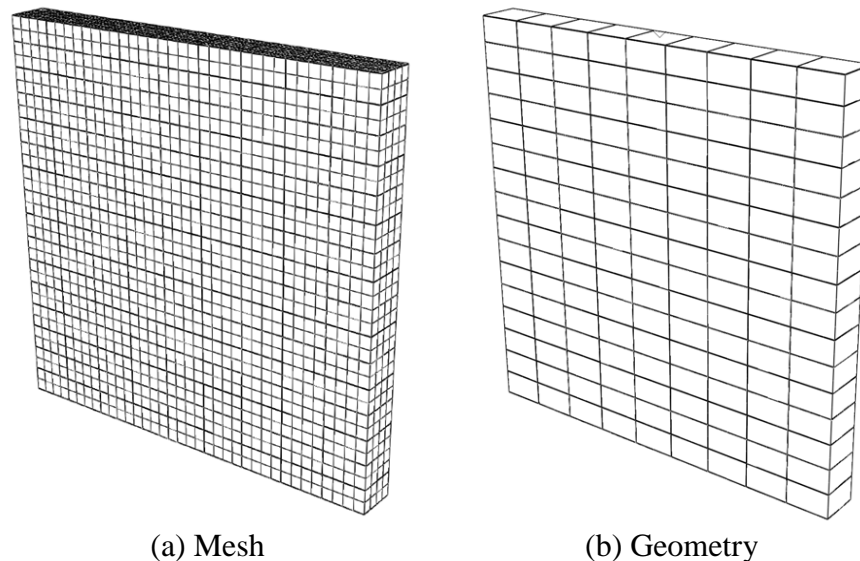


Figure 7-18. (a) General mesh of the wall and (b) General view of the wall

Four displacement-controlled loadings have been applied on top of the wall in different directions. Due to the fact that the non-linear finite element analysis imposes very high computational demand, the loading has been performed only on a particular condition with a

constant compressive load of 120 kN. The obtained load-displacement curves are presented in Figure 7-19 and are compared with the analytical results.

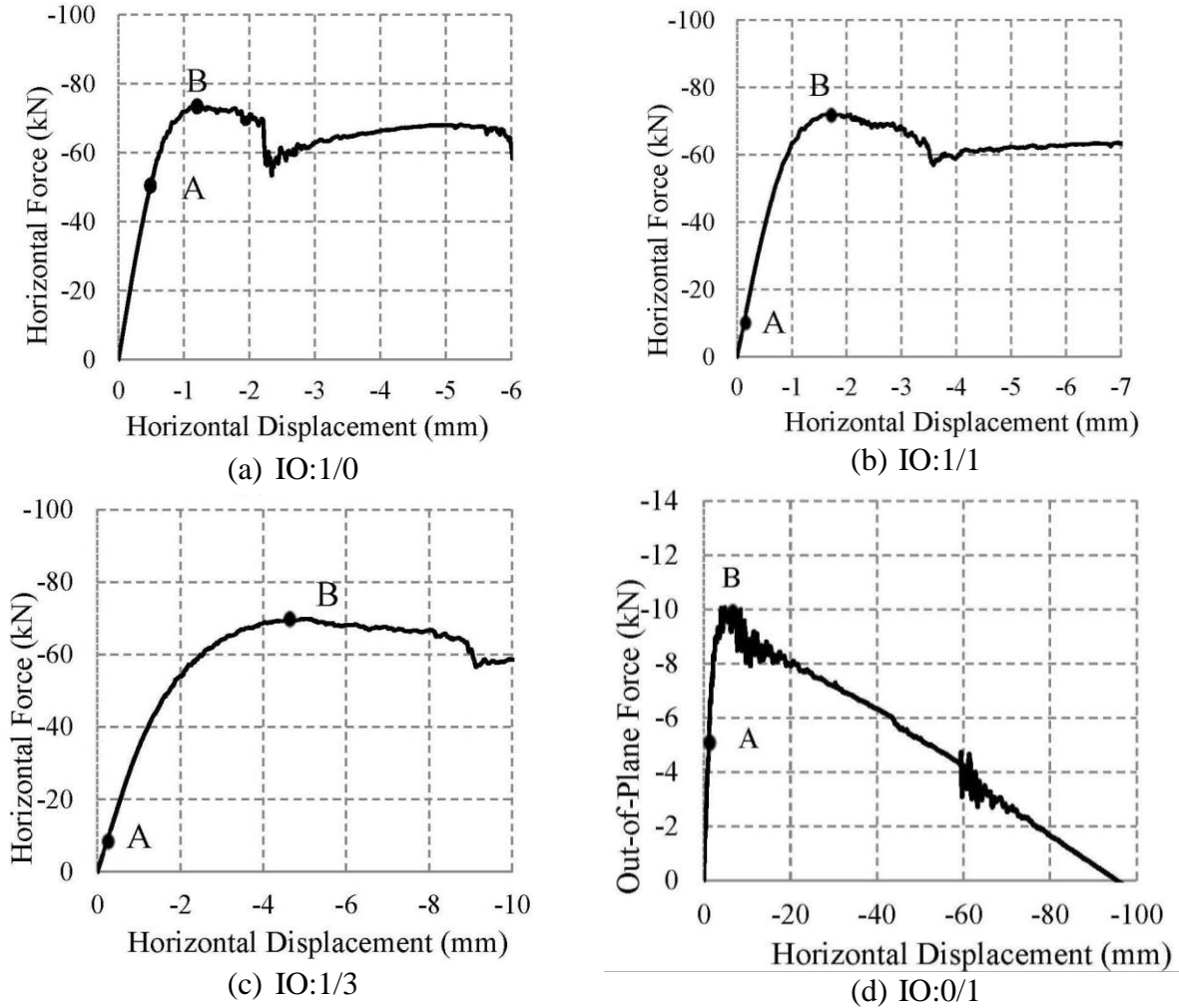


Figure 7-19. Load-displacement results obtained by FE analysis for four different loadings

A simple symbol “IO: x/z ” is used in Figure 7-19 to facilitate the naming of the loading protocols. In this symbolic numbering, x and z , represent the proportion of the in-plane and out-of-plane displacement of the wall, respectively. For example in Figure 7-19 (c), IO:1/3 means that the applied displacement in the out-of-plane direction is three times of the one in the in-plane direction. In Figure 7-19, point “A” represents the obtained value from analytical curves

which shows the first point that the failure has occurred, and point “B” represents the maximum capacity of the wall (based on the finite element results). It is clear that point “A” is located at the end of linear response and beyond that point the nonlinear behavior commences. In case of either in-plane or out-plane loadings, this point is close to the yielding point obtained from the finite element results of the wall (load-displacement curves). However, in the bidirectional loading after point “A” the macro behavior of the wall is still close to linear. This is due to this fact that, in bidirectional loading after minor cracking in the out-of-plane direction, the wall is still generating a large resisting force in the in-plane direction. In addition, by focusing on the values of point “A” and point “B”, it can be realized that how far/close the obtained interaction curve is from the ultimate capacity of the wall. In other words, it shows the additional resistance of the wall after initiation of the damage. It should be noted that for bidirectional loadings, after initiation of the nonlinear response, the direction of the load changes and it is not necessarily in the direction of the imposed displacement. Figure 7-20 shows the variation of the direction of load for model IO:1/10 and IO:1/20 as the imposed deformation increases. As shown in Figure 7-20, in the nonlinear regime the direction of the load is more toward the IP direction.

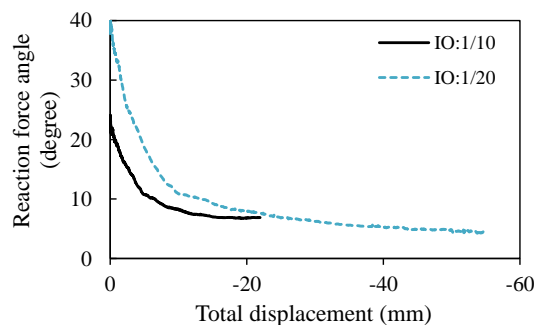
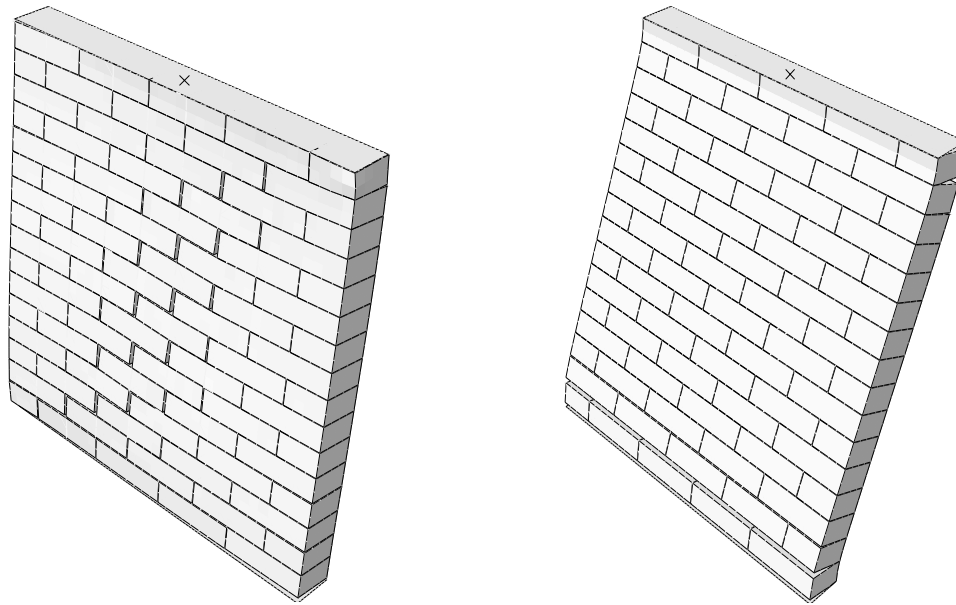


Figure 7-20. Variation of the direction of load for IO:1/3

Figure 7-21 represents the deformed shapes of the wall for case “IO:1/3” and “IO:0/1” obtained from FE analysis.



(a) IO:1/3 at 10 mm displacement ($\times 7$) (b) IO:0/1 at 85 mm displacement ($\times 3$)

Figure 7-21. Deformed shape obtained by FE analysis

7.8 Conclusion

In this section, different possible failure modes have been discussed for URM shear walls. The intent of this study is to investigate the initiation of damage while the compressive traction and loading angle change. A MATLAB code has been developed which at each stage, based on different values of compressive traction and loading direction, calculates the failure forces according to the possible failure modes, either in the bricks or mortar. The lowest value has been considered for the final and predominant failure mode. Moreover, different examples are presented to examine different possible shapes for interaction curves, and to interpret the variation of the URM wall capacity in various loading scenarios.

Interaction curves show a sharp drop as the direction of loading changes from in-plane to out-of-plane direction. Furthermore, interaction curves show that for different aspect ratios the

capacity of the wall initially increases while the compressive traction increases. After reaching a particular value the failure mode changes from mortar failure to brick failure and interaction curves start to shrink.

For a particular case the derived analytical yield surface has been compared with nonlinear FE results. It is shown that the analytical results are in a good agreement with the finite element prediction for the onset of failure for the particular cases of in-plane or out-of-plane loadings. However, in the bidirectional loadings the wall has a significant resistant after initiation of the damage. This in fact is a limitation of the analytical solution.

The derived interaction curves can have a great utility for engineers to assess an initial estimate of failure of URM buildings subjected to a combination of in-plane and out-of-plane loadings, and more so, the derived procedures can be effectively used for simplified preliminary analysis.

SECTION 8

BIDIRECTIONAL EXPERIMENTAL STUDY ON MASONRY WALLS AND VALIDATION OF NUMERICAL MODELS

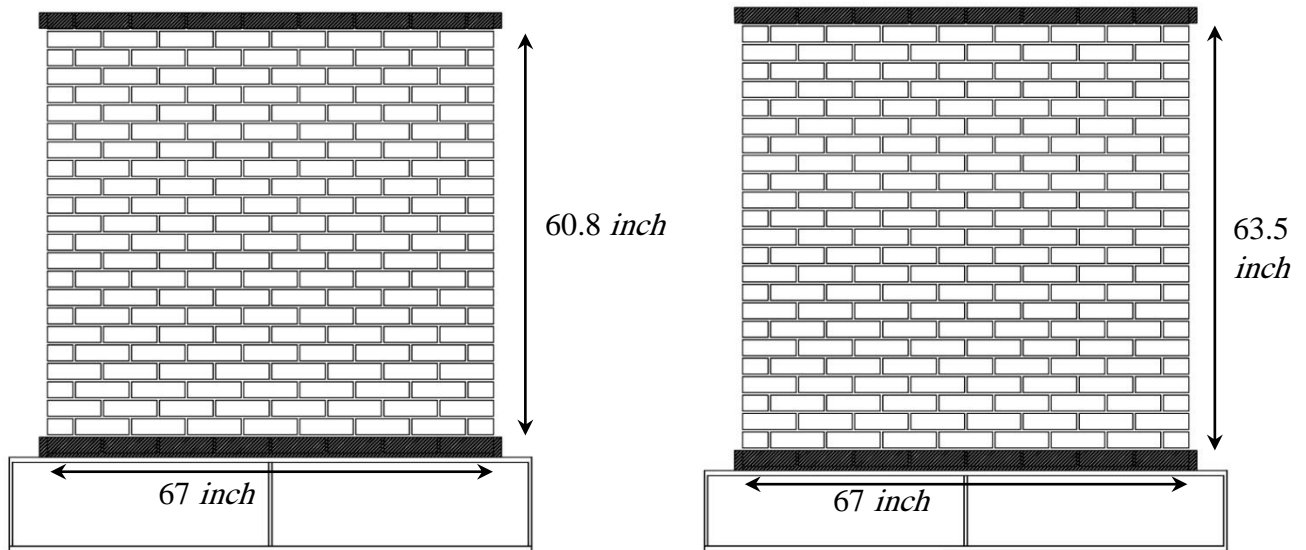
8.1 Introduction

Many researchers have investigated the experimental behavior of unreinforced masonry (URM) walls in the in-plane (IP) or out-of-plane (OP) directions. Very few studies have investigated the bidirectional behavior of URM walls, either experimentally or numerically. In this section the experimental results of six URM walls are presented. The walls were tested with a combination of in-plane and out-of-plane loadings along with monotonic and cyclic loading protocols for different walls. Moreover, different boundary conditions were considered for different walls to investigate the influence of rotation of top plane of the wall on the failure mechanisms of the walls. Different samples were constructed and tested to capture the material properties of the brick and mortar for each wall. The results of the tests were recorded with a host of high precision data acquisition systems and presented in this section. Finally, using the proposed numerical procedure in section 5, along with the material properties obtained from the sample tests, a numerical modeling is performed for each wall and the results are compared.

8.2 Description of the test set-up

To investigate bidirectional behavior of URM walls, six walls were constructed and tested on the strong floor laboratory of University at Buffalo. Two types of bricks were supplied, a high strength brick (brown color) and a low strength brick (red color). Five walls were built using a high strength brick and one wall was constructed with a low strength brick. In building the walls,

type “N” mortar was used and the bricks have the same dimensions of 8”, 4”, 2.4” in width, thickness and height, respectively (20.3×10.1×6.1 *cm*). Attention was paid to maintaining the dimension of the mortar constant at 3/8 *inch* (about 10 *mm*) in all horizontal and vertical joints. As shown in Figure 8-1, two different geometrical configurations were used for constructing the walls. The first configuration had 24 rows of bricks (type *I*) and the second configuration had 25 rows of bricks (type *II*). The first row of brick was buried in the mortar for all walls and the last row of the brick was deactivated (Figure 8-2, Figure 8-3) to have a consistent behavior (crack) on the entire wall.



(a) Masonry wall type *I*

(b) Masonry wall type *II*

Figure 8-1. Different geometrical configurations

Table 8-1 shows the type of bricks and geometrical configurations used in building the six walls. As shown in Table 8-1, two walls had configuration of type *I* and four walls had configuration of type *II*. Moreover, five walls were constructed using the high strength brick and a wall (wall 6) was constructed using the low strength brick.

Table 8-1. Types of brick and geometry for different walls

Wall	Type of bricks	Geometrical configuration
Wall 1 and Wall 2	High strength bricks	Type I
Wall 3, Wall 4 and Wall 5	High strength bricks	Type II
Wall 6	Low strength bricks	Type II



Figure 8-2. Wall type II (the first row of brick is buried into the mortar)



Figure 8-3. Boundary condition for the top plane of the walls

As shown in Figure 8-4 two vertical actuators applied the axial load to the wall that represents the gravity load, and a horizontal actuator applied the deformation-controlled horizontal load. The vertical actuators transferred the axial load to the top beam (which was

almost rigid and we call it rigid beam). The rigid beam distributed the load to the top of the wall. As shown in Figure 8-4 four columns were assigned as an out-of-plane (OP) support to control such deformation of the wall.

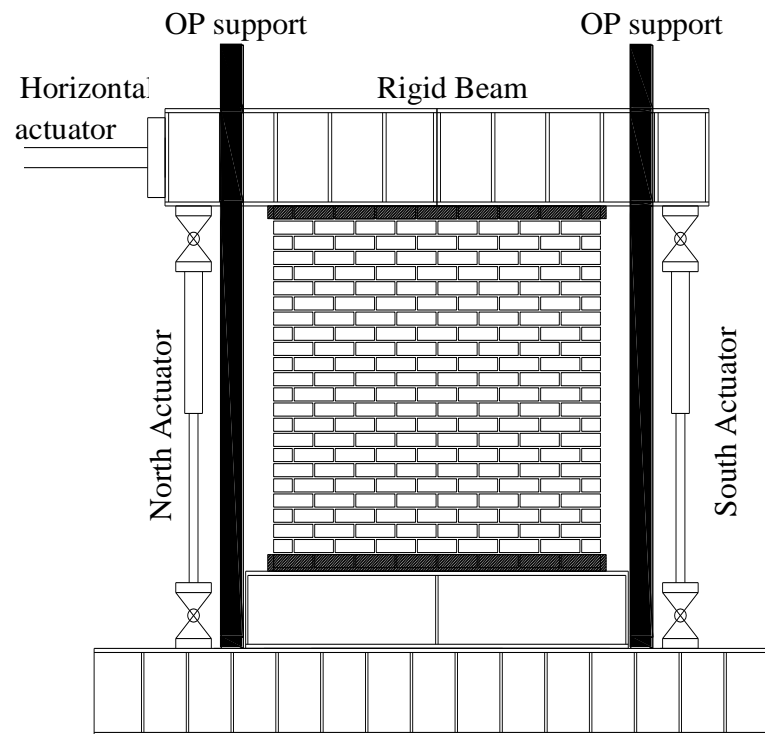


Figure 8-4. Test setup

After construction of each wall, nine different samples (see Figure 8-5) were constructed to determine the properties of the brick and mortar used in the wall specimens. These specimens included three samples for determining the shear properties of the mortar, three masonry prisms to capture the uniaxial compressive behavior of the bricks, and three samples to obtain the tensile properties of the mortar. Moreover, three cubic samples of mortar were built to measure the uniaxial compressive capacity of the mortar. The extracted data from the specimen tests are used in the validation of the numerical procedure for modeling the walls, which was discussed in section 5.



(a) Shear test



(b) Compression test

Figure 8-5. Specimens for material testing

Figure 8-5 (a) shows a specimen for the shear test of the mortar and Figure 8-5 (b) presents a masonry prism for determining the uniaxial compressive properties of the brick. Four transducers were used to measure strain of the samples under uniaxial compression test (Figure 8-6). The average of the strains was used in the presentation of the stress-strain curves in the following sections.



(a) Low strength brick (red)



(b) High strength brick (brown)

Figure 8-6. Compression test on bricks

The test setup for measuring the shear properties of the mortar is shown in Figure 8-7. Two load cells were used for measuring the vertical and confinement loads (see the solid arrow) and a transducer was used to measure the vertical displacement of the joint.



Figure 8-7. Test setup for measuring the shear properties

8.3 *Material properties*

As mentioned earlier, different masonry samples were constructed for each wall, to determine the material properties of the walls. All tests were conducted using a displacement-controlled loading, and the results of the experimental tests on the specimens are presented in this section. The density of the low and high strength bricks were 0.0789 lb/in^3 (2184 kg/m^3) and 0.0921 lb/in^3 (2550 kg/m^3), respectively. Figure 8-8 and Figure 8-9 show the uniaxial compressive behavior of the two different types of brick used for construction of the walls. The first type of brick (brown) had a very high stiffness and strength, in contrast to the second type of brick (red). In Figure 8-8 and Figure 8-9 (and for the rest of the figures in this section), the modulus of elasticity is calculated considering 1/3 of the peak stress.

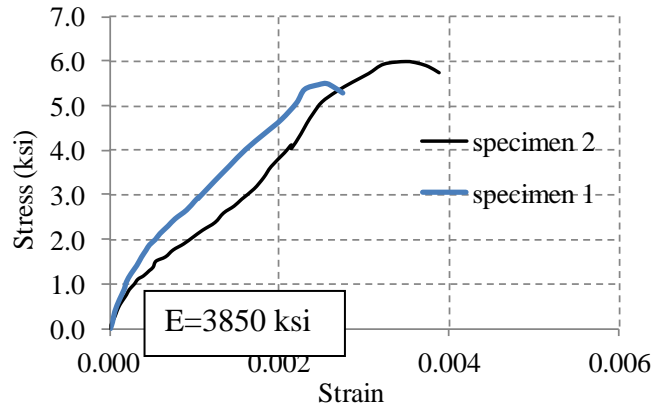


Figure 8-8. Stress-strain curve for the high strength bricks (brown brick)

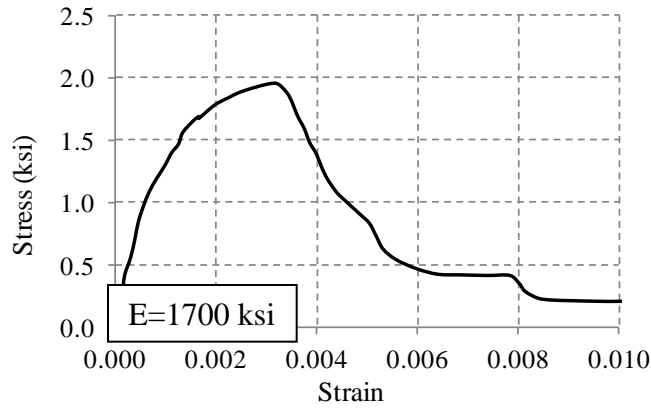


Figure 8-9. Stress-strain curve for a low strength brick (red brick)

Figure 8-10 shows a high strength brick after uniaxial compression test. A very brittle behavior was observed for this type of brick.



Figure 8-10. A damaged high strength brick after uniaxial compression test

Figure 8-11 and Figure 8-12 show the stress-strain curves of the uniaxial compression test on the masonry prisms, for the high and low strength bricks, respectively. It is interesting to note that the two types of masonry prisms have almost similar modulus of elasticity. The reason is attributed to the fact that, in both types of masonry prisms, type “N” mortar was used. Bricks and mortar behave like springs in series in the masonry prisms; therefore, the modulus of elasticity for the combination is mostly controlled by the lowest modulus of elasticity, which in this case is mortar.

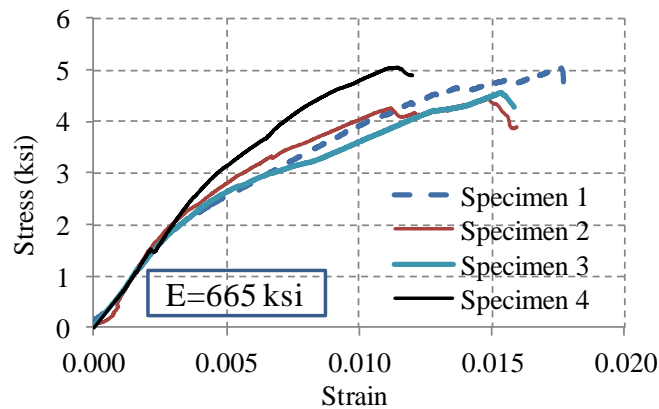


Figure 8-11. Stress-strain curve for masonry prisms constructed by high strength bricks

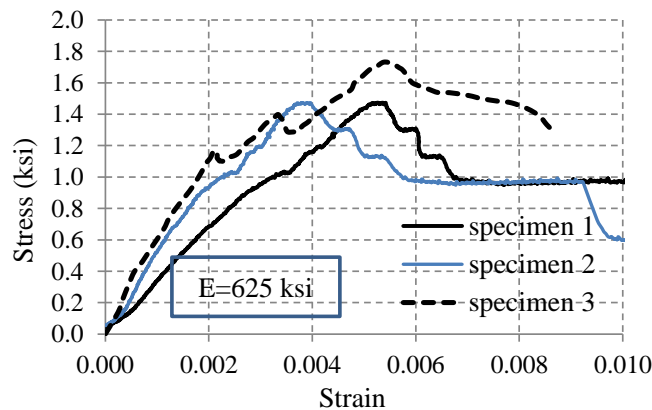


Figure 8-12. Stress-strain curve for masonry prisms constructed by low strength bricks

A damaged masonry prism after uniaxial compression test is shown in Figure 8-13. It was observed that the nonlinear behavior was mainly concentrated in the bricks, and the mortar remained without any apparent damage. This observation justifies the proposed yield surface of the mortar, presented in section 5, that no yield surface should be defined in high compressions for mortar if brick is modeled using elasto-plastic elements.



Figure 8-13. A damaged masonry prism after compression test

The properties of the bricks based on the results of the uniaxial compression test on bricks and masonry prisms are presented in Table 8-2 and Table 8-3. The parameters of Table 8-2 and Table 8-3 are based on the ideal mathematical stress-strain curve described in section 3. This ideal curve is represented in Figure 8-14 (Lourenco 1996).

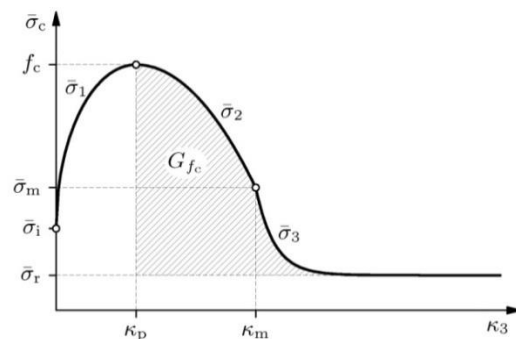


Figure 8-14. Idealized stress-strain curve (Lourenco 1996)

As shown in Figure 8-14, a combination of three functions determines the stress-strain curve of the brick. Later this stress-strain curve is used as an input data for the numerical modeling, and specifically for the concrete damaged material model in ABAQUS.

Table 8-2. Material properties of high strength brick

Elastic		Compressive			Tensile		
E ksi	ν	f_c' ksi	κ_p	κ_m	f_t' ksi	G_f^I kip/in	G_f^{II} kip/in
3850 (26500 MPa)	0.15	5 (35 MPa)	0.0069	0.0115	0.5 (3.5 MPa)	0.00074 (130 N/m)	0.0074 (1300 N/m)

Table 8-3. Material properties of low strength brick

Elastic		Compressive			Tensile		
E ksi	ν	f_c' ksi	κ_p	κ_m	f_t' ksi	G_f^I kip/in	G_f^{II} kip/in
1700 (11700 MPa)	0.15	1.4 (9.6 MPa)	0.002	0.0035	0.14 (0.96 MPa)	0.00034 (60 N/m)	0.0034 (600 N/m)

The results of the shear tests under two different confinement pressures of 0.93 ksi and 1.2 ksi are presented in Figure 8-15. The shear properties of the joint are calculated based on the stress-displacement curve of Figure 8-15 and are presented in Table 8-4. Moreover, in Figure 8-15 the experimental results are compared with the numerical model of section 5.4.2 (an exponential curve), considering the material properties of Table 8-4 and Table 8-5.

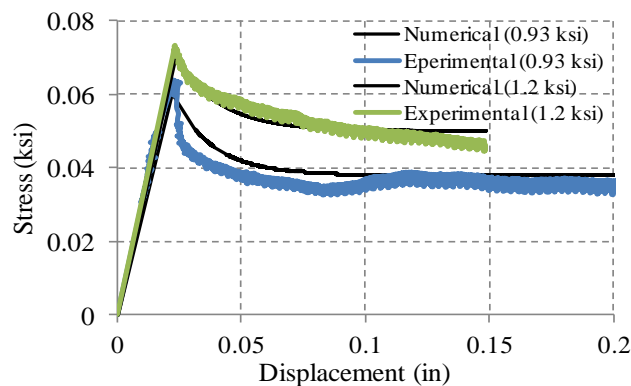


Figure 8-15. Joint behavior under shear displacement considering different confinement pressures

Table 8-4 . Joint properties for walls constructed by high strength bricks

Elastic				Shear		Tension	
k_n kip/in ³	k_s kip/in ³	$\tan \phi$	$\tan \psi$	c ksi	G_f^H kip/in	f_t ksi	G_f^I kip/in
228.4	99.44	0.92	0.0	0.02	0.000357	0.0145	0.0000357
(62 N/mm ³)	(27 N/mm ³)			(0.135 N/mm ²)	(0.0625 N/mm)	(0.1 N/mm ²)	(0.00625 N/mm)

Table 8-5. Joint properties for walls constructed by low strength bricks

Elastic				Shear		Tension	
k_n kip/in ³	k_s kip/in ³	$\tan \phi_0$	$\tan \psi$	c ksi	G_f^H kip/in	f_t ksi	G_f^I kip/in
283.6	121.5	0.9	0.0	0.056	0.000714	0.03625	0.0000714
(77 N/mm ³)	(33 N/mm ³)			(0.38 N/mm ²)	(0.125 N/mm)	(0.25 N/mm ²)	(0.0125 N/mm)

The stress-strain curves of the uniaxial compression test on the cubic mortar samples are presented in Figure 8-16. It should be noted that for the numerical simulations the modulus of elasticity of the mortar should be extracted from the masonry prism test and not from the uniaxial compression test of the cubic mortar samples. The reason is attributed to the fact that, based on the complicated state of stresses and also different curing conditions of the mortar in the wall, the properties of the mortar in the masonry wall and cubic mortar samples are different.

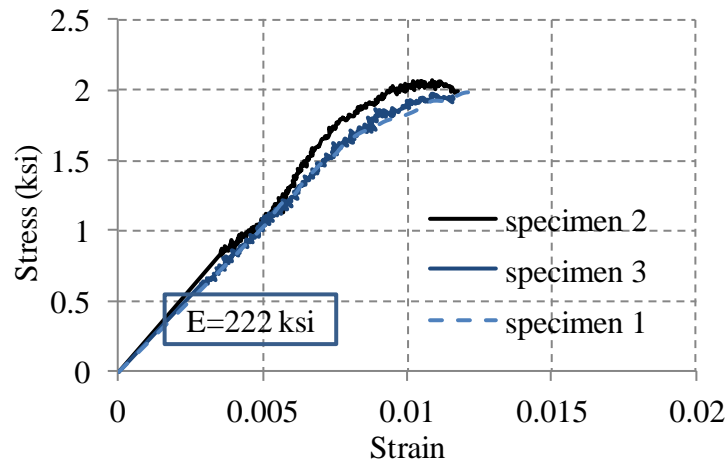


Figure 8-16. Mortar properties

8.4 Loading protocols

Six different loading protocols were considered for testing the walls. Monotonic quasi-static loading was considered for the first and second walls to calibrate the finite element parameters. For the rest of the tests, a cyclic loading with the combination of in-plane and out-of-plane forces is considered. Table 8-6 summarizes the loading cases for different walls.

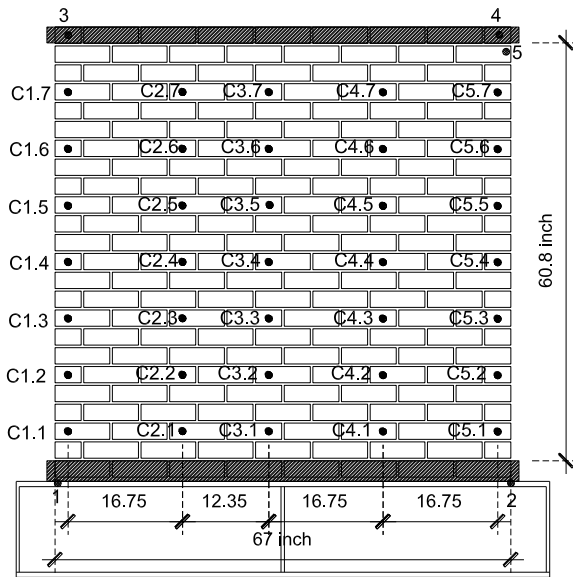
Table 8-6. Loading protocols for the walls

Number	Loading protocol
Wall 1	Monotonic – in-Plane
Wall 2	Monotonic – in-Plane + out-of-plane force
Wall 3	Cyclic – in-Plane
Wall 4	Cyclic – in-Plane + out-of-plane force
Wall 5	Cyclic – in-Plane + out-of-plane deformation
Wall 6	Cyclic – in-Plane + out-of-plane deformation

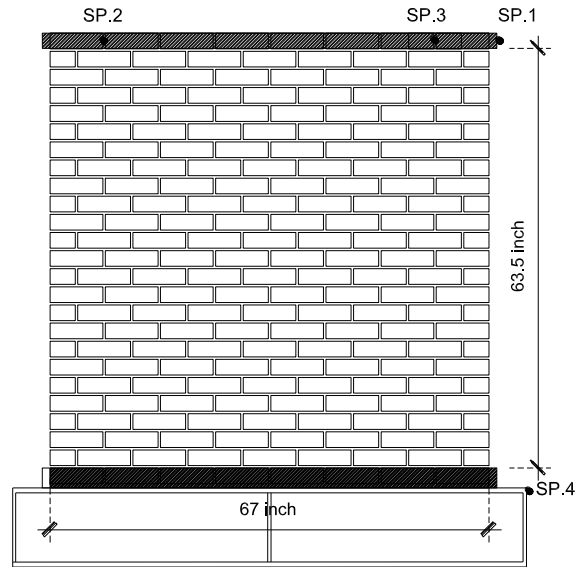
8.5 Experimental results

8.5.1 Testing of Wall 1

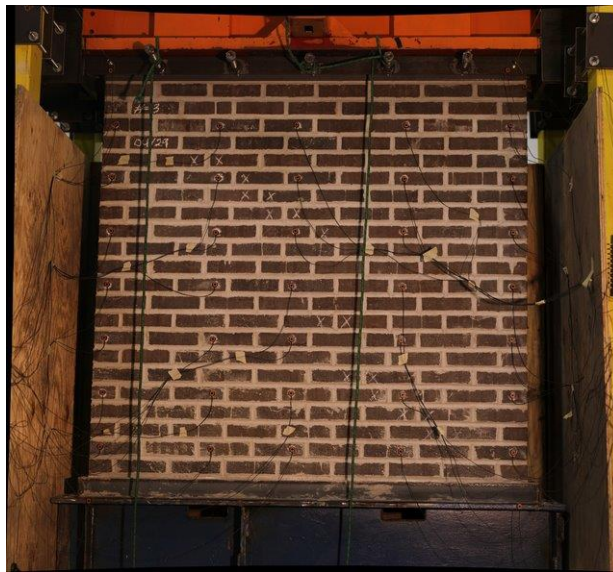
Figure 8-17 presents the general view of wall 1, in addition to the instrumentation of the wall. As shown in Figure 8-17, the wall was instrumented with 40 Krypton LED's and four string potentiometers. SP2 and SP3 measured the out-of-plane (OP) deformations of the wall and SP1 and SP4 measured the in-plane (IP) deformations of the top and bottom of the wall, respectively. In the first step of loading, the axial load was applied on top of the wall (22 kips (98 kN) including the weight of the rigid beam), using two vertical actuators with identical loads. Afterward, while keeping the axial load constant, a deformation-controlled load was applied horizontally at top of the wall. Due to the imposed boundary conditions, the rigid beam at top of the wall was allowed to rotate while the horizontal load was applied. This boundary condition represents a URM wall in a building with a flexible diaphragm.



(a) 40 LED's (Krypton)



(b) Four string pots



Experimental view

Figure 8-17. Instrumentation of the walls

As mentioned earlier first an axial load of 16.5 kip (73.4 kN) was applied, using two vertical actuators. Figure 8-18 presents deformation of the wall while the axial load was applied on the wall, in addition to the initial position of the Krypton LEDs. The deformations in this figure were taken using Krypton LEDs and for the purpose of better presentation are 500 times magnified.

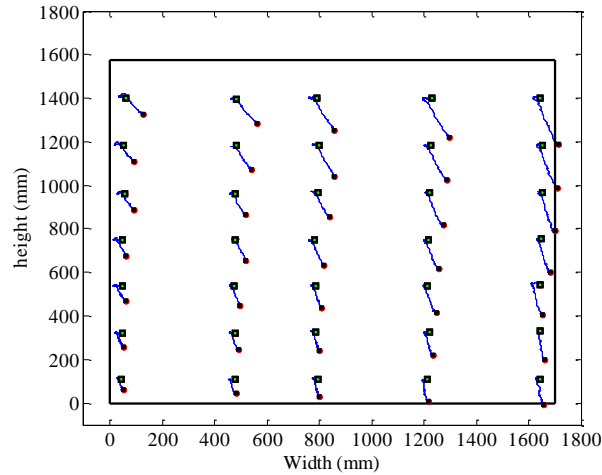


Figure 8-18. Deformation of the wall under the axial load ($\times 500$)

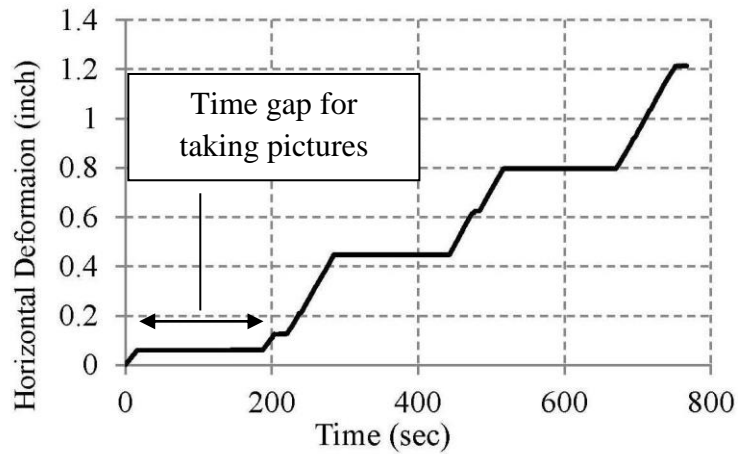


Figure 8-19. Loading protocol for wall 1

Figure 8-19 presents the in-plane deformation-controlled loading protocol that was used for the first wall. As shown in Figure 8-20, throughout the test the axial load was maintained constant in the two vertical actuators.

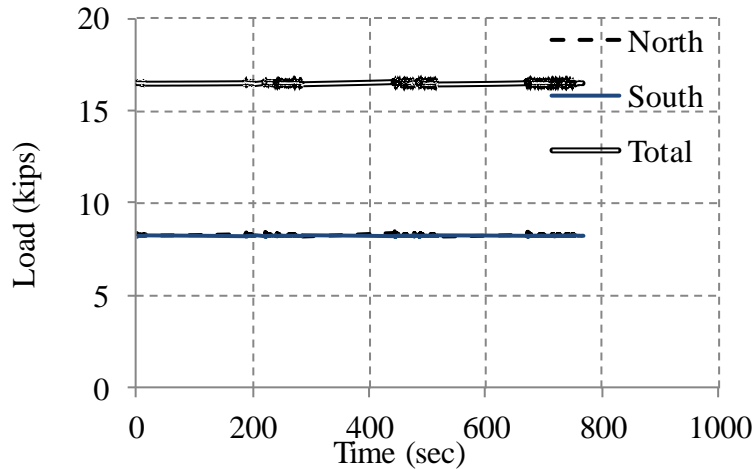


Figure 8-20. Axial loads in vertical actuators

The vertical actuators in this test were not slaved together and worked independently and rotation of the rigid beam was expected within the test. Figure 8-21 presents the axial displacement of the vertical actuators. According to Figure 8-21, north actuator is elongated and that led to an opening in the north side of the wall (see Figure 8-24).

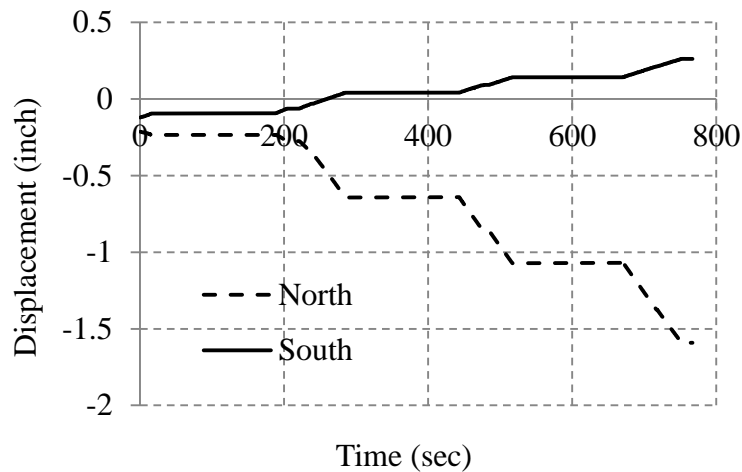


Figure 8-21. Axial displacement of the north and south vertical actuators

The load-displacement curve of wall 1 is presented in Figure 8-22. The wall initially started to behave elastically and after the onset of cracking in the bottom of the wall (see Figure 8-24), the

nonlinear behavior followed a rocking failure mode. In this test the failure was concentrated in the first row of the brick and no nonlinearity was observed in the rest of the wall (Figure 8-24).

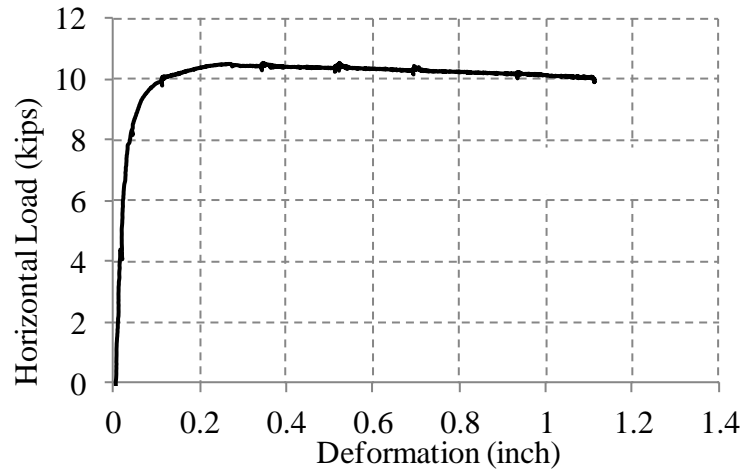


Figure 8-22. Load - displacement of wall 1 (experimental)

8.5.1.1 Comparison of the experimental and finite element results of wall 1

The finite element model of wall 1 is shown in Figure 8-23. As described in section 5, interface elements have been located between the bricks and also in the middle of the bricks (potential cracks). The obtained material properties of the specimen tests have been used for different elements in the FE model. The bottom face of the wall was completely restrained and the axial load was applied at two corners of the top plane. In the first step of loading, the axial load has been applied on the top plane of the wall and then in the second step of loading, the top plane of the wall was subjected to a quasi-static loading, according to the loading protocol of Table 8-6.

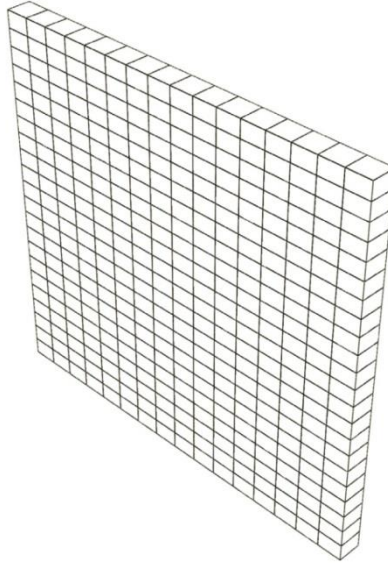
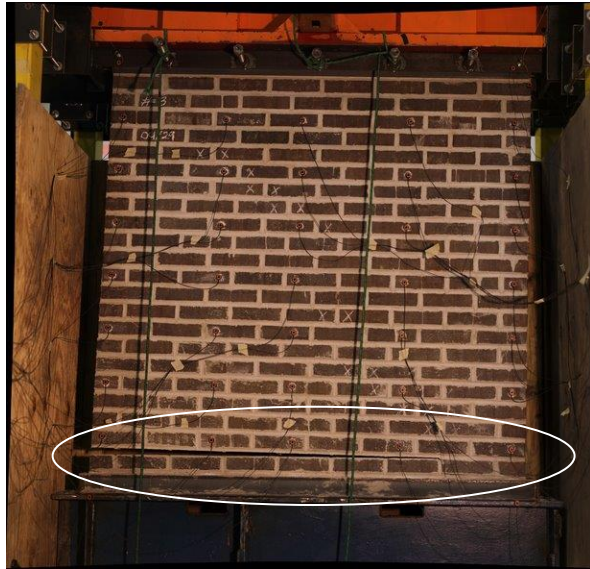
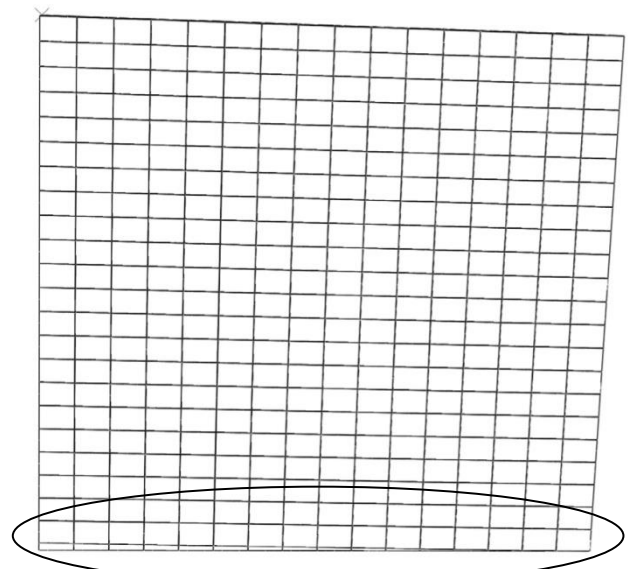


Figure 8-23. Finite element model of wall 1

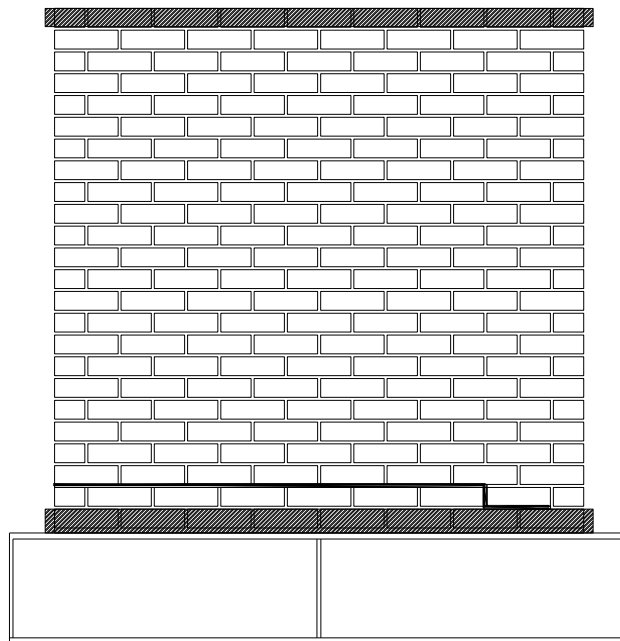
The experimentally obtained crack is compared to the numerical results in Figure 8-24. As shown in Figure 8-24, the propagated crack in the numerical model is in good agreement to the experimentally obtained crack. The cracks in this figure are highlighted with a white elliptic. Both models showed that opening of first or second row of the brick was the governing failure mode.



(a) Experimentally obtained crack pattern after 0.75" displacement of the top plane



(b) Numerical results after 0.75" displacement of the top plane



(c) Experimentally obtained crack pattern

Figure 8-24. Comparison of the crack propagation in the experimental and numerical models

Load-displacement curves obtained by the numerical and experimental models are presented in Figure 8-25. In the linear regime the behavior in the numerical and experimental models are identical. In the non-linear regime the peak force in the numerical results is about

15% higher than the experimental results. The reason is attributed to the fact that, in the experimental model after elongation of the north vertical actuator the horizontal actuator did not remain horizontal; however, in the numerical model the in-plane force was horizontally applied to the wall throughout the analysis.

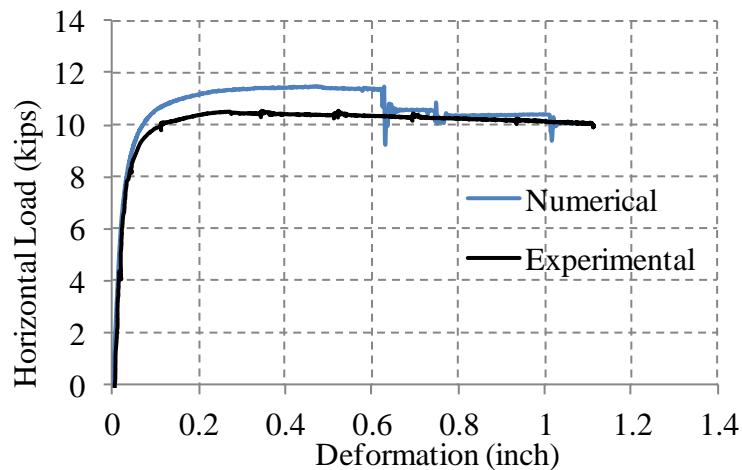


Figure 8-25. Load-displacement curves of the numerical and experimental models

In addition to the numerical comparison, the experimental results could be compared to the empirical formulation presented in ASCE 41 (2006). ASCE 41 predicts the stiffness of cantilever shear walls as follow:

$$k = \frac{1}{\frac{h_{eff}^3}{3 E_m I_g} + \frac{h_{eff}}{A_v G_m}} \quad (8-1)$$

where,

h_{eff} = wall height;

A_v = shear area

I_g = moment of inertia for the gross section representing uncracked behavior

E_m = masonry elastic modulus

G_m = masonry shear modulus

Using the elastic and shear modulus of the masonry prism, the predicted stiffness of the wall based on ASCE 41 is 522 *kip/inch* (91454.4 *kN/m*), which comparing to the experimental results of 257 *kip/inch* (45026.4 *kN/m*) is overestimated. ASCE 41 (2006) proposes three formulations to calculate the ultimate capacity of the wall based on different failure modes which include (i) rocking (ii) shear and (iii) compression failure modes. The failure mode with the lowest value shows the predominant failure mode. For rocking failure mode the peak strength follows,

$$Q_{CE} = V_r = 0.9 \alpha P_D \frac{L}{h_{eff}} \quad (8-2)$$

where,

h_{eff} = height to resultant of lateral force;

L = length of wall

P_D = superimposed dead load at the top of the wall

V_r = strength of wall

α = factor equal to 0.5 for cantilever wall, or equal to 1.0 for fixed-fixed wall pier

lower-bound masonry shear strength, v_{mL} , shall be determined, in accordance with

$$v_{mL} = \frac{0.75 \left(0.75 v_{tL} + \frac{P_D}{A_n} \right)}{1.5} \quad (8-3)$$

where,

P_D = superimposed dead load at the top of the wall

A_n = area of net mortared/grouted section of a wall

v_{tL} = lower-bound bed-joint shear strength

Using equation (8-2) and (8-3) the peak in-plane resisting load for rocking and shear failure modes are 11 kip (49 kN) and 13 kip (57.8 kN), respectively. Based on ASCE 41 the lesser force should be considered for the final failure mode of the wall, which for this wall corresponds to the rocking mode. For wall 1, ASCE 41 prediction for the failure mode and the peak force is in good agreement with the experimental results.

In the second phase of the experimental study, the damaged wall 1 was tested for the second time with modified boundary conditions. In this phase in addition to the constant axial load (according to Figure 8-26), the boundary conditions for the rigid beam was imposed in such a way that the rigid beam remained level throughout the testing, which was achieved by slaving the north vertical actuator to the south vertical actuator. The summation of the vertical loads remained constant and the distribution of the vertical load varied between the vertical actuators throughout the test (Figure 8-26). As shown in Figure 8-27, in this phase of the test the failure mode changed from rocking mode to diagonal crack.

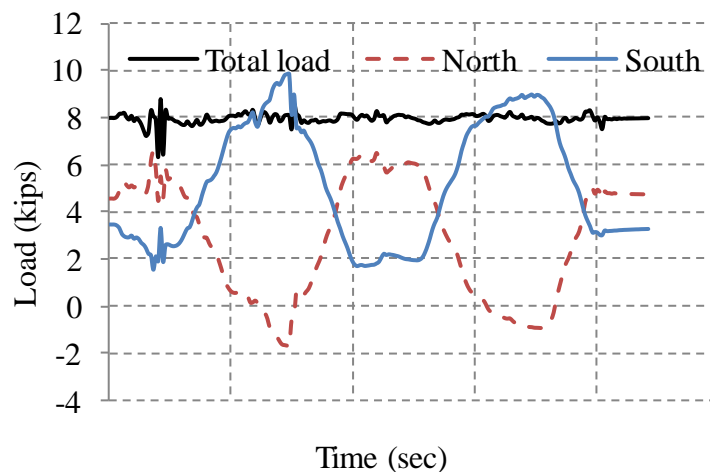


Figure 8-26. Distribution of the axial load in the vertical actuators

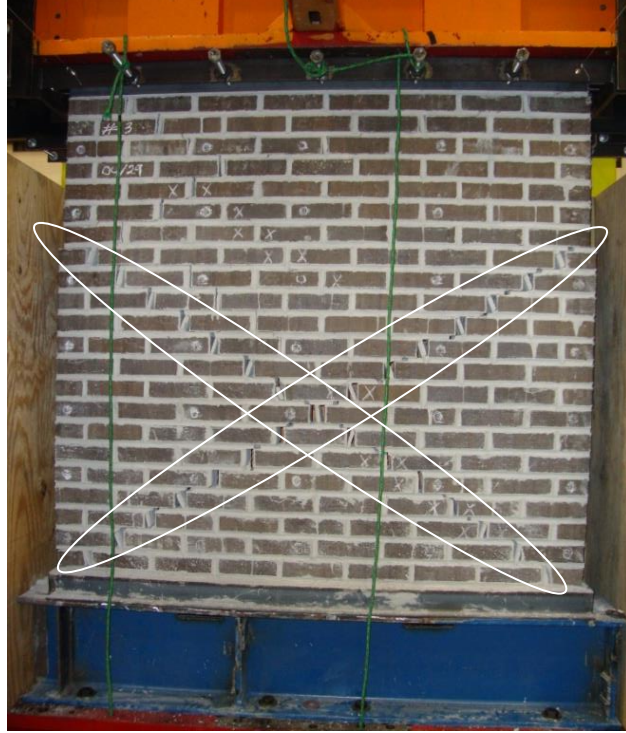


Figure 8-27. Propagated cracks in wall 1 (experimental) – second phase of the test

The load-displacement curve for the cyclic loading of wall 1 is presented in Figure 8-28. Some vibration can be seen in the results due to the relatively high loading rate used for the test. As shown in Figure 8-28, after reaching the maximum elastic load, the resisting force remained constant. The constant resisting force was generated by the frictional force created on the surfaces located on the diagonal cracks.

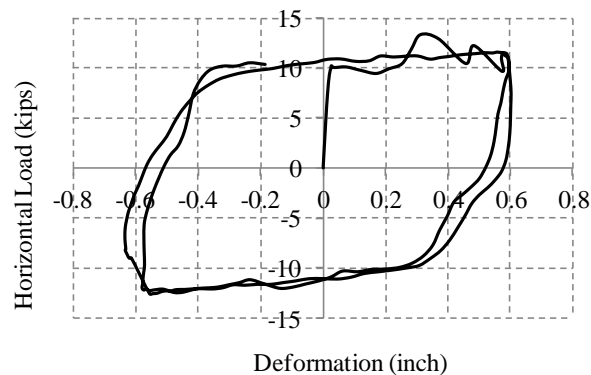


Figure 8-28. Load-displacement curve for cyclic testing of wall 1

Figure 8-29 presents the comparison between the numerical and experimental load-displacement curves. In this figure, the numerical results are presented considering two different values for κ (stiffness degradation factor, see section 5). The numerical result for “ $\kappa = 0.76$ ” is closer to the experimental results than the numerical results for “ $\kappa = 1$ ”. As discussed in section 5, “ $\kappa = 0.76$ ” is a typical value for stiffness degradation in concrete.

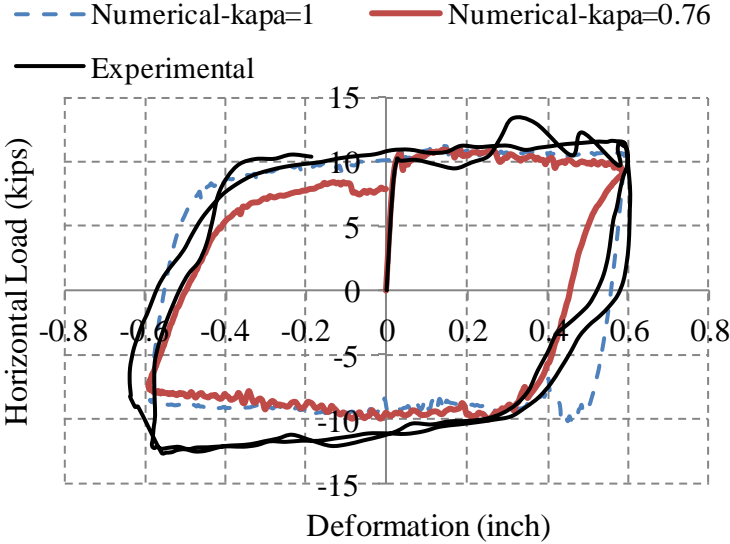
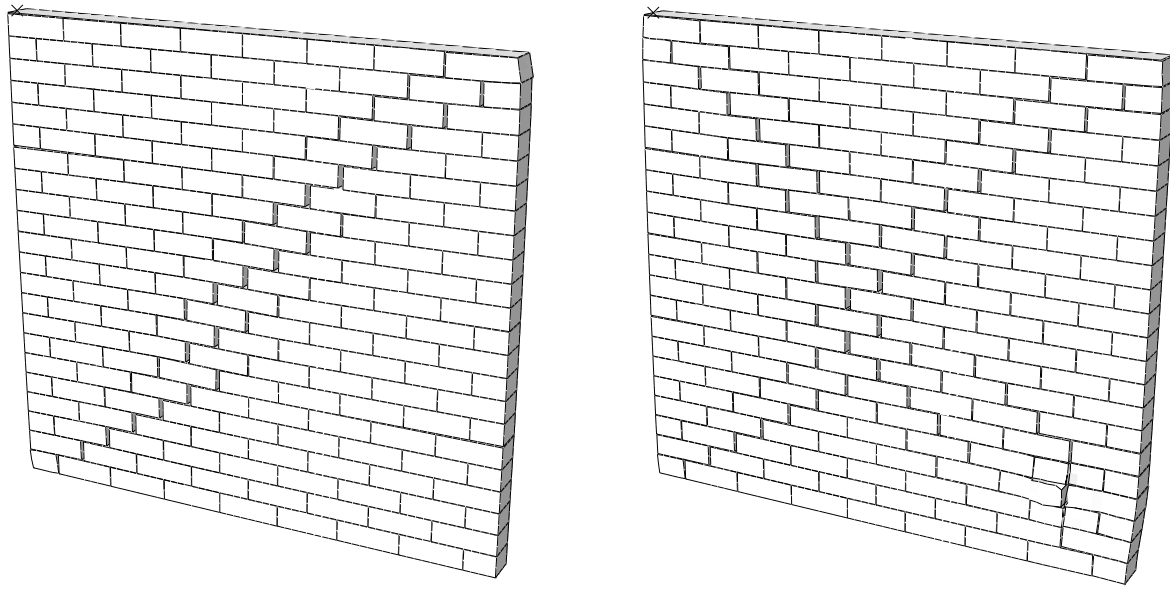


Figure 8-29. Comparison of numerical and experimental results

In Figure 8-30 crack propagation obtained from the numerical model is presented, which similar to the experimental observations, shows propagation of two perpendicular diagonal cracks in the wall. As shown in Figure 8-30 (a), after displacement of the top plane of the wall toward left, a diagonal crack has propagated from the top right corner to the left bottom corner of the wall. As the direction of the load changed (Figure 8-30 (b)), a new diagonal crack perpendicular to the first diagonal crack has propagated.



(a) Numerical results at -0.6'' deformation
($\times 2$)

(b) Numerical results at the end of loading
(real scale)

Figure 8-30. Crack propagation obtained from the numerical modeling

Using ASCE 41 (2006) proposed equations presented in equations (8-2) and (8-3), the failure forces for rocking and shear failure modes are 13 *kip* (57.8 *kN*) and 9 *kip* (40 *kN*), respectively. Based on ASCE 41 the failure mode is shear which is in agreement with the experimental observations; however, the predicted failure force of ASCE 41 under predicts the experimental results.

8.5.2 Testing of Wall 2

Bidirectional behavior of masonry walls could be investigated using two approaches to impose the out-of-plane loading, a deformation-controlled loading or a force-controlled loading. In the first approach (deformation-controlled loading), two actuators were needed to impose the out-of-plane deformation-controlled loading that based on the resources of the lab was not chosen. The second approach (force-controlled loading) could be performed by hanging a weight in the out-

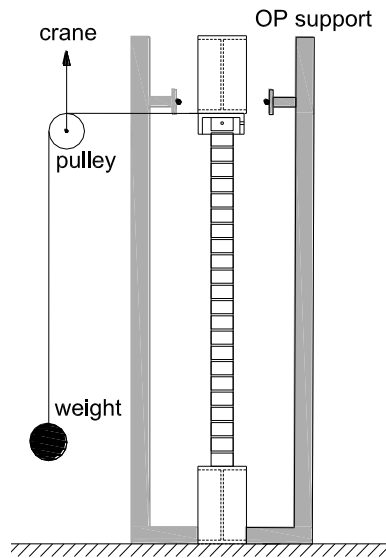
of-plane direction (Figure 8-31 (b)) that was more practical and was chosen for the second wall. The second wall was tested using a quasi-static monotonic in-plane displacement-controlled loading, with contribution of an out-of-plane load of 75 *lb*. Throughout the test, the south vertical actuator was force-controlled, maintaining a constant force of 6.5 *kips* (28.9 *kN*); however, the north vertical actuator was displacement-controlled in such a way that the rigid beam remained level during the test. This boundary condition, in contrast to wall 1, created a confined condition for the wall; therefore, more crushed bricks were observed comparing to the rest of the tests. In order to apply the out-of-plane load, first the axial load was applied, and then while keeping the axial load constant, the out-of-plane force was imposed (equal to 75 *lb* – see Figure 8-31). Afterward, the horizontal monotonic in-plane load was gradually applied.



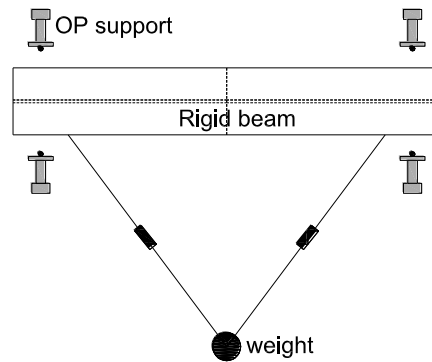
(a) A view of the wall 2



(b) Out-of-plane loading set-up



(c) Side view



(d) Plan view

Figure 8-31. Experimental set-up for wall 2

After completion of the diagonal crack, the direction of the monotonic loading was reversed to see the behavior of the cracked wall in the opposite direction, as shown in Figure 8-32.

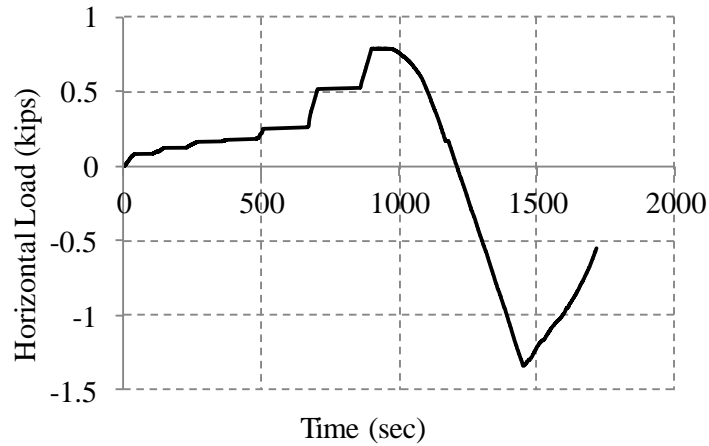


Figure 8-32. Loading protocol for wall 2

The load-displacement curve for wall 2 is presented in Figure 8-33. Due to the high confinement of the wall in the loading toward the positive direction, the resisting force was three times greater than the resisting force in wall 1. Once the direction of the loading changed the total axial load on the wall clearly decreased and therefore, the peak resisting force in the load reversal was much lower than the peak load in the opposite direction (Figure 8-33).

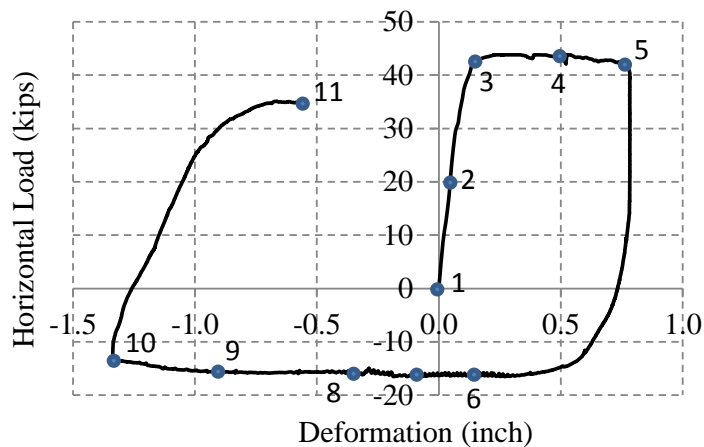


Figure 8-33. Load-displacement curve for wall 2

Considering 1/3 of the peak load in Figure 8-33, stiffness of the wall is 240 *kip/inch*. Using modulus of elasticity and shear modulus of the masonry prism, the predicted stiffness of the wall

based on ASCE 41 is 490 kip/inch (85848 kN/m) which comparing to the experimental results of 240 kip/inch (42048 kN/m) is much higher.

Figure 8-34 shows the displacement of the south and north vertical actuators versus time. It is clear that two actuators moved together and the rigid beam was maintained level throughout the test. By comparing Figure 8-32 and Figure 8-34 it can be concluded that, when the loading was toward the positive direction, the top rigid beam moved toward bottom, which shows a great confinement of the wall.

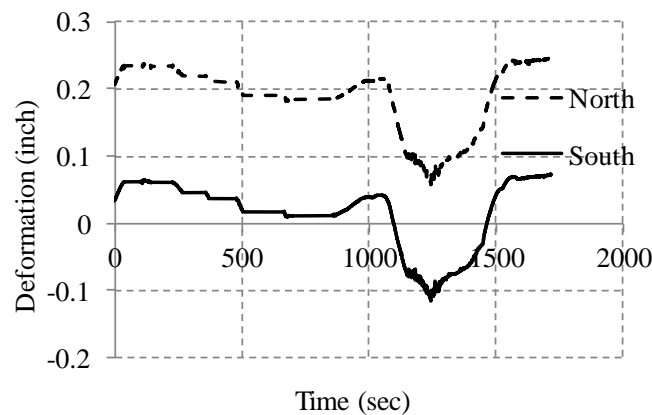


Figure 8-34. Displacment of the vertical actuators

Figure 8-35 presents the out-of-plane deformation of the rigid beam in the south and north corners of the wall. For the purpose of safety and to stop the wall from collapsing in the out-of-plane direction, two supports were assigned close to the rigid beam and at a distance of 2.5 inch (6.35 cm) from the wall. As shown in Figure 8-35 the north part of the rigid beam came in contact with the out-of-plane support while the horizontal load was applied. During the test the out-of-plane deformation of the wall was gradually increased and in case of not supporting the wall in the out-of-plane direction, the wall would collapse due to the large out-of-plane deformation.

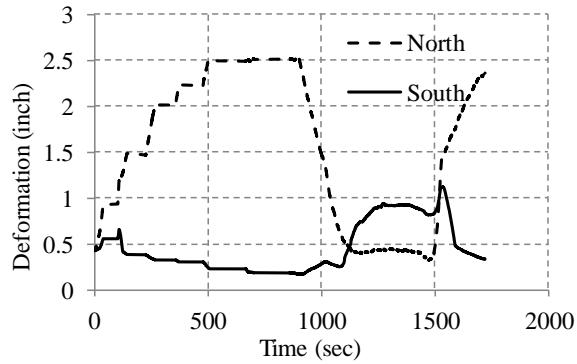


Figure 8-35. OP displacement of the north and south side of the top plane of the wall

The deformation map of the wall, obtained by Krypton LED's, under full cyclic loading is presented in Figure 8-36. In this figure the deformations are magnified to better demonstrate the deformation map of the wall. Based on Figure 8-36, the right and bottom LED's did not have much deformation when compared to the rest of the LED's. In fact, after propagation of the diagonal crack, application of a greater load only led to more opening of the existing diagonal crack and not much deformation took place in the bottom right portion of the wall. The peak residual opening in the wall, at the end of the test was about 33 mm (1.3 inch), as shown in Figure 8-36. In addition, Figure 8-36 shows that throughout the test the right and top portions of the wall moved according to the movement of the rigid beam (see Krypton LED 4 and 5). Therefore, no sliding occurred between the wall and the top rigid beam.

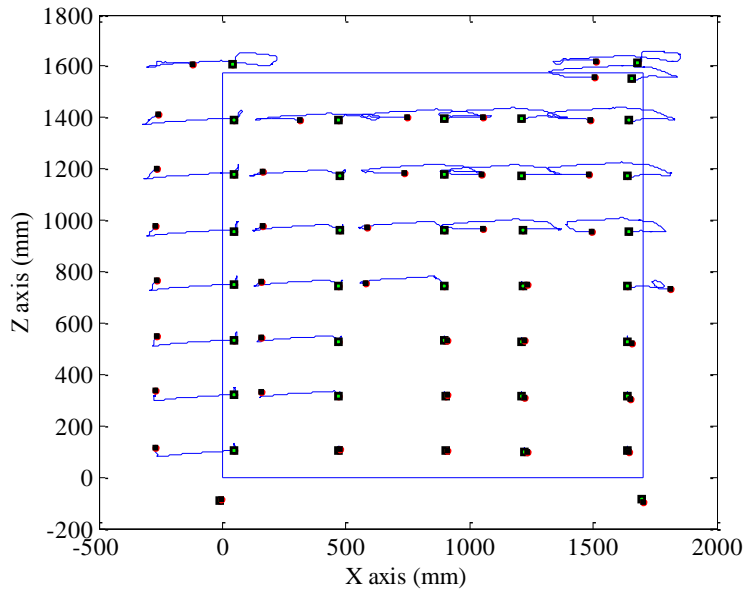
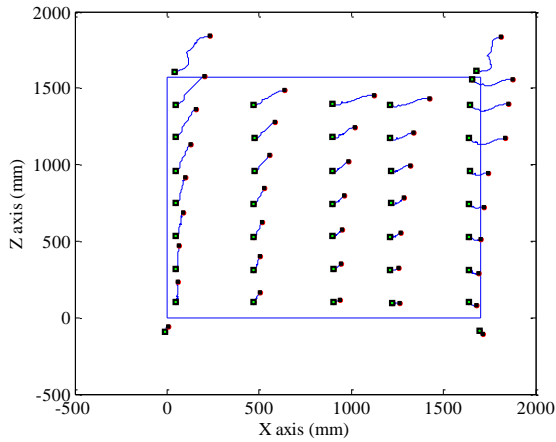
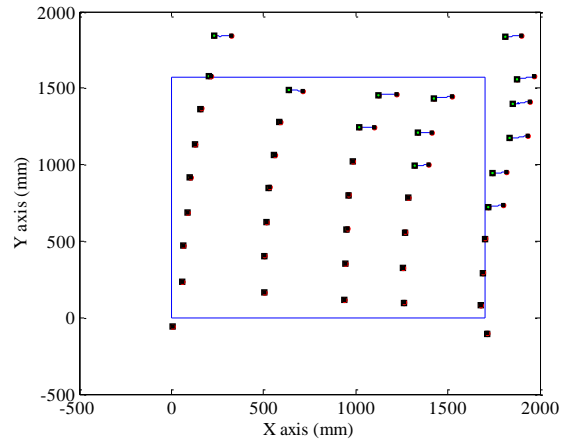


Figure 8-36. In-plane movement of LED's ($\times 10$)

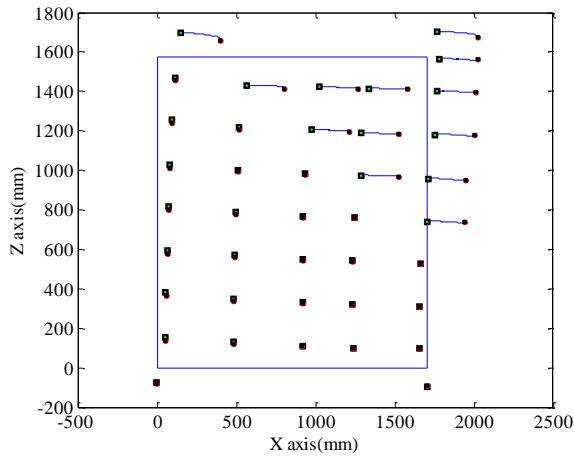
Figure 8-37 presents the deformation of LED's in different stages of loading, according to the marked points in Figure 8-33. For instance, Figure 8-37 (a) presents the deformation map as the loading in Figure 8-33 increases from point 1 to point 2. In this stage of loading the wall was entirely elastic and no major damage could be seen in the wall. In Figure 8-37 (b) and (c) LED's in the top and right side of the wall had much larger deformation comparing to the rest of LED's. This result is in accord with the observations in the lab and Figure 8-40 which shows propagation of a diagonal crack in the wall.



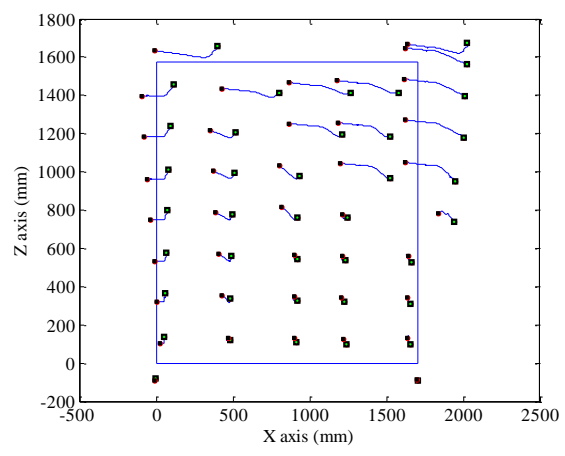
(a) Loading from point 1 to point 2 ($\times 50$)



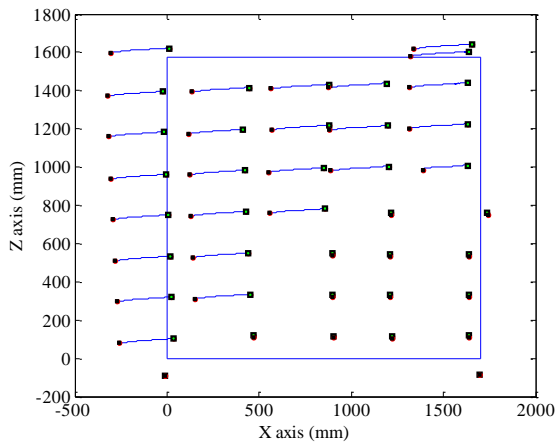
(b) Loading from point 2 to point 3 ($\times 50$)



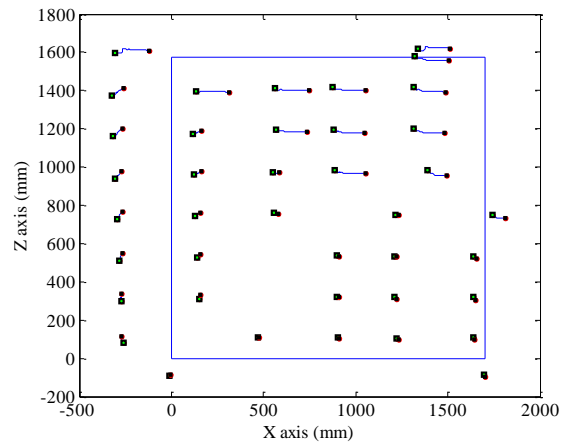
(d) Loading from point 3 to point 5 ($\times 20$)



(e) Loading from point 5 to point 7 ($\times 20$)



(f) Loading from point 7 to point 10 ($\times 10$)



(g) Loading from point 10 to point 11 ($\times 10$)

Figure 8-37. Deformation of Krypton LED's in different stages of loading

Further application of the horizontal load only led to more propagation of the existing diagonal crack in Figure 8-37 (c). As the direction of the load changed, first the existing crack in the wall was closed (Figure 8-37 (d)), and then followed by a new diagonal crack, perpendicular to the existing propagated crack (Figure 8-37 (e)).

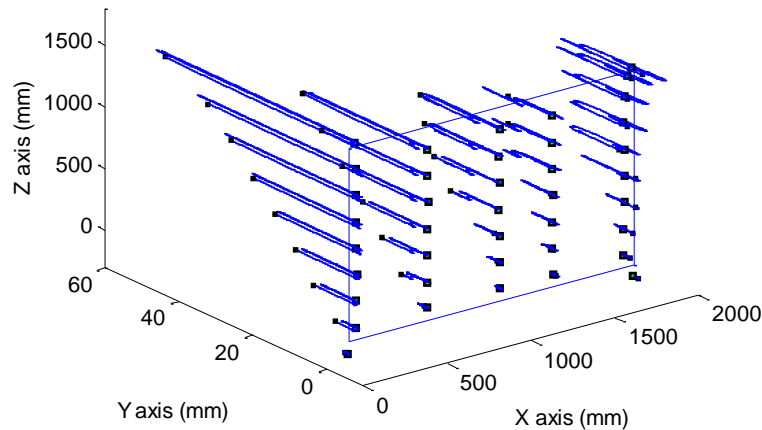
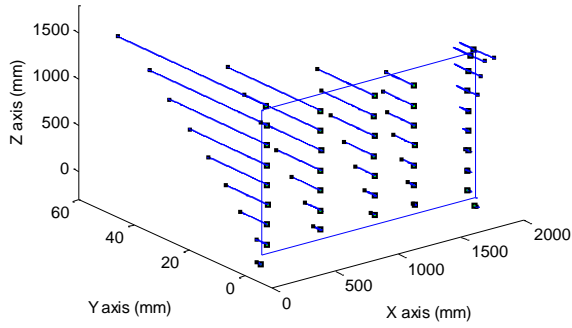
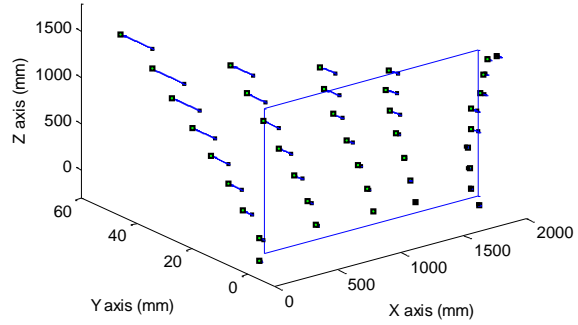


Figure 8-38. 3-D movement of LED's (real scale)

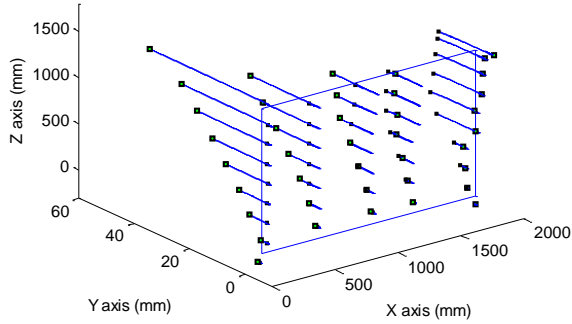
Figure 8-38 presents the three-dimensional deformation of LED's throughout the loading, according to the marked points in Figure 8-33. As shown in Figure 8-38 the out-of-plane deformation of the wall was much greater than the in-plane deformation. As discussed in the previous section, in case of not providing an out-of-plane support, the wall would collapse due to the large out-of-plane deformation. In Figure 8-38, the smaller square points represent the location of the wall in the final stage of loading. Based on Figure 8-38 it can be concluded that a relative residual OP deformation has taken place which is mostly clear and visible in the surfaces that the diagonal crack took place.



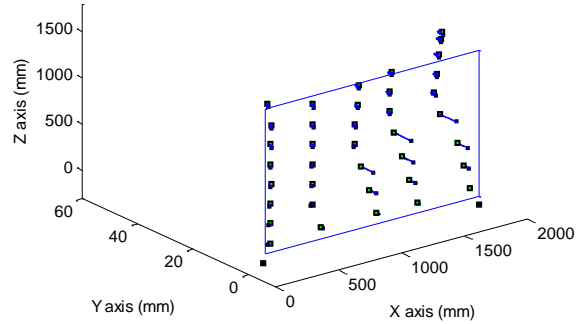
(a) Loading from point 1 to point 3



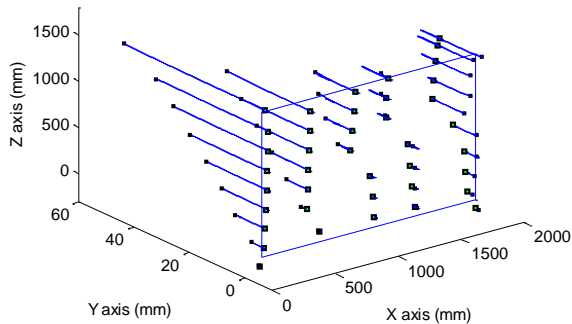
(b) Loading from point 3 to point 5



(c) Loading from point 5 to point 7



(d) Loading from point 7 to point 10

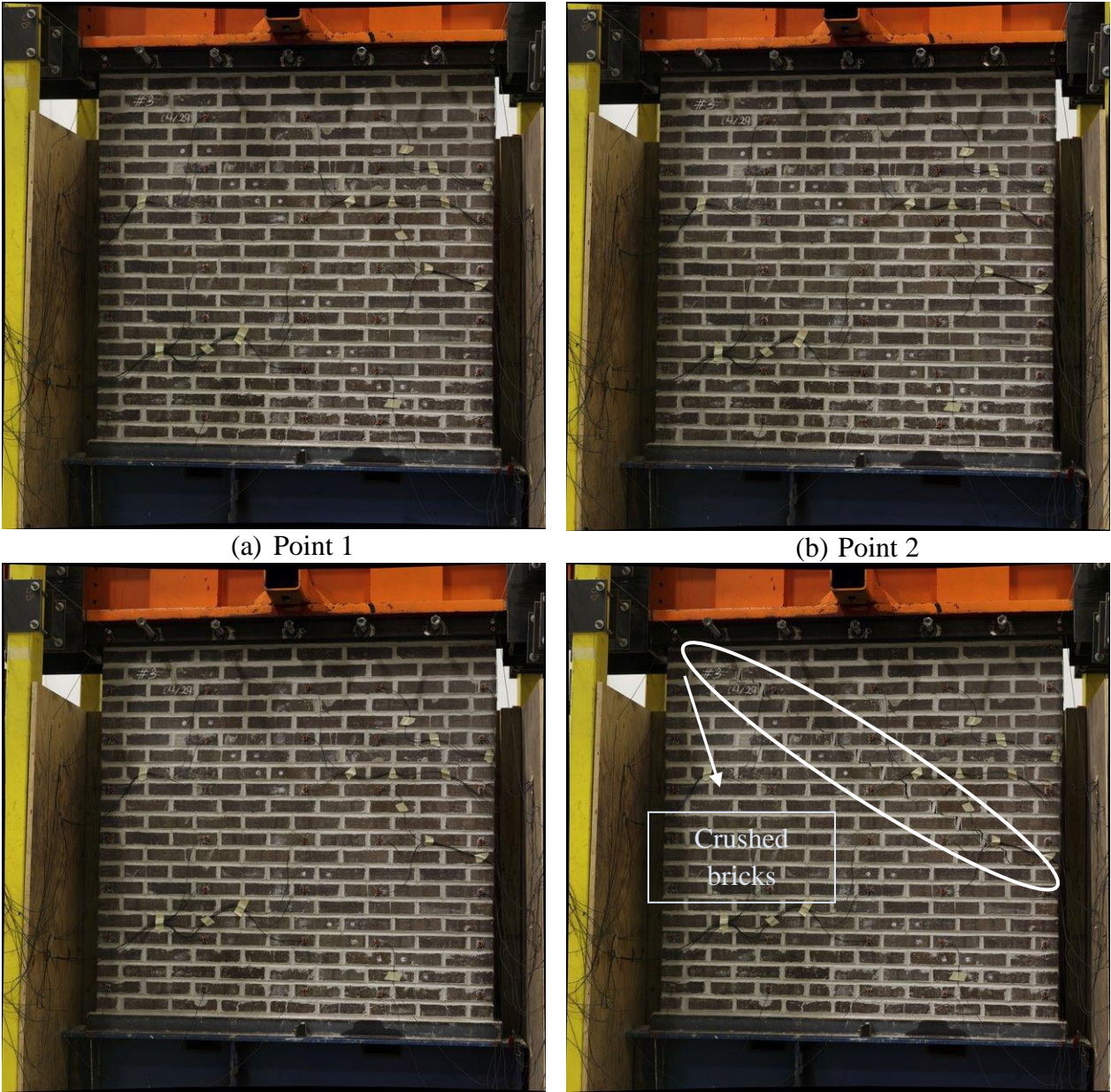


(e) Loading from point 7 to point 11

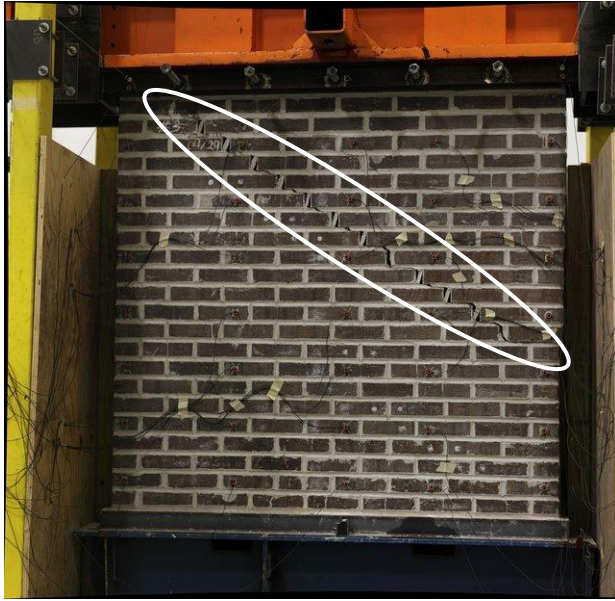
Figure 8-39. 3-D displacement of LED's in different stages of loading (real scale)

Figure 8-39 presents the 3-D displacement of LED's during different stages of loading, according to the marked points in Figure 8-33. In the first stage of loading the north side of the top plane of the wall had a large deformation in the OP direction and came in contact with the support (Figure 8-39 (a)). In addition to the effect of out-of-plane load, due to the out-of-plane force component of the inclined horizontal actuator, the wall was subjected to a significant torsion. In this stage, the wall was still in the linear regime and all points deformed proportional

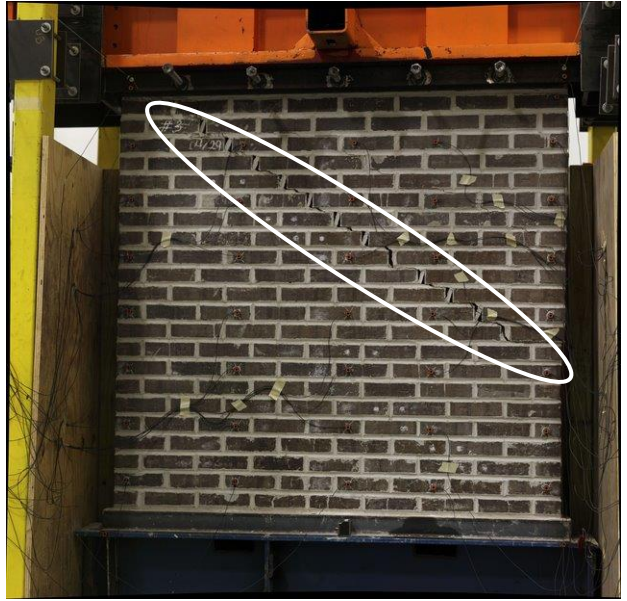
to their height. However, according to Figure 8-39 (c) to (e) it is clear that the OP deformation did not remain linear and a relative and residual displacement in the OP direction took place along the height. Figure 8-40 presents experimental pictures of the wall in different stages of loading, according to the marked points in Figure 8-33 that shows propagation of two diagonal cracks in the wall. Moreover, due to the high confinement of the wall in this test, a number of bricks crushed in the top left corner of the wall (Figure 8-40 (d)).



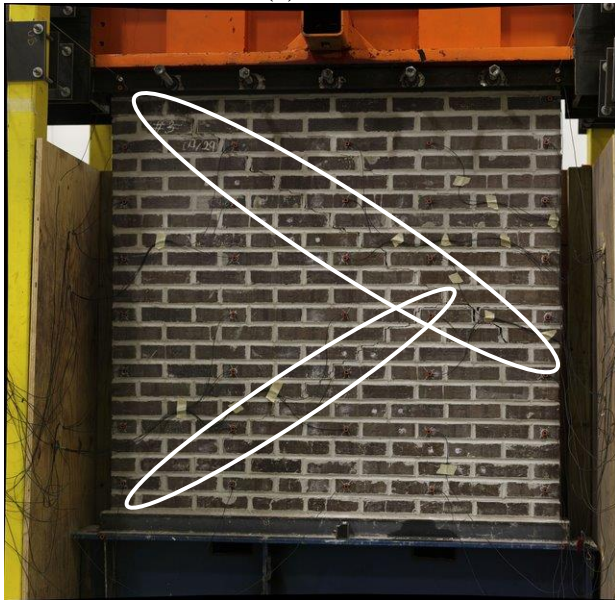
(c) Point 3



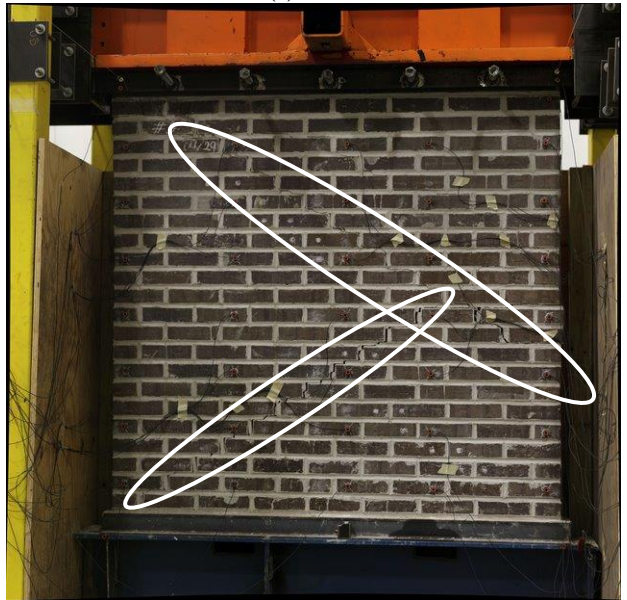
(d) Point 4



(e) Point 5

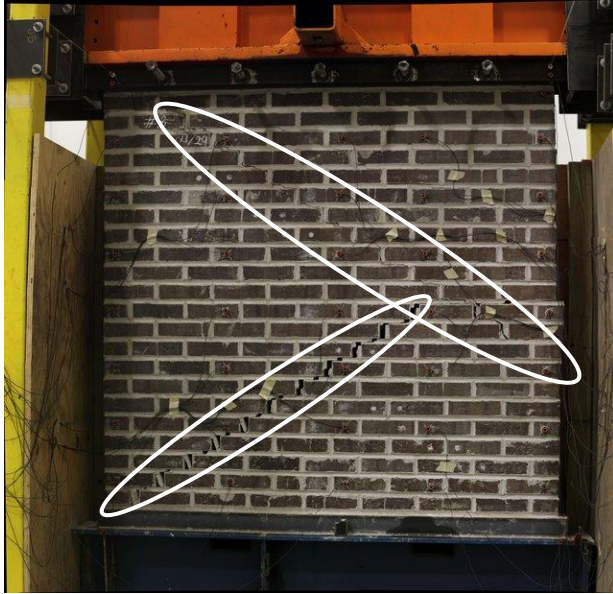


(f) Point 6

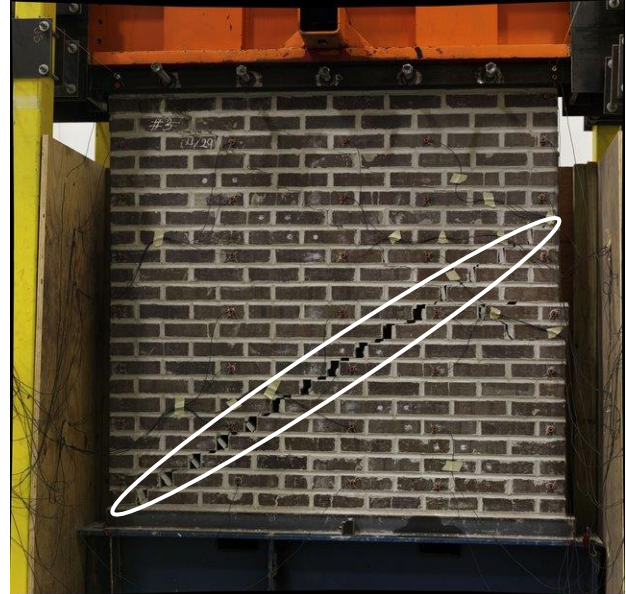


(g) Point 7

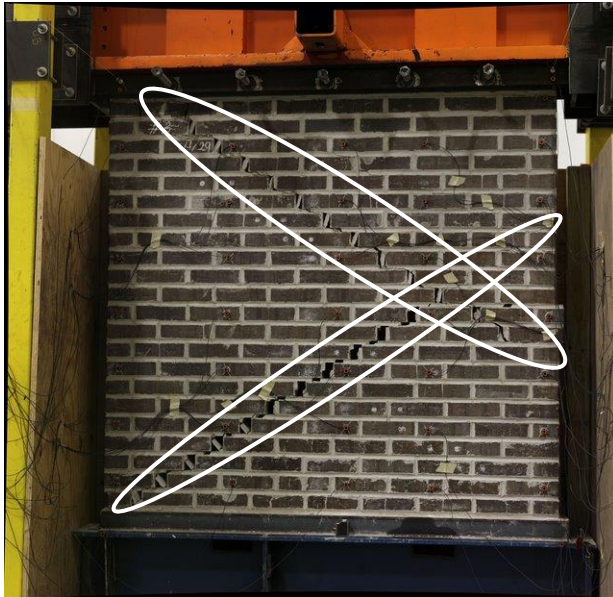
(h) Point 8



(i) Point 9



(j) Point 10



(k) Point 11

Figure 8-40. Crack propagation of the wall in different stages of loading

8.5.2.1 Numerical simulation of wall 2

In this section the finite element model of wall 2 has been generated and subjected to five different loading conditions, including an IP loading with a constant axial load, an IP loading with a confined boundary condition, and three simulations including an OP force with different magnitudes (50, 100 and 150 lb).

To impose the boundary condition for the confined wall, first the axial load has been applied (22 kips), second the vertical displacement of the top plane is restrained and then an IP load has been applied. For the rest of the models first the axial load, second the OP force, and consequently the IP load has been applied while keeping the axial and OP forces constant. In all loading protocols the top plane was constrained to remain level throughout the loading.

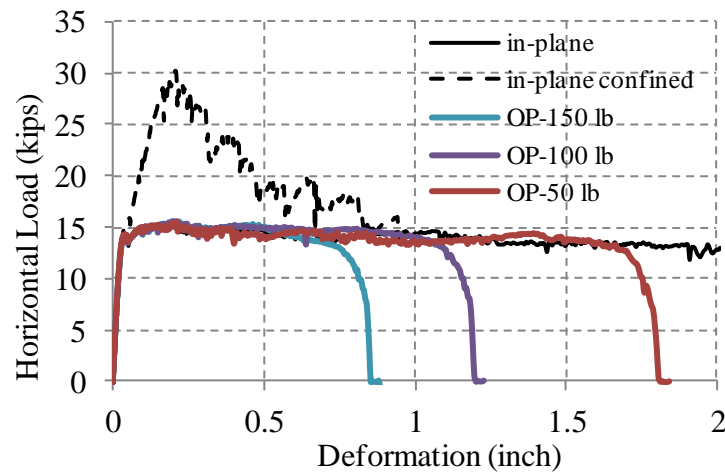


Figure 8-41. Load-displacement curves obtained by the numerical model considering different OP loads

As shown in Figure 8-41 the confined model (dashed line) has the greatest peak force. All the models initially have identical behavior (stiffness and force); however, those models with out-of-plane loading collapse after a particular in-plane displacement. Figure 8-42 presents the relation between in-plane and out-of-plane displacements for the models with out-of-plane loadings. Initially the OP displacement is very small; however, for the larger in-plane displacements the out-of-plane displacement significantly increases and finally the wall collapses in the out-of-plane direction. For models with more out-of-plane force the collapse takes place in a smaller in-plane deformation.

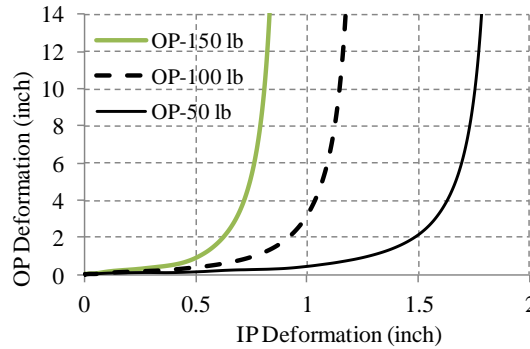


Figure 8-42. Proportion of IP and OP deformations

8.5.3 Testing of Wall 3

The third wall was tested in the in-plane direction and with a cyclic loading protocol. In the first step of loading the axial load was applied on the top plane of the wall (12.5 kip+5.5 kip weight of the rigid beam), afterward, while keeping the axial load constant, a deformation-controlled cyclic loading was applied horizontally at top of the wall (Figure 8-43). The vertical actuators applied the axial load while keeping the top rigid beam level.

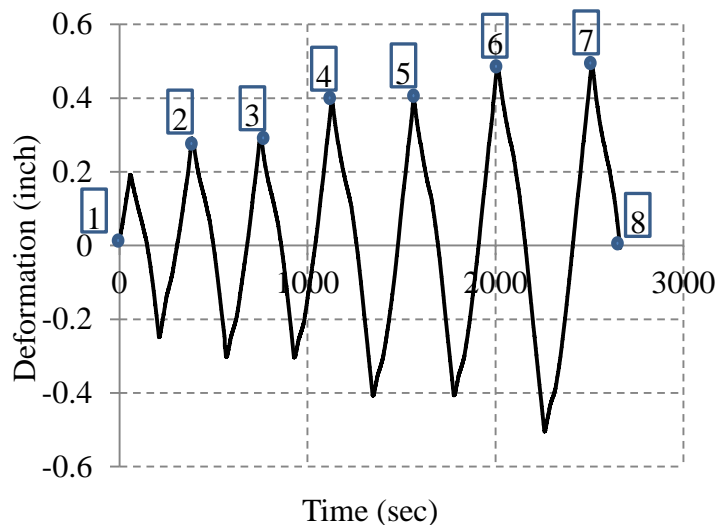


Figure 8-43. Cyclic loading protocol for the third wall

The load-displacement curve obtained from the test is presented in Figure 8-44. Unfortunately, due to some technical problems the controller did not save the data for the first three cycles (two cycles with 0.1 inch displacement and a cycle with 0.2 inch displacement). In this figure, the displacement is presented using the Krypton LED 5 data, as shown in Figure 8-17. As it is clear in Figure 8-44, the cyclic loading was associated with degradation in stiffness and slightly in strength. However, finally the maximum strength of the wall remained constant which corresponds to the frictional force. Not much stiffness and strength degradation can be seen in the loops with the same displacement amplitude.

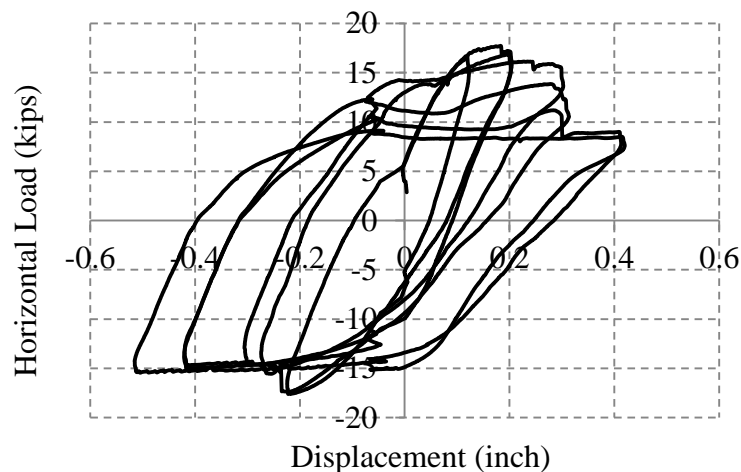


Figure 8-44. In-plane load-displacement curve of wall 3

Figure 8-45 represents the vertical displacement of the north and south vertical actuators. As shown in Figure 8-45, throughout the test the north and south vertical actuators moved together and the rigid beam remained level.

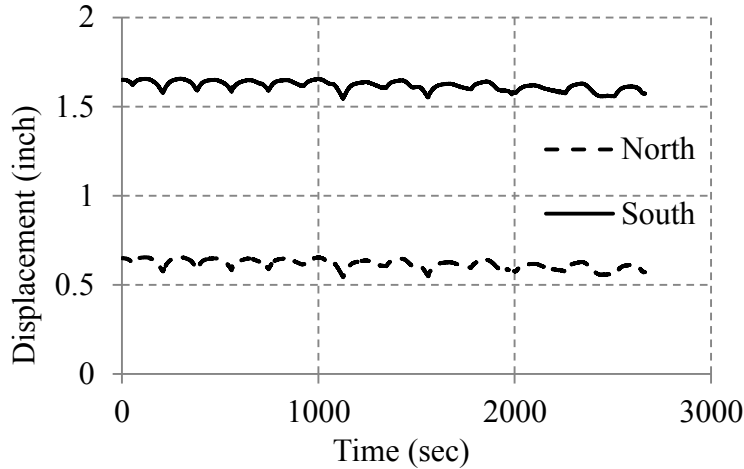


Figure 8-45. Displacement of the north and south vertical actuators

The rigid beam remained level while maintaining a constant axial load on the top of the wall; therefore, at each time increment, the controller distributed the axial load in two vertical actuators in such a way that the summation of the axial loads remained constant (12.1 *kip*). Figure 8-46 presents the distribution of the axial load in the north and south vertical actuators. For all numerical simulations the weight of the rigid beam should be added to the vertical load presented in Figure 8-46 (5.5 *kip*). The boundary condition for this wall represents a URM wall in a building with a rigid diaphragm.

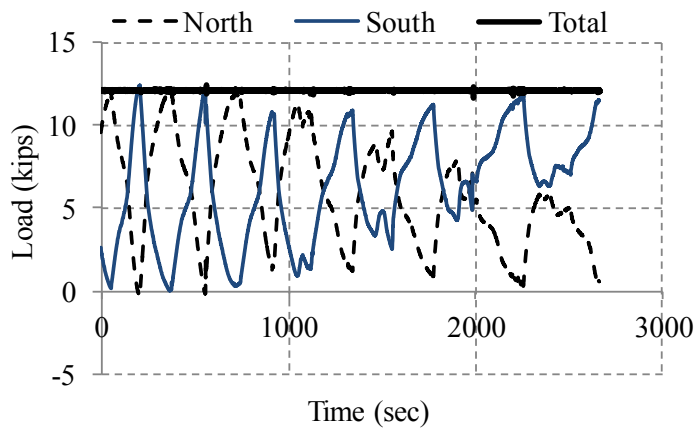


Figure 8-46. Distribution of the axial load in the north and south vertical actuators

The deformation map of the wall under the axial load is presented in Figure 8-47. As expected, all of the points had an almost vertical deformation. Moreover, based on the elasticity theory, upper points had more deformations when compared to the lower points.

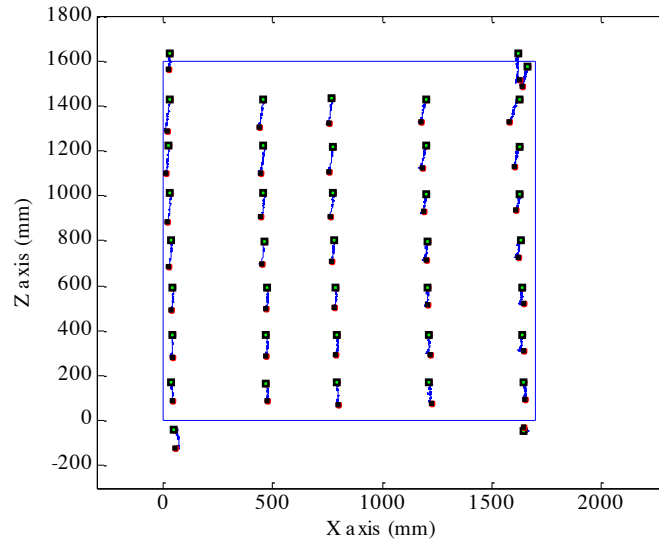


Figure 8-47. Deformation of the wall under the axial load ($\times 500$)

Figure 8-48 presents the deformation map of the wall under full cyclic loading. According to Figure 8-48, after propagation of the diagonal crack, right and left side of the wall increasingly separated in each cycle. The peak residual opening in the wall, at the end of the test was about 40 mm, as shown in Figure 8-48. Throughout the test, the right and top portion of the wall moved according to the movement of the rigid beam, which indicates that no sliding took place between the wall and support.

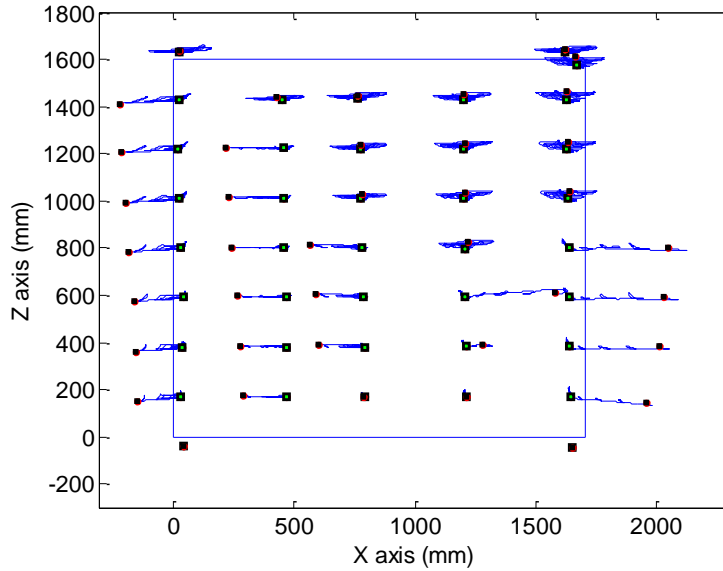
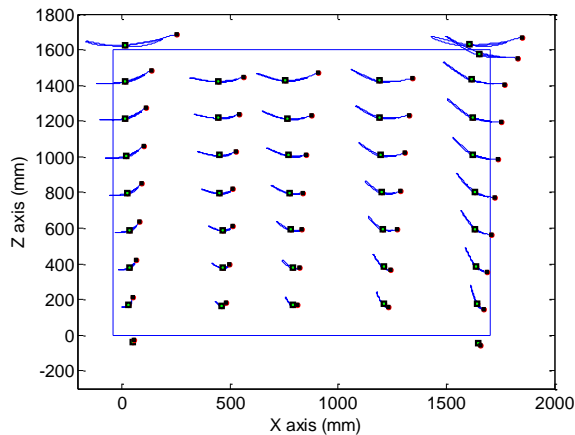
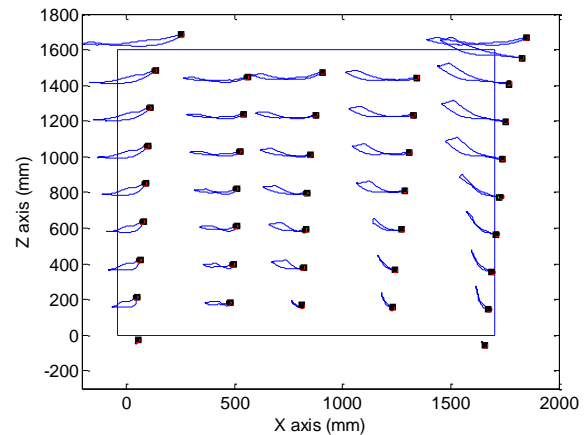


Figure 8-48. Deformation of the wall under cyclic loading ($\times 10$)

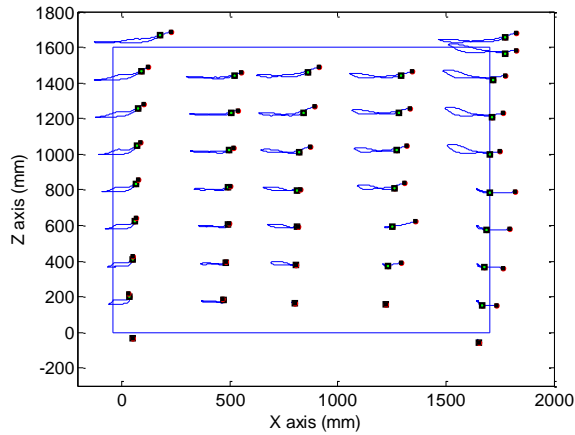
The incremental motion of the wall is presented in Figure 8-49, according to the marked points in Figure 8-43. In Figure 8-49 (a) and (b) almost all of the points moved proportionally to their height; therefore, not much nonlinearity has taken place. However, in the rest of the figures (Figure 8-49 (e) to (g)) Krypton LED's did not move proportionally to their heights and that indicates nonlinear behavior and propagation of diagonal cracks. From Figure 8-49 (c), gradually the right side of the wall separated from the left side of the wall and the distance increased until end of the loading (Figure 8-49 (g)).



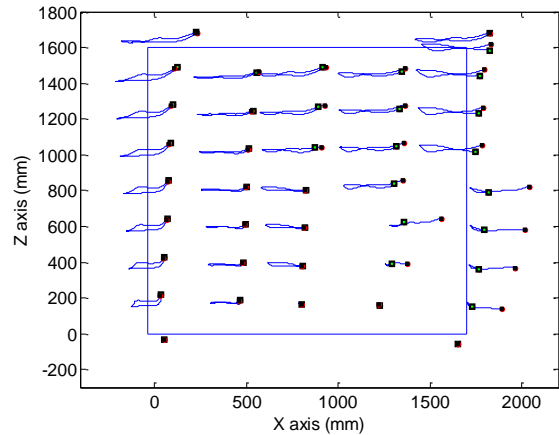
(a) Loading from point 1 to point 2 ($\times 30$)



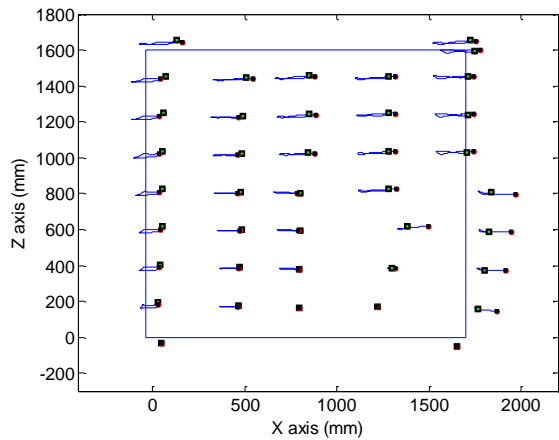
(b) Loading from point 2 to point 3 ($\times 30$)



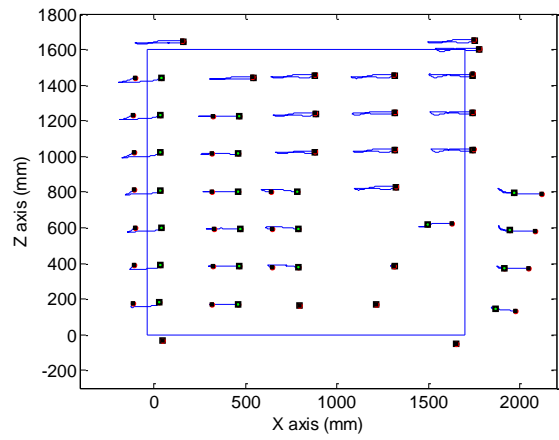
(c) Loading from point 3 to point 4 ($\times 20$)



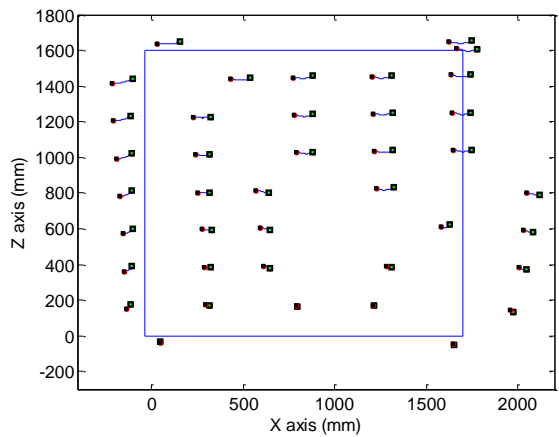
(d) Loading from point 4 to point 5 ($\times 20$)



(e) Loading from point 5 to point 6 ($\times 10$)



(f) Loading from point 6 to point 7 ($\times 10$)



(g) Loading from point 7 to point 8 ($\times 10$)

Figure 8-49. Deformation of the wall in different stages of loading

Figure 8-49 (c) to (g) indicates onset of the crack and separation of the bottom right portion of the wall, which is in accord to the experimental observations in Figure 8-50. Figure 8-50 presents crack propagation obtained from the test in different steps of the loading, according to the marked points in Figure 8-43. Propagation of the diagonal crack was observed from Figure 8-43 (c) and it became more visible in Figure 8-43 (d) to (h).



(a) Point 1



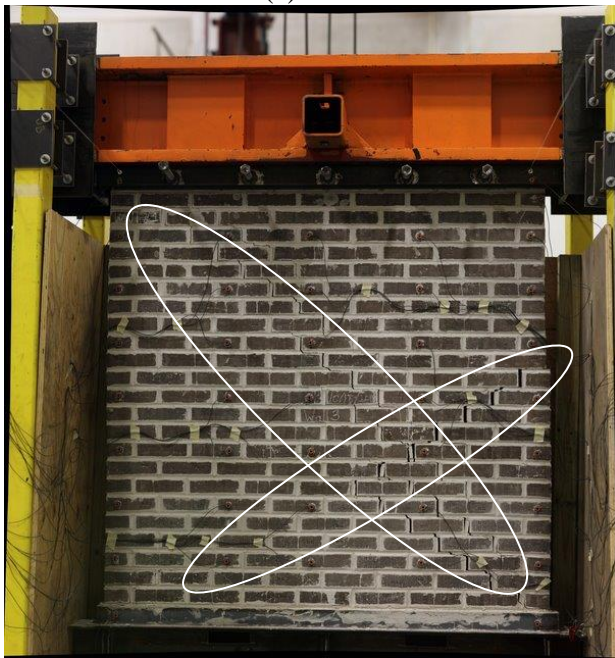
(b) Point 2



(c) Point 3



(d) Point 4



(e) Point 5



(f) Point 6

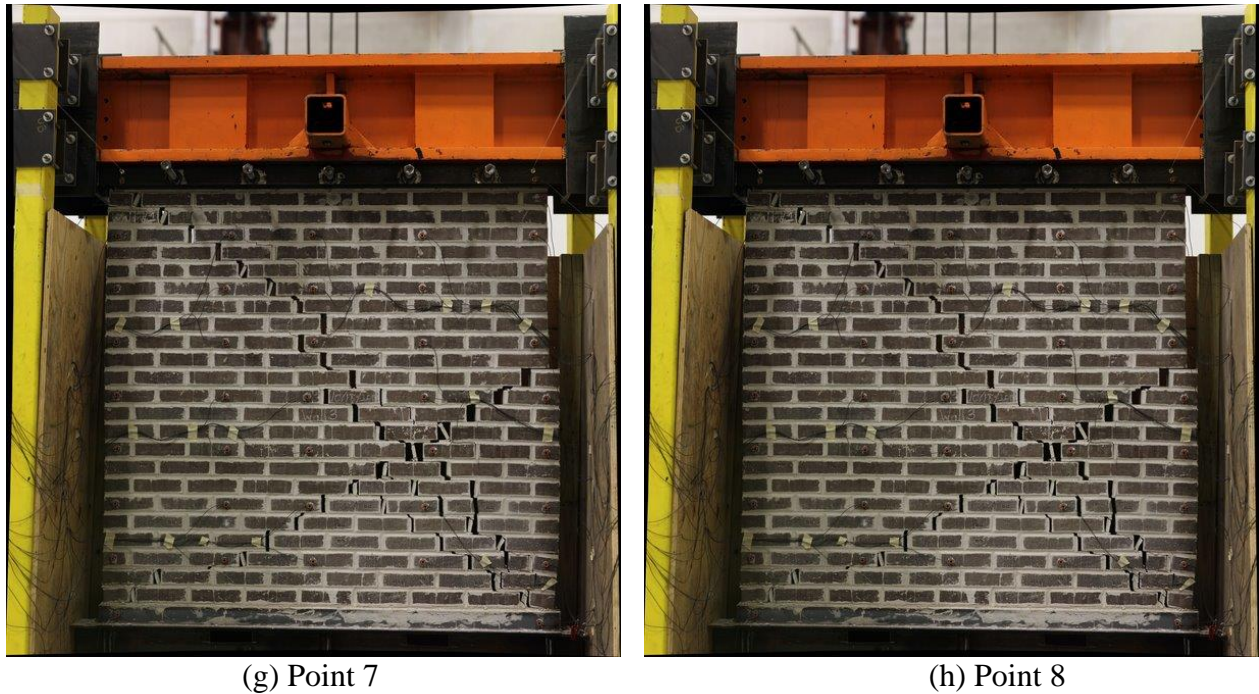


Figure 8-50. Crack propagation of the wall in different stages of loading

8.5.3.1 Comparison of the experimental and finite element results of wall 3

A finite element model using the material model of section 8.2 has been generated to perform the numerical comparisons. Based on the experimental observations, not much degradation has been seen in the cycles with the same amplitude; therefore, in order to decrease the computational effort and analysis time, a cyclic loading without repeated cycles and according to Figure 8-51 has been used for the numerical loading protocol.

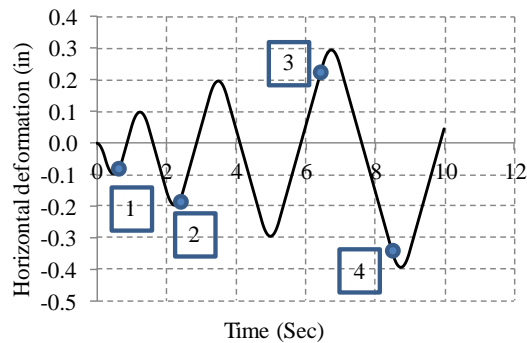
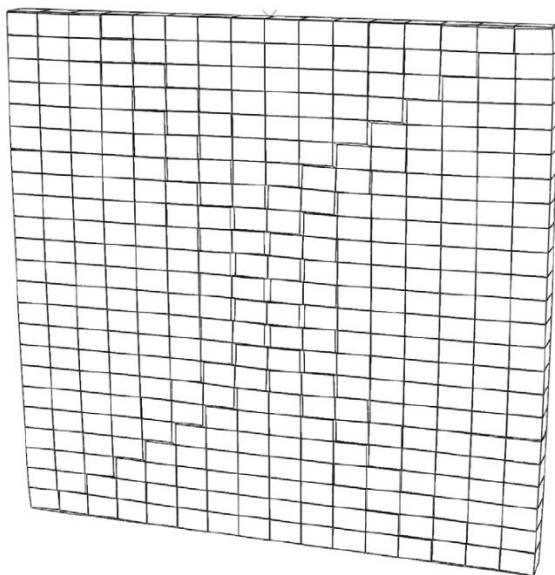


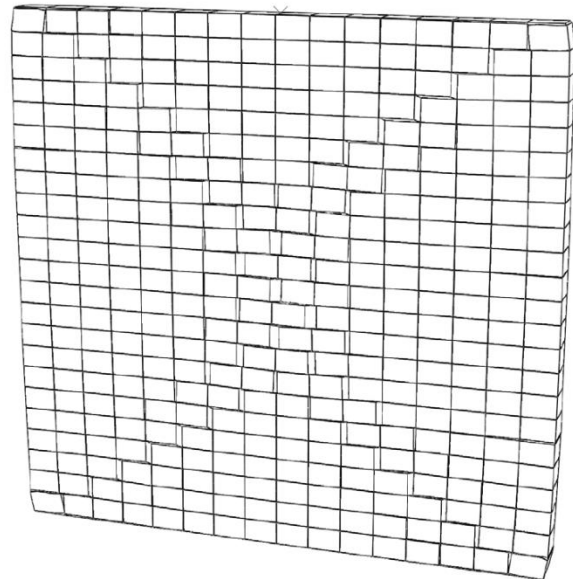
Figure 8-51. Loading-protocol for numerical model

In Figure 8-53 the experimental results are simultaneously plotted with the numerical results, considering " $\kappa = 0.95$ ". It is clear that the numerical stiffness degradation is in good agreement to the experimentally obtained results.

The crack propagation in different stages of loading, according to the marked points in Figure 8-51, is presented in Figure 8-54. As the top plane of the wall moves toward left or right direction, a diagonal crack respective to the direction of the deformation propagates. Similar to the experimental observations in Figure 8-50, numerical results show that as the displacement of the top plane increases the propagated crack in the diagonal line opens more without any clear damage to the rest of the wall.



(a) Point 1 ($\times 15$)



(b) Point 2 ($\times 15$)

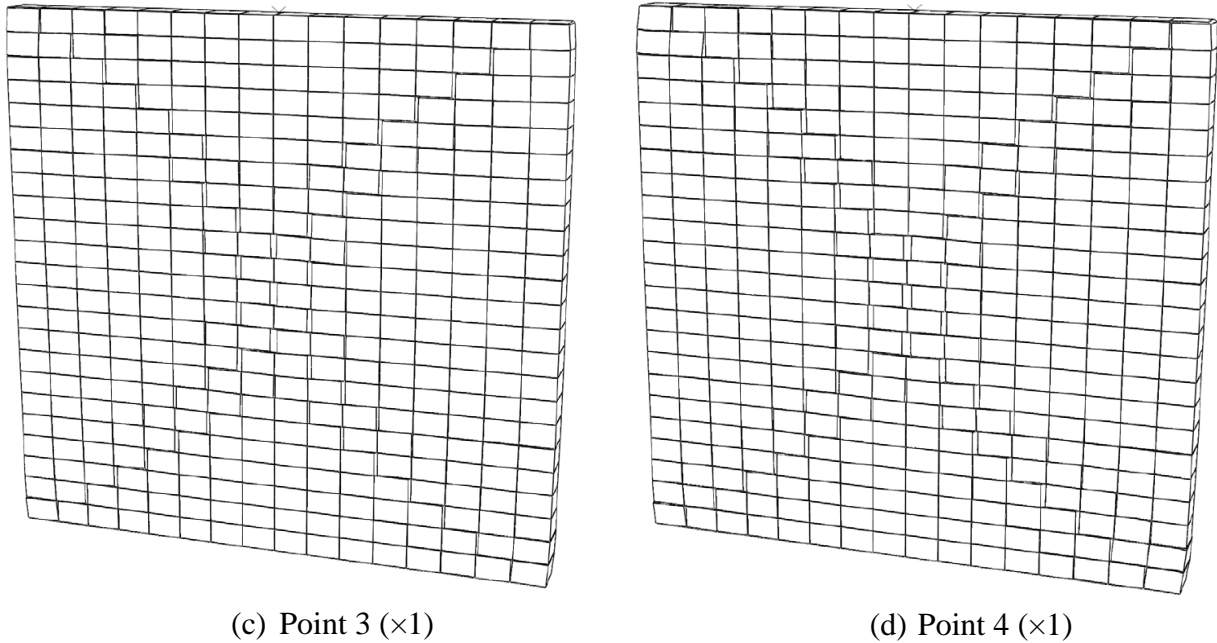


Figure 8-54. Numerical simulation of crack propagation in the wall

Using ASCE 41 (2006) proposed equations (equations (8-2) and (8-3)), the failure forces for rocking and shear dominated failure modes are 17 *kip* and 11 *kip*, respectively. Based on ASCE 41 the failure mode is shear which is in accord with the experimental observations; however, the proposed equation for failure force of ASCE 41 under predicts the experimental results.

8.5.4 Testing of Wall 4

The fourth wall was tested in the in-plane direction using a cyclic loading protocol and with the contribution of an OP force. In the first step of loading the axial load was applied on the top plane of the wall (16.5 *kips* plus 5.5 *kips* weight of the rigid beam), afterward, while keeping the axial load constant, an OP force was applied to the top rigid beam (50 *lb*). After application of the axial and OP forces, the cyclic loading protocol in accordance with Figure 8-55 was applied to the wall. The load protocol of Figure 8-55 is imposed based on the displacement of the rigid beam (SP.1 in Figure 8-17). Later, for presentation of load-displacement curve the displacement of the top plane of the wall is modified based on the Krypton LED 5 data. Throughout the test

the boundary condition for the rigid beam was imposed in such a way that the rigid beam remained level.

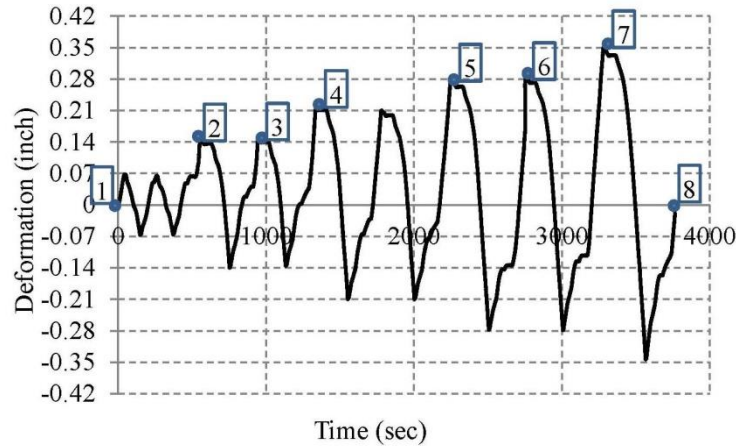


Figure 8-55. Loading protocol for wall 4

The test set-up for application of the OP force is presented in Figure 8-56. For the safety propose an out-of-plane support was considered at the distance of 2.1 *inch* (53 *mm*) from the wall (Figure 8-57).



Figure 8-56. Test set-up for out-of-plane load



Figure 8-57. Support for large out-of-plane deformation of the wall

The experimental load-displacement curves are presented in Figure 8-58. In Figure 8-58 (a) the displacement of SP. 1 is used in presentation of load-displacement curve. To make the result more reliable and practical, in Figure 8-58 (b) the displacement of Krypton LED 5 is used and the results are smoothed. As it is clear in Figure 8-58, the cyclic loading was associated with degradation in stiffness, however, not in the strength. Finally the maximum strength of the wall remained constant that corresponds to the frictional force.

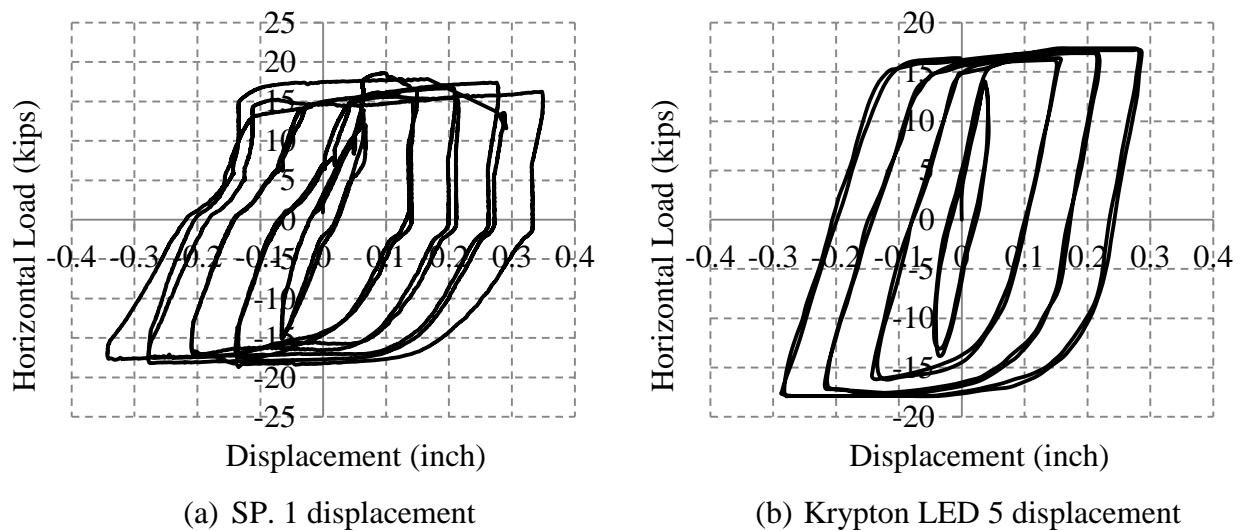


Figure 8-58. Load-displacement of wall 4

As it was mentioned before, the rigid beam remained level throughout the test. Figure 8-59 shows the axial displacement of the north and south vertical actuators. It is clear that throughout the test the north and south side of the rigid beam moved together and the rigid beam remained level.

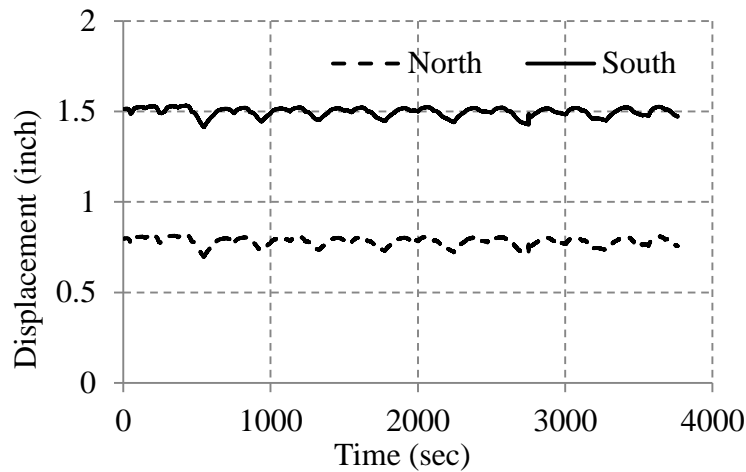


Figure 8-59. Displacement of the north and south vertical actuators

The rigid beam remained level while the total axial load was constant. This goal was achieved by distribution of the axial load in the north and south vertical actuators (Figure 8-60). At each time increment, the total axial load was distributed in two vertical actuators in such a way that the summation of the force remained constant (16.5 kip). Note that, for all numerical simulations weight of the rigid beam should be added to the presented vertical load in Figure 8-60 (5.5 kip).

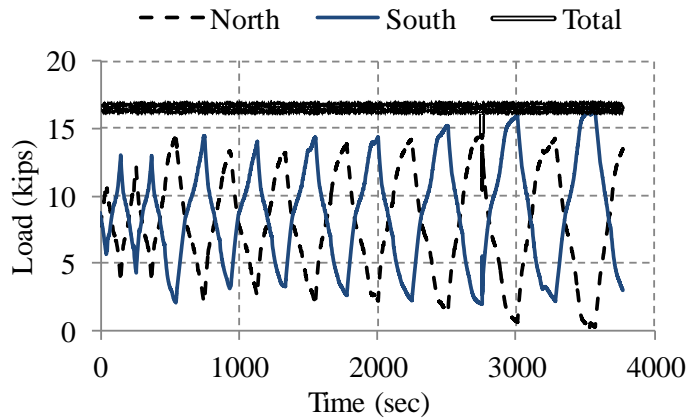


Figure 8-60. Axial loads in the south and north vertical actuators

Figure 8-61 shows the OP displacement of the north and south side of the top plane of the wall throughout the test. In this figure the information of the second and third linear potentiometers (SP.2 and SP.3 in Figure 8-17) is used. According to Figure 8-61, it can be concluded that in each cycle the north side of the top plane came in contact with the OP support. Therefore, if the OP supports were not provided the wall would collapse due to the large OP deformations.

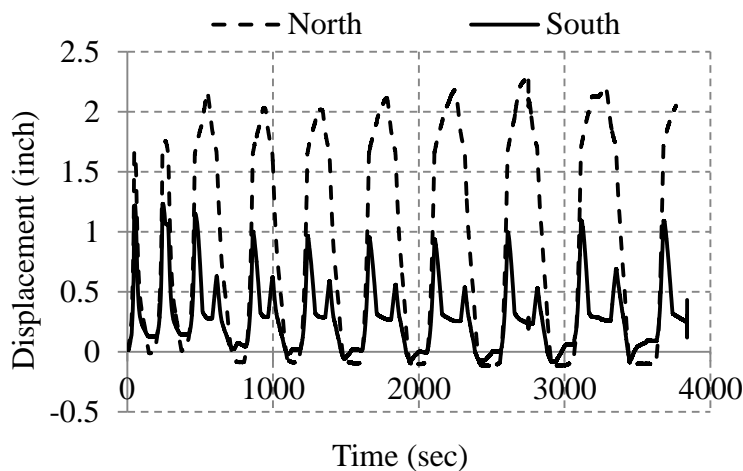


Figure 8-61. OP displacement of the north and south side of the top plane

Figure 8-62 presents the deformation map of the wall under full cyclic loading. The deformations in this figure are 10 times magnified. Clearly, no nonlinearity took place in the top half portion of the wall. Figure 8-62 illustrates that, after propagation of the diagonal crack, right

and left side of the wall increasingly separated in each cycle. The peak residual opening of the wall at the end of the test was about 29 mm (1.14 inch), as shown in Figure 8-62.

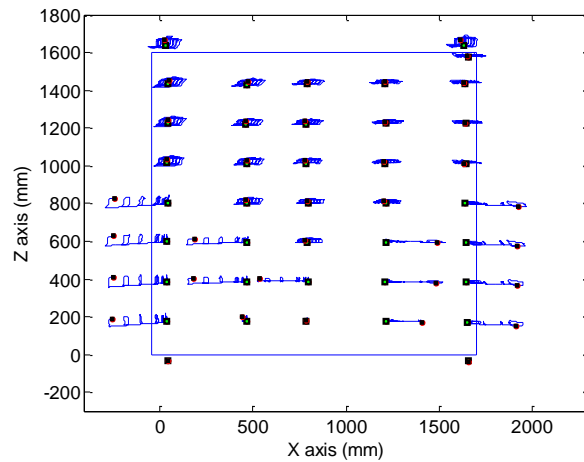
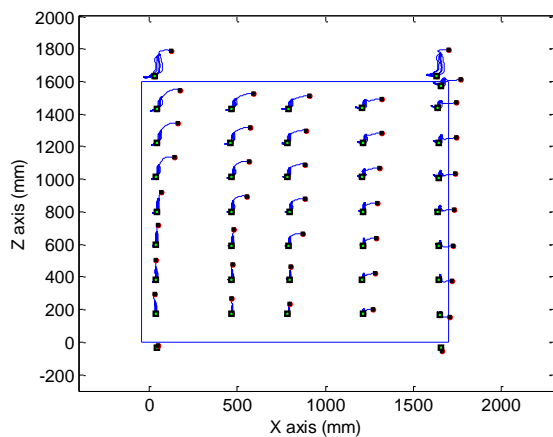
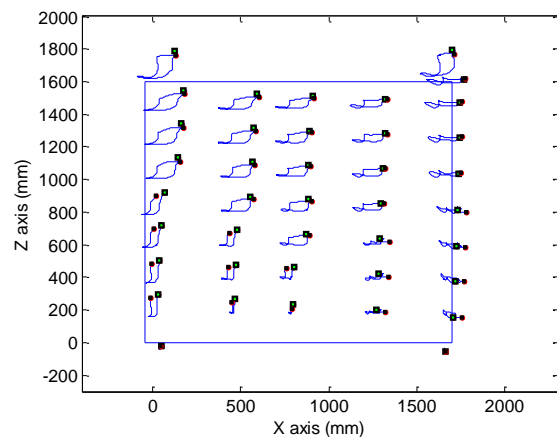


Figure 8-62. Deformation map of the wall under cyclic loading ($\times 10$)

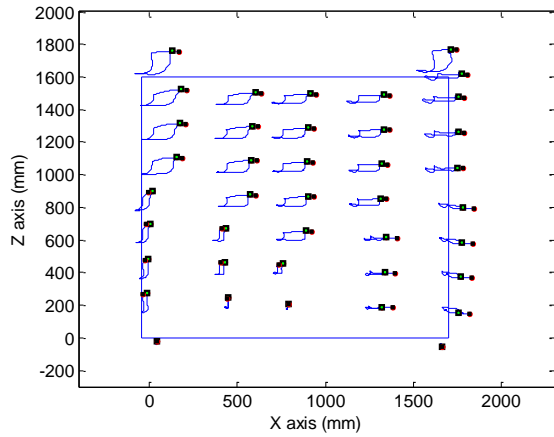
The incremental deformation of the wall is presented in Figure 8-63. In Figure 8-63 (a) and (b) all of the points were moving proportional to their height; therefore no nonlinearity has taken place. However, in the rest of the figures the nonlinearity and the propagation of the diagonal cracks are clear. Figure 8-63 (c) to (g) clearly shows how the right and left bottom portion of the wall separated as the loading increased.



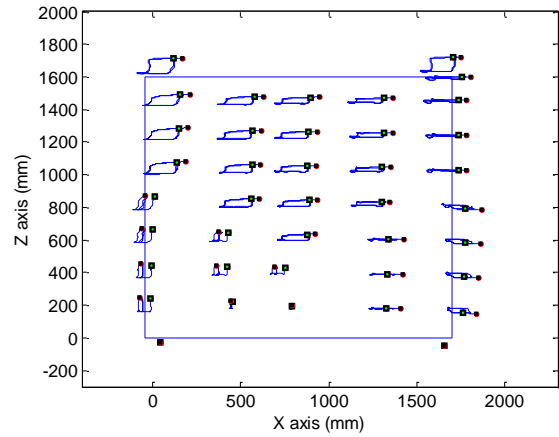
(a) Loading from point 1 to point 2 ($\times 30$)



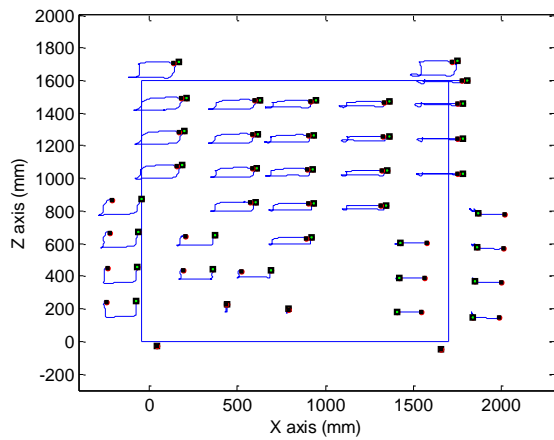
(b) Loading from point 2 to point 3 ($\times 30$)



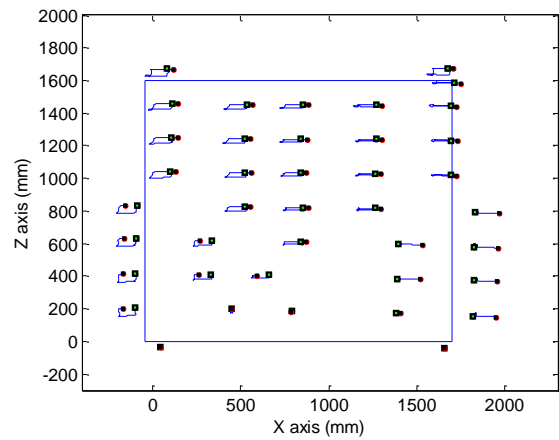
(c) Loading from point 3 to point 4 ($\times 30$)



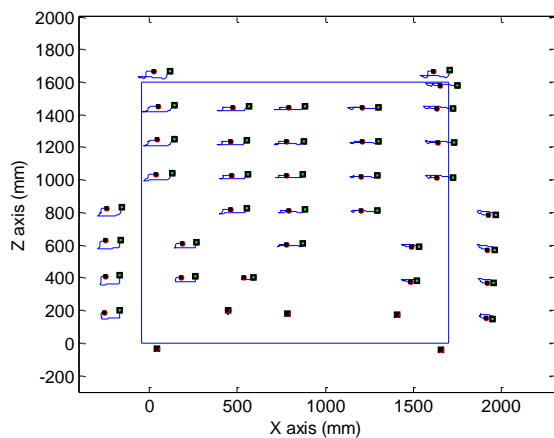
(d) Loading from point 4 to point 5 ($\times 20$)



(e) Loading from point 5 to point 6 ($\times 20$)



(f) Loading from point 6 to point 7 ($\times 10$)



(g) Loading from point 7 to point 8 ($\times 10$)

Figure 8-63. Deformation of the wall in different stages of loading

Figure 8-64 presents the crack propagation obtained from the test in different stages of loading according to the marked points in Figure 8-55. The advantage of Krypton data in Figure 8-63

comparing to the experimental observations in Figure 8-64 is that, the Krypton information can be magnified with any magnification factor to detect any minor propagated crack. However, major cracks can only be detected using experimental observations. For this wall Krypton data (Figure 8-63) and experimental observations show no crack propagation in the top half portion of the wall.



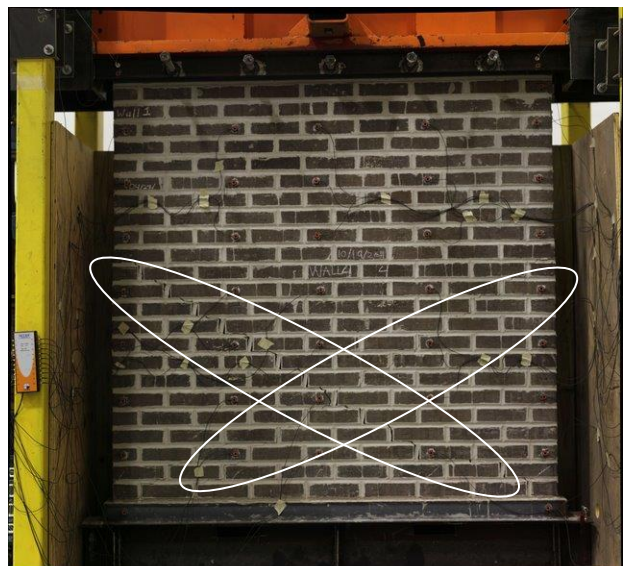
(a) Point 1



(b) Point 2



(c) Point 3



(d) Point 4

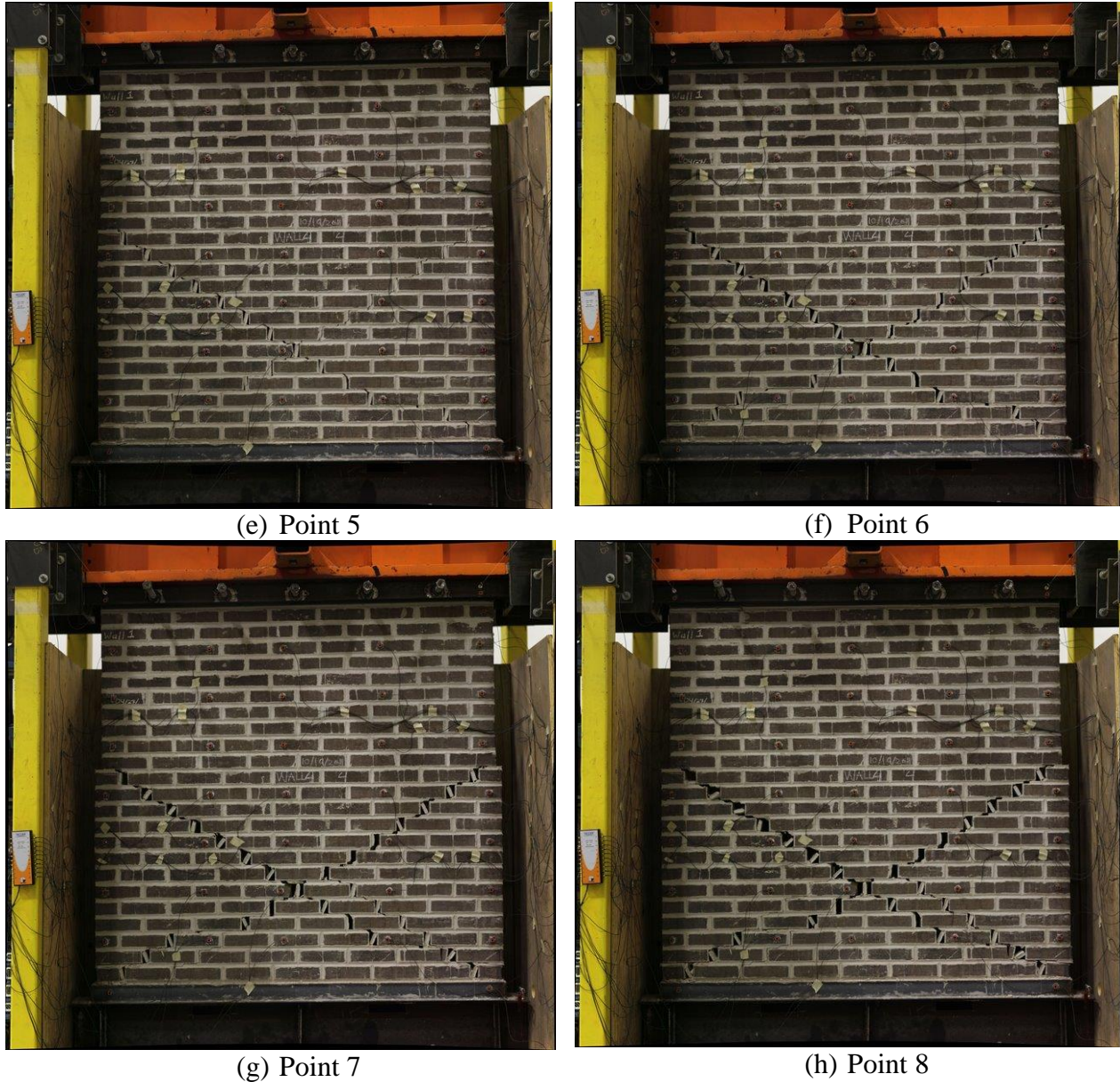


Figure 8-64. Crack propagation in different stages of loading

Figure 8-65 shows the three-dimensional deformation of LED's throughout the loading, after the axial load was applied. According to Figure 8-65, the OP deformation of the wall was much greater than the IP deformation. In fact, as discussed earlier, in case of not providing the OP supports, the wall would collapse due to the large OP deformation. In this figure the location of LED's are not modified along the Y axis. The initial location of LED's shows that after application of the axial load the wall was not completely flat, especially in the south side of the

wall. This could have occurred due to many reasons. For instance, the wall could have been constructed not perfectly from the beginning. Moreover, the top plane of the wall was not completely flat and after the rigid beam applied the axial load, the wall was deformed non-uniformly along the Y axis. This non-uniformity cannot be considered in the numerical simulations and some discrepancy between the experimental and numerical results are expected.

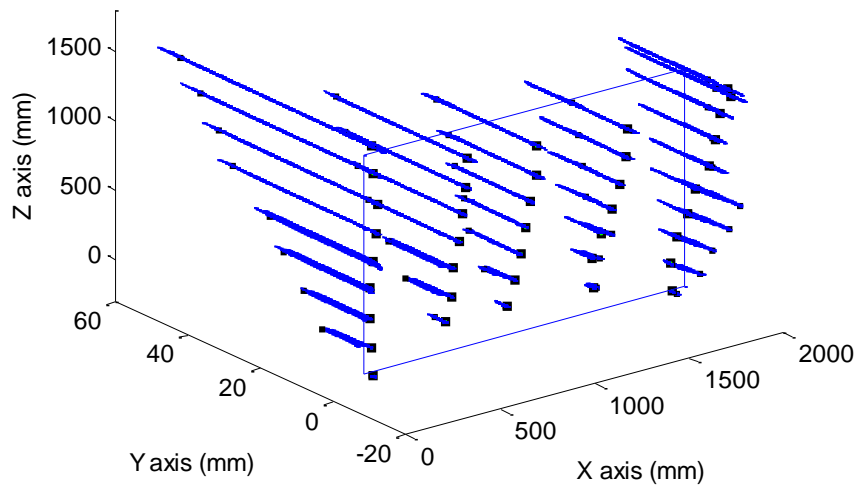
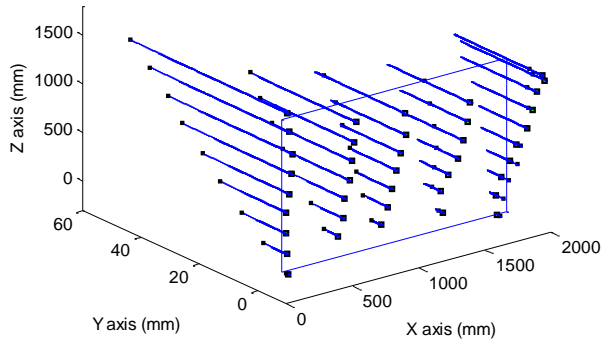
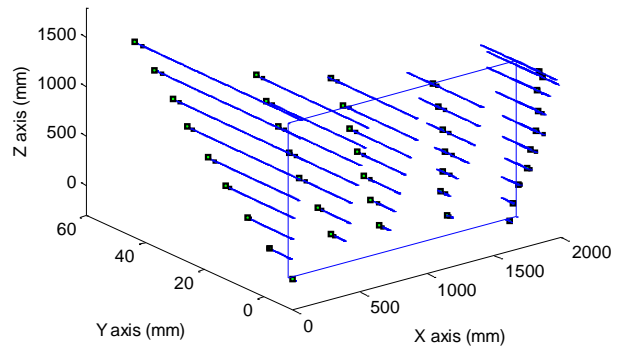


Figure 8-65. Three-dimensional deformation of the wall under cyclic loading (real scale)

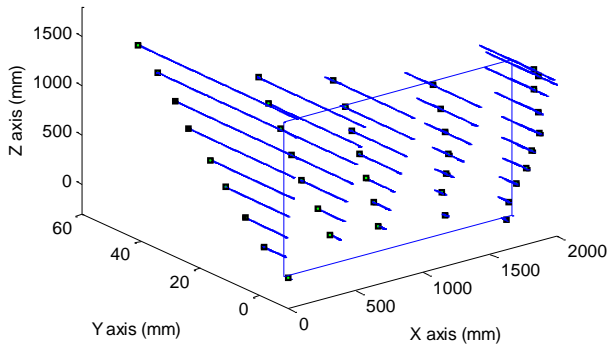
Figure 8-66 presents the motion of LED's during different stages of loading, according to the marked points in Figure 8-55. During the first stage of loading the north side of the top plane had a large displacement in the OP direction and came in contact with the support (Figure 8-66 (a)). In this stage of loading the wall was still in the linear regime and all points were deforming proportional to their height. However, in Figure 8-66 (g) it is clear that the OP deformation did not remain linear and some relative motions have taken place in the OP direction along the height. This fact is confirmed by the experimental observations as shown in Figure 8-67. According to Figure 8-66, it is clear that a significant torsion was imposed to the wall throughout the test.



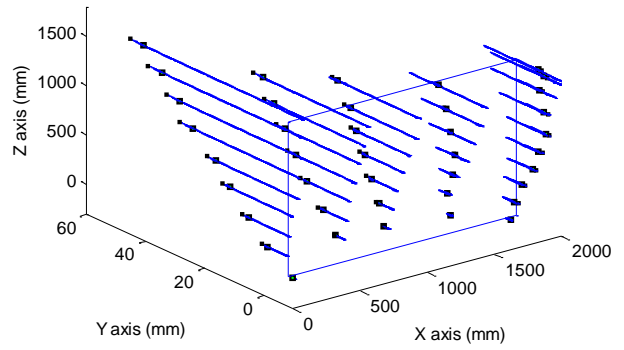
(a) Loading from point 1 to point 2



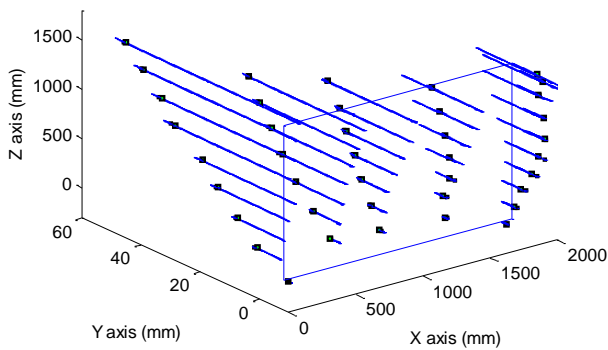
(b) Loading from point 2 to point 3



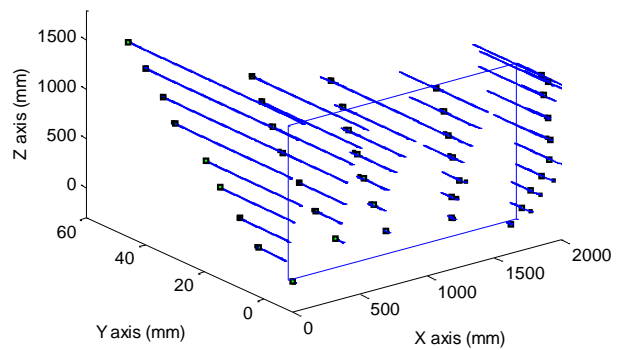
(c) Loading from point 3 to point 4



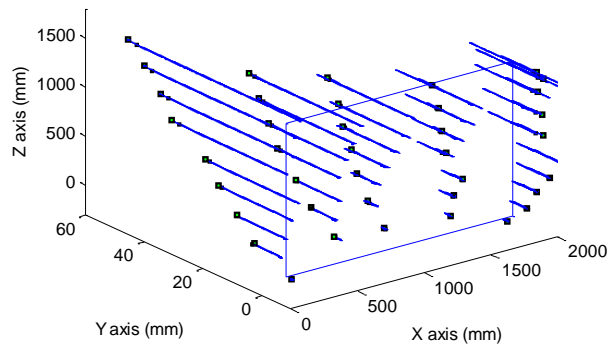
(d) Loading from point 4 to point 5



(e) Loading from point 5 to point 6



(f) Loading from point 6 to point 7



(g) Loading from point 7 to point 8

Figure 8-66. Three-dimensional deformation of the wall in different stages of loading (real scale)



Figure 8-67. Out-of-plane gap in the joints at the end of the test

8.5.4.1 Comparison of the experimental and finite element results of wall 4

A finite element model using the material model of section 8.2 has been generated to perform the numerical modeling. Based on the experimental observations, not much stiffness/strength degradation has been seen in cycles with the same amplitudes. Therefore, a cyclic loading according to Figure 8-51 and without repeated cycles has been used for the numerical loading-protocol, to decrease the computational demand.

In Figure 8-68 experimental results is presented along with the numerical results for in-plane loading. Although a significant torsion was imposed to the wall in the process of the cyclic loading, due to the restraining of the wall in the OP direction, the experimental results are very close to the numerical results for the IP loading presented in Figure 8-68 (b).

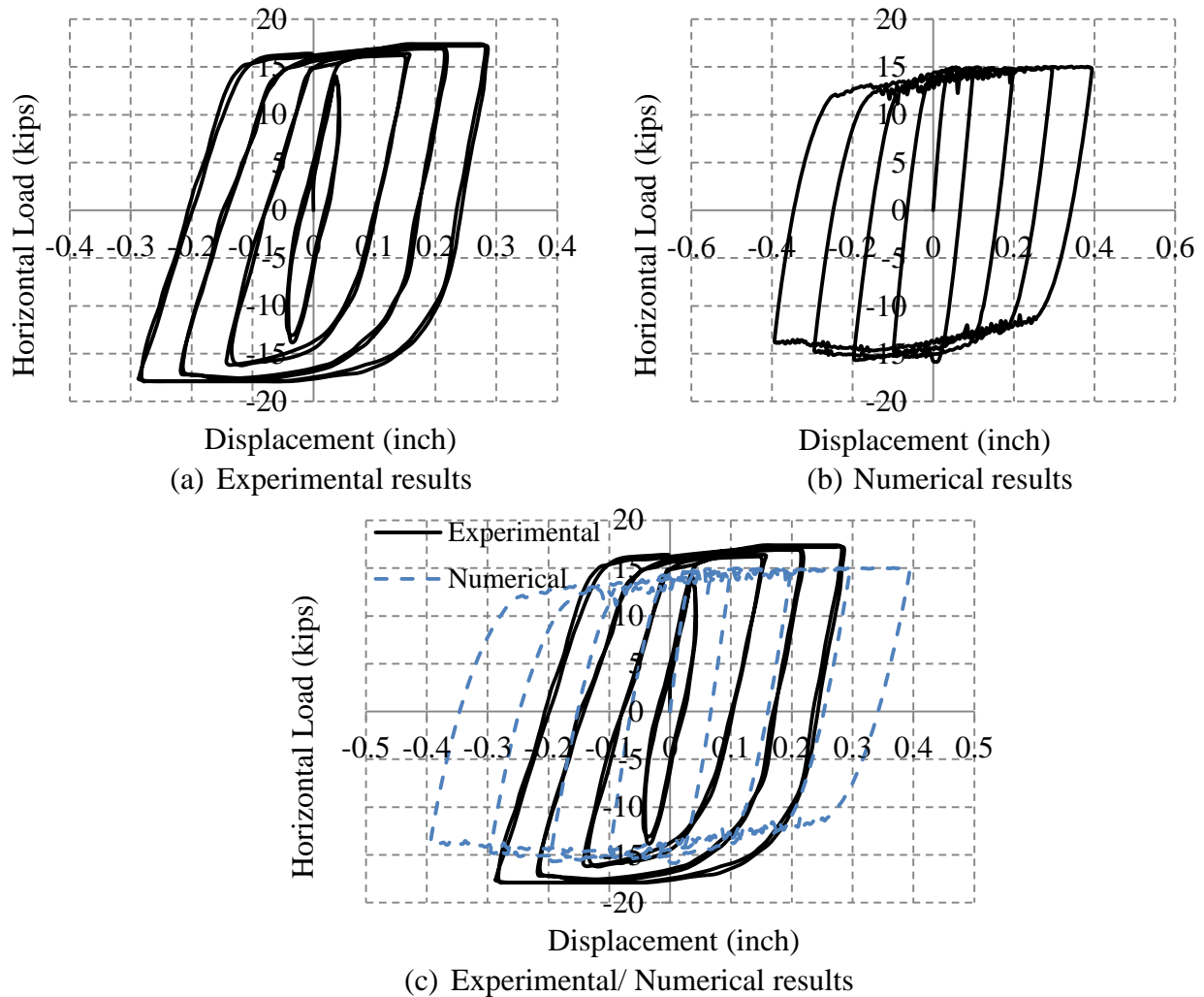


Figure 8-68. Comparison of the numerical and experimental load-displacement curves

In addition to the numerical modeling, the experimental results can be compared with the proposed empirical equations of ASCE 41 (2006). Using ASCE 41 formulation for the stiffness of walls with full restraint against rotation at its top and bottom,

$$k = \frac{1}{\frac{h_{eff}^3}{12 E_m I_g} + \frac{h_{eff}}{A_v G_m}} = 926 \text{ kip/in}$$

The stiffness of the wall based on the experimental data is 410 *kip/in* (71832 *kN/m*) which is about half of the stiffness obtained from ASCE formulation. The wall in this test was subjected to out-of-plane deformation and torsion; therefore, discrepancy of the results is expected from the in-plane stiffness. However, the difference between the experimental results and ASCE 41 prediction is significant.

Using ASCE 41 proposed equations (equations (8-2) and (8-3)), the failure forces for rocking and shear failure modes are 22 *kip* (98 *kN*) and 13 *kip* (57.8 *kN*), respectively. Based on ASCE 41 the failure mode is shear which is in agreement with the experimental observations; however, the predicted failure force of ASCE 41 underestimates the experimental results significantly.

8.5.5 Testing of Wall 5

The fifth wall was tested in the in-plane direction with contribution of an out-of-plane deformation. According to Figure 8-69 (a) in the first step of loading the axial load was applied on the top plane of the wall (16.5 *kip*+5.5 *kip* the weight of the rigid beam), afterward, while keeping the axial load constant, an OP force was applied to the top plane of the wall (285 *lb*). Application of the OP force caused 0.4 *inch* displacement of the top plane in the OP direction. Then, using two rollers beside the rigid beam the boundary condition was imposed in such a way that any OP displacement of the rigid beam was restrained (Figure 8-69 (b)). After application of the axial load and imposing the proper boundary condition for the OP displacement, the cyclic displacement-controlled loading of Figure 8-70 was applied to the wall. The vertical boundary

condition for the rigid beam was imposed in such a way that the rigid beam remained level throughout the test.

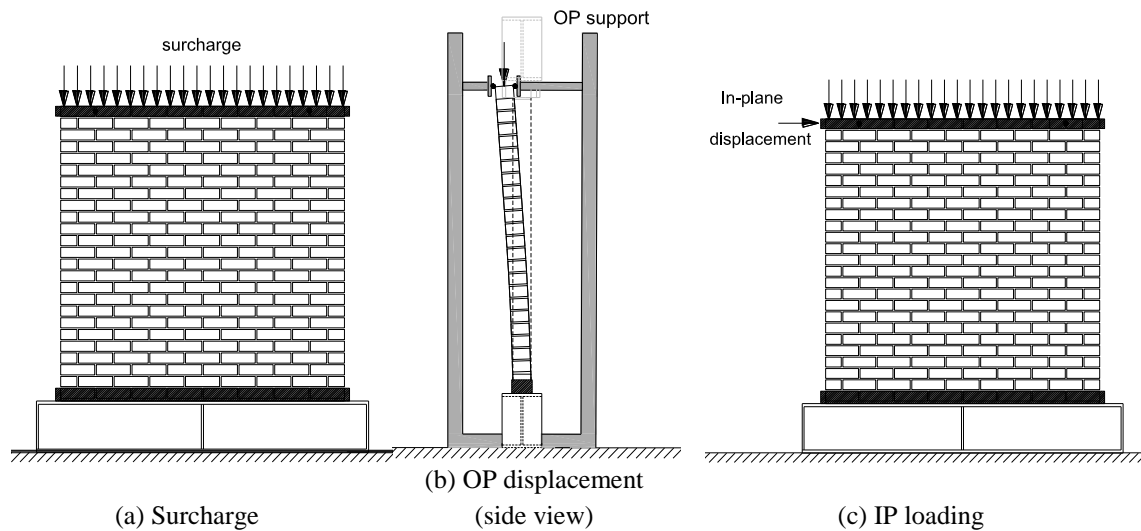


Figure 8-69. Combination of IP and OP loadings

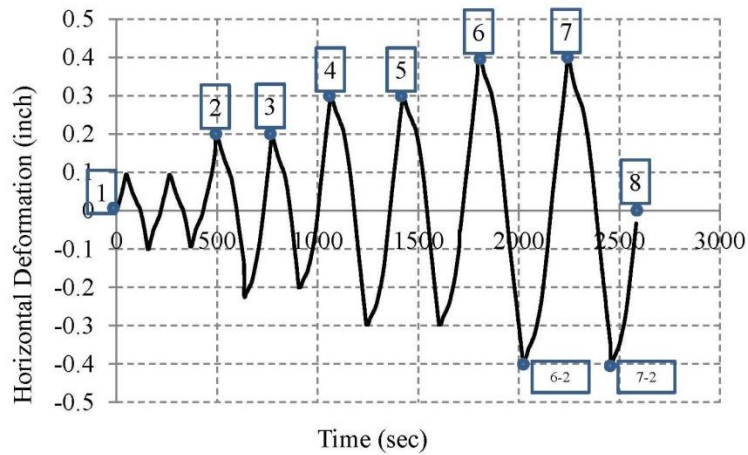


Figure 8-70. Cyclic loading protocol of wall 5

The experimental load-displacement curve is presented in Figure 8-71. In this figure the deformation of the string potentiometer 1 (SP1 in Figure 8-17) was used for drawing the force-displacement curve. As it is clear in Figure 8-71, the cyclic loading was associated with a slight

degradation in the stiffness. Finally the maximum strength of the wall remained constant which corresponds to the frictional resistance.

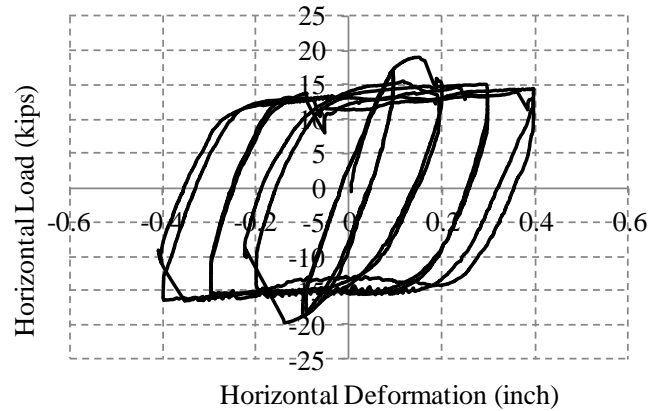


Figure 8-71. In-plane load-displacement of wall 5

Measuring the deformation of the wall from the support is not reliable; a more accurate result will be achieved if the deformation is measured from the top of the wall. Figure 8-72 presents the load-displacement curve of the wall, using the information of Krypton LED 5 shown in Figure 8-17.

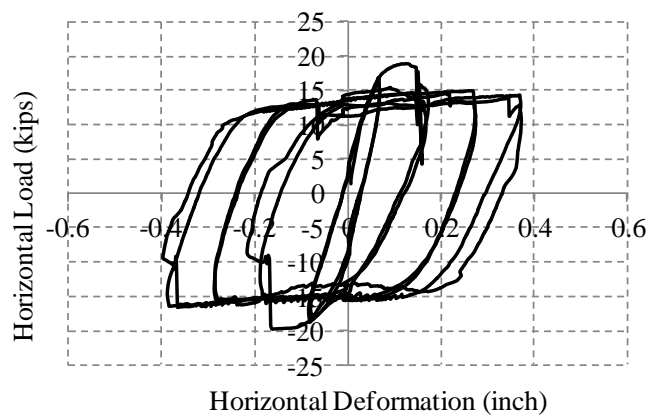


Figure 8-72. In-plane load-displacement using Krypton 5x data

The axial displacement of the north and south vertical actuators are presented in Figure 8-73. It is clear that throughout the test the north and south side of the rigid beam moved together and as it was intended the beam was remained level.

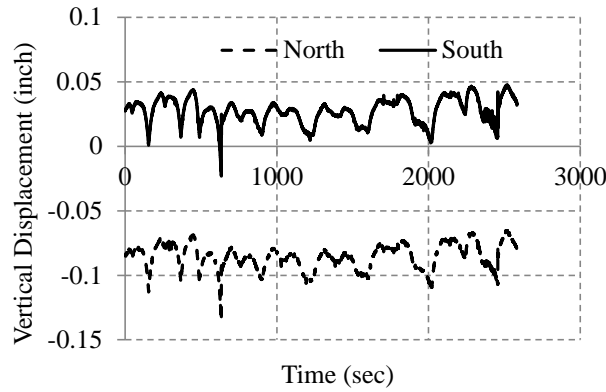


Figure 8-73. Axial displacement of the north and south vertical actuators

To keep the top rigid beam level throughout the test, in each increment of loading the controller distributed the axial load in two vertical actuators in such a way that summation of the axial loads remained constant (16.5 kip), as shown in Figure 8-74. Note that, for all numerical simulations weight of the rigid beam should be added to the presented axial load in Figure 8-74 (5.5 kip). This boundary condition represents a URM wall in a building with a rigid diaphragm.

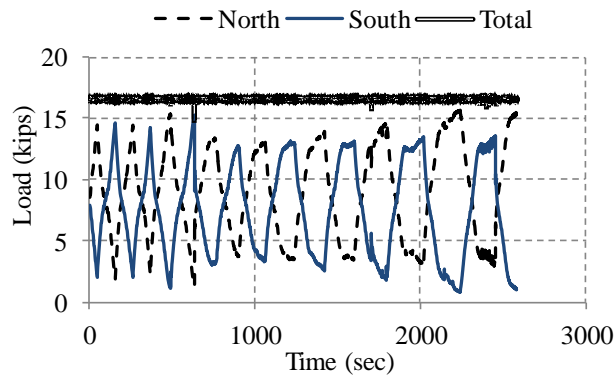


Figure 8-74. Distribution of the axial load in the north and south vertical actuators

The out-of-plane displacement of the south and north side of the top plane is shown in Figure 8-75 while the cyclic load was being applied. Figure 8-75 shows that throughout the test the imposed OP boundary condition maintained the rigid beam in a constant OP displacement; small variations are caused due to the flexibility of the support which is unavoidable.

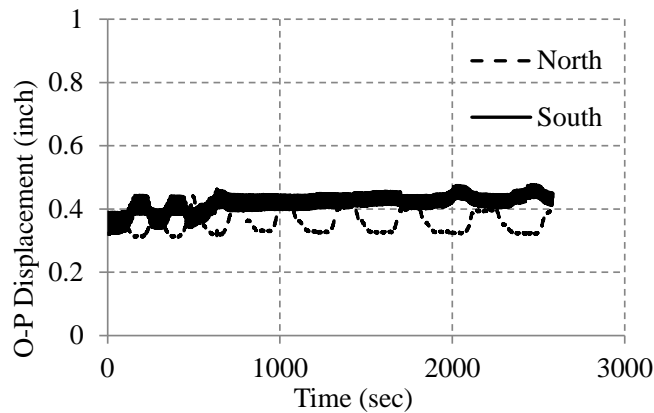


Figure 8-75. Out-of-plane displacement of the north and south side of the top plane

Three-dimensional deformation of LED's after application of the OP force, and with the presence of the axial load is presented in Figure 8-76. The OP displacement of LED's was proportional to their height, which indicates the linear behavior of the wall in this stage of loading.

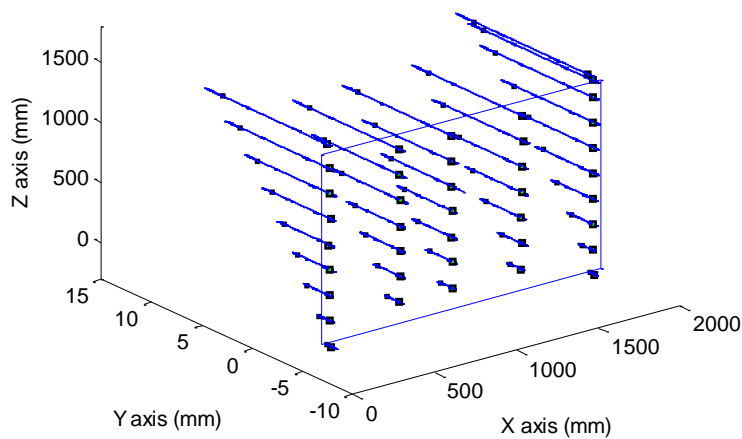


Figure 8-76. Three-dimensional deformation of the wall under OP loading

Figure 8-77 presents the deformation map of the wall under full cyclic loading. Figure 8-77 shows that, after propagation of the diagonal crack, right bottom portion of the wall increasingly separated from the rest of the wall. The peak residual crack opening in the wall, at the end of the test was about 56 mm (2.2 inch), as shown in Figure 8-62. Throughout the test the right and top portion of the wall moved according to the movement of the rigid beam (Krypton 4x and 5x as shown in Figure 8-17). Therefore, no sliding took place between the wall and the boundary condition.

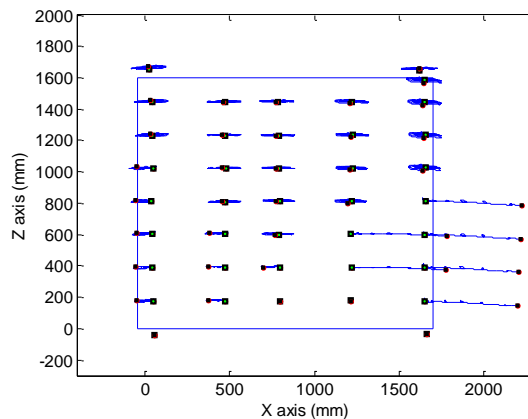
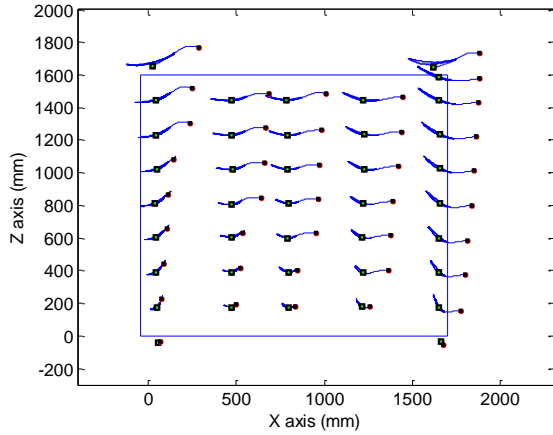
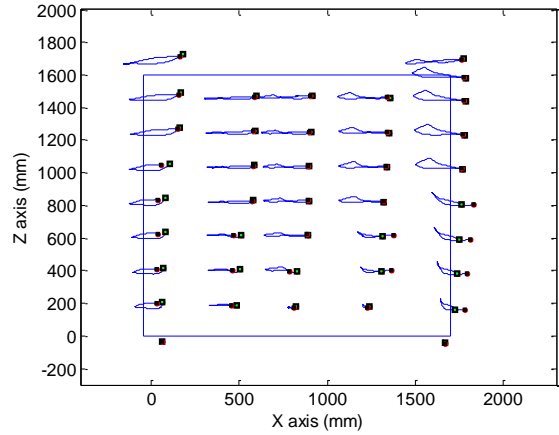


Figure 8-77. Deformation of the wall under cyclic loading ($\times 10$)

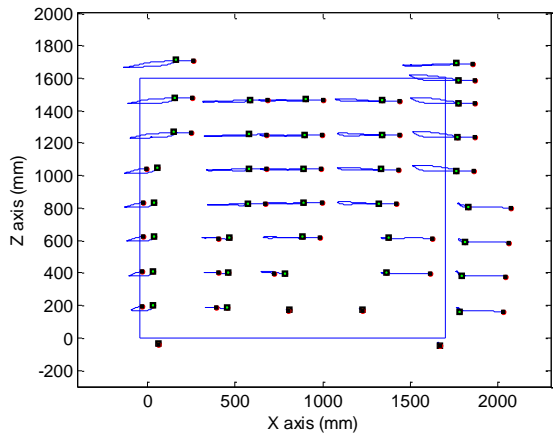
The incremental deformations of the wall are presented in Figure 8-78. The deformations in this figure are based on the marked points in Figure 8-70. In Figure 8-78 (a) and (b) almost all of the points moved proportional to their height, which indicates the linear behavior of the wall in this step of loading. In the rest of the figures the nonlinearity and the propagation of the diagonal cracks are clear. Figure 8-78 (c) to (h) illustrates how the right bottom portion of the wall increasingly separated from the rest of the wall in each cycle.



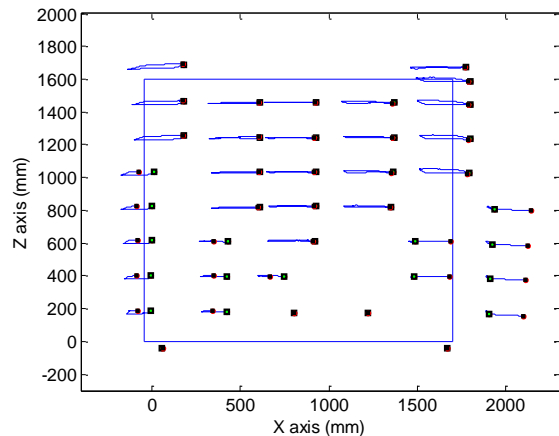
(a) Loading from point 1 to point 2 ($\times 50$)



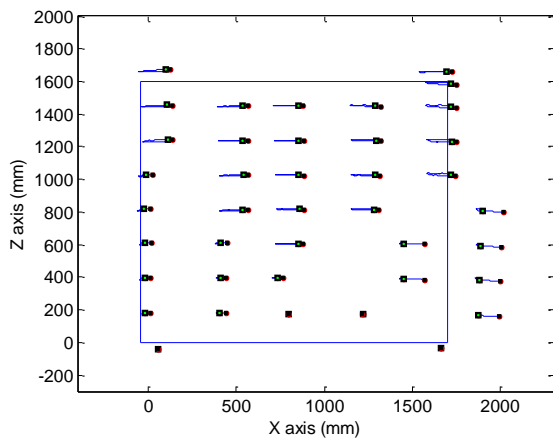
(b) Loading from point 2 to point 3 ($\times 30$)



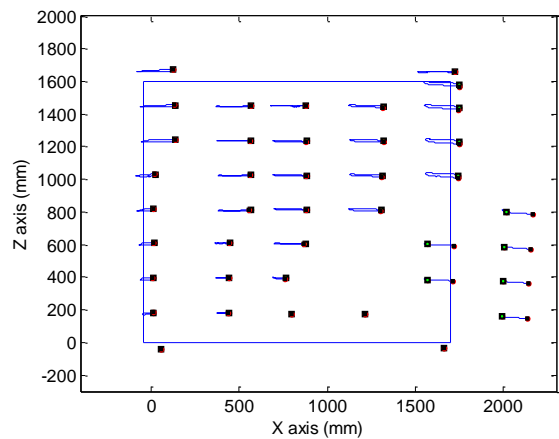
(c) Loading from point 3 to point 4 ($\times 30$)



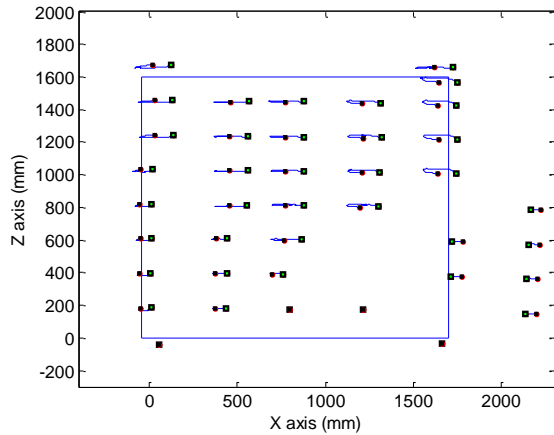
(d) Loading from point 4 to point 5 ($\times 20$)



(e) Loading from point 5 to point 6 ($\times 10$)



(f) Loading from point 6 to point 7 ($\times 10$)



(g) Loading from point 7 to point 8 ($\times 10$)

Figure 8-78. Deformation of the wall in different stages of loadings

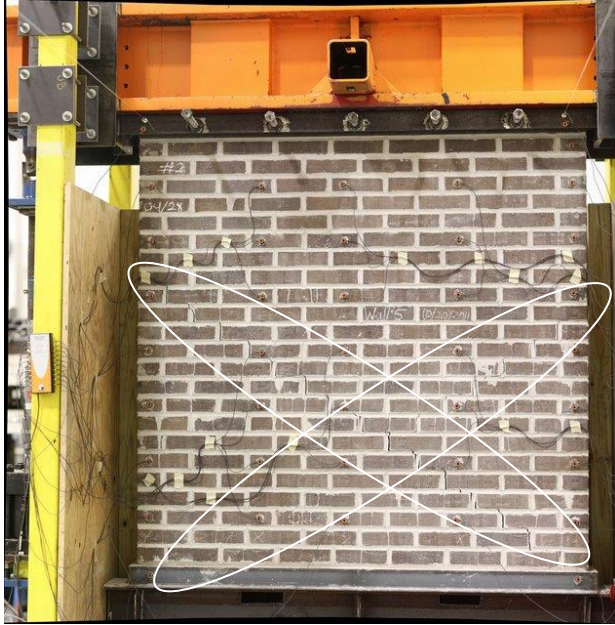
Figure 8-79 presents the crack propagation obtained from the test in different stages of loading, according to the marked points in Figure 8-70. Similar to the Krypton data, the experimental observations in Figure 8-79 shows propagation of a diagonal crack in the wall. Using the Krypton data it is much more convenient to measure the openings in the wall in each step of the loading, since it is possible to magnify the deformations obtained from the Krypton by any appropriate factor.



(a) Point 1



(b) Point 2



(c) Point 3



(d) Point 4



(e) Point 5



(f) Point 6



(g) Point 6-2



(h) Point 7



(i) Point 7-2



(j) Point 8

Figure 8-79. Crack propagation in different stages of loading

8.5.5.1 Comparison of the experimental and finite element results of wall 5

In this section three numerical investigations have been performed, including monotonic IP loading, monotonic IP loading with the contribution of an OP deformation, and cyclic IP loading with the contribution of an OP deformation.

First the experimental results are compared with the numerical in-plane monotonic loading results (Figure 8-80). The numerical simulation shows propagation of the diagonal crack in the monotonic IP deformation of the wall (Figure 8-81). By looking at different stages of loading in Figure 8-81, it can be concluded that, increase in the magnitude of the displacement only causes more opening of the existing crack, without much damage to the rest of the wall (compare (Figure 8-81 (c) and (d)). In the nonlinear regime the load-displacement curve remains constant which corresponds to the frictional force.

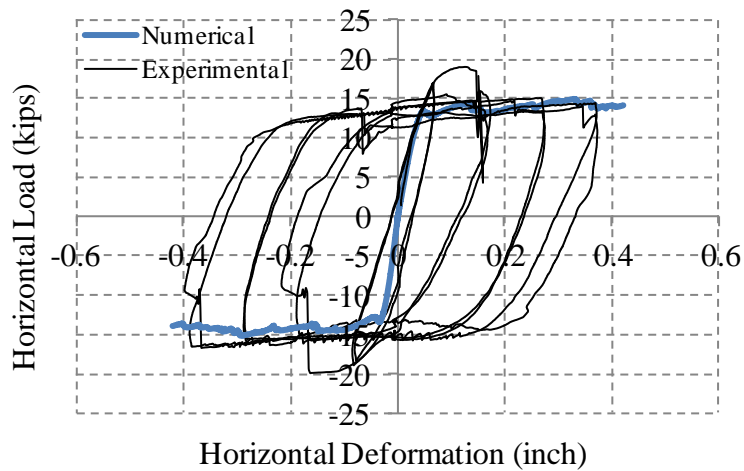
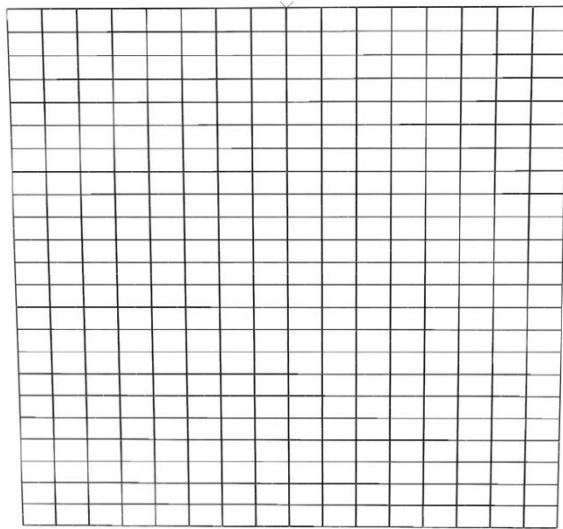
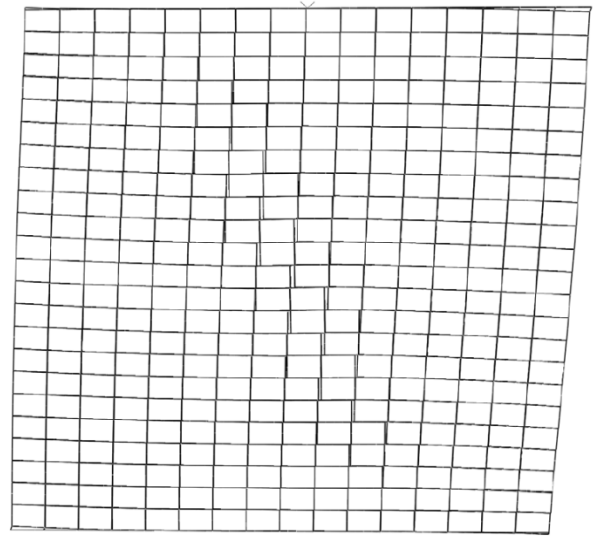


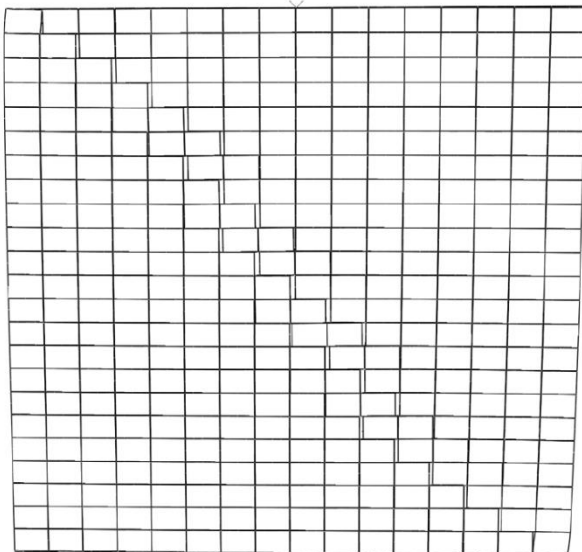
Figure 8-80. Comparison of the experimental results with the in-plane numerical results



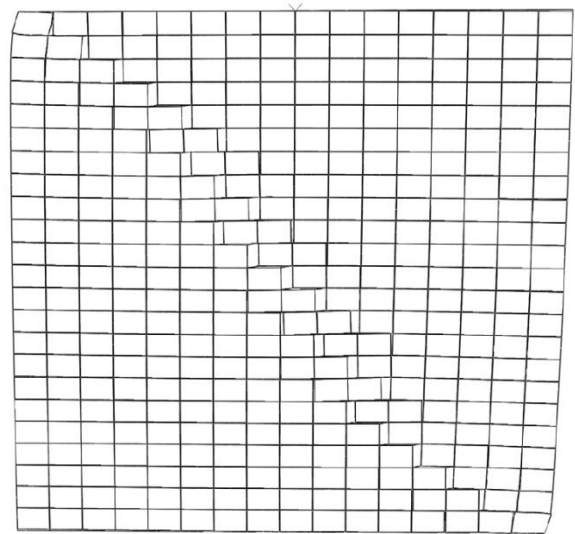
(a) Before start of loading



(b) 0.05 inch displacement (0.12 cm)
(×70)



(c) 0.2 inch displacement (0.5 cm)
(×5)



(d) 0.4 inch displacement (1 cm)
(×5)

Figure 8-81. Crack propagation obtained from the numerical simulations under monotonic IP loading

In the second phase of the numerical simulation, the in-plane load has been applied while the wall was already deformed in the out-of-plane direction (Figure 8-82 (a)). Right after application of the axial load, the OP deformation was imposed to the top plane of the wall (0.4 *inch*), and afterward the IP deformation-controlled loading was applied. The numerical

simulation again shows propagation of the diagonal crack in this phase of the loading (Figure 8-82).

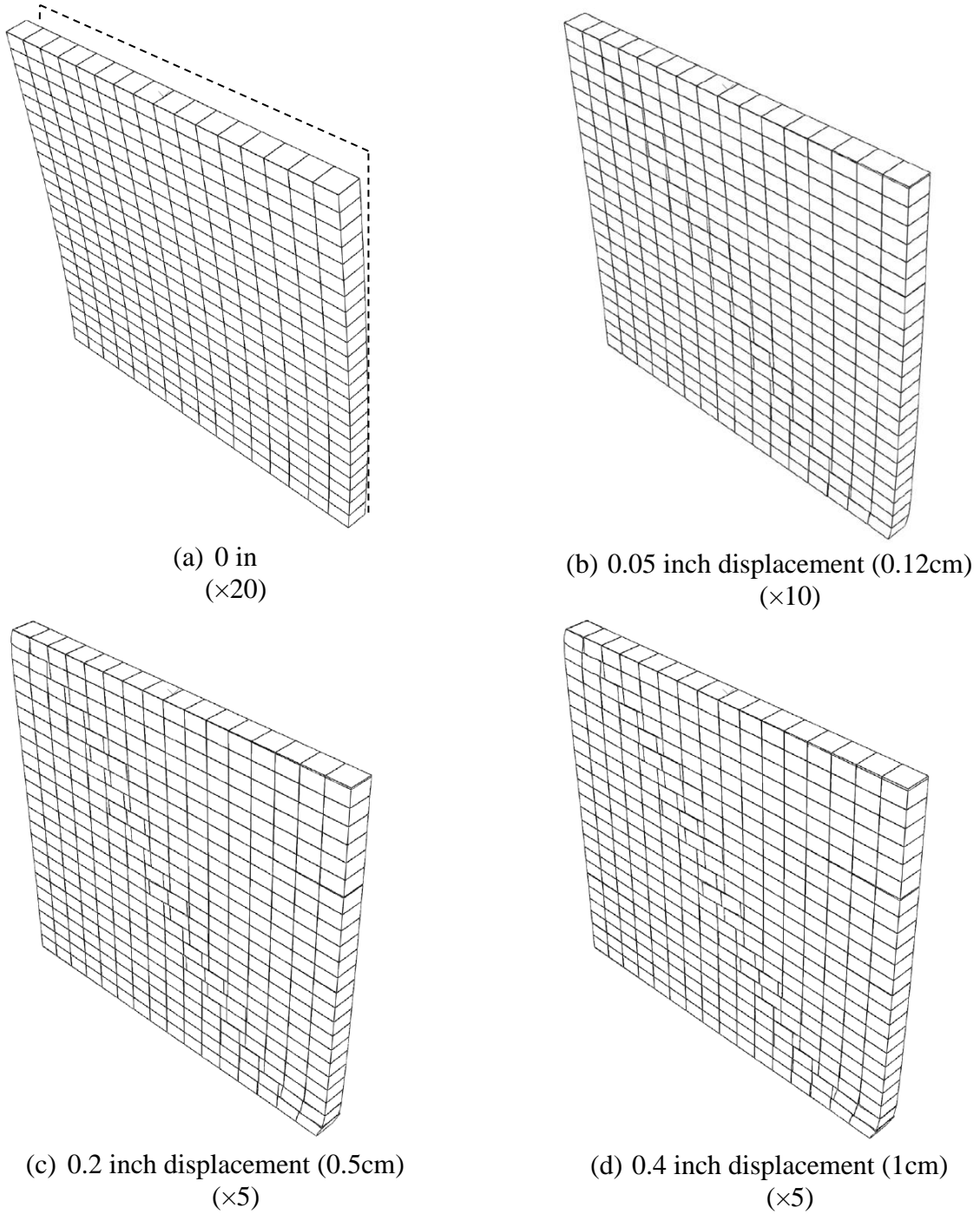


Figure 8-82. Crack propagation obtained from the numerical simulation under monotonic OP/IP loading

For this specific model a large OP force has been applied (285 lb) to deform the wall 0.4 inch (1 cm) in the OP direction. In comparison to the results obtained from IP loading, not much difference can be seen in the response of the model. As shown in Figure 8-83, stiffness and strength of the model with OP deformation are slightly lower than the model without OP deformation.

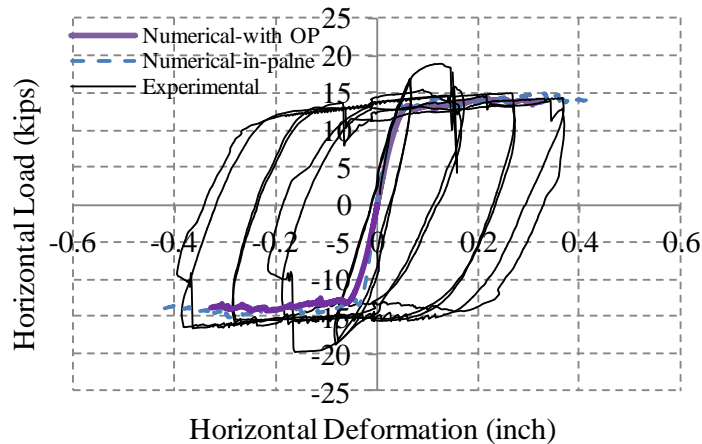


Figure 8-83. Comparison of the experimental and numerical results (monotonic loading)

In the third phase of the numerical simulation, after application of OP deformation, the wall was subjected to the cyclic loading protocol of Figure 8-84.

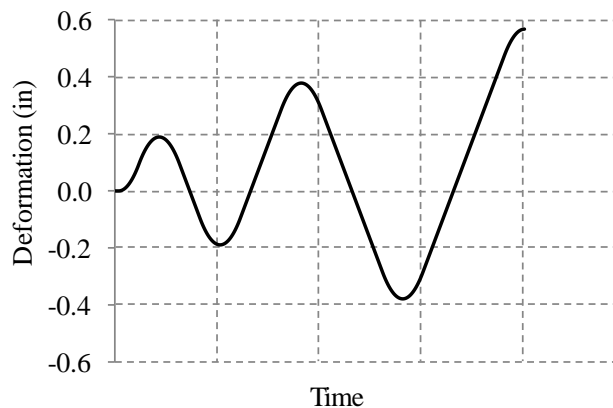


Figure 8-84. Numerical loading protocol

Two different values have been considered for the stiffness degradation factor for the numerical models ($\kappa=1$ and $\kappa=0.76$). Figure 8-85 shows that the obtained numerical results considering no stiffness degradation ($\kappa=1$) is in good agreement to the experimental results.

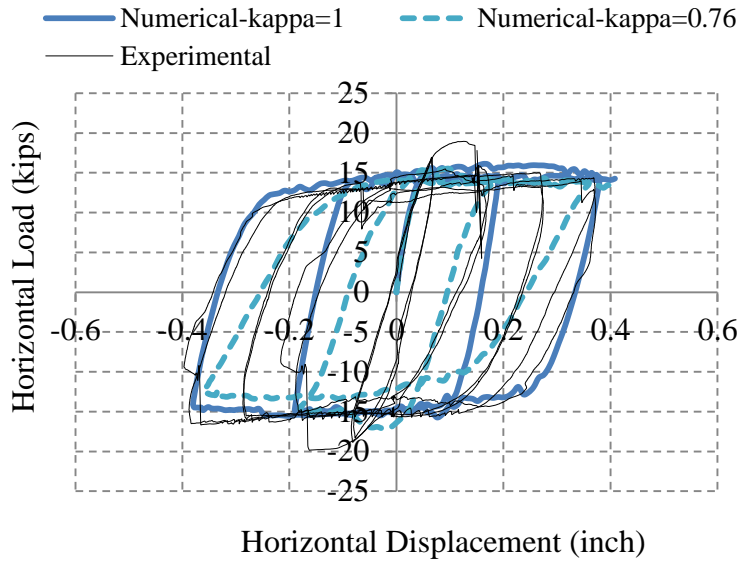


Figure 8-85. Comparison of the numerical and experimental results

A more accurate comparison between the numerical and experimental load-displacement curves is presented in Figure 8-86, with the complete number of loading cycles.

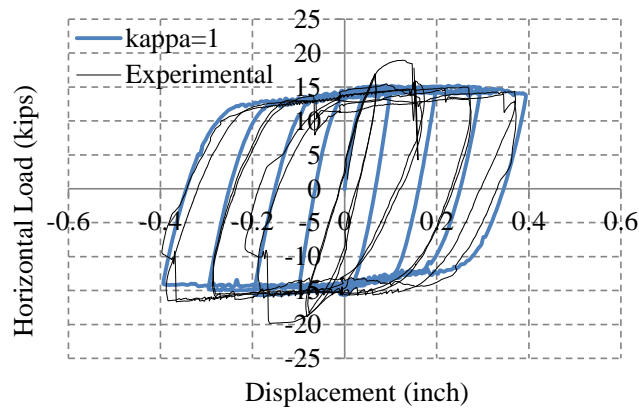


Figure 8-86. Comparison of the experimental and numerical load-displacement curves

Figure 8-87 presents propagation of the diagonal crack in different stages of loading obtained from the numerical simulation. As shown in Figure 8-87 (b), it is clear that after the direction of the load changes the propagated crack in the previous cycle closes and a new diagonal crack propagates in the new direction and almost perpendicular to the previous diagonal crack.

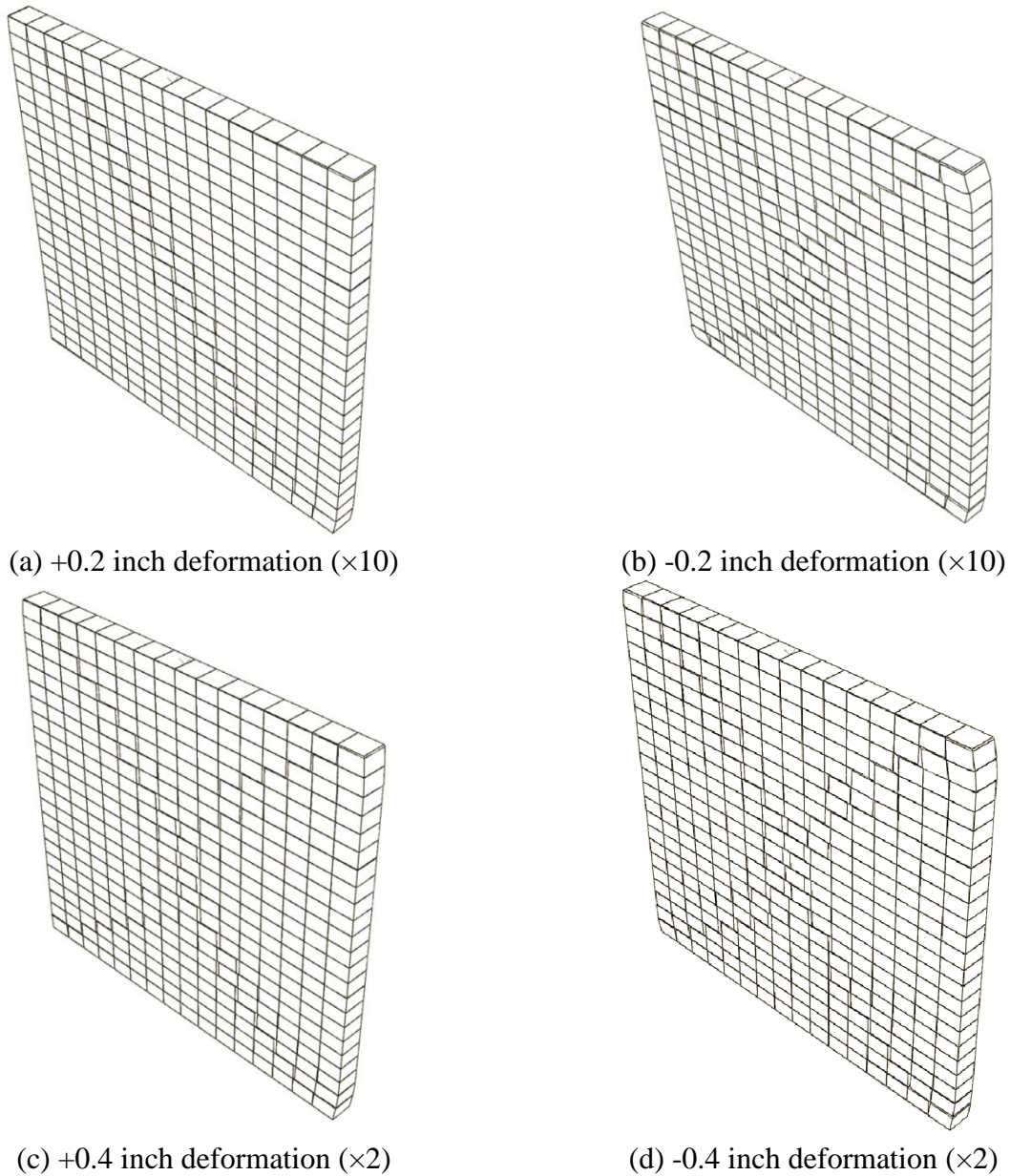


Figure 8-87. Crack propagation under cyclic loading (numerical)

As shown in Figure 8-87, in both experimental and numerical analysis diagonal crack is the dominant failure mode. We note here that the diagonal crack in the experimental model deviates in one aspect and that is the pattern does not reach the corners, but rather at the two-third of the height. One possible explanation is that the quality of the mortar in this region is likely to be higher, as the wall was not constructed in one working day. One other possible explanation is that in the numerical model everything was simulated perfectly and the location of the vertical actuators were assumed to be in the centerline of the wall; however in reality this was not the case. In other words, the imposed moment on the wall in the experimental model was different and more complicated than the numerical model.

The experimental and numerical results can also be compared with the proposed empirical equations of ASCE 41 for stiffness and strength of the wall. Using ASCE 41 formulation for the stiffness of walls with full restraint against rotation at its top and bottom,

$$k = \frac{1}{\frac{h_{eff}^3}{12 E_m I_g} + \frac{h_{eff}}{A_v G_m}} = 926 \text{ kip/in}$$

The stiffness of the wall based on the experimental data is 400 *kip/in* (70080 *kN/m*) which is about half of the stiffness obtained from ASCE formulation. The wall in this test was deformed in the out-of-plane direction and a minor difference is expected from the in-plane stiffness. However, the difference between the experimental and code prediction is significant.

Using ASCE 41 proposed equations (equations (8-2) and (8-3)), the failure forces for rocking and shear failure modes are 22 *kips* (98 *kN*) and 13 *kips* (57.8 *kN*), respectively. Based on ASCE 41 methodology, the failure mode is shear-dominated, which is in accord with the experimental observations; however, the predicted failure force of ASCE 41, underestimates the experimental results.

8.5.6 Testing of Wall 6

Similar to wall 5, wall 6 was tested in the in-plane direction with contribution of an OP deformation. The only difference between wall 5 and 6 was type of the brick which was used for constructing the walls. In contrast to wall 5, for constructing wall 6 low strength brick was used to see the influence of brick type in the failure mode of the wall. In the first step of loading the axial load was applied on the top plane of the wall (16.5 kip+5.5 kip the weight of the rigid beam), afterward, while keeping the axial load constant, an OP force was applied to the wall (360 lb) to generate 0.4 inch (1 cm) OP displacement of the top plane of the wall. Then, the boundary condition was imposed in such a way that any OP displacement of the rigid beam was restrained (see Figure 8-69 (b)). Then the cyclic loading protocol of Figure 8-88 was applied to the wall (Figure 8-69 (c)). In other words, the wall was tested in the in-plane direction while it was deformed in the OP direction.

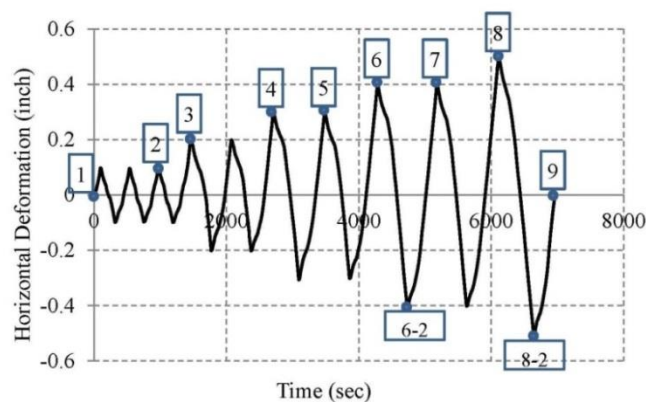


Figure 8-88. Loading protocol for wall 6

The experimental load-displacement curve is presented in Figure 8-89. In this figure the displacement of the string potentiometer 1 (SP1 in Figure 8-17) was used for drawing the force-displacement curve. Based on Figure 8-89, the cyclic loading is associated with a minor

degradation just in the stiffness and not in the strength. Finally the maximum strength of the wall remained constant that corresponds to the frictional force.

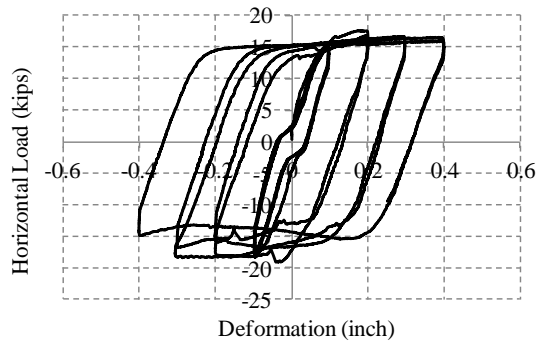


Figure 8-89. Load-displacement of wall 6

Measuring the deformation of the wall from the support or displacement of the rigid beam is not reliable; a more accurate result will be achieved if the displacement is measured from the top of the wall. Figure 8-90 presents the load-displacement of the wall, using the information of Krypton LED 5 shown in Figure 8-17.

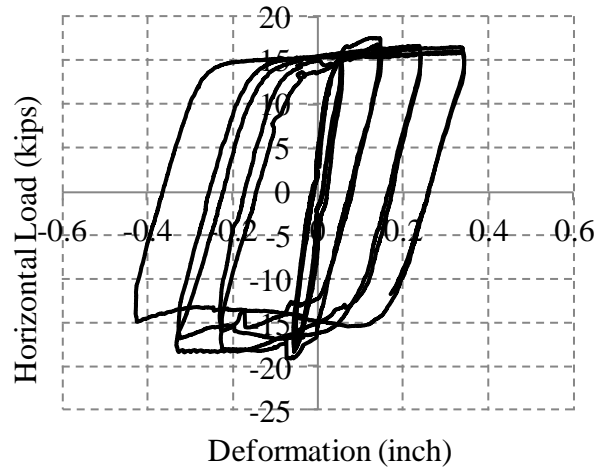


Figure 8-90 Modified load-displacement curve using krypton 5x results

Figure 8-91 represents the axial displacement of the north and south vertical actuators. As it was intended, throughout the test the north and south side of the rigid beam moved together and the rigid beam remained level.

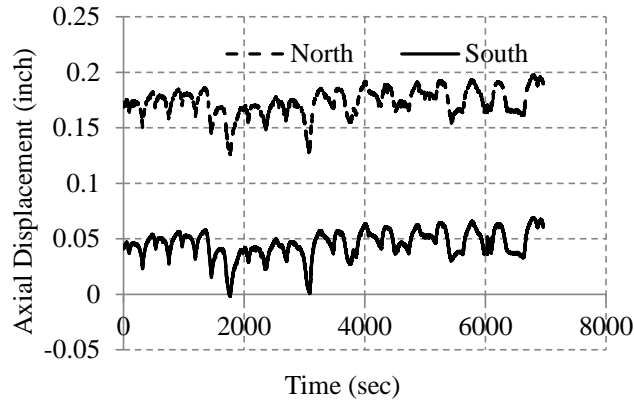


Figure 8-91. Axial displacement of the north and south vertical actuators

Distribution of the axial load in the north and south vertical actuators is presented in Figure 8-92. At each time increment the total axial load was distributed in two vertical actuators in such a way that the summation of the vertical loads remained constant (16.5 kip). Note that, for all numerical simulations the weight of the rigid beam should be added to the presented vertical load in Figure 8-92 (5.5 kip).

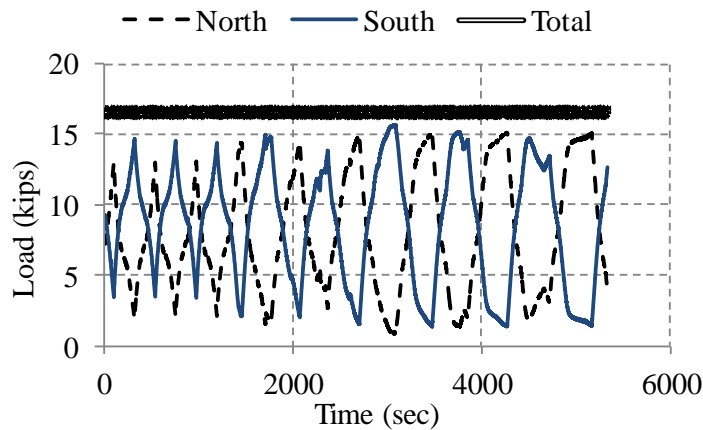


Figure 8-92. Axial loads in the south and north actuators

Figure 8-93 presents the OP displacement of the south and north side of the rigid beam while the cyclic load was being applied. Figure 8-93 shows that throughout the testing, the OP displacement of the rigid beam was constantly maintained about 0.4 inch (1 cm) from the initial plane of the wall; due to the flexibility of the OP supports small variations exist in the OP displacements of the rigid beam.

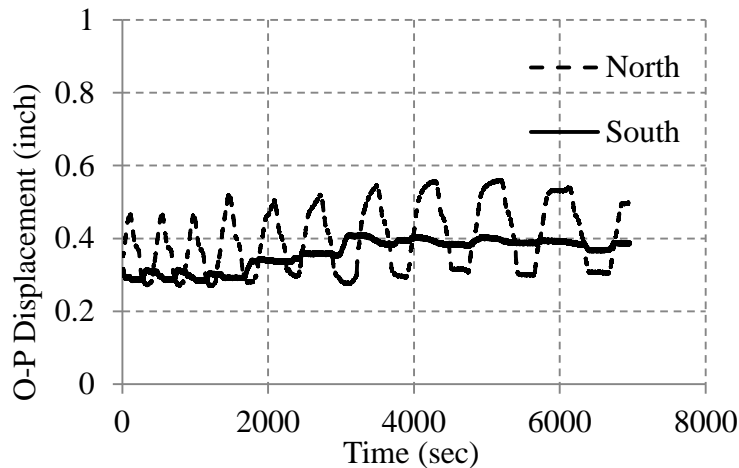


Figure 8-93. OP displacements of the north and south side of the top plane of the wall

The deformation map of the wall under axial load is presented in Figure 8-94. As it is expected, all of the points had an almost vertical deformation. It can be seen that based on the elasticity theory, the upper points had more deformation when compared to the lower points.

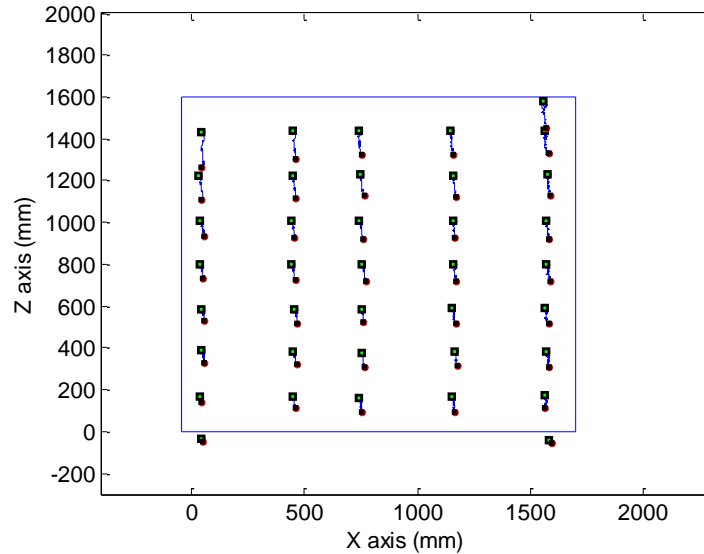


Figure 8-94. Deformation of the wall under the axial load ($\times 300$)

Figure 8-95 presents the three-dimensional deformation of LED's after application of the OP force and with the presence of the axial load. The OP deformations of LED's are proportional to their height, which indicates the linear behavior of the wall in this phase of loading.

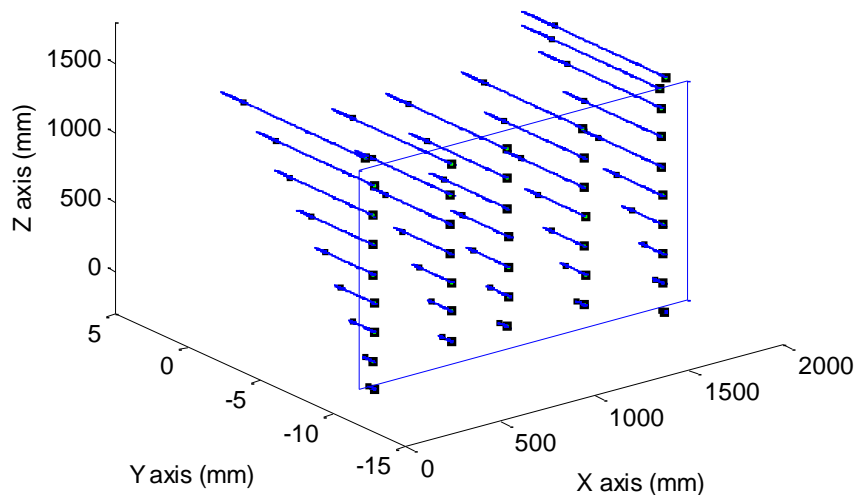


Figure 8-95. Three-dimensional deformation of the wall under OP loading (real scale)

The deformation map of the wall under full cyclic loading is presented in Figure 8-96. Figure 8-96 shows that no full diagonal crack was propagated in this wall. However, due to the

high compressive forces in the corners of the wall, left bottom portion of the wall was initially crushed and then was completely separated from the wall and dropped during the test. Throughout the test the right and top portion of the wall moved according to the motion of the rigid beam (compare the displacement of Krypton 4 and 5); therefore, no sliding took place between the wall and support.

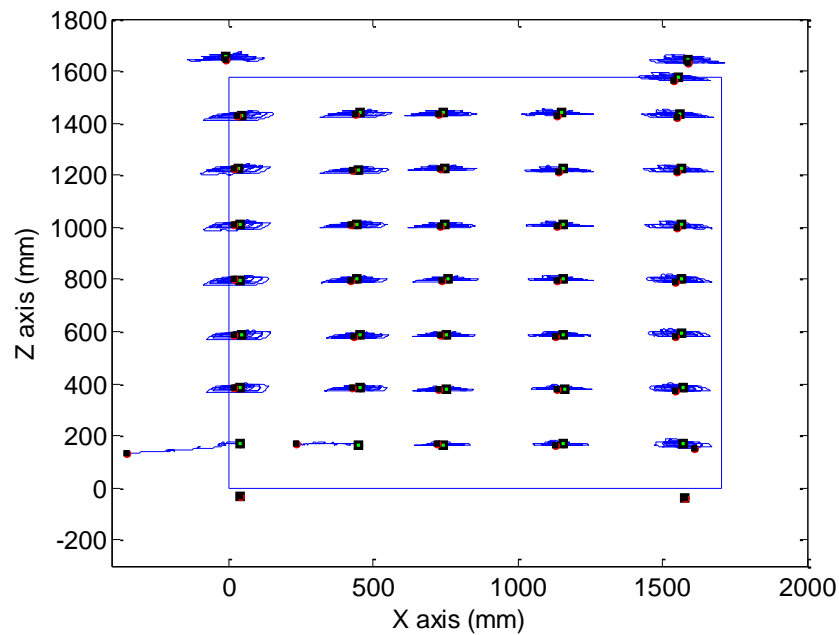
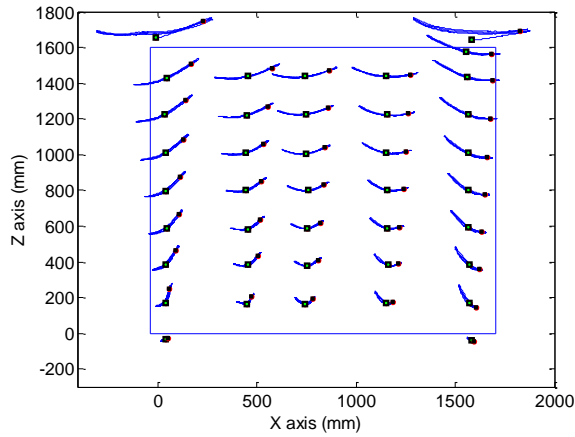
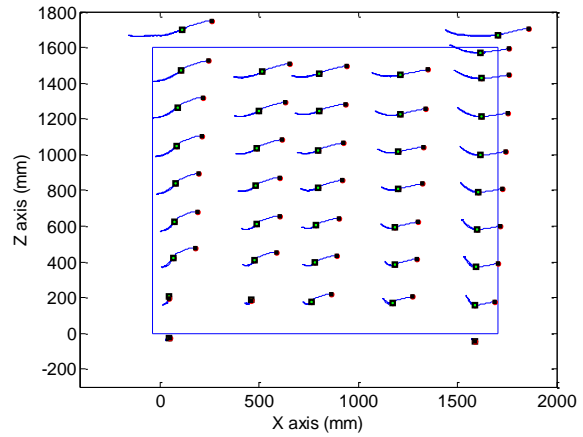


Figure 8-96. Deformation of the wall under cyclic loading ($\times 10$)

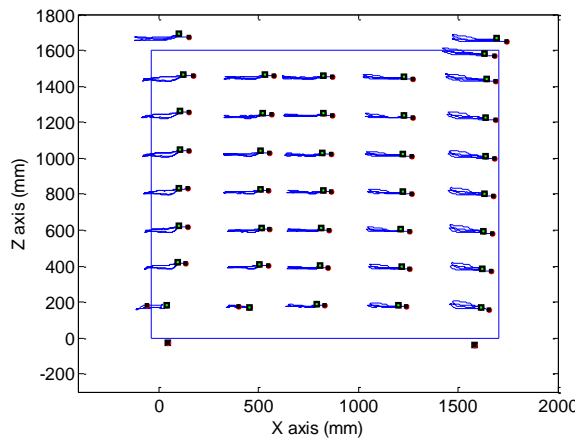
The incremental motion of the wall is presented in Figure 8-97. The information of this figure is based on the marked points in Figure 8-88. In Figure 8-97 (a) and (b) almost all of the points moved together and proportional to their height; therefore, no nonlinearity has taken place. According to Figure 8-97 (c) to (h), diagonal crack was not the dominant failure mode for this wall and the nonlinear mechanism was dominated by crushing the bricks in the corners and sliding of the wall on the second row of the brick.



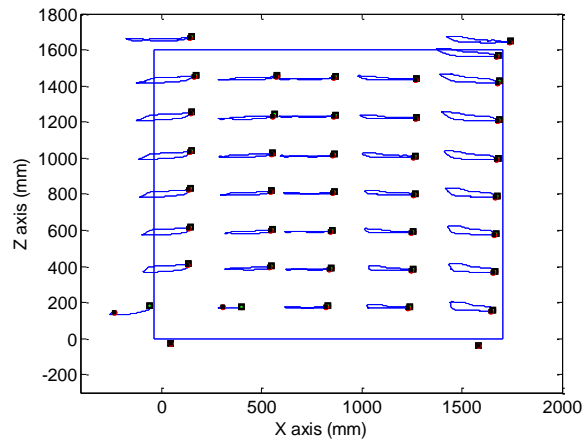
(a) Loading from point 1 to point 2 ($\times 100$)



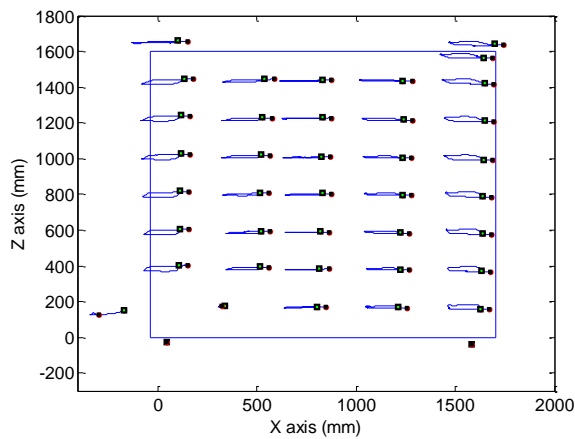
(b) Loading from point 2 to point 3 ($\times 50$)



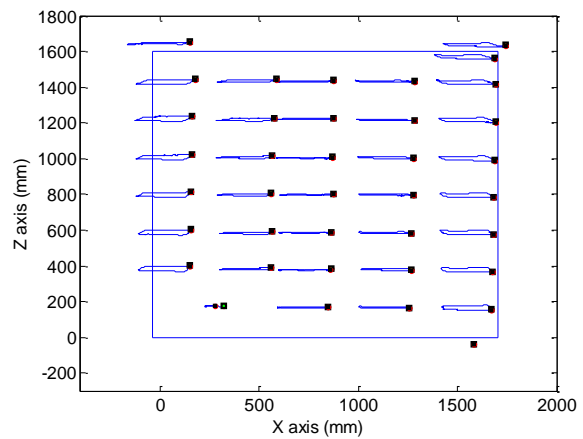
(c) Loading from point 3 to point 4 ($\times 20$)



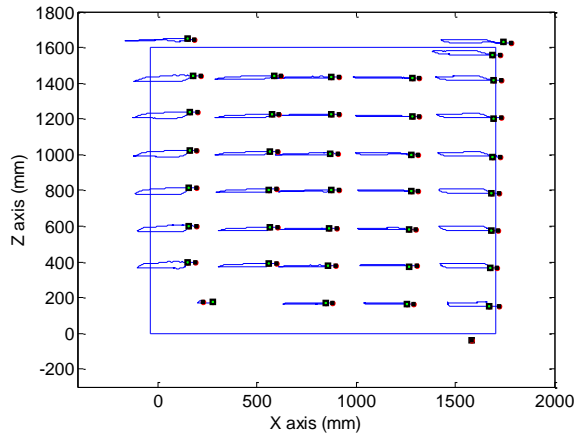
(d) Loading from point 4 to point 5 ($\times 20$)



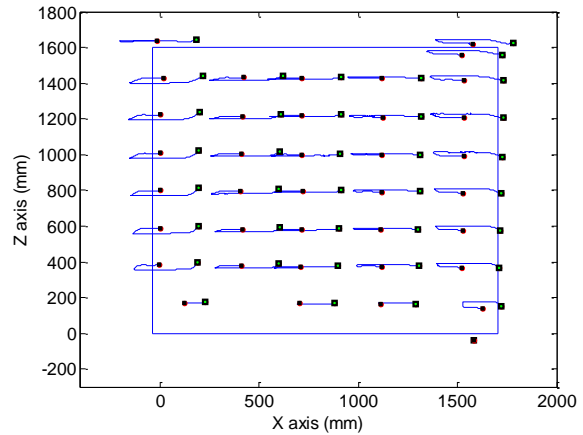
(e) Loading from point 5 to point 6 ($\times 15$)



(f) Loading from point 6 to point 7 ($\times 15$)



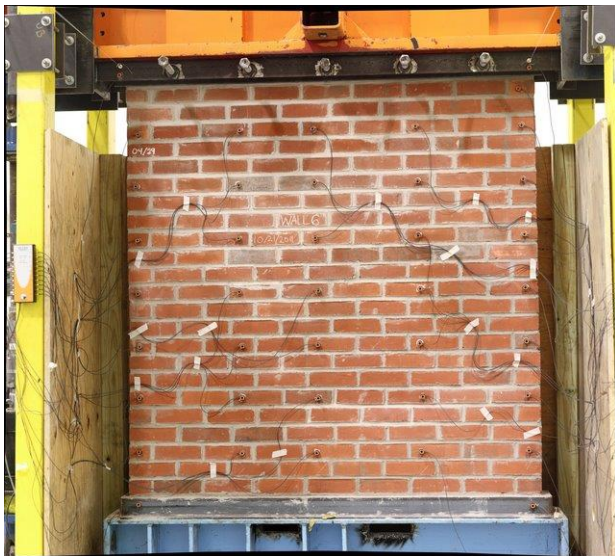
(g) Loading from point 7 to point 8 ($\times 15$)



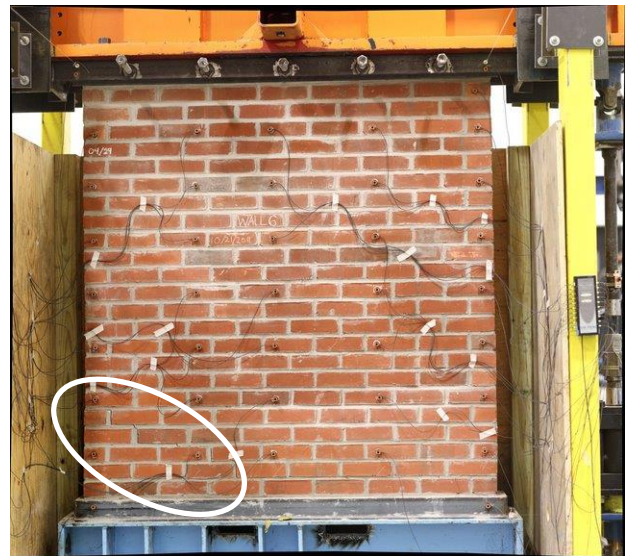
(h) Loading from point 8 to point 9 ($\times 15$)

Figure 8-97. Deformation of the wall in different stages of loadings

Figure 8-98 presents the crack propagation obtained from the test in different stages of loading according to the marked points in Figure 8-88. Experimental observations also show that the failure mode of the wall is crushing of the corners of the wall (see Figure 8-98 (e) to (j)).



(a) Point 1



(b) Point 3



(c) Point 4



(d) Point 5



(e) Point 6



(f) Point 6-2

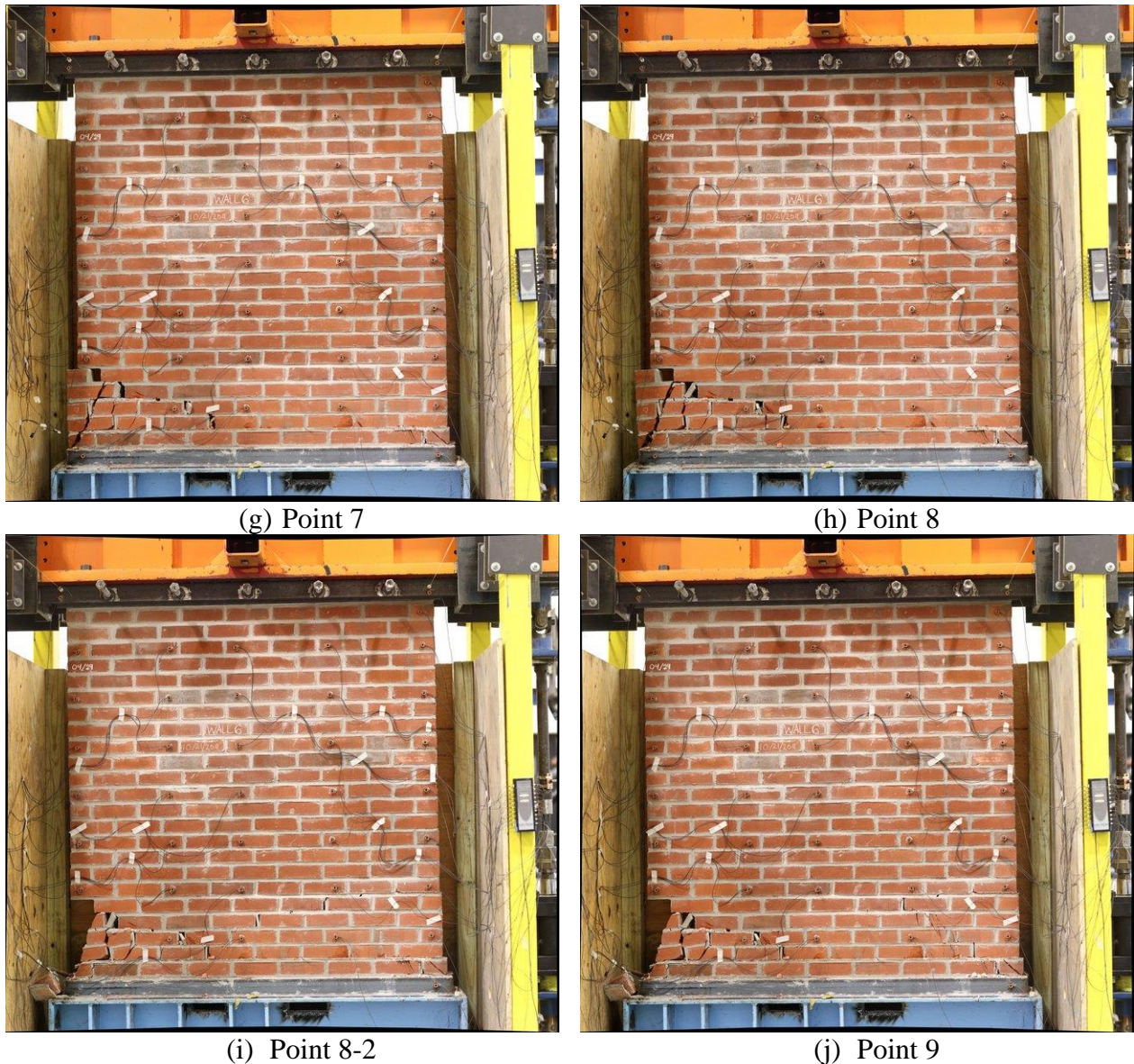
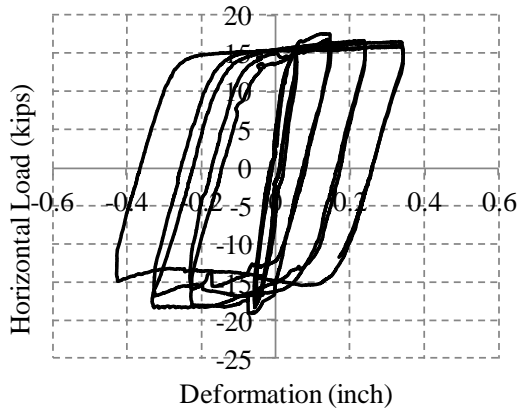


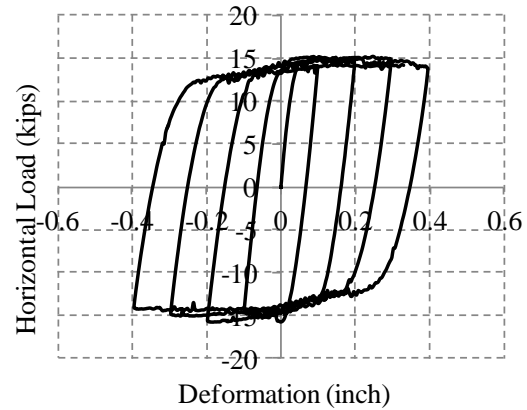
Figure 8-98. Crack propagation in different stages of loading

8.5.6.1 Comparison of the experimental and finite element results of wall 6

Figure 8-99 presents the load-displacement curves obtained from the experimental and numerical models. In this figure the numerical results are presented considering “ $\kappa=1$ ” (no stiffness degradation - see section 5). In this wall due to the use of low strength brick, more failure was seen in the bricks, in comparison to the other walls.



(a) Experimental results



(b) Numerical results ($\kappa = 1$)

Figure 8-99. Comparison of the experimental and numerical load-displacement curves

Figure 8-100 presents the numerical and experimental load-displacement curves on top of each other. It is shown that the numerical results are in good agreement with the experimental results.

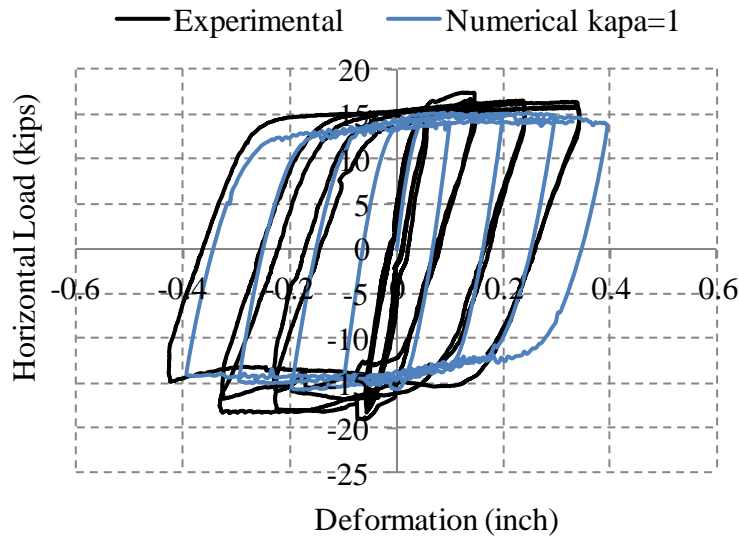


Figure 8-100. Comparison of the numerical and experimental results

The experimental and numerical results can also be compared with the proposed empirical equations of ASCE 41. Using ASCE 41 formulation for the stiffness of walls with full restraint against rotation at its top and bottom,

$$k = \frac{1}{\frac{h_{eff}^3}{12 E_m I_g} + \frac{h_{eff}}{A_v G_m}} = 869 \text{ kip/in}$$

The stiffness of the wall based on the experimental results is 410 *kip/in* (71832 *kN/m*) which is about half of the stiffness obtained from ASCE 41 formulation. The wall in this test was deformed in the out-of-plane direction and a minor difference is expected from the in-plane stiffness. However, the difference between the experimental and code prediction is significant.

For this wall, due to the low strength of the bricks crushing of the bricks at the corners is also expected. For this failure mode ASCE 41 formulation follows,

$$Q_{CL} = V_{tc} = \alpha Q_G \frac{L}{h_{eff}} \left(1 - \frac{f_a}{0.7 f'_m} \right) \quad (8-4)$$

where,

V_{tc} = lower-bound shear strength based on toe compressive stress for wall

f_a = axial compressive stress due to gravity loads

f'_m = lower-bound masonry compressive strength

Q_G = lower-bound axial compressive force

The failure force based on equation (8-4) is 22 *kips* (98 *kN*). Using ASCE 41 proposed equations for rocking and shear failure modes (equations (8-2) and (8-3)), the failure forces are 22 *kip* (98 *kN*) and 17 *kip* (75.6 *kN*), respectively. Based on ASCE 41, the failure mode is shear which is not in accord with the experimental observations; the predicted failure force of ASCE underestimates the experimental results.

8.6 Evaluation of the cyclic performance

The idealized bilinear envelope of the load-displacement curves can be used as a simplified method for evaluating the stiffness, strength and ductility of the URM walls. In this report, the proposed method of Tomázevíc (1999) is utilized that is schematically shown in Figure 8-101 and the results for all tests following this method are presented in Table 8-7. In this method three characteristic points should be identified from the experimental load-displacement curve, including the crack limit state that corresponds to the formation of the first major crack (H_{cr}, d_{cr}), the peak resistance of the wall ($H_{max}, d_{H_{max}}$), and the peak displacement that is attained during the test ($H_{d_{max}}, d_{max}$). In this report, it is assumed that H_{cr} corresponds to $0.7 H_{max}$ (Morandi and Penna 2008). Presented in Table 8-7, the stiffness of the idealized bilinear curve (K_e) is considered to be the ratio of lateral force (H_{cr}) and displacement (d_{cr}) at the crack limit state. It can be seen that the stiffness of Wall-1-phaseI is much lower than the other walls, which is attributed to the boundary condition used for this wall. The peak resistance of the idealized bilinear curve (H_u) is calculated by equating the dissipated energy of the experimental monotonic curve and the idealized curve. In all of the tested walls the ultimate resistance of the idealized curve (H_u) is very close to the peak lateral resistance (H_{max}) since the experimental behaviors are similar to elastic-perfectly plastic behavior. The ultimate ductility is defined as $\mu = d_{max} / d_e$ where in all of the walls d_{max} was attained due to the experimental displacement capacity. As clearly shown in Table 8-7, very high values of ductility are achieved for all walls, which is typical for walls with rocking-flexure failure modes.

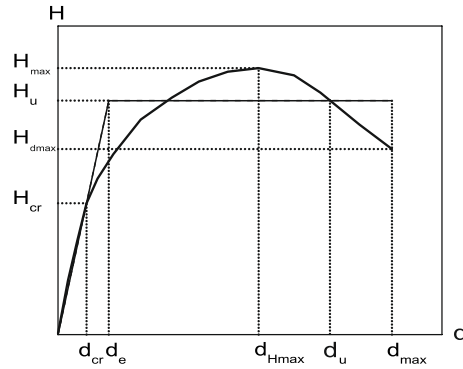


Figure 8-101 Bilinear idealization

Table 8-7 Characteristic values of the experimental envelopes

Wall	K_e kips/inch (kN/mm)	d_e inch (mm)	H_u kips (kN)	H_{max} kips (kN)	d_{Hmax} inch (mm)	d_{max} inch (mm)	Drift (%)	ductility μ
Wall-1-1	243.24 (42.6)	0.04 (1.0)	10.24 (45.5)	10.56 (47.0)	0.52 (13.2)	1.11 (28.2)	1.83	25.71
Wall-2	401.34 (70.3)	0.11 (2.8)	43.18 (192.1)	43.83 (195.0)	0.23 (5.8)	0.78 (19.8)	1.29	7.07
Wall-4	410.59 (71.9)	0.06 (1.5)	17.07 (75.9)	17.4 (77.4)	0.15 (3.8)	0.29 (7.4)	0.45	5.04
Wall-5	401.18 (70.3)	0.05 (1.3)	15.81 (70.3)	18.95 (84.3)	0.13 (3.3)	0.37 (9.4)	0.59	7.24
Wall-6	420.88 (73.7)	0.04 (1.0)	16.33 (72.6)	17.51 (77.9)	0.12 (3.0)	0.44 (11.2)	0.69	11.49

Seismic performance of the walls can also be evaluated by comparing the energy dissipation capacity. The cumulative dissipated energy E_N for Wall-4, Wall-5 and Wall-6 are presented in

Figure 8-102 that is defined as (Vasconcelos and Lourenço 2009):

$$E_N = \frac{1}{H_u d_e} \sum_{i=1}^n E_{idiss} \quad (8-5)$$

where E_{idiss} is the area of each hysteresis loop and n is the load cycle corresponding to a certain lateral drift. In Figure 8-102 the cumulative energy of the first cycle and second cycle (repeated cycle with the same amplitude-see loading protocols) are presented separately. It is noteworthy that although Wall-6 exhibited a different failure mode in comparison with Wall-4 and Wall-5, all of the walls have a similar curve that is due to the frictional forces initiated in the layer of mortar along which the crack propagated. Moreover, it can be seen that the rate of the energy

dissipation increases considerably after reaching the drift corresponding to the peak load (about 0.2%), which is related to the growth of damage after this point.

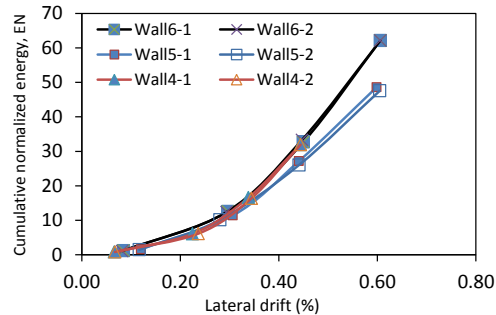


Figure 8-102 Variation of cumulative normalized dissipated energy

8.7 Comparison of the experimental and numerical results with ASCE 41 proposed empirical equations

Comparison between the results obtained by the tests, numerical analysis and ASCE 41 formulations are presented in Table 8-8. As shown in Table 8-9, the numerical prediction of stiffness for all walls is in good agreement to the experimental results. However, the stiffness obtained by ASCE 41 (2006) is about 100% higher than the experimental results for all walls. ASCE 41 prediction for the respective failure modes is in good agreement with the failure modes observed in the experimental tests, except for wall 6; however, the peak resisting force prediction of ASCE 41 is in a range of 35% from the experimental results.

Table 8-8. Comparison between the results

Wall	Stiffness (<i>kips/inch</i>)			Peak resisting force (<i>kips</i>)		
	Experimental	Numerical	ASCE 41	Experimental	Numerical	ASCE 41
Wall 1	260	270	520	10.7	11.5	10.9
Wall 3	-	490	930	17	16	10.8
Wall 4	410	-	930	17	-	13
Wall 5	400	470	930	20	16	13
Wall 6	410	450	870	18	15	16.6

Table 8-9. Differences in the results

Wall	Difference in stiffness (%)		Difference in peak resisting force (%)	
	Numerical	ASCE 41	Numerical	ASCE 41
Wall 1	3.9	100	7.5	1.9
Wall 3	-	-	-5.9	-36.5
Wall 4	-	126.9	-	-23.6
Wall 5	17.5	132.5	-20	-35
Wall 6	9.8	112.2	-16.7	-7.8

8.8 Conclusion

In this section the results of testing six URM walls have been presented. Two different types of bricks have been used for construction of the walls. Five walls were constructed using a high strength brick and a wall with a low strength brick. The walls were tested using different boundary conditions and with different combination of in-plane and out-of-plane loads or deformations. It was observed that restraining the rotation of the top plane of the wall plays a key role in the dominant failure mode of the walls. Wall 1 was first tested while the vertical actuators imposed the vertical forces independently. Accordingly, the rigid beam at top of the wall rotated, and rocking was the dominant failure mode of the wall. Once the vertical actuators were slaved together, the rigid beam remained level throughout the test and diagonal crack was the dominant failure mode. In the second wall, it was observed that more restraining of the vertical motion of the rigid beam, compared to the first wall, caused a significant confinement of the wall and

consequently, the resisting force was significantly increased. Diagonal cracking in addition to the crushing of the bricks in the corner, was the dominant failure mode for this wall.

For the walls tested in the presence of OP forces, it was concluded that due to the OP force, the wall easily collapses because of the accumulative OP deformations. However, in the case of restraining the OP deformation of the wall in a limited range, the peak resisting force would be close to the IP peak resisting force. Finally, a numerical simulation using the proposed numerical procedure of section 5 was performed for each wall and the numerical results were compared with the experimental results. It was shown that the proposed model in the fifth section is capable of accurately predicting the behavior of masonry walls in bidirectional cyclic loadings.

[@Seismicisolation](#)

SECTION 9

CONCLUSIONS AND RECOMMENDATIONS

9.1 Summary

Very few new URM buildings are constructed nowadays; however, unreinforced masonry structures still can be found either as a complete old masonry building or as a part of a new building. Therefore, it is necessary to be able to numerically predict the behavior of URM buildings or the effect of a URM part on a new building, particularly the effect of URM infill or partition walls on the seismic response of buildings. A significant effort of this report is focused on developing new material models and numerical procedures for simulation of URM structures in a meso-scale analysis framework. A part of this report is also devoted to developing macro-yield surfaces for macro-scale analysis of URM walls. Finally, an extensive experimental study was performed on URM walls using different boundary conditions and different types of bricks. A numerical validation was performed for each test and the robustness of the proposed numerical procedure has been validated.

9.2 Conclusions

In this report, three numerical procedures are proposed to model unreinforced masonry buildings. Two of the procedures use an implicit formulation and one uses an explicit formulation. The first numerical procedure, which was discussed in section three, is a simplified model for capturing the monotonic in-plane behavior of masonry walls. In this model, each brick was divided into a number of rigid elements connected together by interface elements. Using interface elements, all linear and nonlinear behavior of URM walls are concentrated in the joints. It led to significantly

decreasing the number of degrees-of-freedom (DOF) of the system and alleviating the computational demand while producing a good agreement with experimentally obtained data.

In section four, a set of interpolation functions was proposed to remedy the discontinuity problem of the constitutive material models with multi-yield surfaces. The interpolation functions were employed to the yield surface presented in section three and the functionality of these interpolation functions was carefully assessed. Finally, it was shown that using the proposed set of interpolation functions, the discontinuity problem can be resolved and the transition between the yield surfaces is easily achieved.

In the first two proposed modeling procedures in section 3 and 4 (in which the material models were extended using an implicit procedure) convergence of the numerical procedures, especially for large deformations, was a significant challenge for modeling of the masonry structures. In the third proposed numerical procedure in section 5, an explicit formulation has been used to model URM walls. Besides using an explicit formulation, the constitutive material model was extended to capture the cyclic three-dimensional behavior of masonry structures. Finally, the proposed constitutive material model was used to model a number of masonry walls and the numerical results were compared to the experimental results. It was shown that the numerical simulations results are in good agreement with the experimental results and evidently, the numerical procedures are capable of predicting different failure modes of URM walls.

Using the developed material model in section 5 (explicit cyclic material model), a numerical investigation has been conducted on the bidirectional behavior of URM walls, in section 6. A URM wall has been subjected to various loadings on its top plane, each time in different directions. It is shown how the failure mode changes from the diagonal crack for the in-

plane loading to the rocking mode for the out-of-plane loading. Moreover, the interaction curves for URM walls are presented, which show the maximum elastic and ultimate capacity of the walls. According to the proposed interaction curves, in the loading cases with an angle between the in-plane and out-of-plane directions, the wall tends to gain the in-plane peak resisting load, although in a larger deformation compared to the in-plane loading.

Generation of the interaction curves using the finite element approach is computationally very extensive. Therefore, an analytical procedure is proposed in section 7 that illustrates the elastic domain of URM walls under combination of in-plane and out-of-plane loads. The interaction curves show the maximum elastic capacity of walls under bidirectional loadings while the gravity load changes. In the plasticity theory, a yield surface is only a function of material parameters; however, the proposed macro-yield surfaces take full account of brick and mortar materials, and geometry of the wall. The interaction curves are developed for different URM walls with various aspect ratios, including a square and wide wall.

Finally, in the last section of this report, a comprehensive well-documented experimental study on URM walls is presented. Six different URM walls were constructed with two different types of brick and were subjected to different types of loading. For testing the walls, different boundary conditions were used. It was observed that restraining the rotation of the top plane of the wall has a key role in the dominant failure mode of the wall. For instance, rocking was the dominant failure mode of wall 1 while the top plane of the wall was allowed to rotate. The failure mode changed to diagonal cracking when the top rigid beam was restrained from rotation. Moreover, it was observed that type of material used for construction of walls has a great influence in the failure mode of URM walls. Walls 5 and 6 were tested using the same loading

protocol and boundary conditions. However, due to the use of different types of brick (low and high strength bricks), different failure modes were observed.

A numerical comparison using the proposed material model of section 5 was performed with the experimental results for each wall and the robustness of the proposed numerical scheme has been verified. Furthermore, the empirical equations of ASCE 41 have been used to derive the stiffness and peak resisting load of the walls. It was clearly shown that the empirical equations of ASCE 41 do not predict stiffness of the walls accurately. In most of the cases, the prediction of ASCE for the failure mode of the walls was accurate; however, estimation of the peak resisting load was in the range of 30% from the experimental results as well as the proposed numerical procedures.

9.3 Recommendations for future research

A list of future research topics relevant to masonry modeling follows based on the gaps in knowledge identified in this study, but not addressed in this report:

1. The developed three-dimensional cyclic material model in this report can be used in development of a comprehensive macro-element which can capture the in-plane and out-of-plane interaction effects.
2. The developed three-dimensional cyclic material model in this report is capable of modeling the behavior of unreinforced masonry structures under earthquake effects. In order to fulfill this purpose, some calibration should be performed using the results of shaking table tests mentioned in the literature review of this report. Afterward, the model

can be used to assess the behavior of any unreinforced masonry building under earthquake excitations.

3. The proposed three-dimensional cyclic material model in this report can be used in the investigation of unreinforced masonry infill walls, either in concrete or steel buildings. This model can also be used to build a comprehensive macro model for investigation of reinforced concrete or steel buildings with URM infill walls under earthquake excitations.
4. A comprehensive investigation can be performed on the response of reinforced masonry structures under either quasi-static or dynamic loadings, using the proposed three-dimensional model in this report.
5. The proposed interaction curves in section 7 show the elastic domain (macro-yield surface) for the in-plane and out-of-plane forces while the gravity load changes. The study should be extended to capture the post elastic behavior (macro flow rule) of the wall.
6. In section 8, an experimental investigation has been presented on the bidirectional behavior of unreinforced masonry walls using quasi-static loadings. This investigation can be extended to study the bidirectional behavior of unreinforced masonry walls under any excitation effect rather than a quasi-static load.

SECTION 10

REFERENCES

- American Society of Civil Engineers (2007), *Seismic rehabilitation of existing buildings*, 41-06, Reston, VA
- Abaqus version 6.9 [computer software]. SIMULIA, The Dassault Systèmes Providence, RI.
- Bathe, K.-J. (1995). *Finite Element Procedures*, Prentice Hall.
- Beer, G. (1985). "An isoparametric joint/interface element for finite element analysis." *International Journal for Numerical Methods in Engineering*, 21(Copyright 1985, IEE), 585-600.
- Bothara, J. K., Dhakal, R. P., and Mander, J. B. (2010). "Seismic performance of an unreinforced masonry building: An experimental investigation." *Earthquake Engineering and Structural Dynamics*, 39(Compendex), 45-68.
- Casolo, and S. (2004). "Modelling in-plane micro-structure of masonry walls by rigid elements." *International Journal of Solids and Structures*, 41(13), 3625-3641.
- Casolo, S., and Pena, F. (2007). "Rigid element model for in-plane dynamics of masonry walls considering hysteretic behaviour and damage." *Earthquake Engineering and Structural Dynamics*, 36(Compendex), 1029-1048.
- Chaimoon, K., and Attard, M. M. (2007). "Modeling of unreinforced masonry walls under shear and compression." *Engineering Structures*, 29(Compendex), 2056-2068.
- Chen, S. Y., Moon, F. L., and Yi, T. (2008). "A macroelement for the nonlinear analysis of in-plane unreinforced masonry piers." *Engineering Structures*, 30(Compendex), 2242-2252.
- Cundall, P. A. "A computer model for simulating progressive, large-scale movements in blocky rock systems." *Proc., Rock fracture; Vol. 1*, Int. Soc. Rock Mech.
- Cusatis, G., Bazant, Z. P., and Cedolin, L. (2003). "Confinement-shear lattice model for concrete damage in tension and compression: I. Theory." *Journal of Engineering Mechanics*, 129(GEOBASE), 1439-1448.
- Cusatis, G., Bazant, Z. P., and Cedolin, L. (2003). "Confinement-shear lattice model for concrete damage in tension and compression: II. Computation and validation." *Journal of Engineering Mechanics*, 129(GEOBASE), 1449-1458.
- Cusatis, G., Bazant, Z. P., and Cedolin, L. (2006). "Confinement-shear lattice CSL model for fracture propagation in concrete." *Computer Methods in Applied Mechanics and Engineering*, 195(Copyright 2007, The Institution of Engineering and Technology), 7154-7171.
- Cusatis, G., and Cedolin, L. (2007). "Two-scale study of concrete fracturing behavior." *Engineering Fracture Mechanics*, 74(Compendex), 3-17.

- da Porto, F., Grendene, M., and Modena, C. (2009). "Estimation of load reduction factors for clay masonry walls." *Earthquake Engineering & Structural Dynamics*, 38(10), 1155-1174.
- DIANA, version 2008 [computer software]. *User manual*, Netherland.
- Dolek, M., and Fajfar, P. (2008). "The effect of masonry infills on the seismic response of a four-storey reinforced concrete frame - a deterministic assessment." *Engineering Structures*, 30(Compendex), 1991-2001.
- FEMA (Federal Emergency Management Agency). (2000). "Prestandard and commentary for the seismic rehabilitation of buildings." 356, Washington, DC.
- Ghabaoussi, J., Wilson, E. L., and Isenberg, J. (1973). "Finite element for rock joints and interfaces." *American Society of Civil Engineers, Journal of the Soil Mechanics and Foundations Division*, 99(Compendex), 833-884.
- Giambanco, G., Rizzo, S., and Spallino, R. (2001). "Numerical analysis of masonry structures via interface models." *Computer Methods in Applied Mechanics and Engineering*, 190(Copyright 2001, IEE), 6493-6511.
- Gilbert, M., Burnett, S., Molyneaux, T., Beattie, G., and Hobbs, B. (2007). "The performance of unreinforced masonry walls subjected to low-velocity impacts: Finite element analysis." *International Journal of Impact Engineering*, 34(Copyright 2007, The Institution of Engineering and Technology), 1433-1450.
- Gopalaratnam, V. S., and Shah, S. P. (1985). "Softening response of plain concrete in direct tension." *Journal of the American Concrete Institute*, 82(Compendex), 310-323.
- Griffith, M. C., Vaculik, J., Lam, N. T. K., Wilson, J., and Lumantarna, E. (2007). "Cyclic testing of unreinforced masonry walls in two-way bending." *Earthquake Engineering & Structural Dynamics*, 36(6), 801-821.
- Haider, W. (2007). "In-plane response of wide spaced reinforced masonry shear walls." PhD dissertation, Central Queensland University, Australia.
- Hashemi, A., and Mosalam, K. M. (2007). "Seismic Evaluation of Reinforced Concrete Buildings Including Effects of Masonry Infill Walls." University of California, Berkeley, Berkeley.
- Hohberg, J.-M. (1992). "A joint element for the nonlinear dynamic analysis of arch dams." Institute of Structural Engineering ETH Zurich Basel etc.
- Hrennikoff, A. (1941). "Solution of problems of elasticity by the framework method." *J. Appl. Mech. Tech. Phys.*, 12, 169-175.
- UDEC - Universal distinct element code Version 4.0 (2004). [computer software] User manual."Minneapolis (MN, USA).
- LS-DYNA (1998) [computer software] "User manual." Livermore software technology corporation.
- Kadysiewski, S., and Mosalam, K. M. (2009). "Modeling of Unreinforced Masonry Infill Walls Considering In-Plane and Out-of-Plane Interaction." University of California, Berkeley.

- Karapitta, L., Mouzakis, H., and Carydis, P. (2010). "Explicit finite-element analysis for the in-plane cyclic behavior of unreinforced masonry structures." *Earthquake Engineering & Structural Dynamics*, n/a-n/a.
- Kawai, T. (1978). "New discrete models and their application to seismic response analysis of structures." *Nuclear Engineering and Design*, 48(Copyright 1978, IEE), 207-229.
- Lee, J., and Fenves, G. L. (1998). "Plastic-Damage Model for Cyclic Loading of Concrete Structures." *Journal of Engineering Mechanics*, 124, 892-900.
- Lourenco, P. (1996). "Computational Strategies for Masonry Structures." PhD Dissertation, Delft University, Netherlands.
- Lubliner, J. (1990). "Plasticity Theory." Macmillan Publishing Company, New York.
- Lubliner, J., Oliver, J., Oller, S., and Onate, E. (1989). "Plastic-damage model for concrete." *International Journal of Solids and Structures*, 25(Compendex), 299-326.
- Mohebbkhan, A., Tasnimi, A. A., and Moghadam, H. A. (2008). "Nonlinear analysis of masonry-infilled steel frames with openings using discrete element method." *Journal of Constructional Steel Research*, 64(Compendex), 1463-1472.
- Morandi, G. M. P., and Penna, A. "Experimental in-plane cyclic response of masonry walls with clay units." *Proc., The 14th World Conference on Earthquake Engineering*.
- Oliveira, D. V., and Lourenco, P. B. (2004). "Implementation and validation of a constitutive model for the cyclic behaviour of interface elements." *Computers & Structures*, 82(17-19), 1451-1461.
- Oliveira, D. V., and Lourenco, P. B. "Implementation and validation of a constitutive model for the cyclic behaviour of interface elements." *Proc., Computational Mechanics in Portugal, April 17, 2003 - April 19, 2003*, Elsevier Ltd, 1451-1461.
- Page, A. W. (1978). "Finite element model for masonry." *J. Struc. Div., ASCE*, 104 (8)(Compendex), 1267- 1285.
- Paquette, J., and Bruneau, M. (2006). "Pseudo-dynamic testing of unreinforced masonry building with flexible diaphragm and comparison with existing procedures." *Construction & Building Materials*, 20(Copyright 2006, IEE), 220-228.
- Paquette, J., Bruneau, M., and Brzev, S. (2004). "Seismic testing of repaired unreinforced masonry building having flexible diaphragm." *Journal of Structural Engineering*, 130(Compendex), 1487-1496.
- Park, J., Towashiraporn, P., Craig, J. I., and Goodno, B. J. (2009). "Seismic fragility analysis of low-rise unreinforced masonry structures." *Engineering Structures*, 31(Compendex), 125-137.
- Pasticier, L., Amadio, C., and Fragiaco, M. (2008). "Non-linear seismic analysis and vulnerability evaluation of a masonry building by means of the SAP2000 V.10 code." *Earthquake Engineering and Structural Dynamics*, 37(Compendex), 467-485.
- Pluijm, R. V. D. (1992). "Material properties of masonry and its components under tension and shear." *Proc. 6th Canadian Masonry Symposium*, 675-686.
- Pluijm, R. V. D. (1993). "Shear behavior of bed joints." *Proc. 6th North American*, 125-136.

- Pluijm, R. V. D. "Shear behavior of bed joints." *Proc., Proc. 6th North American Masonry Conf.*, Drexel University, 125-136.
- Pluijm, R. V. D., and Vermeltoort, A. T. (1991). "Deformation controlled tension and compression tests in units, mortar and masonry." TNO-Bouw, Delft, Netherlands.
- Pluijm, V. d. (1992). "Material properties of masonry and its components under tension and shear." *Proc. 6th Canadian Masonry Symposium*, S. V.V. Neis, Saskatchewan, ed.Canada, 675-686.
- Pluijm, V. d. (1993). "Shear behavior of bed joints." *6th North American Masonry Conf.*, A. A. Hamid, and H. G. Harris, eds.Drexel University, Philadelphia, Pennsylvania, USA, 125-136.
- Pluijm, V. d. (1993). "Shear behavior of bed joints." *Proc. 6th North American Masonry Conf.*, A. A. H. a. H. G. Harris, ed.Drexel University, Philadelphia, Pennsylvania, USA, 125-136.
- Pujol, S., and Fick, D. (2010). "The test of a full-scale three-story RC structure with masonry infill walls." *Engineering Structures*, 32(Compendex), 3112-3121.
- Rabinovitch, O., and Madah, H. (2011). "Finite element modeling and shake-table testing of unidirectional infill masonry walls under out-of-plane dynamic loads." (Compendex).
- Raijmakers, T. M. J., and Vermeltoort, A. T. (1992). "Deformation controlled tests in masonry shear walls." Report B-92-1156, TNO-Bouw, Delft.
- Reinhardt, H. W. (1984). "Fracture mechanics of an elastic softening material like concrete." *Heron*, 29(Compendex).
- Roelfstra, P. E. (1988). "Numerical concrete." PhD, Ecole Polytechnique Fédérale de Lausanne, Switzerland.
- Schellekens, J. C. J. (1992). "Computational strategies for composite structures." PhD, Delft University of Technology, Delft.
- Schellekens, J. C. J., and De Borst, R. (1993). "On the numerical integrations of interface elements." *International Journal for Numerical Methods in Engineering*, 36(Compendex), 43-66.
- Schlangen, E. (1995). "Computational aspects of fracture simulations with lattice models." *Fracture mechanics of concrete structures*, 913-928.
- Schlangen, E., and Garboczi, E. J. (1997). "Fracture simulations of concrete using lattice models: computational aspects." *Engineering Fracture Mechanics*, 57(Compendex), 319-332.
- Senthivel, R., and Lourenco, P. B. (2009). "Finite element modelling of deformation characteristics of historical stone masonry shear walls." *Engineering Structures*, 31(Compendex), 1930-1943.
- Stavridis, A. (2009). "Analytical and Experimental Study of Seismic Performance of Reinforced Concrete Frames Infilled with Masonry Walls." PhD Dissertation, University of California, San Diego, San Diego.

- Stavridis, A., and Shing, P. B. (2010). "Finite-element modeling of nonlinear behavior of masonry-infilled RC frames." *Journal of Structural Engineering*, 136(Compendex), 285-296.
- Tomázevíc, M. (1999). *Earthquake-resistant design of masonry buildings*, Imperial College Press.
- Tu, Y.-H., Chuang, T.-H., Liu, P.-M., and Yang, Y.-S. (2010). "Out-of-plane shaking table tests on unreinforced masonry panels in RC frames." *Engineering Structures*, 32(Compendex), 3925-3935.
- Vasconcelos, G., and Lourenço, P. (2009). "In-plane experimental behavior of stone masonry walls under cyclic loading." *Journal of Structural Engineering*, 135(10), 1269-1277.
- Vermeltfoort, A. T., and Raijmakers, T. M. J. (1993). "Deformation controlled tests in masonry shear walls, Part 2." Report TUE/BKO/93.08, Eindhoven University of Technology, Netherlands.
- Vermeltfoort, V. D. P. a. (1991). "Deformation controlled tension and compression tests in units, mortar and masonry." TNO-Bouw, Netherlands.
- Zdenek P. Bazant, L. C. (1991). *Stability of Structures: Elastic, Inelastic, Fracture, and Damage Theories*, Dover Publications.
- Zienkiewicz OC, T. R. (1991). *The Finite Element Method*, McGraw-Hill, London.
- Zubelewicz, A., and Bazant, Z. P. (1987). "Interface element modeling of fracture in aggregate composites." *Journal of Engineering Mechanics*, 113(Compendex), 1619-1630.

[@Seismicisolation](#)

MCEER Technical Reports

MCEER publishes technical reports on a variety of subjects written by authors funded through MCEER. These reports are available from both MCEER Publications and the National Technical Information Service (NTIS). Requests for reports should be directed to MCEER Publications, MCEER, University at Buffalo, State University of New York, 133A Ketter Hall, Buffalo, New York 14260. Reports can also be requested through NTIS, P.O. Box 1425, Springfield, Virginia 22151. NTIS accession numbers are shown in parenthesis, if available.

- NCEER-87-0001 "First-Year Program in Research, Education and Technology Transfer," 3/5/87, (PB88-134275, A04, MF-A01).
- NCEER-87-0002 "Experimental Evaluation of Instantaneous Optimal Algorithms for Structural Control," by R.C. Lin, T.T. Soong and A.M. Reinhorn, 4/20/87, (PB88-134341, A04, MF-A01).
- NCEER-87-0003 "Experimentation Using the Earthquake Simulation Facilities at University at Buffalo," by A.M. Reinhorn and R.L. Ketter, not available.
- NCEER-87-0004 "The System Characteristics and Performance of a Shaking Table," by J.S. Hwang, K.C. Chang and G.C. Lee, 6/1/87, (PB88-134259, A03, MF-A01). This report is available only through NTIS (see address given above).
- NCEER-87-0005 "A Finite Element Formulation for Nonlinear Viscoplastic Material Using a Q Model," by O. Gyebe and G. Dasgupta, 11/2/87, (PB88-213764, A08, MF-A01).
- NCEER-87-0006 "Symbolic Manipulation Program (SMP) - Algebraic Codes for Two and Three Dimensional Finite Element Formulations," by X. Lee and G. Dasgupta, 11/9/87, (PB88-218522, A05, MF-A01).
- NCEER-87-0007 "Instantaneous Optimal Control Laws for Tall Buildings Under Seismic Excitations," by J.N. Yang, A. Akbarpour and P. Ghaemmaghami, 6/10/87, (PB88-134333, A06, MF-A01). This report is only available through NTIS (see address given above).
- NCEER-87-0008 "IDARC: Inelastic Damage Analysis of Reinforced Concrete Frame - Shear-Wall Structures," by Y.J. Park, A.M. Reinhorn and S.K. Kunnath, 7/20/87, (PB88-134325, A09, MF-A01). This report is only available through NTIS (see address given above).
- NCEER-87-0009 "Liquefaction Potential for New York State: A Preliminary Report on Sites in Manhattan and Buffalo," by M. Budhu, V. Vijayakumar, R.F. Giese and L. Baumgras, 8/31/87, (PB88-163704, A03, MF-A01). This report is available only through NTIS (see address given above).
- NCEER-87-0010 "Vertical and Torsional Vibration of Foundations in Inhomogeneous Media," by A.S. Veletsos and K.W. Dotson, 6/1/87, (PB88-134291, A03, MF-A01). This report is only available through NTIS (see address given above).
- NCEER-87-0011 "Seismic Probabilistic Risk Assessment and Seismic Margins Studies for Nuclear Power Plants," by Howard H.M. Hwang, 6/15/87, (PB88-134267, A03, MF-A01). This report is only available through NTIS (see address given above).
- NCEER-87-0012 "Parametric Studies of Frequency Response of Secondary Systems Under Ground-Acceleration Excitations," by Y. Yong and Y.K. Lin, 6/10/87, (PB88-134309, A03, MF-A01). This report is only available through NTIS (see address given above).
- NCEER-87-0013 "Frequency Response of Secondary Systems Under Seismic Excitation," by J.A. HoLung, J. Cai and Y.K. Lin, 7/31/87, (PB88-134317, A05, MF-A01). This report is only available through NTIS (see address given above).
- NCEER-87-0014 "Modelling Earthquake Ground Motions in Seismically Active Regions Using Parametric Time Series Methods," by G.W. Ellis and A.S. Cakmak, 8/25/87, (PB88-134283, A08, MF-A01). This report is only available through NTIS (see address given above).

- NCEER-87-0015 "Detection and Assessment of Seismic Structural Damage," by E. DiPasquale and A.S. Cakmak, 8/25/87, (PB88-163712, A05, MF-A01). This report is only available through NTIS (see address given above).
- NCEER-87-0016 "Pipeline Experiment at Parkfield, California," by J. Isenberg and E. Richardson, 9/15/87, (PB88-163720, A03, MF-A01). This report is available only through NTIS (see address given above).
- NCEER-87-0017 "Digital Simulation of Seismic Ground Motion," by M. Shinozuka, G. Deodatis and T. Harada, 8/31/87, (PB88-155197, A04, MF-A01). This report is available only through NTIS (see address given above).
- NCEER-87-0018 "Practical Considerations for Structural Control: System Uncertainty, System Time Delay and Truncation of Small Control Forces," J.N. Yang and A. Akbarpour, 8/10/87, (PB88-163738, A08, MF-A01). This report is only available through NTIS (see address given above).
- NCEER-87-0019 "Modal Analysis of Nonclassically Damped Structural Systems Using Canonical Transformation," by J.N. Yang, S. Sarkani and F.X. Long, 9/27/87, (PB88-187851, A04, MF-A01).
- NCEER-87-0020 "A Nonstationary Solution in Random Vibration Theory," by J.R. Red-Horse and P.D. Spanos, 11/3/87, (PB88-163746, A03, MF-A01).
- NCEER-87-0021 "Horizontal Impedances for Radially Inhomogeneous Viscoelastic Soil Layers," by A.S. Veletsos and K.W. Dotson, 10/15/87, (PB88-150859, A04, MF-A01).
- NCEER-87-0022 "Seismic Damage Assessment of Reinforced Concrete Members," by Y.S. Chung, C. Meyer and M. Shinozuka, 10/9/87, (PB88-150867, A05, MF-A01). This report is available only through NTIS (see address given above).
- NCEER-87-0023 "Active Structural Control in Civil Engineering," by T.T. Soong, 11/11/87, (PB88-187778, A03, MF-A01).
- NCEER-87-0024 "Vertical and Torsional Impedances for Radially Inhomogeneous Viscoelastic Soil Layers," by K.W. Dotson and A.S. Veletsos, 12/87, (PB88-187786, A03, MF-A01).
- NCEER-87-0025 "Proceedings from the Symposium on Seismic Hazards, Ground Motions, Soil-Liquefaction and Engineering Practice in Eastern North America," October 20-22, 1987, edited by K.H. Jacob, 12/87, (PB88-188115, A23, MF-A01). This report is available only through NTIS (see address given above).
- NCEER-87-0026 "Report on the Whittier-Narrows, California, Earthquake of October 1, 1987," by J. Pantelic and A. Reinhorn, 11/87, (PB88-187752, A03, MF-A01). This report is available only through NTIS (see address given above).
- NCEER-87-0027 "Design of a Modular Program for Transient Nonlinear Analysis of Large 3-D Building Structures," by S. Srivastav and J.F. Abel, 12/30/87, (PB88-187950, A05, MF-A01). This report is only available through NTIS (see address given above).
- NCEER-87-0028 "Second-Year Program in Research, Education and Technology Transfer," 3/8/88, (PB88-219480, A04, MF-A01).
- NCEER-88-0001 "Workshop on Seismic Computer Analysis and Design of Buildings With Interactive Graphics," by W. McGuire, J.F. Abel and C.H. Conley, 1/18/88, (PB88-187760, A03, MF-A01). This report is only available through NTIS (see address given above).
- NCEER-88-0002 "Optimal Control of Nonlinear Flexible Structures," by J.N. Yang, F.X. Long and D. Wong, 1/22/88, (PB88-213772, A06, MF-A01).
- NCEER-88-0003 "Substructuring Techniques in the Time Domain for Primary-Secondary Structural Systems," by G.D. Manolis and G. Juhn, 2/10/88, (PB88-213780, A04, MF-A01).
- NCEER-88-0004 "Iterative Seismic Analysis of Primary-Secondary Systems," by A. Singhal, L.D. Lutes and P.D. Spanos, 2/23/88, (PB88-213798, A04, MF-A01).
- NCEER-88-0005 "Stochastic Finite Element Expansion for Random Media," by P.D. Spanos and R. Ghanem, 3/14/88, (PB88-213806, A03, MF-A01).

- NCEER-88-0006 "Combining Structural Optimization and Structural Control," by F.Y. Cheng and C.P. Pantelides, 1/10/88, (PB88-213814, A05, MF-A01).
- NCEER-88-0007 "Seismic Performance Assessment of Code-Designed Structures," by H.H-M. Hwang, J-W. Jaw and H-J. Shau, 3/20/88, (PB88-219423, A04, MF-A01). This report is only available through NTIS (see address given above).
- NCEER-88-0008 "Reliability Analysis of Code-Designed Structures Under Natural Hazards," by H.H-M. Hwang, H. Ushiba and M. Shinozuka, 2/29/88, (PB88-229471, A07, MF-A01). This report is only available through NTIS (see address given above).
- NCEER-88-0009 "Seismic Fragility Analysis of Shear Wall Structures," by J-W Jaw and H.H-M. Hwang, 4/30/88, (PB89-102867, A04, MF-A01).
- NCEER-88-0010 "Base Isolation of a Multi-Story Building Under a Harmonic Ground Motion - A Comparison of Performances of Various Systems," by F-G Fan, G. Ahmadi and I.G. Tadjbakhsh, 5/18/88, (PB89-122238, A06, MF-A01). This report is only available through NTIS (see address given above).
- NCEER-88-0011 "Seismic Floor Response Spectra for a Combined System by Green's Functions," by F.M. Lavelle, L.A. Bergman and P.D. Spanos, 5/1/88, (PB89-102875, A03, MF-A01).
- NCEER-88-0012 "A New Solution Technique for Randomly Excited Hysteretic Structures," by G.Q. Cai and Y.K. Lin, 5/16/88, (PB89-102883, A03, MF-A01).
- NCEER-88-0013 "A Study of Radiation Damping and Soil-Structure Interaction Effects in the Centrifuge," by K. Weissman, supervised by J.H. Prevost, 5/24/88, (PB89-144703, A06, MF-A01).
- NCEER-88-0014 "Parameter Identification and Implementation of a Kinematic Plasticity Model for Frictional Soils," by J.H. Prevost and D.V. Griffiths, not available.
- NCEER-88-0015 "Two- and Three- Dimensional Dynamic Finite Element Analyses of the Long Valley Dam," by D.V. Griffiths and J.H. Prevost, 6/17/88, (PB89-144711, A04, MF-A01).
- NCEER-88-0016 "Damage Assessment of Reinforced Concrete Structures in Eastern United States," by A.M. Reinhorn, M.J. Seidel, S.K. Kunnath and Y.J. Park, 6/15/88, (PB89-122220, A04, MF-A01). This report is only available through NTIS (see address given above).
- NCEER-88-0017 "Dynamic Compliance of Vertically Loaded Strip Foundations in Multilayered Viscoelastic Soils," by S. Ahmad and A.S.M. Israil, 6/17/88, (PB89-102891, A04, MF-A01).
- NCEER-88-0018 "An Experimental Study of Seismic Structural Response With Added Viscoelastic Dampers," by R.C. Lin, Z. Liang, T.T. Soong and R.H. Zhang, 6/30/88, (PB89-122212, A05, MF-A01). This report is available only through NTIS (see address given above).
- NCEER-88-0019 "Experimental Investigation of Primary - Secondary System Interaction," by G.D. Manolis, G. Juhn and A.M. Reinhorn, 5/27/88, (PB89-122204, A04, MF-A01).
- NCEER-88-0020 "A Response Spectrum Approach For Analysis of Nonclassically Damped Structures," by J.N. Yang, S. Sarkani and F.X. Long, 4/22/88, (PB89-102909, A04, MF-A01).
- NCEER-88-0021 "Seismic Interaction of Structures and Soils: Stochastic Approach," by A.S. Veletsos and A.M. Prasad, 7/21/88, (PB89-122196, A04, MF-A01). This report is only available through NTIS (see address given above).
- NCEER-88-0022 "Identification of the Serviceability Limit State and Detection of Seismic Structural Damage," by E. DiPasquale and A.S. Cakmak, 6/15/88, (PB89-122188, A05, MF-A01). This report is available only through NTIS (see address given above).
- NCEER-88-0023 "Multi-Hazard Risk Analysis: Case of a Simple Offshore Structure," by B.K. Bhartia and E.H. Vanmarcke, 7/21/88, (PB89-145213, A05, MF-A01).

- NCEER-88-0024 "Automated Seismic Design of Reinforced Concrete Buildings," by Y.S. Chung, C. Meyer and M. Shinozuka, 7/5/88, (PB89-122170, A06, MF-A01). This report is available only through NTIS (see address given above).
- NCEER-88-0025 "Experimental Study of Active Control of MDOF Structures Under Seismic Excitations," by L.L. Chung, R.C. Lin, T.T. Soong and A.M. Reinhorn, 7/10/88, (PB89-122600, A04, MF-A01).
- NCEER-88-0026 "Earthquake Simulation Tests of a Low-Rise Metal Structure," by J.S. Hwang, K.C. Chang, G.C. Lee and R.L. Ketter, 8/1/88, (PB89-102917, A04, MF-A01).
- NCEER-88-0027 "Systems Study of Urban Response and Reconstruction Due to Catastrophic Earthquakes," by F. Kozin and H.K. Zhou, 9/22/88, (PB90-162348, A04, MF-A01).
- NCEER-88-0028 "Seismic Fragility Analysis of Plane Frame Structures," by H.H-M. Hwang and Y.K. Low, 7/31/88, (PB89-131445, A06, MF-A01).
- NCEER-88-0029 "Response Analysis of Stochastic Structures," by A. Kardara, C. Bucher and M. Shinozuka, 9/22/88, (PB89-174429, A04, MF-A01).
- NCEER-88-0030 "Nonnormal Accelerations Due to Yielding in a Primary Structure," by D.C.K. Chen and L.D. Lutes, 9/19/88, (PB89-131437, A04, MF-A01).
- NCEER-88-0031 "Design Approaches for Soil-Structure Interaction," by A.S. Veletsos, A.M. Prasad and Y. Tang, 12/30/88, (PB89-174437, A03, MF-A01). This report is available only through NTIS (see address given above).
- NCEER-88-0032 "A Re-evaluation of Design Spectra for Seismic Damage Control," by C.J. Turkstra and A.G. Tallin, 11/7/88, (PB89-145221, A05, MF-A01).
- NCEER-88-0033 "The Behavior and Design of Noncontact Lap Splices Subjected to Repeated Inelastic Tensile Loading," by V.E. Sagan, P. Gergely and R.N. White, 12/8/88, (PB89-163737, A08, MF-A01).
- NCEER-88-0034 "Seismic Response of Pile Foundations," by S.M. Mamoon, P.K. Banerjee and S. Ahmad, 11/1/88, (PB89-145239, A04, MF-A01).
- NCEER-88-0035 "Modeling of R/C Building Structures With Flexible Floor Diaphragms (IDARC2)," by A.M. Reinhorn, S.K. Kunnath and N. Panahshahi, 9/7/88, (PB89-207153, A07, MF-A01).
- NCEER-88-0036 "Solution of the Dam-Reservoir Interaction Problem Using a Combination of FEM, BEM with Particular Integrals, Modal Analysis, and Substructuring," by C-S. Tsai, G.C. Lee and R.L. Ketter, 12/31/88, (PB89-207146, A04, MF-A01).
- NCEER-88-0037 "Optimal Placement of Actuators for Structural Control," by F.Y. Cheng and C.P. Pantelides, 8/15/88, (PB89-162846, A05, MF-A01).
- NCEER-88-0038 "Teflon Bearings in Aseismic Base Isolation: Experimental Studies and Mathematical Modeling," by A. Mokha, M.C. Constantinou and A.M. Reinhorn, 12/5/88, (PB89-218457, A10, MF-A01). This report is available only through NTIS (see address given above).
- NCEER-88-0039 "Seismic Behavior of Flat Slab High-Rise Buildings in the New York City Area," by P. Weidlinger and M. Ettouney, 10/15/88, (PB90-145681, A04, MF-A01).
- NCEER-88-0040 "Evaluation of the Earthquake Resistance of Existing Buildings in New York City," by P. Weidlinger and M. Ettouney, 10/15/88, not available.
- NCEER-88-0041 "Small-Scale Modeling Techniques for Reinforced Concrete Structures Subjected to Seismic Loads," by W. Kim, A. El-Attar and R.N. White, 11/22/88, (PB89-189625, A05, MF-A01).
- NCEER-88-0042 "Modeling Strong Ground Motion from Multiple Event Earthquakes," by G.W. Ellis and A.S. Cakmak, 10/15/88, (PB89-174445, A03, MF-A01).

- NCEER-88-0043 "Nonstationary Models of Seismic Ground Acceleration," by M. Grigoriu, S.E. Ruiz and E. Rosenblueth, 7/15/88, (PB89-189617, A04, MF-A01).
- NCEER-88-0044 "SARCF User's Guide: Seismic Analysis of Reinforced Concrete Frames," by Y.S. Chung, C. Meyer and M. Shinozuka, 11/9/88, (PB89-174452, A08, MF-A01).
- NCEER-88-0045 "First Expert Panel Meeting on Disaster Research and Planning," edited by J. Pantelic and J. Stoyke, 9/15/88, (PB89-174460, A05, MF-A01).
- NCEER-88-0046 "Preliminary Studies of the Effect of Degrading Infill Walls on the Nonlinear Seismic Response of Steel Frames," by C.Z. Chrysostomou, P. Gergely and J.F. Abel, 12/19/88, (PB89-208383, A05, MF-A01).
- NCEER-88-0047 "Reinforced Concrete Frame Component Testing Facility - Design, Construction, Instrumentation and Operation," by S.P. Pessiki, C. Conley, T. Bond, P. Gergely and R.N. White, 12/16/88, (PB89-174478, A04, MF-A01).
- NCEER-89-0001 "Effects of Protective Cushion and Soil Compliancy on the Response of Equipment Within a Seismically Excited Building," by J.A. HoLung, 2/16/89, (PB89-207179, A04, MF-A01).
- NCEER-89-0002 "Statistical Evaluation of Response Modification Factors for Reinforced Concrete Structures," by H.H-M. Hwang and J-W. Jaw, 2/17/89, (PB89-207187, A05, MF-A01).
- NCEER-89-0003 "Hysteretic Columns Under Random Excitation," by G-Q. Cai and Y.K. Lin, 1/9/89, (PB89-196513, A03, MF-A01).
- NCEER-89-0004 "Experimental Study of 'Elephant Foot Bulge' Instability of Thin-Walled Metal Tanks," by Z-H. Jia and R.L. Ketter, 2/22/89, (PB89-207195, A03, MF-A01).
- NCEER-89-0005 "Experiment on Performance of Buried Pipelines Across San Andreas Fault," by J. Isenberg, E. Richardson and T.D. O'Rourke, 3/10/89, (PB89-218440, A04, MF-A01). This report is available only through NTIS (see address given above).
- NCEER-89-0006 "A Knowledge-Based Approach to Structural Design of Earthquake-Resistant Buildings," by M. Subramani, P. Gergely, C.H. Conley, J.F. Abel and A.H. Zaghaw, 1/15/89, (PB89-218465, A06, MF-A01).
- NCEER-89-0007 "Liquefaction Hazards and Their Effects on Buried Pipelines," by T.D. O'Rourke and P.A. Lane, 2/1/89, (PB89-218481, A09, MF-A01).
- NCEER-89-0008 "Fundamentals of System Identification in Structural Dynamics," by H. Imai, C-B. Yun, O. Maruyama and M. Shinozuka, 1/26/89, (PB89-207211, A04, MF-A01).
- NCEER-89-0009 "Effects of the 1985 Michoacan Earthquake on Water Systems and Other Buried Lifelines in Mexico," by A.G. Ayala and M.J. O'Rourke, 3/8/89, (PB89-207229, A06, MF-A01).
- NCEER-89-R010 "NCEER Bibliography of Earthquake Education Materials," by K.E.K. Ross, Second Revision, 9/1/89, (PB90-125352, A05, MF-A01). This report is replaced by NCEER-92-0018.
- NCEER-89-0011 "Inelastic Three-Dimensional Response Analysis of Reinforced Concrete Building Structures (IDARC-3D), Part I - Modeling," by S.K. Kunnath and A.M. Reinhorn, 4/17/89, (PB90-114612, A07, MF-A01). This report is available only through NTIS (see address given above).
- NCEER-89-0012 "Recommended Modifications to ATC-14," by C.D. Poland and J.O. Malley, 4/12/89, (PB90-108648, A15, MF-A01).
- NCEER-89-0013 "Repair and Strengthening of Beam-to-Column Connections Subjected to Earthquake Loading," by M. Corazao and A.J. Durrani, 2/28/89, (PB90-109885, A06, MF-A01).
- NCEER-89-0014 "Program EXKAL2 for Identification of Structural Dynamic Systems," by O. Maruyama, C-B. Yun, M. Hoshiya and M. Shinozuka, 5/19/89, (PB90-109877, A09, MF-A01).

- NCEER-89-0015 "Response of Frames With Bolted Semi-Rigid Connections, Part I - Experimental Study and Analytical Predictions," by P.J. DiCorso, A.M. Reinhorn, J.R. Dickerson, J.B. Radzimirski and W.L. Harper, 6/1/89, not available.
- NCEER-89-0016 "ARMA Monte Carlo Simulation in Probabilistic Structural Analysis," by P.D. Spanos and M.P. Mignolet, 7/10/89, (PB90-109893, A03, MF-A01).
- NCEER-89-P017 "Preliminary Proceedings from the Conference on Disaster Preparedness - The Place of Earthquake Education in Our Schools," Edited by K.E.K. Ross, 6/23/89, (PB90-108606, A03, MF-A01).
- NCEER-89-0017 "Proceedings from the Conference on Disaster Preparedness - The Place of Earthquake Education in Our Schools," Edited by K.E.K. Ross, 12/31/89, (PB90-207895, A012, MF-A02). This report is available only through NTIS (see address given above).
- NCEER-89-0018 "Multidimensional Models of Hysteretic Material Behavior for Vibration Analysis of Shape Memory Energy Absorbing Devices, by E.J. Graesser and F.A. Cozzarelli, 6/7/89, (PB90-164146, A04, MF-A01).
- NCEER-89-0019 "Nonlinear Dynamic Analysis of Three-Dimensional Base Isolated Structures (3D-BASIS)," by S. Nagarajaiah, A.M. Reinhorn and M.C. Constantinou, 8/3/89, (PB90-161936, A06, MF-A01). This report has been replaced by NCEER-93-0011.
- NCEER-89-0020 "Structural Control Considering Time-Rate of Control Forces and Control Rate Constraints," by F.Y. Cheng and C.P. Pantelides, 8/3/89, (PB90-120445, A04, MF-A01).
- NCEER-89-0021 "Subsurface Conditions of Memphis and Shelby County," by K.W. Ng, T-S. Chang and H-H.M. Hwang, 7/26/89, (PB90-120437, A03, MF-A01).
- NCEER-89-0022 "Seismic Wave Propagation Effects on Straight Jointed Buried Pipelines," by K. Elhmadi and M.J. O'Rourke, 8/24/89, (PB90-162322, A10, MF-A02).
- NCEER-89-0023 "Workshop on Serviceability Analysis of Water Delivery Systems," edited by M. Grigoriu, 3/6/89, (PB90-127424, A03, MF-A01).
- NCEER-89-0024 "Shaking Table Study of a 1/5 Scale Steel Frame Composed of Tapered Members," by K.C. Chang, J.S. Hwang and G.C. Lee, 9/18/89, (PB90-160169, A04, MF-A01).
- NCEER-89-0025 "DYNA1D: A Computer Program for Nonlinear Seismic Site Response Analysis - Technical Documentation," by Jean H. Prevost, 9/14/89, (PB90-161944, A07, MF-A01). This report is available only through NTIS (see address given above).
- NCEER-89-0026 "1:4 Scale Model Studies of Active Tendon Systems and Active Mass Dampers for Aseismic Protection," by A.M. Reinhorn, T.T. Soong, R.C. Lin, Y.P. Yang, Y. Fukao, H. Abe and M. Nakai, 9/15/89, (PB90-173246, A10, MF-A02). This report is available only through NTIS (see address given above).
- NCEER-89-0027 "Scattering of Waves by Inclusions in a Nonhomogeneous Elastic Half Space Solved by Boundary Element Methods," by P.K. Hadley, A. Askar and A.S. Cakmak, 6/15/89, (PB90-145699, A07, MF-A01).
- NCEER-89-0028 "Statistical Evaluation of Deflection Amplification Factors for Reinforced Concrete Structures," by H.H.M. Hwang, J-W. Jaw and A.L. Ch'ng, 8/31/89, (PB90-164633, A05, MF-A01).
- NCEER-89-0029 "Bedrock Accelerations in Memphis Area Due to Large New Madrid Earthquakes," by H.H.M. Hwang, C.H.S. Chen and G. Yu, 11/7/89, (PB90-162330, A04, MF-A01).
- NCEER-89-0030 "Seismic Behavior and Response Sensitivity of Secondary Structural Systems," by Y.Q. Chen and T.T. Soong, 10/23/89, (PB90-164658, A08, MF-A01).
- NCEER-89-0031 "Random Vibration and Reliability Analysis of Primary-Secondary Structural Systems," by Y. Ibrahim, M. Grigoriu and T.T. Soong, 11/10/89, (PB90-161951, A04, MF-A01).

- NCEER-89-0032 "Proceedings from the Second U.S. - Japan Workshop on Liquefaction, Large Ground Deformation and Their Effects on Lifelines, September 26-29, 1989," Edited by T.D. O'Rourke and M. Hamada, 12/1/89, (PB90-209388, A22, MF-A03).
- NCEER-89-0033 "Deterministic Model for Seismic Damage Evaluation of Reinforced Concrete Structures," by J.M. Bracci, A.M. Reinhorn, J.B. Mander and S.K. Kunnath, 9/27/89, (PB91-108803, A06, MF-A01).
- NCEER-89-0034 "On the Relation Between Local and Global Damage Indices," by E. DiPasquale and A.S. Cakmak, 8/15/89, (PB90-173865, A05, MF-A01).
- NCEER-89-0035 "Cyclic Undrained Behavior of Nonplastic and Low Plasticity Silts," by A.J. Walker and H.E. Stewart, 7/26/89, (PB90-183518, A10, MF-A01).
- NCEER-89-0036 "Liquefaction Potential of Surficial Deposits in the City of Buffalo, New York," by M. Budhu, R. Giese and L. Baumgrass, 1/17/89, (PB90-208455, A04, MF-A01).
- NCEER-89-0037 "A Deterministic Assessment of Effects of Ground Motion Incoherence," by A.S. Veletsos and Y. Tang, 7/15/89, (PB90-164294, A03, MF-A01).
- NCEER-89-0038 "Workshop on Ground Motion Parameters for Seismic Hazard Mapping," July 17-18, 1989, edited by R.V. Whitman, 12/1/89, (PB90-173923, A04, MF-A01).
- NCEER-89-0039 "Seismic Effects on Elevated Transit Lines of the New York City Transit Authority," by C.J. Costantino, C.A. Miller and E. Heymsfield, 12/26/89, (PB90-207887, A06, MF-A01).
- NCEER-89-0040 "Centrifugal Modeling of Dynamic Soil-Structure Interaction," by K. Weissman, Supervised by J.H. Prevost, 5/10/89, (PB90-207879, A07, MF-A01).
- NCEER-89-0041 "Linearized Identification of Buildings With Cores for Seismic Vulnerability Assessment," by I-K. Ho and A.E. Aktan, 11/1/89, (PB90-251943, A07, MF-A01).
- NCEER-90-0001 "Geotechnical and Lifeline Aspects of the October 17, 1989 Loma Prieta Earthquake in San Francisco," by T.D. O'Rourke, H.E. Stewart, F.T. Blackburn and T.S. Dickerman, 1/90, (PB90-208596, A05, MF-A01).
- NCEER-90-0002 "Nonnormal Secondary Response Due to Yielding in a Primary Structure," by D.C.K. Chen and L.D. Lutes, 2/28/90, (PB90-251976, A07, MF-A01).
- NCEER-90-0003 "Earthquake Education Materials for Grades K-12," by K.E.K. Ross, 4/16/90, (PB91-251984, A05, MF-A05). This report has been replaced by NCEER-92-0018.
- NCEER-90-0004 "Catalog of Strong Motion Stations in Eastern North America," by R.W. Busby, 4/3/90, (PB90-251984, A05, MF-A01).
- NCEER-90-0005 "NCEER Strong-Motion Data Base: A User Manual for the GeoBase Release (Version 1.0 for the Sun3)," by P. Friberg and K. Jacob, 3/31/90 (PB90-258062, A04, MF-A01).
- NCEER-90-0006 "Seismic Hazard Along a Crude Oil Pipeline in the Event of an 1811-1812 Type New Madrid Earthquake," by H.H.M. Hwang and C-H.S. Chen, 4/16/90, (PB90-258054, A04, MF-A01).
- NCEER-90-0007 "Site-Specific Response Spectra for Memphis Sheahan Pumping Station," by H.H.M. Hwang and C.S. Lee, 5/15/90, (PB91-108811, A05, MF-A01).
- NCEER-90-0008 "Pilot Study on Seismic Vulnerability of Crude Oil Transmission Systems," by T. Ariman, R. Dobry, M. Grigoriu, F. Kozin, M. O'Rourke, T. O'Rourke and M. Shinozuka, 5/25/90, (PB91-108837, A06, MF-A01).
- NCEER-90-0009 "A Program to Generate Site Dependent Time Histories: EQGEN," by G.W. Ellis, M. Srinivasan and A.S. Cakmak, 1/30/90, (PB91-108829, A04, MF-A01).
- NCEER-90-0010 "Active Isolation for Seismic Protection of Operating Rooms," by M.E. Talbott, Supervised by M. Shinozuka, 6/8/9, (PB91-110205, A05, MF-A01).

- NCEER-90-0011 "Program LINEARID for Identification of Linear Structural Dynamic Systems," by C-B. Yun and M. Shinozuka, 6/25/90, (PB91-110312, A08, MF-A01).
- NCEER-90-0012 "Two-Dimensional Two-Phase Elasto-Plastic Seismic Response of Earth Dams," by A.N. Yiagos, Supervised by J.H. Prevost, 6/20/90, (PB91-110197, A13, MF-A02).
- NCEER-90-0013 "Secondary Systems in Base-Isolated Structures: Experimental Investigation, Stochastic Response and Stochastic Sensitivity," by G.D. Manolis, G. Juhn, M.C. Constantinou and A.M. Reinhorn, 7/1/90, (PB91-110320, A08, MF-A01).
- NCEER-90-0014 "Seismic Behavior of Lightly-Reinforced Concrete Column and Beam-Column Joint Details," by S.P. Pessiki, C.H. Conley, P. Gergely and R.N. White, 8/22/90, (PB91-108795, A11, MF-A02).
- NCEER-90-0015 "Two Hybrid Control Systems for Building Structures Under Strong Earthquakes," by J.N. Yang and A. Daniellians, 6/29/90, (PB91-125393, A04, MF-A01).
- NCEER-90-0016 "Instantaneous Optimal Control with Acceleration and Velocity Feedback," by J.N. Yang and Z. Li, 6/29/90, (PB91-125401, A03, MF-A01).
- NCEER-90-0017 "Reconnaissance Report on the Northern Iran Earthquake of June 21, 1990," by M. Mehrain, 10/4/90, (PB91-125377, A03, MF-A01).
- NCEER-90-0018 "Evaluation of Liquefaction Potential in Memphis and Shelby County," by T.S. Chang, P.S. Tang, C.S. Lee and H. Hwang, 8/10/90, (PB91-125427, A09, MF-A01).
- NCEER-90-0019 "Experimental and Analytical Study of a Combined Sliding Disc Bearing and Helical Steel Spring Isolation System," by M.C. Constantinou, A.S. Mokha and A.M. Reinhorn, 10/4/90, (PB91-125385, A06, MF-A01). This report is available only through NTIS (see address given above).
- NCEER-90-0020 "Experimental Study and Analytical Prediction of Earthquake Response of a Sliding Isolation System with a Spherical Surface," by A.S. Mokha, M.C. Constantinou and A.M. Reinhorn, 10/11/90, (PB91-125419, A05, MF-A01).
- NCEER-90-0021 "Dynamic Interaction Factors for Floating Pile Groups," by G. Gazetas, K. Fan, A. Kaynia and E. Kausel, 9/10/90, (PB91-170381, A05, MF-A01).
- NCEER-90-0022 "Evaluation of Seismic Damage Indices for Reinforced Concrete Structures," by S. Rodriguez-Gomez and A.S. Cakmak, 9/30/90, PB91-171322, A06, MF-A01).
- NCEER-90-0023 "Study of Site Response at a Selected Memphis Site," by H. Desai, S. Ahmad, E.S. Gazetas and M.R. Oh, 10/11/90, (PB91-196857, A03, MF-A01).
- NCEER-90-0024 "A User's Guide to Strongmo: Version 1.0 of NCEER's Strong-Motion Data Access Tool for PCs and Terminals," by P.A. Friberg and C.A.T. Susch, 11/15/90, (PB91-171272, A03, MF-A01).
- NCEER-90-0025 "A Three-Dimensional Analytical Study of Spatial Variability of Seismic Ground Motions," by L-L. Hong and A.H.-S. Ang, 10/30/90, (PB91-170399, A09, MF-A01).
- NCEER-90-0026 "MUMOID User's Guide - A Program for the Identification of Modal Parameters," by S. Rodriguez-Gomez and E. DiPasquale, 9/30/90, (PB91-171298, A04, MF-A01).
- NCEER-90-0027 "SARCF-II User's Guide - Seismic Analysis of Reinforced Concrete Frames," by S. Rodriguez-Gomez, Y.S. Chung and C. Meyer, 9/30/90, (PB91-171280, A05, MF-A01).
- NCEER-90-0028 "Viscous Dampers: Testing, Modeling and Application in Vibration and Seismic Isolation," by N. Makris and M.C. Constantinou, 12/20/90 (PB91-190561, A06, MF-A01).
- NCEER-90-0029 "Soil Effects on Earthquake Ground Motions in the Memphis Area," by H. Hwang, C.S. Lee, K.W. Ng and T.S. Chang, 8/2/90, (PB91-190751, A05, MF-A01).

- NCEER-91-0001 "Proceedings from the Third Japan-U.S. Workshop on Earthquake Resistant Design of Lifeline Facilities and Countermeasures for Soil Liquefaction, December 17-19, 1990," edited by T.D. O'Rourke and M. Hamada, 2/1/91, (PB91-179259, A99, MF-A04).
- NCEER-91-0002 "Physical Space Solutions of Non-Proportionally Damped Systems," by M. Tong, Z. Liang and G.C. Lee, 1/15/91, (PB91-179242, A04, MF-A01).
- NCEER-91-0003 "Seismic Response of Single Piles and Pile Groups," by K. Fan and G. Gazetas, 1/10/91, (PB92-174994, A04, MF-A01).
- NCEER-91-0004 "Damping of Structures: Part 1 - Theory of Complex Damping," by Z. Liang and G. Lee, 10/10/91, (PB92-197235, A12, MF-A03).
- NCEER-91-0005 "3D-BASIS - Nonlinear Dynamic Analysis of Three Dimensional Base Isolated Structures: Part II," by S. Nagarajaiah, A.M. Reinhorn and M.C. Constantinou, 2/28/91, (PB91-190553, A07, MF-A01). This report has been replaced by NCEER-93-0011.
- NCEER-91-0006 "A Multidimensional Hysteretic Model for Plasticity Deforming Metals in Energy Absorbing Devices," by E.J. Graesser and F.A. Cozzarelli, 4/9/91, (PB92-108364, A04, MF-A01).
- NCEER-91-0007 "A Framework for Customizable Knowledge-Based Expert Systems with an Application to a KBES for Evaluating the Seismic Resistance of Existing Buildings," by E.G. Ibarra-Anaya and S.J. Fenves, 4/9/91, (PB91-210930, A08, MF-A01).
- NCEER-91-0008 "Nonlinear Analysis of Steel Frames with Semi-Rigid Connections Using the Capacity Spectrum Method," by G.G. Deierlein, S-H. Hsieh, Y-J. Shen and J.F. Abel, 7/2/91, (PB92-113828, A05, MF-A01).
- NCEER-91-0009 "Earthquake Education Materials for Grades K-12," by K.E.K. Ross, 4/30/91, (PB91-212142, A06, MF-A01). This report has been replaced by NCEER-92-0018.
- NCEER-91-0010 "Phase Wave Velocities and Displacement Phase Differences in a Harmonically Oscillating Pile," by N. Makris and G. Gazetas, 7/8/91, (PB92-108356, A04, MF-A01).
- NCEER-91-0011 "Dynamic Characteristics of a Full-Size Five-Story Steel Structure and a 2/5 Scale Model," by K.C. Chang, G.C. Yao, G.C. Lee, D.S. Hao and Y.C. Yeh, 7/2/91, (PB93-116648, A06, MF-A02).
- NCEER-91-0012 "Seismic Response of a 2/5 Scale Steel Structure with Added Viscoelastic Dampers," by K.C. Chang, T.T. Soong, S-T. Oh and M.L. Lai, 5/17/91, (PB92-110816, A05, MF-A01).
- NCEER-91-0013 "Earthquake Response of Retaining Walls; Full-Scale Testing and Computational Modeling," by S. Alampalli and A-W.M. Elgamal, 6/20/91, not available.
- NCEER-91-0014 "3D-BASIS-M: Nonlinear Dynamic Analysis of Multiple Building Base Isolated Structures," by P.C. Tsopelas, S. Nagarajaiah, M.C. Constantinou and A.M. Reinhorn, 5/28/91, (PB92-113885, A09, MF-A02).
- NCEER-91-0015 "Evaluation of SEAOC Design Requirements for Sliding Isolated Structures," by D. Theodossiou and M.C. Constantinou, 6/10/91, (PB92-114602, A11, MF-A03).
- NCEER-91-0016 "Closed-Loop Modal Testing of a 27-Story Reinforced Concrete Flat Plate-Core Building," by H.R. Somaprasad, T. Toksoy, H. Yoshiyuki and A.E. Aktan, 7/15/91, (PB92-129980, A07, MF-A02).
- NCEER-91-0017 "Shake Table Test of a 1/6 Scale Two-Story Lightly Reinforced Concrete Building," by A.G. El-Attar, R.N. White and P. Gergely, 2/28/91, (PB92-222447, A06, MF-A02).
- NCEER-91-0018 "Shake Table Test of a 1/8 Scale Three-Story Lightly Reinforced Concrete Building," by A.G. El-Attar, R.N. White and P. Gergely, 2/28/91, (PB93-116630, A08, MF-A02).
- NCEER-91-0019 "Transfer Functions for Rigid Rectangular Foundations," by A.S. Veletsos, A.M. Prasad and W.H. Wu, 7/31/91, not available.

- NCEER-91-0020 "Hybrid Control of Seismic-Excited Nonlinear and Inelastic Structural Systems," by J.N. Yang, Z. Li and A. Daniellians, 8/1/91, (PB92-143171, A06, MF-A02).
- NCEER-91-0021 "The NCEER-91 Earthquake Catalog: Improved Intensity-Based Magnitudes and Recurrence Relations for U.S. Earthquakes East of New Madrid," by L. Seeber and J.G. Armbruster, 8/28/91, (PB92-176742, A06, MF-A02).
- NCEER-91-0022 "Proceedings from the Implementation of Earthquake Planning and Education in Schools: The Need for Change - The Roles of the Changemakers," by K.E.K. Ross and F. Winslow, 7/23/91, (PB92-129998, A12, MF-A03).
- NCEER-91-0023 "A Study of Reliability-Based Criteria for Seismic Design of Reinforced Concrete Frame Buildings," by H.H.M. Hwang and H-M. Hsu, 8/10/91, (PB92-140235, A09, MF-A02).
- NCEER-91-0024 "Experimental Verification of a Number of Structural System Identification Algorithms," by R.G. Ghanem, H. Gavin and M. Shinozuka, 9/18/91, (PB92-176577, A18, MF-A04).
- NCEER-91-0025 "Probabilistic Evaluation of Liquefaction Potential," by H.H.M. Hwang and C.S. Lee, 11/25/91, (PB92-143429, A05, MF-A01).
- NCEER-91-0026 "Instantaneous Optimal Control for Linear, Nonlinear and Hysteretic Structures - Stable Controllers," by J.N. Yang and Z. Li, 11/15/91, (PB92-163807, A04, MF-A01).
- NCEER-91-0027 "Experimental and Theoretical Study of a Sliding Isolation System for Bridges," by M.C. Constantinou, A. Kartoum, A.M. Reinhorn and P. Bradford, 11/15/91, (PB92-176973, A10, MF-A03).
- NCEER-92-0001 "Case Studies of Liquefaction and Lifeline Performance During Past Earthquakes, Volume 1: Japanese Case Studies," Edited by M. Hamada and T. O'Rourke, 2/17/92, (PB92-197243, A18, MF-A04).
- NCEER-92-0002 "Case Studies of Liquefaction and Lifeline Performance During Past Earthquakes, Volume 2: United States Case Studies," Edited by T. O'Rourke and M. Hamada, 2/17/92, (PB92-197250, A20, MF-A04).
- NCEER-92-0003 "Issues in Earthquake Education," Edited by K. Ross, 2/3/92, (PB92-222389, A07, MF-A02).
- NCEER-92-0004 "Proceedings from the First U.S. - Japan Workshop on Earthquake Protective Systems for Bridges," Edited by I.G. Buckle, 2/4/92, (PB94-142239, A99, MF-A06).
- NCEER-92-0005 "Seismic Ground Motion from a Haskell-Type Source in a Multiple-Layered Half-Space," A.P. Theoharis, G. Deodatis and M. Shinozuka, 1/2/92, not available.
- NCEER-92-0006 "Proceedings from the Site Effects Workshop," Edited by R. Whitman, 2/29/92, (PB92-197201, A04, MF-A01).
- NCEER-92-0007 "Engineering Evaluation of Permanent Ground Deformations Due to Seismically-Induced Liquefaction," by M.H. Baziari, R. Dobry and A-W.M. Elgarnal, 3/24/92, (PB92-222421, A13, MF-A03).
- NCEER-92-0008 "A Procedure for the Seismic Evaluation of Buildings in the Central and Eastern United States," by C.D. Poland and J.O. Malley, 4/2/92, (PB92-222439, A20, MF-A04).
- NCEER-92-0009 "Experimental and Analytical Study of a Hybrid Isolation System Using Friction Controllable Sliding Bearings," by M.Q. Feng, S. Fujii and M. Shinozuka, 5/15/92, (PB93-150282, A06, MF-A02).
- NCEER-92-0010 "Seismic Resistance of Slab-Column Connections in Existing Non-Ductile Flat-Plate Buildings," by A.J. Durrani and Y. Du, 5/18/92, (PB93-116812, A06, MF-A02).
- NCEER-92-0011 "The Hysteretic and Dynamic Behavior of Brick Masonry Walls Upgraded by Ferrocement Coatings Under Cyclic Loading and Strong Simulated Ground Motion," by H. Lee and S.P. Prawel, 5/11/92, not available.
- NCEER-92-0012 "Study of Wire Rope Systems for Seismic Protection of Equipment in Buildings," by G.F. Demetriades, M.C. Constantinou and A.M. Reinhorn, 5/20/92, (PB93-116655, A08, MF-A02).

- NCEER-92-0013 "Shape Memory Structural Dampers: Material Properties, Design and Seismic Testing," by P.R. Witting and F.A. Cozzarelli, 5/26/92, (PB93-116663, A05, MF-A01).
- NCEER-92-0014 "Longitudinal Permanent Ground Deformation Effects on Buried Continuous Pipelines," by M.J. O'Rourke, and C. Nordberg, 6/15/92, (PB93-116671, A08, MF-A02).
- NCEER-92-0015 "A Simulation Method for Stationary Gaussian Random Functions Based on the Sampling Theorem," by M. Grigoriu and S. Balopoulou, 6/11/92, (PB93-127496, A05, MF-A01).
- NCEER-92-0016 "Gravity-Load-Designed Reinforced Concrete Buildings: Seismic Evaluation of Existing Construction and Detailing Strategies for Improved Seismic Resistance," by G.W. Hoffmann, S.K. Kunnath, A.M. Reinhorn and J.B. Mander, 7/15/92, (PB94-142007, A08, MF-A02).
- NCEER-92-0017 "Observations on Water System and Pipeline Performance in the Limón Area of Costa Rica Due to the April 22, 1991 Earthquake," by M. O'Rourke and D. Ballantyne, 6/30/92, (PB93-126811, A06, MF-A02).
- NCEER-92-0018 "Fourth Edition of Earthquake Education Materials for Grades K-12," Edited by K.E.K. Ross, 8/10/92, (PB93-114023, A07, MF-A02).
- NCEER-92-0019 "Proceedings from the Fourth Japan-U.S. Workshop on Earthquake Resistant Design of Lifeline Facilities and Countermeasures for Soil Liquefaction," Edited by M. Hamada and T.D. O'Rourke, 8/12/92, (PB93-163939, A99, MF-E11).
- NCEER-92-0020 "Active Bracing System: A Full Scale Implementation of Active Control," by A.M. Reinhorn, T.T. Soong, R.C. Lin, M.A. Riley, Y.P. Wang, S. Aizawa and M. Higashino, 8/14/92, (PB93-127512, A06, MF-A02).
- NCEER-92-0021 "Empirical Analysis of Horizontal Ground Displacement Generated by Liquefaction-Induced Lateral Spreads," by S.F. Bartlett and T.L. Youd, 8/17/92, (PB93-188241, A06, MF-A02).
- NCEER-92-0022 "IDARC Version 3.0: Inelastic Damage Analysis of Reinforced Concrete Structures," by S.K. Kunnath, A.M. Reinhorn and R.F. Lobo, 8/31/92, (PB93-227502, A07, MF-A02).
- NCEER-92-0023 "A Semi-Empirical Analysis of Strong-Motion Peaks in Terms of Seismic Source, Propagation Path and Local Site Conditions, by M. Kamiyama, M.J. O'Rourke and R. Flores-Berrones, 9/9/92, (PB93-150266, A08, MF-A02).
- NCEER-92-0024 "Seismic Behavior of Reinforced Concrete Frame Structures with Nonductile Details, Part I: Summary of Experimental Findings of Full Scale Beam-Column Joint Tests," by A. Beres, R.N. White and P. Gergely, 9/30/92, (PB93-227783, A05, MF-A01).
- NCEER-92-0025 "Experimental Results of Repaired and Retrofitted Beam-Column Joint Tests in Lightly Reinforced Concrete Frame Buildings," by A. Beres, S. El-Borgi, R.N. White and P. Gergely, 10/29/92, (PB93-227791, A05, MF-A01).
- NCEER-92-0026 "A Generalization of Optimal Control Theory: Linear and Nonlinear Structures," by J.N. Yang, Z. Li and S. Vongchavalitkul, 11/2/92, (PB93-188621, A05, MF-A01).
- NCEER-92-0027 "Seismic Resistance of Reinforced Concrete Frame Structures Designed Only for Gravity Loads: Part I - Design and Properties of a One-Third Scale Model Structure," by J.M. Bracci, A.M. Reinhorn and J.B. Mander, 12/1/92, (PB94-104502, A08, MF-A02).
- NCEER-92-0028 "Seismic Resistance of Reinforced Concrete Frame Structures Designed Only for Gravity Loads: Part II - Experimental Performance of Subassemblages," by L.E. Aycaardi, J.B. Mander and A.M. Reinhorn, 12/1/92, (PB94-104510, A08, MF-A02).
- NCEER-92-0029 "Seismic Resistance of Reinforced Concrete Frame Structures Designed Only for Gravity Loads: Part III - Experimental Performance and Analytical Study of a Structural Model," by J.M. Bracci, A.M. Reinhorn and J.B. Mander, 12/1/92, (PB93-227528, A09, MF-A01).

- NCEER-92-0030 "Evaluation of Seismic Retrofit of Reinforced Concrete Frame Structures: Part I - Experimental Performance of Retrofitted Subassemblages," by D. Choudhuri, J.B. Mander and A.M. Reinhorn, 12/8/92, (PB93-198307, A07, MF-A02).
- NCEER-92-0031 "Evaluation of Seismic Retrofit of Reinforced Concrete Frame Structures: Part II - Experimental Performance and Analytical Study of a Retrofitted Structural Model," by J.M. Bracci, A.M. Reinhorn and J.B. Mander, 12/8/92, (PB93-198315, A09, MF-A03).
- NCEER-92-0032 "Experimental and Analytical Investigation of Seismic Response of Structures with Supplemental Fluid Viscous Dampers," by M.C. Constantinou and M.D. Symans, 12/21/92, (PB93-191435, A10, MF-A03). This report is available only through NTIS (see address given above).
- NCEER-92-0033 "Reconnaissance Report on the Cairo, Egypt Earthquake of October 12, 1992," by M. Khater, 12/23/92, (PB93-188621, A03, MF-A01).
- NCEER-92-0034 "Low-Level Dynamic Characteristics of Four Tall Flat-Plate Buildings in New York City," by H. Gavin, S. Yuan, J. Grossman, E. Pekelis and K. Jacob, 12/28/92, (PB93-188217, A07, MF-A02).
- NCEER-93-0001 "An Experimental Study on the Seismic Performance of Brick-Infilled Steel Frames With and Without Retrofit," by J.B. Mander, B. Nair, K. Wojtkowski and J. Ma, 1/29/93, (PB93-227510, A07, MF-A02).
- NCEER-93-0002 "Social Accounting for Disaster Preparedness and Recovery Planning," by S. Cole, E. Pantoja and V. Razak, 2/22/93, (PB94-142114, A12, MF-A03).
- NCEER-93-0003 "Assessment of 1991 NEHRP Provisions for Nonstructural Components and Recommended Revisions," by T.T. Soong, G. Chen, Z. Wu, R-H. Zhang and M. Grigoriu, 3/1/93, (PB93-188639, A06, MF-A02).
- NCEER-93-0004 "Evaluation of Static and Response Spectrum Analysis Procedures of SEAOC/UBC for Seismic Isolated Structures," by C.W. Winters and M.C. Constantinou, 3/23/93, (PB93-198299, A10, MF-A03).
- NCEER-93-0005 "Earthquakes in the Northeast - Are We Ignoring the Hazard? A Workshop on Earthquake Science and Safety for Educators," edited by K.E.K. Ross, 4/2/93, (PB94-103066, A09, MF-A02).
- NCEER-93-0006 "Inelastic Response of Reinforced Concrete Structures with Viscoelastic Braces," by R.F. Lobo, J.M. Bracci, K.L. Shen, A.M. Reinhorn and T.T. Soong, 4/5/93, (PB93-227486, A05, MF-A02).
- NCEER-93-0007 "Seismic Testing of Installation Methods for Computers and Data Processing Equipment," by K. Kosar, T.T. Soong, K.L. Shen, J.A. HoLung and Y.K. Lin, 4/12/93, (PB93-198299, A07, MF-A02).
- NCEER-93-0008 "Retrofit of Reinforced Concrete Frames Using Added Dampers," by A. Reinhorn, M. Constantinou and C. Li, not available.
- NCEER-93-0009 "Seismic Behavior and Design Guidelines for Steel Frame Structures with Added Viscoelastic Dampers," by K.C. Chang, M.L. Lai, T.T. Soong, D.S. Hao and Y.C. Yeh, 5/1/93, (PB94-141959, A07, MF-A02).
- NCEER-93-0010 "Seismic Performance of Shear-Critical Reinforced Concrete Bridge Piers," by J.B. Mander, S.M. Waheed, M.T.A. Chaudhary and S.S. Chen, 5/12/93, (PB93-227494, A08, MF-A02).
- NCEER-93-0011 "3D-BASIS-TABS: Computer Program for Nonlinear Dynamic Analysis of Three Dimensional Base Isolated Structures," by S. Nagarajaiah, C. Li, A.M. Reinhorn and M.C. Constantinou, 8/2/93, (PB94-141819, A09, MF-A02).
- NCEER-93-0012 "Effects of Hydrocarbon Spills from an Oil Pipeline Break on Ground Water," by O.J. Helweg and H.H.M. Hwang, 8/3/93, (PB94-141942, A06, MF-A02).
- NCEER-93-0013 "Simplified Procedures for Seismic Design of Nonstructural Components and Assessment of Current Code Provisions," by M.P. Singh, L.E. Suarez, E.E. Matheu and G.O. Maldonado, 8/4/93, (PB94-141827, A09, MF-A02).
- NCEER-93-0014 "An Energy Approach to Seismic Analysis and Design of Secondary Systems," by G. Chen and T.T. Soong, 8/6/93, (PB94-142767, A11, MF-A03).

- NCEER-93-0015 "Proceedings from School Sites: Becoming Prepared for Earthquakes - Commemorating the Third Anniversary of the Loma Prieta Earthquake," Edited by F.E. Winslow and K.E.K. Ross, 8/16/93, (PB94-154275, A16, MF-A02).
- NCEER-93-0016 "Reconnaissance Report of Damage to Historic Monuments in Cairo, Egypt Following the October 12, 1992 Dahshur Earthquake," by D. Sykora, D. Look, G. Croci, E. Karaesmen and E. Karaesmen, 8/19/93, (PB94-142221, A08, MF-A02).
- NCEER-93-0017 "The Island of Guam Earthquake of August 8, 1993," by S.W. Swan and S.K. Harris, 9/30/93, (PB94-141843, A04, MF-A01).
- NCEER-93-0018 "Engineering Aspects of the October 12, 1992 Egyptian Earthquake," by A.W. Elgamal, M. Amer, K. Adalier and A. Abul-Fadl, 10/7/93, (PB94-141983, A05, MF-A01).
- NCEER-93-0019 "Development of an Earthquake Motion Simulator and its Application in Dynamic Centrifuge Testing," by I. Krstelj, Supervised by J.H. Prevost, 10/23/93, (PB94-181773, A-10, MF-A03).
- NCEER-93-0020 "NCEER-Taisei Corporation Research Program on Sliding Seismic Isolation Systems for Bridges: Experimental and Analytical Study of a Friction Pendulum System (FPS)," by M.C. Constantinou, P. Tsopelas, Y-S. Kim and S. Okamoto, 11/1/93, (PB94-142775, A08, MF-A02).
- NCEER-93-0021 "Finite Element Modeling of Elastomeric Seismic Isolation Bearings," by L.J. Billings, Supervised by R. Shepherd, 11/8/93, not available.
- NCEER-93-0022 "Seismic Vulnerability of Equipment in Critical Facilities: Life-Safety and Operational Consequences," by K. Porter, G.S. Johnson, M.M. Zadeh, C. Scawthorn and S. Eder, 11/24/93, (PB94-181765, A16, MF-A03).
- NCEER-93-0023 "Hokkaido Nansei-oki, Japan Earthquake of July 12, 1993, by P.I. Yanev and C.R. Scawthorn, 12/23/93, (PB94-181500, A07, MF-A01).
- NCEER-94-0001 "An Evaluation of Seismic Serviceability of Water Supply Networks with Application to the San Francisco Auxiliary Water Supply System," by I. Markov, Supervised by M. Grigoriu and T. O'Rourke, 1/21/94, (PB94-204013, A07, MF-A02).
- NCEER-94-0002 "NCEER-Taisei Corporation Research Program on Sliding Seismic Isolation Systems for Bridges: Experimental and Analytical Study of Systems Consisting of Sliding Bearings, Rubber Restoring Force Devices and Fluid Dampers," Volumes I and II, by P. Tsopelas, S. Okamoto, M.C. Constantinou, D. Ozaki and S. Fujii, 2/4/94, (PB94-181740, A09, MF-A02 and PB94-181757, A12, MF-A03).
- NCEER-94-0003 "A Markov Model for Local and Global Damage Indices in Seismic Analysis," by S. Rahman and M. Grigoriu, 2/18/94, (PB94-206000, A12, MF-A03).
- NCEER-94-0004 "Proceedings from the NCEER Workshop on Seismic Response of Masonry Infills," edited by D.P. Abrams, 3/1/94, (PB94-180783, A07, MF-A02).
- NCEER-94-0005 "The Northridge, California Earthquake of January 17, 1994: General Reconnaissance Report," edited by J.D. Goltz, 3/11/94, (PB94-193943, A10, MF-A03).
- NCEER-94-0006 "Seismic Energy Based Fatigue Damage Analysis of Bridge Columns: Part I - Evaluation of Seismic Capacity," by G.A. Chang and J.B. Mander, 3/14/94, (PB94-219185, A11, MF-A03).
- NCEER-94-0007 "Seismic Isolation of Multi-Story Frame Structures Using Spherical Sliding Isolation Systems," by T.M. Al-Hussaini, V.A. Zayas and M.C. Constantinou, 3/17/94, (PB94-193745, A09, MF-A02).
- NCEER-94-0008 "The Northridge, California Earthquake of January 17, 1994: Performance of Highway Bridges," edited by I.G. Buckle, 3/24/94, (PB94-193851, A06, MF-A02).
- NCEER-94-0009 "Proceedings of the Third U.S.-Japan Workshop on Earthquake Protective Systems for Bridges," edited by I.G. Buckle and I. Friedland, 3/31/94, (PB94-195815, A99, MF-A06).

- NCEER-94-0010 "3D-BASIS-ME: Computer Program for Nonlinear Dynamic Analysis of Seismically Isolated Single and Multiple Structures and Liquid Storage Tanks," by P.C. Tsopelas, M.C. Constantinou and A.M. Reinhorn, 4/12/94, (PB94-204922, A09, MF-A02).
- NCEER-94-0011 "The Northridge, California Earthquake of January 17, 1994: Performance of Gas Transmission Pipelines," by T.D. O'Rourke and M.C. Palmer, 5/16/94, (PB94-204989, A05, MF-A01).
- NCEER-94-0012 "Feasibility Study of Replacement Procedures and Earthquake Performance Related to Gas Transmission Pipelines," by T.D. O'Rourke and M.C. Palmer, 5/25/94, (PB94-206638, A09, MF-A02).
- NCEER-94-0013 "Seismic Energy Based Fatigue Damage Analysis of Bridge Columns: Part II - Evaluation of Seismic Demand," by G.A. Chang and J.B. Mander, 6/1/94, (PB95-18106, A08, MF-A02).
- NCEER-94-0014 "NCEER-Taisei Corporation Research Program on Sliding Seismic Isolation Systems for Bridges: Experimental and Analytical Study of a System Consisting of Sliding Bearings and Fluid Restoring Force/Damping Devices," by P. Tsopelas and M.C. Constantinou, 6/13/94, (PB94-219144, A10, MF-A03).
- NCEER-94-0015 "Generation of Hazard-Consistent Fragility Curves for Seismic Loss Estimation Studies," by H. Hwang and J-R. Huo, 6/14/94, (PB95-181996, A09, MF-A02).
- NCEER-94-0016 "Seismic Study of Building Frames with Added Energy-Absorbing Devices," by W.S. Pong, C.S. Tsai and G.C. Lee, 6/20/94, (PB94-219136, A10, A03).
- NCEER-94-0017 "Sliding Mode Control for Seismic-Excited Linear and Nonlinear Civil Engineering Structures," by J. Yang, J. Wu, A. Agrawal and Z. Li, 6/21/94, (PB95-138483, A06, MF-A02).
- NCEER-94-0018 "3D-BASIS-TABS Version 2.0: Computer Program for Nonlinear Dynamic Analysis of Three Dimensional Base Isolated Structures," by A.M. Reinhorn, S. Nagarajaiah, M.C. Constantinou, P. Tsopelas and R. Li, 6/22/94, (PB95-182176, A08, MF-A02).
- NCEER-94-0019 "Proceedings of the International Workshop on Civil Infrastructure Systems: Application of Intelligent Systems and Advanced Materials on Bridge Systems," Edited by G.C. Lee and K.C. Chang, 7/18/94, (PB95-252474, A20, MF-A04).
- NCEER-94-0020 "Study of Seismic Isolation Systems for Computer Floors," by V. Lambrou and M.C. Constantinou, 7/19/94, (PB95-138533, A10, MF-A03).
- NCEER-94-0021 "Proceedings of the U.S.-Italian Workshop on Guidelines for Seismic Evaluation and Rehabilitation of Unreinforced Masonry Buildings," Edited by D.P. Abrams and G.M. Calvi, 7/20/94, (PB95-138749, A13, MF-A03).
- NCEER-94-0022 "NCEER-Taisei Corporation Research Program on Sliding Seismic Isolation Systems for Bridges: Experimental and Analytical Study of a System Consisting of Lubricated PTFE Sliding Bearings and Mild Steel Dampers," by P. Tsopelas and M.C. Constantinou, 7/22/94, (PB95-182184, A08, MF-A02).
- NCEER-94-0023 "Development of Reliability-Based Design Criteria for Buildings Under Seismic Load," by Y.K. Wen, H. Hwang and M. Shinozuka, 8/1/94, (PB95-211934, A08, MF-A02).
- NCEER-94-0024 "Experimental Verification of Acceleration Feedback Control Strategies for an Active Tendon System," by S.J. Dyke, B.F. Spencer, Jr., P. Quast, M.K. Sain, D.C. Kaspari, Jr. and T.T. Soong, 8/29/94, (PB95-212320, A05, MF-A01).
- NCEER-94-0025 "Seismic Retrofitting Manual for Highway Bridges," Edited by I.G. Buckle and I.F. Friedland, published by the Federal Highway Administration (PB95-212676, A15, MF-A03).
- NCEER-94-0026 "Proceedings from the Fifth U.S.-Japan Workshop on Earthquake Resistant Design of Lifeline Facilities and Countermeasures Against Soil Liquefaction," Edited by T.D. O'Rourke and M. Hamada, 11/7/94, (PB95-220802, A99, MF-E08).

- NCEER-95-0001 “Experimental and Analytical Investigation of Seismic Retrofit of Structures with Supplemental Damping: Part 1 - Fluid Viscous Damping Devices,” by A.M. Reinhorn, C. Li and M.C. Constantinou, 1/3/95, (PB95-266599, A09, MF-A02).
- NCEER-95-0002 “Experimental and Analytical Study of Low-Cycle Fatigue Behavior of Semi-Rigid Top-And-Seat Angle Connections,” by G. Pekcan, J.B. Mander and S.S. Chen, 1/5/95, (PB95-220042, A07, MF-A02).
- NCEER-95-0003 “NCEER-ATC Joint Study on Fragility of Buildings,” by T. Anagnos, C. Rojahn and A.S. Kiremidjian, 1/20/95, (PB95-220026, A06, MF-A02).
- NCEER-95-0004 “Nonlinear Control Algorithms for Peak Response Reduction,” by Z. Wu, T.T. Soong, V. Gattulli and R.C. Lin, 2/16/95, (PB95-220349, A05, MF-A01).
- NCEER-95-0005 “Pipeline Replacement Feasibility Study: A Methodology for Minimizing Seismic and Corrosion Risks to Underground Natural Gas Pipelines,” by R.T. Eguchi, H.A. Seligson and D.G. Honegger, 3/2/95, (PB95-252326, A06, MF-A02).
- NCEER-95-0006 “Evaluation of Seismic Performance of an 11-Story Frame Building During the 1994 Northridge Earthquake,” by F. Naeim, R. DiSulio, K. Benuska, A. Reinhorn and C. Li, not available.
- NCEER-95-0007 “Prioritization of Bridges for Seismic Retrofitting,” by N. Basöz and A.S. Kiremidjian, 4/24/95, (PB95-252300, A08, MF-A02).
- NCEER-95-0008 “Method for Developing Motion Damage Relationships for Reinforced Concrete Frames,” by A. Singhal and A.S. Kiremidjian, 5/11/95, (PB95-266607, A06, MF-A02).
- NCEER-95-0009 “Experimental and Analytical Investigation of Seismic Retrofit of Structures with Supplemental Damping: Part II - Friction Devices,” by C. Li and A.M. Reinhorn, 7/6/95, (PB96-128087, A11, MF-A03).
- NCEER-95-0010 “Experimental Performance and Analytical Study of a Non-Ductile Reinforced Concrete Frame Structure Retrofitted with Elastomeric Spring Dampers,” by G. Pekcan, J.B. Mander and S.S. Chen, 7/14/95, (PB96-137161, A08, MF-A02).
- NCEER-95-0011 “Development and Experimental Study of Semi-Active Fluid Damping Devices for Seismic Protection of Structures,” by M.D. Symans and M.C. Constantinou, 8/3/95, (PB96-136940, A23, MF-A04).
- NCEER-95-0012 “Real-Time Structural Parameter Modification (RSPM): Development of Innervated Structures,” by Z. Liang, M. Tong and G.C. Lee, 4/11/95, (PB96-137153, A06, MF-A01).
- NCEER-95-0013 “Experimental and Analytical Investigation of Seismic Retrofit of Structures with Supplemental Damping: Part III - Viscous Damping Walls,” by A.M. Reinhorn and C. Li, 10/1/95, (PB96-176409, A11, MF-A03).
- NCEER-95-0014 “Seismic Fragility Analysis of Equipment and Structures in a Memphis Electric Substation,” by J-R. Huo and H.H.M. Hwang, 8/10/95, (PB96-128087, A09, MF-A02).
- NCEER-95-0015 “The Hanshin-Awaji Earthquake of January 17, 1995: Performance of Lifelines,” Edited by M. Shinozuka, 11/3/95, (PB96-176383, A15, MF-A03).
- NCEER-95-0016 “Highway Culvert Performance During Earthquakes,” by T.L. Youd and C.J. Beckman, available as NCEER-96-0015.
- NCEER-95-0017 “The Hanshin-Awaji Earthquake of January 17, 1995: Performance of Highway Bridges,” Edited by I.G. Buckle, 12/1/95, not available.
- NCEER-95-0018 “Modeling of Masonry Infill Panels for Structural Analysis,” by A.M. Reinhorn, A. Madan, R.E. Valles, Y. Reichmann and J.B. Mander, 12/8/95, (PB97-110886, MF-A01, A06).
- NCEER-95-0019 “Optimal Polynomial Control for Linear and Nonlinear Structures,” by A.K. Agrawal and J.N. Yang, 12/11/95, (PB96-168737, A07, MF-A02).

- NCEER-95-0020 "Retrofit of Non-Ductile Reinforced Concrete Frames Using Friction Dampers," by R.S. Rao, P. Gergely and R.N. White, 12/22/95, (PB97-133508, A10, MF-A02).
- NCEER-95-0021 "Parametric Results for Seismic Response of Pile-Supported Bridge Bents," by G. Mylonakis, A. Nikolaou and G. Gazetas, 12/22/95, (PB97-100242, A12, MF-A03).
- NCEER-95-0022 "Kinematic Bending Moments in Seismically Stressed Piles," by A. Nikolaou, G. Mylonakis and G. Gazetas, 12/23/95, (PB97-113914, MF-A03, A13).
- NCEER-96-0001 "Dynamic Response of Unreinforced Masonry Buildings with Flexible Diaphragms," by A.C. Costley and D.P. Abrams, 10/10/96, (PB97-133573, MF-A03, A15).
- NCEER-96-0002 "State of the Art Review: Foundations and Retaining Structures," by I. Po Lam, not available.
- NCEER-96-0003 "Ductility of Rectangular Reinforced Concrete Bridge Columns with Moderate Confinement," by N. Wehbe, M. Saiidi, D. Sanders and B. Douglas, 11/7/96, (PB97-133557, A06, MF-A02).
- NCEER-96-0004 "Proceedings of the Long-Span Bridge Seismic Research Workshop," edited by I.G. Buckle and I.M. Friedland, not available.
- NCEER-96-0005 "Establish Representative Pier Types for Comprehensive Study: Eastern United States," by J. Kulicki and Z. Prucz, 5/28/96, (PB98-119217, A07, MF-A02).
- NCEER-96-0006 "Establish Representative Pier Types for Comprehensive Study: Western United States," by R. Imbsen, R.A. Schamber and T.A. Osterkamp, 5/28/96, (PB98-118607, A07, MF-A02).
- NCEER-96-0007 "Nonlinear Control Techniques for Dynamical Systems with Uncertain Parameters," by R.G. Ghanem and M.I. Bujakov, 5/27/96, (PB97-100259, A17, MF-A03).
- NCEER-96-0008 "Seismic Evaluation of a 30-Year Old Non-Ductile Highway Bridge Pier and Its Retrofit," by J.B. Mander, B. Mahmoodzadegan, S. Bhadra and S.S. Chen, 5/31/96, (PB97-110902, MF-A03, A10).
- NCEER-96-0009 "Seismic Performance of a Model Reinforced Concrete Bridge Pier Before and After Retrofit," by J.B. Mander, J.H. Kim and C.A. Ligozio, 5/31/96, (PB97-110910, MF-A02, A10).
- NCEER-96-0010 "IDARC2D Version 4.0: A Computer Program for the Inelastic Damage Analysis of Buildings," by R.E. Valles, A.M. Reinhorn, S.K. Kunnath, C. Li and A. Madan, 6/3/96, (PB97-100234, A17, MF-A03).
- NCEER-96-0011 "Estimation of the Economic Impact of Multiple Lifeline Disruption: Memphis Light, Gas and Water Division Case Study," by S.E. Chang, H.A. Seligson and R.T. Eguchi, 8/16/96, (PB97-133490, A11, MF-A03).
- NCEER-96-0012 "Proceedings from the Sixth Japan-U.S. Workshop on Earthquake Resistant Design of Lifeline Facilities and Countermeasures Against Soil Liquefaction, Edited by M. Hamada and T. O'Rourke, 9/11/96, (PB97-133581, A99, MF-A06).
- NCEER-96-0013 "Chemical Hazards, Mitigation and Preparedness in Areas of High Seismic Risk: A Methodology for Estimating the Risk of Post-Earthquake Hazardous Materials Release," by H.A. Seligson, R.T. Eguchi, K.J. Tierney and K. Richmond, 11/7/96, (PB97-133565, MF-A02, A08).
- NCEER-96-0014 "Response of Steel Bridge Bearings to Reversed Cyclic Loading," by J.B. Mander, D-K. Kim, S.S. Chen and G.J. Premus, 11/13/96, (PB97-140735, A12, MF-A03).
- NCEER-96-0015 "Highway Culvert Performance During Past Earthquakes," by T.L. Youd and C.J. Beckman, 11/25/96, (PB97-133532, A06, MF-A01).
- NCEER-97-0001 "Evaluation, Prevention and Mitigation of Pounding Effects in Building Structures," by R.E. Valles and A.M. Reinhorn, 2/20/97, (PB97-159552, A14, MF-A03).
- NCEER-97-0002 "Seismic Design Criteria for Bridges and Other Highway Structures," by C. Rojahn, R. Mayes, D.G. Anderson, J. Clark, J.H. Hom, R.V. Nutt and M.J. O'Rourke, 4/30/97, (PB97-194658, A06, MF-A03).

- NCEER-97-0003 "Proceedings of the U.S.-Italian Workshop on Seismic Evaluation and Retrofit," Edited by D.P. Abrams and G.M. Calvi, 3/19/97, (PB97-194666, A13, MF-A03).
- NCEER-97-0004 "Investigation of Seismic Response of Buildings with Linear and Nonlinear Fluid Viscous Dampers," by A.A. Seleemah and M.C. Constantinou, 5/21/97, (PB98-109002, A15, MF-A03).
- NCEER-97-0005 "Proceedings of the Workshop on Earthquake Engineering Frontiers in Transportation Facilities," edited by G.C. Lee and I.M. Friedland, 8/29/97, (PB98-128911, A25, MR-A04).
- NCEER-97-0006 "Cumulative Seismic Damage of Reinforced Concrete Bridge Piers," by S.K. Kunnath, A. El-Bahy, A. Taylor and W. Stone, 9/2/97, (PB98-108814, A11, MF-A03).
- NCEER-97-0007 "Structural Details to Accommodate Seismic Movements of Highway Bridges and Retaining Walls," by R.A. Imbsen, R.A. Schamber, E. Thorkildsen, A. Kartoum, B.T. Martin, T.N. Rosser and J.M. Kulicki, 9/3/97, (PB98-108996, A09, MF-A02).
- NCEER-97-0008 "A Method for Earthquake Motion-Damage Relationships with Application to Reinforced Concrete Frames," by A. Singhal and A.S. Kiremidjian, 9/10/97, (PB98-108988, A13, MF-A03).
- NCEER-97-0009 "Seismic Analysis and Design of Bridge Abutments Considering Sliding and Rotation," by K. Fishman and R. Richards, Jr., 9/15/97, (PB98-108897, A06, MF-A02).
- NCEER-97-0010 "Proceedings of the FHWA/NCEER Workshop on the National Representation of Seismic Ground Motion for New and Existing Highway Facilities," edited by I.M. Friedland, M.S. Power and R.L. Mayes, 9/22/97, (PB98-128903, A21, MF-A04).
- NCEER-97-0011 "Seismic Analysis for Design or Retrofit of Gravity Bridge Abutments," by K.L. Fishman, R. Richards, Jr. and R.C. Divito, 10/2/97, (PB98-128937, A08, MF-A02).
- NCEER-97-0012 "Evaluation of Simplified Methods of Analysis for Yielding Structures," by P. Tsopelas, M.C. Constantinou, C.A. Kircher and A.S. Whittaker, 10/31/97, (PB98-128929, A10, MF-A03).
- NCEER-97-0013 "Seismic Design of Bridge Columns Based on Control and Repairability of Damage," by C-T. Cheng and J.B. Mander, 12/8/97, (PB98-144249, A11, MF-A03).
- NCEER-97-0014 "Seismic Resistance of Bridge Piers Based on Damage Avoidance Design," by J.B. Mander and C-T. Cheng, 12/10/97, (PB98-144223, A09, MF-A02).
- NCEER-97-0015 "Seismic Response of Nominally Symmetric Systems with Strength Uncertainty," by S. Balopoulou and M. Grigoriu, 12/23/97, (PB98-153422, A11, MF-A03).
- NCEER-97-0016 "Evaluation of Seismic Retrofit Methods for Reinforced Concrete Bridge Columns," by T.J. Wipf, F.W. Klaiber and F.M. Russo, 12/28/97, (PB98-144215, A12, MF-A03).
- NCEER-97-0017 "Seismic Fragility of Existing Conventional Reinforced Concrete Highway Bridges," by C.L. Mullen and A.S. Cakmak, 12/30/97, (PB98-153406, A08, MF-A02).
- NCEER-97-0018 "Loss Assessment of Memphis Buildings," edited by D.P. Abrams and M. Shinozuka, 12/31/97, (PB98-144231, A13, MF-A03).
- NCEER-97-0019 "Seismic Evaluation of Frames with Infill Walls Using Quasi-static Experiments," by K.M. Mosalam, R.N. White and P. Gergely, 12/31/97, (PB98-153455, A07, MF-A02).
- NCEER-97-0020 "Seismic Evaluation of Frames with Infill Walls Using Pseudo-dynamic Experiments," by K.M. Mosalam, R.N. White and P. Gergely, 12/31/97, (PB98-153430, A07, MF-A02).
- NCEER-97-0021 "Computational Strategies for Frames with Infill Walls: Discrete and Smeared Crack Analyses and Seismic Fragility," by K.M. Mosalam, R.N. White and P. Gergely, 12/31/97, (PB98-153414, A10, MF-A02).

- NCEER-97-0022 "Proceedings of the NCEER Workshop on Evaluation of Liquefaction Resistance of Soils," edited by T.L. Youd and I.M. Idriss, 12/31/97, (PB98-155617, A15, MF-A03).
- MCEER-98-0001 "Extraction of Nonlinear Hysteretic Properties of Seismically Isolated Bridges from Quick-Release Field Tests," by Q. Chen, B.M. Douglas, E.M. Maragakis and I.G. Buckle, 5/26/98, (PB99-118838, A06, MF-A01).
- MCEER-98-0002 "Methodologies for Evaluating the Importance of Highway Bridges," by A. Thomas, S. Eshenaur and J. Kulicki, 5/29/98, (PB99-118846, A10, MF-A02).
- MCEER-98-0003 "Capacity Design of Bridge Piers and the Analysis of Overstrength," by J.B. Mander, A. Dutta and P. Goel, 6/1/98, (PB99-118853, A09, MF-A02).
- MCEER-98-0004 "Evaluation of Bridge Damage Data from the Loma Prieta and Northridge, California Earthquakes," by N. Basoz and A. Kiremidjian, 6/2/98, (PB99-118861, A15, MF-A03).
- MCEER-98-0005 "Screening Guide for Rapid Assessment of Liquefaction Hazard at Highway Bridge Sites," by T. L. Youd, 6/16/98, (PB99-118879, A06, not available on microfiche).
- MCEER-98-0006 "Structural Steel and Steel/Concrete Interface Details for Bridges," by P. Ritchie, N. Kauh and J. Kulicki, 7/13/98, (PB99-118945, A06, MF-A01).
- MCEER-98-0007 "Capacity Design and Fatigue Analysis of Confined Concrete Columns," by A. Dutta and J.B. Mander, 7/14/98, (PB99-118960, A14, MF-A03).
- MCEER-98-0008 "Proceedings of the Workshop on Performance Criteria for Telecommunication Services Under Earthquake Conditions," edited by A.J. Schiff, 7/15/98, (PB99-118952, A08, MF-A02).
- MCEER-98-0009 "Fatigue Analysis of Unconfined Concrete Columns," by J.B. Mander, A. Dutta and J.H. Kim, 9/12/98, (PB99-123655, A10, MF-A02).
- MCEER-98-0010 "Centrifuge Modeling of Cyclic Lateral Response of Pile-Cap Systems and Seat-Type Abutments in Dry Sands," by A.D. Gadre and R. Dobry, 10/2/98, (PB99-123606, A13, MF-A03).
- MCEER-98-0011 "IDARC-BRIDGE: A Computational Platform for Seismic Damage Assessment of Bridge Structures," by A.M. Reinhorn, V. Simeonov, G. Mylonakis and Y. Reichman, 10/2/98, (PB99-162919, A15, MF-A03).
- MCEER-98-0012 "Experimental Investigation of the Dynamic Response of Two Bridges Before and After Retrofitting with Elastomeric Bearings," by D.A. Wendichansky, S.S. Chen and J.B. Mander, 10/2/98, (PB99-162927, A15, MF-A03).
- MCEER-98-0013 "Design Procedures for Hinge Restrainers and Hinge Sear Width for Multiple-Frame Bridges," by R. Des Roches and G.L. Fenves, 11/3/98, (PB99-140477, A13, MF-A03).
- MCEER-98-0014 "Response Modification Factors for Seismically Isolated Bridges," by M.C. Constantinou and J.K. Quarshie, 11/3/98, (PB99-140485, A14, MF-A03).
- MCEER-98-0015 "Proceedings of the U.S.-Italy Workshop on Seismic Protective Systems for Bridges," edited by I.M. Friedland and M.C. Constantinou, 11/3/98, (PB2000-101711, A22, MF-A04).
- MCEER-98-0016 "Appropriate Seismic Reliability for Critical Equipment Systems: Recommendations Based on Regional Analysis of Financial and Life Loss," by K. Porter, C. Scawthorn, C. Taylor and N. Blais, 11/10/98, (PB99-157265, A08, MF-A02).
- MCEER-98-0017 "Proceedings of the U.S. Japan Joint Seminar on Civil Infrastructure Systems Research," edited by M. Shinozuka and A. Rose, 11/12/98, (PB99-156713, A16, MF-A03).
- MCEER-98-0018 "Modeling of Pile Footings and Drilled Shafts for Seismic Design," by I. PoLam, M. Kapuskar and D. Chaudhuri, 12/21/98, (PB99-157257, A09, MF-A02).

- MCEER-99-0001 "Seismic Evaluation of a Masonry Infilled Reinforced Concrete Frame by Pseudodynamic Testing," by S.G. Buonopane and R.N. White, 2/16/99, (PB99-162851, A09, MF-A02).
- MCEER-99-0002 "Response History Analysis of Structures with Seismic Isolation and Energy Dissipation Systems: Verification Examples for Program SAP2000," by J. Scheller and M.C. Constantinou, 2/22/99, (PB99-162869, A08, MF-A02).
- MCEER-99-0003 "Experimental Study on the Seismic Design and Retrofit of Bridge Columns Including Axial Load Effects," by A. Dutta, T. Kokorina and J.B. Mander, 2/22/99, (PB99-162877, A09, MF-A02).
- MCEER-99-0004 "Experimental Study of Bridge Elastomeric and Other Isolation and Energy Dissipation Systems with Emphasis on Uplift Prevention and High Velocity Near-source Seismic Excitation," by A. Kasalanati and M. C. Constantinou, 2/26/99, (PB99-162885, A12, MF-A03).
- MCEER-99-0005 "Truss Modeling of Reinforced Concrete Shear-flexure Behavior," by J.H. Kim and J.B. Mander, 3/8/99, (PB99-163693, A12, MF-A03).
- MCEER-99-0006 "Experimental Investigation and Computational Modeling of Seismic Response of a 1:4 Scale Model Steel Structure with a Load Balancing Supplemental Damping System," by G. Pekcan, J.B. Mander and S.S. Chen, 4/2/99, (PB99-162893, A11, MF-A03).
- MCEER-99-0007 "Effect of Vertical Ground Motions on the Structural Response of Highway Bridges," by M.R. Button, C.J. Cronin and R.L. Mayes, 4/10/99, (PB2000-101411, A10, MF-A03).
- MCEER-99-0008 "Seismic Reliability Assessment of Critical Facilities: A Handbook, Supporting Documentation, and Model Code Provisions," by G.S. Johnson, R.E. Sheppard, M.D. Quilici, S.J. Eder and C.R. Scawthorn, 4/12/99, (PB2000-101701, A18, MF-A04).
- MCEER-99-0009 "Impact Assessment of Selected MCEER Highway Project Research on the Seismic Design of Highway Structures," by C. Rojahn, R. Mayes, D.G. Anderson, J.H. Clark, D'Appolonia Engineering, S. Gloyd and R.V. Nutt, 4/14/99, (PB99-162901, A10, MF-A02).
- MCEER-99-0010 "Site Factors and Site Categories in Seismic Codes," by R. Dobry, R. Ramos and M.S. Power, 7/19/99, (PB2000-101705, A08, MF-A02).
- MCEER-99-0011 "Restrainer Design Procedures for Multi-Span Simply-Supported Bridges," by M.J. Randall, M. Saiidi, E. Maragakis and T. Isakovic, 7/20/99, (PB2000-101702, A10, MF-A02).
- MCEER-99-0012 "Property Modification Factors for Seismic Isolation Bearings," by M.C. Constantinou, P. Tsopelas, A. Kasalanati and E. Wolff, 7/20/99, (PB2000-103387, A11, MF-A03).
- MCEER-99-0013 "Critical Seismic Issues for Existing Steel Bridges," by P. Ritchie, N. Kauh and J. Kulicki, 7/20/99, (PB2000-101697, A09, MF-A02).
- MCEER-99-0014 "Nonstructural Damage Database," by A. Kao, T.T. Soong and A. Vender, 7/24/99, (PB2000-101407, A06, MF-A01).
- MCEER-99-0015 "Guide to Remedial Measures for Liquefaction Mitigation at Existing Highway Bridge Sites," by H.G. Cooke and J. K. Mitchell, 7/26/99, (PB2000-101703, A11, MF-A03).
- MCEER-99-0016 "Proceedings of the MCEER Workshop on Ground Motion Methodologies for the Eastern United States," edited by N. Abrahamson and A. Becker, 8/11/99, (PB2000-103385, A07, MF-A02).
- MCEER-99-0017 "Quindío, Colombia Earthquake of January 25, 1999: Reconnaissance Report," by A.P. Asfura and P.J. Flores, 10/4/99, (PB2000-106893, A06, MF-A01).
- MCEER-99-0018 "Hysteretic Models for Cyclic Behavior of Deteriorating Inelastic Structures," by M.V. Sivaselvan and A.M. Reinhorn, 11/5/99, (PB2000-103386, A08, MF-A02).

- MCEER-99-0019 "Proceedings of the 7th U.S.- Japan Workshop on Earthquake Resistant Design of Lifeline Facilities and Countermeasures Against Soil Liquefaction," edited by T.D. O'Rourke, J.P. Bardet and M. Hamada, 11/19/99, (PB2000-103354, A99, MF-A06).
- MCEER-99-0020 "Development of Measurement Capability for Micro-Vibration Evaluations with Application to Chip Fabrication Facilities," by G.C. Lee, Z. Liang, J.W. Song, J.D. Shen and W.C. Liu, 12/1/99, (PB2000-105993, A08, MF-A02).
- MCEER-99-0021 "Design and Retrofit Methodology for Building Structures with Supplemental Energy Dissipating Systems," by G. Pekcan, J.B. Mander and S.S. Chen, 12/31/99, (PB2000-105994, A11, MF-A03).
- MCEER-00-0001 "The Marmara, Turkey Earthquake of August 17, 1999: Reconnaissance Report," edited by C. Scawthorn; with major contributions by M. Bruneau, R. Eguchi, T. Holzer, G. Johnson, J. Mander, J. Mitchell, W. Mitchell, A. Papageorgiou, C. Scaethorn, and G. Webb, 3/23/00, (PB2000-106200, A11, MF-A03).
- MCEER-00-0002 "Proceedings of the MCEER Workshop for Seismic Hazard Mitigation of Health Care Facilities," edited by G.C. Lee, M. Ettouney, M. Grigoriu, J. Hauer and J. Nigg, 3/29/00, (PB2000-106892, A08, MF-A02).
- MCEER-00-0003 "The Chi-Chi, Taiwan Earthquake of September 21, 1999: Reconnaissance Report," edited by G.C. Lee and C.H. Loh, with major contributions by G.C. Lee, M. Bruneau, I.G. Buckle, S.E. Chang, P.J. Flores, T.D. O'Rourke, M. Shinozuka, T.T. Soong, C-H. Loh, K-C. Chang, Z-J. Chen, J-S. Hwang, M-L. Lin, G-Y. Liu, K-C. Tsai, G.C. Yao and C-L. Yen, 4/30/00, (PB2001-100980, A10, MF-A02).
- MCEER-00-0004 "Seismic Retrofit of End-Sway Frames of Steel Deck-Truss Bridges with a Supplemental Tendon System: Experimental and Analytical Investigation," by G. Pekcan, J.B. Mander and S.S. Chen, 7/1/00, (PB2001-100982, A10, MF-A02).
- MCEER-00-0005 "Sliding Fragility of Unrestrained Equipment in Critical Facilities," by W.H. Chong and T.T. Soong, 7/5/00, (PB2001-100983, A08, MF-A02).
- MCEER-00-0006 "Seismic Response of Reinforced Concrete Bridge Pier Walls in the Weak Direction," by N. Abo-Shadi, M. Saiidi and D. Sanders, 7/17/00, (PB2001-100981, A17, MF-A03).
- MCEER-00-0007 "Low-Cycle Fatigue Behavior of Longitudinal Reinforcement in Reinforced Concrete Bridge Columns," by J. Brown and S.K. Kunnath, 7/23/00, (PB2001-104392, A08, MF-A02).
- MCEER-00-0008 "Soil Structure Interaction of Bridges for Seismic Analysis," I. PoLam and H. Law, 9/25/00, (PB2001-105397, A08, MF-A02).
- MCEER-00-0009 "Proceedings of the First MCEER Workshop on Mitigation of Earthquake Disaster by Advanced Technologies (MEDAT-1), edited by M. Shinozuka, D.J. Inman and T.D. O'Rourke, 11/10/00, (PB2001-105399, A14, MF-A03).
- MCEER-00-0010 "Development and Evaluation of Simplified Procedures for Analysis and Design of Buildings with Passive Energy Dissipation Systems, Revision 01," by O.M. Ramirez, M.C. Constantinou, C.A. Kircher, A.S. Whittaker, M.W. Johnson, J.D. Gomez and C. Chrysostomou, 11/16/01, (PB2001-105523, A23, MF-A04).
- MCEER-00-0011 "Dynamic Soil-Foundation-Structure Interaction Analyses of Large Caissons," by C-Y. Chang, C-M. Mok, Z-L. Wang, R. Settgast, F. Waggoner, M.A. Ketchum, H.M. Gonnermann and C-C. Chin, 12/30/00, (PB2001-104373, A07, MF-A02).
- MCEER-00-0012 "Experimental Evaluation of Seismic Performance of Bridge Restrainers," by A.G. Vlassis, E.M. Maragakis and M. Saiid Saiidi, 12/30/00, (PB2001-104354, A09, MF-A02).
- MCEER-00-0013 "Effect of Spatial Variation of Ground Motion on Highway Structures," by M. Shinozuka, V. Saxena and G. Deodatis, 12/31/00, (PB2001-108755, A13, MF-A03).
- MCEER-00-0014 "A Risk-Based Methodology for Assessing the Seismic Performance of Highway Systems," by S.D. Werner, C.E. Taylor, J.E. Moore, II, J.S. Walton and S. Cho, 12/31/00, (PB2001-108756, A14, MF-A03).

- MCEER-01-0001 “Experimental Investigation of P-Delta Effects to Collapse During Earthquakes,” by D. Vian and M. Bruneau, 6/25/01, (PB2002-100534, A17, MF-A03).
- MCEER-01-0002 “Proceedings of the Second MCEER Workshop on Mitigation of Earthquake Disaster by Advanced Technologies (MEDAT-2),” edited by M. Bruneau and D.J. Inman, 7/23/01, (PB2002-100434, A16, MF-A03).
- MCEER-01-0003 “Sensitivity Analysis of Dynamic Systems Subjected to Seismic Loads,” by C. Roth and M. Grigoriu, 9/18/01, (PB2003-100884, A12, MF-A03).
- MCEER-01-0004 “Overcoming Obstacles to Implementing Earthquake Hazard Mitigation Policies: Stage 1 Report,” by D.J. Alesch and W.J. Petak, 12/17/01, (PB2002-107949, A07, MF-A02).
- MCEER-01-0005 “Updating Real-Time Earthquake Loss Estimates: Methods, Problems and Insights,” by C.E. Taylor, S.E. Chang and R.T. Eguchi, 12/17/01, (PB2002-107948, A05, MF-A01).
- MCEER-01-0006 “Experimental Investigation and Retrofit of Steel Pile Foundations and Pile Bents Under Cyclic Lateral Loadings,” by A. Shama, J. Mander, B. Blabac and S. Chen, 12/31/01, (PB2002-107950, A13, MF-A03).
- MCEER-02-0001 “Assessment of Performance of Bolu Viaduct in the 1999 Duzce Earthquake in Turkey” by P.C. Roussis, M.C. Constantinou, M. Erdik, E. Durukal and M. Dicleli, 5/8/02, (PB2003-100883, A08, MF-A02).
- MCEER-02-0002 “Seismic Behavior of Rail Counterweight Systems of Elevators in Buildings,” by M.P. Singh, Rildova and L.E. Suarez, 5/27/02. (PB2003-100882, A11, MF-A03).
- MCEER-02-0003 “Development of Analysis and Design Procedures for Spread Footings,” by G. Mylonakis, G. Gazetas, S. Nikolaou and A. Chauncey, 10/02/02, (PB2004-101636, A13, MF-A03, CD-A13).
- MCEER-02-0004 “Bare-Earth Algorithms for Use with SAR and LIDAR Digital Elevation Models,” by C.K. Huyck, R.T. Eguchi and B. Houshmand, 10/16/02, (PB2004-101637, A07, CD-A07).
- MCEER-02-0005 “Review of Energy Dissipation of Compression Members in Concentrically Braced Frames,” by K.Lee and M. Bruneau, 10/18/02, (PB2004-101638, A10, CD-A10).
- MCEER-03-0001 “Experimental Investigation of Light-Gauge Steel Plate Shear Walls for the Seismic Retrofit of Buildings” by J. Berman and M. Bruneau, 5/2/03, (PB2004-101622, A10, MF-A03, CD-A10).
- MCEER-03-0002 “Statistical Analysis of Fragility Curves,” by M. Shinozuka, M.Q. Feng, H. Kim, T. Uzawa and T. Ueda, 6/16/03, (PB2004-101849, A09, CD-A09).
- MCEER-03-0003 “Proceedings of the Eighth U.S.-Japan Workshop on Earthquake Resistant Design of Lifeline Facilities and Countermeasures Against Liquefaction,” edited by M. Hamada, J.P. Bardet and T.D. O’Rourke, 6/30/03, (PB2004-104386, A99, CD-A99).
- MCEER-03-0004 “Proceedings of the PRC-US Workshop on Seismic Analysis and Design of Special Bridges,” edited by L.C. Fan and G.C. Lee, 7/15/03, (PB2004-104387, A14, CD-A14).
- MCEER-03-0005 “Urban Disaster Recovery: A Framework and Simulation Model,” by S.B. Miles and S.E. Chang, 7/25/03, (PB2004-104388, A07, CD-A07).
- MCEER-03-0006 “Behavior of Underground Piping Joints Due to Static and Dynamic Loading,” by R.D. Meis, M. Maragakis and R. Siddharthan, 11/17/03, (PB2005-102194, A13, MF-A03, CD-A00).
- MCEER-04-0001 “Experimental Study of Seismic Isolation Systems with Emphasis on Secondary System Response and Verification of Accuracy of Dynamic Response History Analysis Methods,” by E. Wolff and M. Constantinou, 1/16/04 (PB2005-102195, A99, MF-E08, CD-A00).
- MCEER-04-0002 “Tension, Compression and Cyclic Testing of Engineered Cementitious Composite Materials,” by K. Kesner and S.L. Billington, 3/1/04, (PB2005-102196, A08, CD-A08).

- MCEER-04-0003 “Cyclic Testing of Braces Laterally Restrained by Steel Studs to Enhance Performance During Earthquakes,” by O.C. Celik, J.W. Berman and M. Bruneau, 3/16/04, (PB2005-102197, A13, MF-A03, CD-A00).
- MCEER-04-0004 “Methodologies for Post Earthquake Building Damage Detection Using SAR and Optical Remote Sensing: Application to the August 17, 1999 Marmara, Turkey Earthquake,” by C.K. Huyck, B.J. Adams, S. Cho, R.T. Eguchi, B. Mansouri and B. Houshmand, 6/15/04, (PB2005-104888, A10, CD-A00).
- MCEER-04-0005 “Nonlinear Structural Analysis Towards Collapse Simulation: A Dynamical Systems Approach,” by M.V. Sivaselvan and A.M. Reinhorn, 6/16/04, (PB2005-104889, A11, MF-A03, CD-A00).
- MCEER-04-0006 “Proceedings of the Second PRC-US Workshop on Seismic Analysis and Design of Special Bridges,” edited by G.C. Lee and L.C. Fan, 6/25/04, (PB2005-104890, A16, CD-A00).
- MCEER-04-0007 “Seismic Vulnerability Evaluation of Axially Loaded Steel Built-up Laced Members,” by K. Lee and M. Bruneau, 6/30/04, (PB2005-104891, A16, CD-A00).
- MCEER-04-0008 “Evaluation of Accuracy of Simplified Methods of Analysis and Design of Buildings with Damping Systems for Near-Fault and for Soft-Soil Seismic Motions,” by E.A. Pavlou and M.C. Constantinou, 8/16/04, (PB2005-104892, A08, MF-A02, CD-A00).
- MCEER-04-0009 “Assessment of Geotechnical Issues in Acute Care Facilities in California,” by M. Lew, T.D. O’Rourke, R. Dobry and M. Koch, 9/15/04, (PB2005-104893, A08, CD-A00).
- MCEER-04-0010 “Scissor-Jack-Damper Energy Dissipation System,” by A.N. Sigaher-Boyle and M.C. Constantinou, 12/1/04 (PB2005-108221).
- MCEER-04-0011 “Seismic Retrofit of Bridge Steel Truss Piers Using a Controlled Rocking Approach,” by M. Pollino and M. Bruneau, 12/20/04 (PB2006-105795).
- MCEER-05-0001 “Experimental and Analytical Studies of Structures Seismically Isolated with an Uplift-Restraint Isolation System,” by P.C. Roussis and M.C. Constantinou, 1/10/05 (PB2005-108222).
- MCEER-05-0002 “A Versatile Experimentation Model for Study of Structures Near Collapse Applied to Seismic Evaluation of Irregular Structures,” by D. Kusumastuti, A.M. Reinhorn and A. Rutenberg, 3/31/05 (PB2006-101523).
- MCEER-05-0003 “Proceedings of the Third PRC-US Workshop on Seismic Analysis and Design of Special Bridges,” edited by L.C. Fan and G.C. Lee, 4/20/05, (PB2006-105796).
- MCEER-05-0004 “Approaches for the Seismic Retrofit of Braced Steel Bridge Piers and Proof-of-Concept Testing of an Eccentrically Braced Frame with Tubular Link,” by J.W. Berman and M. Bruneau, 4/21/05 (PB2006-101524).
- MCEER-05-0005 “Simulation of Strong Ground Motions for Seismic Fragility Evaluation of Nonstructural Components in Hospitals,” by A. Wanitkorkul and A. Filiatrault, 5/26/05 (PB2006-500027).
- MCEER-05-0006 “Seismic Safety in California Hospitals: Assessing an Attempt to Accelerate the Replacement or Seismic Retrofit of Older Hospital Facilities,” by D.J. Alesch, L.A. Arendt and W.J. Petak, 6/6/05 (PB2006-105794).
- MCEER-05-0007 “Development of Seismic Strengthening and Retrofit Strategies for Critical Facilities Using Engineered Cementitious Composite Materials,” by K. Kesner and S.L. Billington, 8/29/05 (PB2006-111701).
- MCEER-05-0008 “Experimental and Analytical Studies of Base Isolation Systems for Seismic Protection of Power Transformers,” by N. Murota, M.Q. Feng and G-Y. Liu, 9/30/05 (PB2006-111702).
- MCEER-05-0009 “3D-BASIS-ME-MB: Computer Program for Nonlinear Dynamic Analysis of Seismically Isolated Structures,” by P.C. Tsopelas, P.C. Roussis, M.C. Constantinou, R. Buchanan and A.M. Reinhorn, 10/3/05 (PB2006-111703).
- MCEER-05-0010 “Steel Plate Shear Walls for Seismic Design and Retrofit of Building Structures,” by D. Vian and M. Bruneau, 12/15/05 (PB2006-111704).

- MCEER-05-0011 "The Performance-Based Design Paradigm," by M.J. Astrella and A. Whittaker, 12/15/05 (PB2006-111705).
- MCEER-06-0001 "Seismic Fragility of Suspended Ceiling Systems," H. Badillo-Almaraz, A.S. Whittaker, A.M. Reinhorn and G.P. Cimellaro, 2/4/06 (PB2006-111706).
- MCEER-06-0002 "Multi-Dimensional Fragility of Structures," by G.P. Cimellaro, A.M. Reinhorn and M. Bruneau, 3/1/06 (PB2007-106974, A09, MF-A02, CD A00).
- MCEER-06-0003 "Built-Up Shear Links as Energy Dissipators for Seismic Protection of Bridges," by P. Dusicka, A.M. Itani and I.G. Buckle, 3/15/06 (PB2006-111708).
- MCEER-06-0004 "Analytical Investigation of the Structural Fuse Concept," by R.E. Vargas and M. Bruneau, 3/16/06 (PB2006-111709).
- MCEER-06-0005 "Experimental Investigation of the Structural Fuse Concept," by R.E. Vargas and M. Bruneau, 3/17/06 (PB2006-111710).
- MCEER-06-0006 "Further Development of Tubular Eccentrically Braced Frame Links for the Seismic Retrofit of Braced Steel Truss Bridge Piers," by J.W. Berman and M. Bruneau, 3/27/06 (PB2007-105147).
- MCEER-06-0007 "REDARS Validation Report," by S. Cho, C.K. Huyck, S. Ghosh and R.T. Eguchi, 8/8/06 (PB2007-106983).
- MCEER-06-0008 "Review of Current NDE Technologies for Post-Earthquake Assessment of Retrofitted Bridge Columns," by J.W. Song, Z. Liang and G.C. Lee, 8/21/06 (PB2007-106984).
- MCEER-06-0009 "Liquefaction Remediation in Silty Soils Using Dynamic Compaction and Stone Columns," by S. Thevanayagam, G.R. Martin, R. Nashed, T. Shenthan, T. Kanagalingam and N. Ecemis, 8/28/06 (PB2007-106985).
- MCEER-06-0010 "Conceptual Design and Experimental Investigation of Polymer Matrix Composite Infill Panels for Seismic Retrofitting," by W. Jung, M. Chiewanichakorn and A.J. Aref, 9/21/06 (PB2007-106986).
- MCEER-06-0011 "A Study of the Coupled Horizontal-Vertical Behavior of Elastomeric and Lead-Rubber Seismic Isolation Bearings," by G.P. Warn and A.S. Whittaker, 9/22/06 (PB2007-108679).
- MCEER-06-0012 "Proceedings of the Fourth PRC-US Workshop on Seismic Analysis and Design of Special Bridges: Advancing Bridge Technologies in Research, Design, Construction and Preservation," Edited by L.C. Fan, G.C. Lee and L. Ziang, 10/12/06 (PB2007-109042).
- MCEER-06-0013 "Cyclic Response and Low Cycle Fatigue Characteristics of Plate Steels," by P. Dusicka, A.M. Itani and I.G. Buckle, 11/1/06 (PB2007-106987).
- MCEER-06-0014 "Proceedings of the Second US-Taiwan Bridge Engineering Workshop," edited by W.P. Yen, J. Shen, J-Y. Chen and M. Wang, 11/15/06 (PB2008-500041).
- MCEER-06-0015 "User Manual and Technical Documentation for the REDARSTM Import Wizard," by S. Cho, S. Ghosh, C.K. Huyck and S.D. Werner, 11/30/06 (PB2007-114766).
- MCEER-06-0016 "Hazard Mitigation Strategy and Monitoring Technologies for Urban and Infrastructure Public Buildings: Proceedings of the China-US Workshops," edited by X.Y. Zhou, A.L. Zhang, G.C. Lee and M. Tong, 12/12/06 (PB2008-500018).
- MCEER-07-0001 "Static and Kinetic Coefficients of Friction for Rigid Blocks," by C. Kafali, S. Fathali, M. Grigoriu and A.S. Whittaker, 3/20/07 (PB2007-114767).
- MCEER-07-0002 "Hazard Mitigation Investment Decision Making: Organizational Response to Legislative Mandate," by L.A. Arendt, D.J. Alesch and W.J. Petak, 4/9/07 (PB2007-114768).
- MCEER-07-0003 "Seismic Behavior of Bidirectional-Resistant Ductile End Diaphragms with Unbonded Braces in Straight or Skewed Steel Bridges," by O. Celik and M. Bruneau, 4/11/07 (PB2008-105141).

- MCEER-07-0004 "Modeling Pile Behavior in Large Pile Groups Under Lateral Loading," by A.M. Dodds and G.R. Martin, 4/16/07(PB2008-105142).
- MCEER-07-0005 "Experimental Investigation of Blast Performance of Seismically Resistant Concrete-Filled Steel Tube Bridge Piers," by S. Fujikura, M. Bruneau and D. Lopez-Garcia, 4/20/07 (PB2008-105143).
- MCEER-07-0006 "Seismic Analysis of Conventional and Isolated Liquefied Natural Gas Tanks Using Mechanical Analogs," by I.P. Christovasilis and A.S. Whittaker, 5/1/07, not available.
- MCEER-07-0007 "Experimental Seismic Performance Evaluation of Isolation/Restraint Systems for Mechanical Equipment – Part 1: Heavy Equipment Study," by S. Fathali and A. Filiatrault, 6/6/07 (PB2008-105144).
- MCEER-07-0008 "Seismic Vulnerability of Timber Bridges and Timber Substructures," by A.A. Sharma, J.B. Mander, I.M. Friedland and D.R. Allicock, 6/7/07 (PB2008-105145).
- MCEER-07-0009 "Experimental and Analytical Study of the XY-Friction Pendulum (XY-FP) Bearing for Bridge Applications," by C.C. Marin-Artieda, A.S. Whittaker and M.C. Constantinou, 6/7/07 (PB2008-105191).
- MCEER-07-0010 "Proceedings of the PRC-US Earthquake Engineering Forum for Young Researchers," Edited by G.C. Lee and X.Z. Qi, 6/8/07 (PB2008-500058).
- MCEER-07-0011 "Design Recommendations for Perforated Steel Plate Shear Walls," by R. Purba and M. Bruneau, 6/18/07, (PB2008-105192).
- MCEER-07-0012 "Performance of Seismic Isolation Hardware Under Service and Seismic Loading," by M.C. Constantinou, A.S. Whittaker, Y. Kalpakidis, D.M. Fenz and G.P. Warn, 8/27/07, (PB2008-105193).
- MCEER-07-0013 "Experimental Evaluation of the Seismic Performance of Hospital Piping Subassemblies," by E.R. Goodwin, E. Maragakis and A.M. Itani, 9/4/07, (PB2008-105194).
- MCEER-07-0014 "A Simulation Model of Urban Disaster Recovery and Resilience: Implementation for the 1994 Northridge Earthquake," by S. Miles and S.E. Chang, 9/7/07, (PB2008-106426).
- MCEER-07-0015 "Statistical and Mechanistic Fragility Analysis of Concrete Bridges," by M. Shinozuka, S. Banerjee and S-H. Kim, 9/10/07, (PB2008-106427).
- MCEER-07-0016 "Three-Dimensional Modeling of Inelastic Buckling in Frame Structures," by M. Schachter and AM. Reinhorn, 9/13/07, (PB2008-108125).
- MCEER-07-0017 "Modeling of Seismic Wave Scattering on Pile Groups and Caissons," by I. Po Lam, H. Law and C.T. Yang, 9/17/07 (PB2008-108150).
- MCEER-07-0018 "Bridge Foundations: Modeling Large Pile Groups and Caissons for Seismic Design," by I. Po Lam, H. Law and G.R. Martin (Coordinating Author), 12/1/07 (PB2008-111190).
- MCEER-07-0019 "Principles and Performance of Roller Seismic Isolation Bearings for Highway Bridges," by G.C. Lee, Y.C. Ou, Z. Liang, T.C. Niu and J. Song, 12/10/07 (PB2009-110466).
- MCEER-07-0020 "Centrifuge Modeling of Permeability and Pinning Reinforcement Effects on Pile Response to Lateral Spreading," by L.L. Gonzalez-Lagos, T. Abdoun and R. Dobry, 12/10/07 (PB2008-111191).
- MCEER-07-0021 "Damage to the Highway System from the Pisco, Perú Earthquake of August 15, 2007," by J.S. O'Connor, L. Mesa and M. Nykamp, 12/10/07, (PB2008-108126).
- MCEER-07-0022 "Experimental Seismic Performance Evaluation of Isolation/Restraint Systems for Mechanical Equipment – Part 2: Light Equipment Study," by S. Fathali and A. Filiatrault, 12/13/07 (PB2008-111192).
- MCEER-07-0023 "Fragility Considerations in Highway Bridge Design," by M. Shinozuka, S. Banerjee and S.H. Kim, 12/14/07 (PB2008-111193).

- MCEER-07-0024 "Performance Estimates for Seismically Isolated Bridges," by G.P. Warn and A.S. Whittaker, 12/30/07 (PB2008-112230).
- MCEER-08-0001 "Seismic Performance of Steel Girder Bridge Superstructures with Conventional Cross Frames," by L.P. Carden, A.M. Itani and I.G. Buckle, 1/7/08, (PB2008-112231).
- MCEER-08-0002 "Seismic Performance of Steel Girder Bridge Superstructures with Ductile End Cross Frames with Seismic Isolators," by L.P. Carden, A.M. Itani and I.G. Buckle, 1/7/08 (PB2008-112232).
- MCEER-08-0003 "Analytical and Experimental Investigation of a Controlled Rocking Approach for Seismic Protection of Bridge Steel Truss Piers," by M. Pollino and M. Bruneau, 1/21/08 (PB2008-112233).
- MCEER-08-0004 "Linking Lifeline Infrastructure Performance and Community Disaster Resilience: Models and Multi-Stakeholder Processes," by S.E. Chang, C. Pasion, K. Tatebe and R. Ahmad, 3/3/08 (PB2008-112234).
- MCEER-08-0005 "Modal Analysis of Generally Damped Linear Structures Subjected to Seismic Excitations," by J. Song, Y-L. Chu, Z. Liang and G.C. Lee, 3/4/08 (PB2009-102311).
- MCEER-08-0006 "System Performance Under Multi-Hazard Environments," by C. Kafali and M. Grigoriu, 3/4/08 (PB2008-112235).
- MCEER-08-0007 "Mechanical Behavior of Multi-Spherical Sliding Bearings," by D.M. Fenz and M.C. Constantinou, 3/6/08 (PB2008-112236).
- MCEER-08-0008 "Post-Earthquake Restoration of the Los Angeles Water Supply System," by T.H.P. Tabucchi and R.A. Davidson, 3/7/08 (PB2008-112237).
- MCEER-08-0009 "Fragility Analysis of Water Supply Systems," by A. Jacobson and M. Grigoriu, 3/10/08 (PB2009-105545).
- MCEER-08-0010 "Experimental Investigation of Full-Scale Two-Story Steel Plate Shear Walls with Reduced Beam Section Connections," by B. Qu, M. Bruneau, C-H. Lin and K-C. Tsai, 3/17/08 (PB2009-106368).
- MCEER-08-0011 "Seismic Evaluation and Rehabilitation of Critical Components of Electrical Power Systems," S. Ersoy, B. Feizi, A. Ashrafi and M. Ala Saadeghvaziri, 3/17/08 (PB2009-105546).
- MCEER-08-0012 "Seismic Behavior and Design of Boundary Frame Members of Steel Plate Shear Walls," by B. Qu and M. Bruneau, 4/26/08 . (PB2009-106744).
- MCEER-08-0013 "Development and Appraisal of a Numerical Cyclic Loading Protocol for Quantifying Building System Performance," by A. Filiatrault, A. Wanitkorkul and M. Constantinou, 4/27/08 (PB2009-107906).
- MCEER-08-0014 "Structural and Nonstructural Earthquake Design: The Challenge of Integrating Specialty Areas in Designing Complex, Critical Facilities," by W.J. Petak and D.J. Alesch, 4/30/08 (PB2009-107907).
- MCEER-08-0015 "Seismic Performance Evaluation of Water Systems," by Y. Wang and T.D. O'Rourke, 5/5/08 (PB2009-107908).
- MCEER-08-0016 "Seismic Response Modeling of Water Supply Systems," by P. Shi and T.D. O'Rourke, 5/5/08 (PB2009-107910).
- MCEER-08-0017 "Numerical and Experimental Studies of Self-Centering Post-Tensioned Steel Frames," by D. Wang and A. Filiatrault, 5/12/08 (PB2009-110479).
- MCEER-08-0018 "Development, Implementation and Verification of Dynamic Analysis Models for Multi-Spherical Sliding Bearings," by D.M. Fenz and M.C. Constantinou, 8/15/08 (PB2009-107911).
- MCEER-08-0019 "Performance Assessment of Conventional and Base Isolated Nuclear Power Plants for Earthquake Blast Loadings," by Y.N. Huang, A.S. Whittaker and N. Luco, 10/28/08 (PB2009-107912).

- MCEER-08-0020 “Remote Sensing for Resilient Multi-Hazard Disaster Response – Volume I: Introduction to Damage Assessment Methodologies,” by B.J. Adams and R.T. Eguchi, 11/17/08 (PB2010-102695).
- MCEER-08-0021 “Remote Sensing for Resilient Multi-Hazard Disaster Response – Volume II: Counting the Number of Collapsed Buildings Using an Object-Oriented Analysis: Case Study of the 2003 Bam Earthquake,” by L. Gusella, C.K. Huyck and B.J. Adams, 11/17/08 (PB2010-100925).
- MCEER-08-0022 “Remote Sensing for Resilient Multi-Hazard Disaster Response – Volume III: Multi-Sensor Image Fusion Techniques for Robust Neighborhood-Scale Urban Damage Assessment,” by B.J. Adams and A. McMillan, 11/17/08 (PB2010-100926).
- MCEER-08-0023 “Remote Sensing for Resilient Multi-Hazard Disaster Response – Volume IV: A Study of Multi-Temporal and Multi-Resolution SAR Imagery for Post-Katrina Flood Monitoring in New Orleans,” by A. McMillan, J.G. Morley, B.J. Adams and S. Chesworth, 11/17/08 (PB2010-100927).
- MCEER-08-0024 “Remote Sensing for Resilient Multi-Hazard Disaster Response – Volume V: Integration of Remote Sensing Imagery and VIEWS™ Field Data for Post-Hurricane Charley Building Damage Assessment,” by J.A. Womble, K. Mehta and B.J. Adams, 11/17/08 (PB2009-115532).
- MCEER-08-0025 “Building Inventory Compilation for Disaster Management: Application of Remote Sensing and Statistical Modeling,” by P. Sarabandi, A.S. Kiremidjian, R.T. Eguchi and B. J. Adams, 11/20/08 (PB2009-110484).
- MCEER-08-0026 “New Experimental Capabilities and Loading Protocols for Seismic Qualification and Fragility Assessment of Nonstructural Systems,” by R. Retamales, G. Mosqueda, A. Filiatrault and A. Reinhorn, 11/24/08 (PB2009-110485).
- MCEER-08-0027 “Effects of Heating and Load History on the Behavior of Lead-Rubber Bearings,” by I.V. Kalpakidis and M.C. Constantinou, 12/1/08 (PB2009-115533).
- MCEER-08-0028 “Experimental and Analytical Investigation of Blast Performance of Seismically Resistant Bridge Piers,” by S.Fujikura and M. Bruneau, 12/8/08 (PB2009-115534).
- MCEER-08-0029 “Evolutionary Methodology for Aseismic Decision Support,” by Y. Hu and G. Dargush, 12/15/08.
- MCEER-08-0030 “Development of a Steel Plate Shear Wall Bridge Pier System Conceived from a Multi-Hazard Perspective,” by D. Keller and M. Bruneau, 12/19/08 (PB2010-102696).
- MCEER-09-0001 “Modal Analysis of Arbitrarily Damped Three-Dimensional Linear Structures Subjected to Seismic Excitations,” by Y.L. Chu, J. Song and G.C. Lee, 1/31/09 (PB2010-100922).
- MCEER-09-0002 “Air-Blast Effects on Structural Shapes,” by G. Ballantyne, A.S. Whittaker, A.J. Aref and G.F. Dargush, 2/2/09 (PB2010-102697).
- MCEER-09-0003 “Water Supply Performance During Earthquakes and Extreme Events,” by A.L. Bonneau and T.D. O’Rourke, 2/16/09 (PB2010-100923).
- MCEER-09-0004 “Generalized Linear (Mixed) Models of Post-Earthquake Ignitions,” by R.A. Davidson, 7/20/09 (PB2010-102698).
- MCEER-09-0005 “Seismic Testing of a Full-Scale Two-Story Light-Frame Wood Building: NEESWood Benchmark Test,” by I.P. Christovasilis, A. Filiatrault and A. Wanitkorkul, 7/22/09 (PB2012-102401).
- MCEER-09-0006 “IDARC2D Version 7.0: A Program for the Inelastic Damage Analysis of Structures,” by A.M. Reinhorn, H. Roh, M. Sivaselvan, S.K. Kunnath, R.E. Valles, A. Madan, C. Li, R. Lobo and Y.J. Park, 7/28/09 (PB2010-103199).
- MCEER-09-0007 “Enhancements to Hospital Resiliency: Improving Emergency Planning for and Response to Hurricanes,” by D.B. Hess and L.A. Arendt, 7/30/09 (PB2010-100924).

- MCEER-09-0008 “Assessment of Base-Isolated Nuclear Structures for Design and Beyond-Design Basis Earthquake Shaking,” by Y.N. Huang, A.S. Whittaker, R.P. Kennedy and R.L. Mayes, 8/20/09 (PB2010-102699).
- MCEER-09-0009 “Quantification of Disaster Resilience of Health Care Facilities,” by G.P. Cimellaro, C. Fumo, A.M. Reinhorn and M. Bruneau, 9/14/09 (PB2010-105384).
- MCEER-09-0010 “Performance-Based Assessment and Design of Squat Reinforced Concrete Shear Walls,” by C.K. Gulec and A.S. Whittaker, 9/15/09 (PB2010-102700).
- MCEER-09-0011 “Proceedings of the Fourth US-Taiwan Bridge Engineering Workshop,” edited by W.P. Yen, J.J. Shen, T.M. Lee and R.B. Zheng, 10/27/09 (PB2010-500009).
- MCEER-09-0012 “Proceedings of the Special International Workshop on Seismic Connection Details for Segmental Bridge Construction,” edited by W. Phillip Yen and George C. Lee, 12/21/09 (PB2012-102402).
- MCEER-10-0001 “Direct Displacement Procedure for Performance-Based Seismic Design of Multistory Woodframe Structures,” by W. Pang and D. Rosowsky, 4/26/10 (PB2012-102403).
- MCEER-10-0002 “Simplified Direct Displacement Design of Six-Story NEESWood Capstone Building and Pre-Test Seismic Performance Assessment,” by W. Pang, D. Rosowsky, J. van de Lindt and S. Pei, 5/28/10 (PB2012-102404).
- MCEER-10-0003 “Integration of Seismic Protection Systems in Performance-Based Seismic Design of Woodframed Structures,” by J.K. Shinde and M.D. Symans, 6/18/10 (PB2012-102405).
- MCEER-10-0004 “Modeling and Seismic Evaluation of Nonstructural Components: Testing Frame for Experimental Evaluation of Suspended Ceiling Systems,” by A.M. Reinhorn, K.P. Ryu and G. Maddaloni, 6/30/10 (PB2012-102406).
- MCEER-10-0005 “Analytical Development and Experimental Validation of a Structural-Fuse Bridge Pier Concept,” by S. El-Bahey and M. Bruneau, 10/1/10 (PB2012-102407).
- MCEER-10-0006 “A Framework for Defining and Measuring Resilience at the Community Scale: The PEOPLES Resilience Framework,” by C.S. Renschler, A.E. Frazier, L.A. Arendt, G.P. Cimellaro, A.M. Reinhorn and M. Bruneau, 10/8/10 (PB2012-102408).
- MCEER-10-0007 “Impact of Horizontal Boundary Elements Design on Seismic Behavior of Steel Plate Shear Walls,” by R. Purba and M. Bruneau, 11/14/10 (PB2012-102409).
- MCEER-10-0008 “Seismic Testing of a Full-Scale Mid-Rise Building: The NEESWood Capstone Test,” by S. Pei, J.W. van de Lindt, S.E. Pryor, H. Shimizu, H. Isoda and D.R. Rammer, 12/1/10 (PB2012-102410).
- MCEER-10-0009 “Modeling the Effects of Detonations of High Explosives to Inform Blast-Resistant Design,” by P. Sherkar, A.S. Whittaker and A.J. Aref, 12/1/10 (PB2012-102411).
- MCEER-10-0010 “L’Aquila Earthquake of April 6, 2009 in Italy: Rebuilding a Resilient City to Withstand Multiple Hazards,” by G.P. Cimellaro, I.P. Christovasilis, A.M. Reinhorn, A. De Stefano and T. Kirova, 12/29/10.
- MCEER-11-0001 “Numerical and Experimental Investigation of the Seismic Response of Light-Frame Wood Structures,” by I.P. Christovasilis and A. Filiatrault, 8/8/11 (PB2012-102412).
- MCEER-11-0002 “Seismic Design and Analysis of a Precast Segmental Concrete Bridge Model,” by M. Anagnostopoulou, A. Filiatrault and A. Aref, 9/15/11.
- MCEER-11-0003 “Proceedings of the Workshop on Improving Earthquake Response of Substation Equipment,” Edited by A.M. Reinhorn, 9/19/11 (PB2012-102413).
- MCEER-11-0004 “LRFD-Based Analysis and Design Procedures for Bridge Bearings and Seismic Isolators,” by M.C. Constantinou, I. Kalpakidis, A. Filiatrault and R.A. Ecker Lay, 9/26/11.

- MCEER-11-0005 “Experimental Seismic Evaluation, Model Parameterization, and Effects of Cold-Formed Steel-Framed Gypsum Partition Walls on the Seismic Performance of an Essential Facility,” by R. Davies, R. Retamales, G. Mosqueda and A. Filiatrault, 10/12/11.
- MCEER-11-0006 “Modeling and Seismic Performance Evaluation of High Voltage Transformers and Bushings,” by A.M. Reinhorn, K. Oikonomou, H. Roh, A. Schiff and L. Kempner, Jr., 10/3/11.
- MCEER-11-0007 “Extreme Load Combinations: A Survey of State Bridge Engineers,” by G.C. Lee, Z. Liang, J.J. Shen and J.S. O’Connor, 10/14/11.
- MCEER-12-0001 “Simplified Analysis Procedures in Support of Performance Based Seismic Design,” by Y.N. Huang and A.S. Whittaker.
- MCEER-12-0002 “Seismic Protection of Electrical Transformer Bushing Systems by Stiffening Techniques,” by M. Koliou, A. Filiatrault, A.M. Reinhorn and N. Oliveto, 6/1/12.
- MCEER-12-0003 “Post-Earthquake Bridge Inspection Guidelines,” by J.S. O’Connor and S. Alampalli, 6/8/12.
- MCEER-12-0004 “Integrated Design Methodology for Isolated Floor Systems in Single-Degree-of-Freedom Structural Fuse Systems,” by S. Cui, M. Bruneau and M.C. Constantinou, 6/13/12.
- MCEER-12-0005 “Characterizing the Rotational Components of Earthquake Ground Motion,” by D. Basu, A.S. Whittaker and M.C. Constantinou, 6/15/12.
- MCEER-12-0006 “Bayesian Fragility for Nonstructural Systems,” by C.H. Lee and M.D. Grigoriu, 9/12/12.
- MCEER-12-0007 “A Numerical Model for Capturing the In-Plane Seismic Response of Interior Metal Stud Partition Walls,” by R.L. Wood and T.C. Hutchinson, 9/12/12.
- MCEER-12-0008 “Assessment of Floor Accelerations in Yielding Buildings,” by J.D. Wieser, G. Pekcan, A.E. Zaghi, A.M. Itani and E. Maragakis, 10/5/12.
- MCEER-13-0001 “Experimental Seismic Study of Pressurized Fire Sprinkler Piping Systems,” by Y. Tian, A. Filiatrault and G. Mosqueda, 4/8/13.
- MCEER-13-0002 “Enhancing Resource Coordination for Multi-Modal Evacuation Planning,” by D.B. Hess, B.W. Conley and C.M. Farrell, 2/8/13.
- MCEER-13-0003 “Seismic Response of Base Isolated Buildings Considering Pounding to Moat Walls,” by A. Masroor and G. Mosqueda, 2/26/13.
- MCEER-13-0004 “Seismic Response Control of Structures Using a Novel Adaptive Passive Negative Stiffness Device,” by D.T.R. Pasala, A.A. Sarlis, S. Nagarajaiah, A.M. Reinhorn, M.C. Constantinou and D.P. Taylor, 6/10/13.
- MCEER-13-0005 “Negative Stiffness Device for Seismic Protection of Structures,” by A.A. Sarlis, D.T.R. Pasala, M.C. Constantinou, A.M. Reinhorn, S. Nagarajaiah and D.P. Taylor, 6/12/13.
- MCEER-13-0006 “Emilia Earthquake of May 20, 2012 in Northern Italy: Rebuilding a Resilient Community to Withstand Multiple Hazards,” by G.P. Cimellaro, M. Chiriatti, A.M. Reinhorn and L. Tirca, June 30, 2013.
- MCEER-13-0007 “Precast Concrete Segmental Components and Systems for Accelerated Bridge Construction in Seismic Regions,” by A.J. Aref, G.C. Lee, Y.C. Ou and P. Sideris, with contributions from K.C. Chang, S. Chen, A. Filiatrault and Y. Zhou, June 13, 2013.
- MCEER-13-0008 “A Study of U.S. Bridge Failures (1980-2012),” by G.C. Lee, S.B. Mohan, C. Huang and B.N. Fard, June 15, 2013.
- MCEER-13-0009 “Development of a Database Framework for Modeling Damaged Bridges,” by G.C. Lee, J.C. Qi and C. Huang, June 16, 2013.

- MCEER-13-0010 “Model of Triple Friction Pendulum Bearing for General Geometric and Frictional Parameters and for Uplift Conditions,” by A.A. Sarlis and M.C. Constantinou, July 1, 2013.
- MCEER-13-0011 “Shake Table Testing of Triple Friction Pendulum Isolators under Extreme Conditions,” by A.A. Sarlis, M.C. Constantinou and A.M. Reinhorn, July 2, 2013.
- MCEER-13-0012 “Theoretical Framework for the Development of MH-LRFD,” by G.C. Lee (coordinating author), H.A. Capers, Jr., C. Huang, J.M. Kulicki, Z. Liang, T. Murphy, J.J.D. Shen, M. Shinozuka and P.W.H. Yen, July 31, 2013.
- MCEER-13-0013 “Seismic Protection of Highway Bridges with Negative Stiffness Devices,” by N.K.A. Attary, M.D. Symans, S. Nagarajaiah, A.M. Reinhorn, M.C. Constantinou, A.A. Sarlis, D.T.R. Pasala, and D.P. Taylor, September 3, 2014.
- MCEER-14-0001 “Simplified Seismic Collapse Capacity-Based Evaluation and Design of Frame Buildings with and without Supplemental Damping Systems,” by M. Hamidia, A. Filiatrault, and A. Aref, May 19, 2014.
- MCEER-14-0002 “Comprehensive Analytical Seismic Fragility of Fire Sprinkler Piping Systems,” by Siavash Soroushian, Emmanuel “Manos” Maragakis, Arash E. Zaghi, Alicia Echevarria, Yuan Tian and Andre Filiatrault, August 26, 2014.
- MCEER-14-0003 “Hybrid Simulation of the Seismic Response of a Steel Moment Frame Building Structure through Collapse,” by M. Del Carpio Ramos, G. Mosqueda and D.G. Lignos, October 30, 2014.
- MCEER-14-0004 “Blast and Seismic Resistant Concrete-Filled Double Skin Tubes and Modified Steel Jacketed Bridge Columns,” by P.P. Fouche and M. Bruneau, June 30, 2015.
- MCEER-14-0005 “Seismic Performance of Steel Plate Shear Walls Considering Various Design Approaches,” by R. Purba and M. Bruneau, October 31, 2014.
- MCEER-14-0006 “Air-Blast Effects on Civil Structures,” by Jinwon Shin, Andrew S. Whittaker, Amjad J. Aref and David Cormie, October 30, 2014.
- MCEER-14-0007 “Seismic Performance Evaluation of Precast Girders with Field-Cast Ultra High Performance Concrete (UHPC) Connections,” by G.C. Lee, C. Huang, J. Song, and J. S. O’Connor, July 31, 2014.
- MCEER-14-0008 “Post-Earthquake Fire Resistance of Ductile Concrete-Filled Double-Skin Tube Columns,” by Reza Imani, Gilberto Mosqueda and Michel Bruneau, December 1, 2014.
- MCEER-14-0009 “Cyclic Inelastic Behavior of Concrete Filled Sandwich Panel Walls Subjected to In-Plane Flexure,” by Y. Alzeni and M. Bruneau, December 19, 2014.
- MCEER-14-0010 “Analytical and Experimental Investigation of Self-Centering Steel Plate Shear Walls,” by D.M. Dowden and M. Bruneau, December 19, 2014.
- MCEER-15-0001 “Seismic Analysis of Multi-story Unreinforced Masonry Buildings with Flexible Diaphragms,” by J. Aleman, G. Mosqueda and A.S. Whittaker, June 12, 2015.
- MCEER-15-0002 “Site Response, Soil-Structure Interaction and Structure-Soil-Structure Interaction for Performance Assessment of Buildings and Nuclear Structures,” by C. Bolisetti and A.S. Whittaker, June 15, 2015.
- MCEER-15-0003 “Stress Wave Attenuation in Solids for Mitigating Impulsive Loadings,” by R. Rafiee-Dehkharghani, A.J. Aref and G. Dargush, August 15, 2015..
- MCEER-15-0004 “Computational, Analytical, and Experimental Modeling of Masonry Structures,” by K.M. Dolatshahi and A.J. Aref, November 16, 2015.



EARTHQUAKE ENGINEERING TO EXTREME EVENTS

University at Buffalo, The State University of New York

133A Ketter Hall ■ Buffalo, New York 14260-4300

Phone: (716) 645-3391 ■ Fax: (716) 645-3399

Email: mceer@buffalo.edu ■ Web: <http://mceer.buffalo.edu>



University at Buffalo The State University of New York

ISSN 1520-295X